

See discussions, stats, and author profiles for this publication at: <https://www.researchgate.net/publication/282914211>

Gold nanomaterials at work in biomedicine

DATASET · OCTOBER 2015

READS

43

5 AUTHORS, INCLUDING:



[Xuan Yang](#)

Georgia Institute of Technology

19 PUBLICATIONS 356 CITATIONS

SEE PROFILE



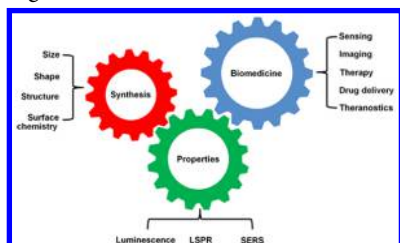
[Miaoxin Yang](#)

Georgia Institute of Technology

21 PUBLICATIONS 1,434 CITATIONS

SEE PROFILE

Gold Nanomaterials at Work in Biomedicine

Xuan Yang,[†] Miaoxin Yang,[‡] Bo Pang,[†] Madeline Vara,[‡] and Younan Xia^{*,†,‡,§}[†]The Wallace H. Coulter Department of Biomedical Engineering, Georgia Institute of Technology and Emory University, Atlanta, Georgia 30332, United States[‡]School of Chemistry and Biochemistry and [§]School of Chemical and Biomolecular Engineering, Georgia Institute of Technology, Atlanta, Georgia 30332, United States

CONTENTS

1. Introduction	10410	4.2.1. Imaging Based on Photoluminescence	10444
1.1. Gold Nanomaterials and Their Optical Properties	10411	4.2.2. Imaging Based on Elastic Light Scattering	10447
1.2. Other Properties of Gold Essential to Biomedical Applications	10412	4.2.3. Imaging Based on Inelastic Light Scattering	10448
1.3. Gold Nanomaterials at Work in Biomedicine	10413	4.2.4. Imaging Based on Photothermal Conversion	10449
2. Chemical Synthesis of Gold Nanomaterials	10414	4.3. Other Imaging Modalities	10451
2.1. Gold Clusters	10414	4.3.1. X-ray CT Imaging	10451
2.2. Conventional Gold Nanoparticles	10416	4.3.2. PET Imaging	10452
2.3. Gold Nanospheres	10418	4.3.3. Cerenkov Luminescence Imaging	10453
2.4. Gold Nanorods	10419	4.4. Drug Delivery	10454
2.5. Gold Nanoplates	10421	4.4.1. Drug Loading	10454
2.6. Gold Nanoshells	10422	4.4.2. Controlled Release	10456
2.7. Gold Nanoboxes, Nanocages, and Nanoframes	10424	4.4.3. Multidrug Resistance	10457
2.8. Other Types of Gold Nanostructures	10427	4.5. Cancer Therapy	10458
2.8.1. Polyhedral Nanocrystals	10427	4.5.1. Photothermal Therapy	10458
2.8.2. Nanostructures with Branched Arms	10428	4.5.2. Photodynamic Therapy	10460
2.9. Postsynthesis Surface Modification	10430	4.5.3. X-ray Radiotherapy	10460
3. Optical Properties of Gold Nanomaterials	10431	4.5.4. Combined Therapy	10461
3.1. Photoluminescence	10431	5. Pharmacokinetics, Biodistribution, Tumor Targeting, and Issues	10462
3.2. Localized Surface Plasmon Resonance	10433	5.1. In Vitro versus in Vivo Applications	10462
3.2.1. The Basics	10433	5.2. Pharmacokinetics	10462
3.2.2. The Mie Theory	10434	5.3. Biodistribution and Tumor Targeting	10462
3.2.3. Tuning Resonance Peaks into the Near-Infrared Region	10435	5.4. Toxicity and Clearance Issues	10465
3.2.4. Measuring the Optical Cross Sections	10436	5.4.1. Long-Term Toxicity	10465
3.3. Surface-Enhanced Raman Scattering	10438	5.4.2. Clearance from the Body	10465
4. Biomedical Applications of Gold Nanomaterials	10440	6. Concluding Remarks	10467
4.1. Optical Sensing	10440	Author Information	10468
4.1.1. Sensing Based on the Photoluminescence of Gold Clusters	10440	Corresponding Author	10468
4.1.2. Sensing Based on Localized Surface Plasmon Resonance	10442	Notes	10468
4.1.3. Sensing Based on Surface-Enhanced Raman Scattering	10443	Biographies	10468
4.1.4. Sensing Based on Photoluminescence Quenching	10444	Acknowledgments	10469
4.2. Optical Imaging	10444	References	10469

1. INTRODUCTION

Gold is a precious metal with a characteristic bright and beautiful hue known as the golden yellow color.¹ As of 2012, a total of 174,100 tons of Au has been mined in human history, which, in terms of volume, corresponds to roughly 9020 m³, or simply a solid cube of 21 m on each side.² If we were to evenly distribute all of this Au among the world population of 7

Special Issue: Nanoparticles in Medicine**Received:** March 31, 2015**Published:** August 21, 2015

billion, each person would be able to receive approximately 25 g, which is, fortunately, enough for crafting a typical wedding ring of approximately 20 g in mass. The current world consumption of newly produced Au is roughly 50% in jewelry, 40% in investments, and 10% in other industries.³ This market distribution can be largely attributed to the extremely low abundance of Au in the Earth's crust, which is only 5 parts per billion (ppb).⁴ The relative scarcity therefore makes Au one of the most valuable metals in the world, and a reason why it has been widely accepted as currency dating back to ancient times. The first international Au currency appeared in 564 B.C. when King Croesus improved the refining techniques for Au to mint the world's first standardized Au coin with a uniform Au content, named "croesid".⁵ The historical popularity of Au in the jewelry industry can be attributed to both its notable, long-lasting metal luster and its relative material rarity and value. Owing to its malleability, Au can also be easily formed into different shapes, and even hammered into very thin sheets or stretched into fine threads.^{6,7} Even goldsmiths in ancient times knew how to hammer Au into leaf as thin as 500 atoms thick (i.e., 144 nm). Such thin leafs later contributed to the development of modern science, providing one of the critical components (Au foil bombarded by α particles) for the Rutherford backscattering experiment, which led to the establishment of the atomic nucleus model.

When processed into sub-100 nm structures, Au shows a unique host of new properties distinct from bulk Au. In the fourth century, Au flakes were introduced into glass to craft the famous Lycurgus Cup, which can display complementary green or red color depending on how it is exposed to light. Later on, Au flakes were widely used in stained glass to produce church windows of various colors, notably the striking ruby red color shown in Figure 1A.⁸ These examples represent some of the earliest applications of manmade nanomaterials. At the time, the nanostructured nature of such materials remained unknown due to the critical lack of the scientific foundations and characterization tools needed for resolving such minuscule structures. Rather, artisans of those times relied purely on their experience to produce arts and crafts in a more or less controllable and reproducible fashion. The first scientific report on the production of Au nanomaterials can instead be traced to the ground-breaking work by Michael Faraday on Au colloids.⁹ In 1857, Faraday discovered that "fine particles" could be formed by treating aqueous HAuCl_4 with phosphorus dissolved in CS_2 in a two-phase system. The aqueous suspension of such "fine particles" displayed a beautiful, ruby red color (Figure 1B),¹⁰ completely distinct from the golden yellow color intrinsic to bulk Au. However, there was no theory at the time to explain why such "fine particles" would produce a ruby red color. It is interesting to note that studies over the past few decades have demonstrated that "fine particles" of Au can also be engineered to display an entire spectrum of varying colors (Figure 1C).¹¹

1.1. Gold Nanomaterials and Their Optical Properties

Following Faraday's discovery, many famous scientists, including Richard Zsigmondy and Theodor Svedberg (1925 and 1926 Nobel Laureates in Chemistry, respectively), studied these "fine particles", finally leading to their identification as nanoscale structures made of Au. In 1908, a German physicist named Gustav Mie further established, by solving the Maxwell equations, that the intense red color displayed by Faraday's samples could be attributed to the absorption and scattering of

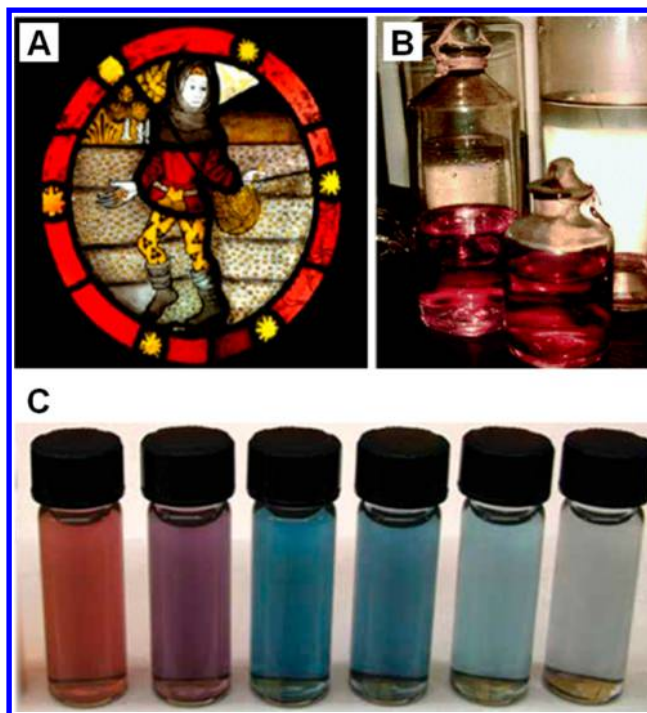


Figure 1. Examples of Au in a number of different formats: (A) nanoparticles in ancient church windows as indicated by the striking red stain, (B) nanoparticles in Faraday's colloidal samples, and (C) nanocages with different wall thicknesses and thus distinctive colors. (A) Reprinted with permission from ref 8. Copyright Victoria and Albert Museum, London. (B) Reprinted with permission from ref 10. Copyright Royal Institution. (C) Reprinted with permission from ref 11. Copyright 2007 Nature Publishing Group.

light by the Au nanoparticles contained within the samples.¹² When light impinges on a Au nanoparticle, the free electrons of the metal will immediately sense the electromagnetic field and begin to oscillate collectively relative to the lattice of positive ions at the same frequency as the incident light. Figure 2A shows a schematic illustration of this phenomenon for a Au nanosphere. This phenomenon is commonly known as localized surface plasmon resonance (LSPR), which can occur in any nanomaterial with an adequately high density of free electrons, including those made of metals and heavily doped semiconductors.^{13–17} In general, this process can be divided into two types of light-matter interactions: *scattering*, in which the incident light is re-radiated at the same frequency but into all directions, and *absorption*, in which the light is converted to heat (i.e., phonons or vibrations of the crystal lattice). Together, these two processes lead to extinction (extinction = scattering + absorption) or attenuation in intensity for the incident light. In addition, strong electric fields are generated on the surface of the nanostructure, which can be used to greatly enhance the optical signals (e.g., fluorescence or Raman scattering) arising from molecular species in the vicinity of the surface.^{18–22} As discussed in greater detail in section 4 of this review, these light-matter interactions can be harnessed to develop new probes or tools for biomedical applications.

The LSPR properties (e.g., the peak position and the ratio of scattering to absorption) of a Au nanostructure are determined by a number of parameters, including the size, shape, structure, and morphology, as well as the environment surrounding the surface of the nanostructure.¹³ In general, the LSPR peak of a Au nanostructure will be shifted when the dielectric constant of

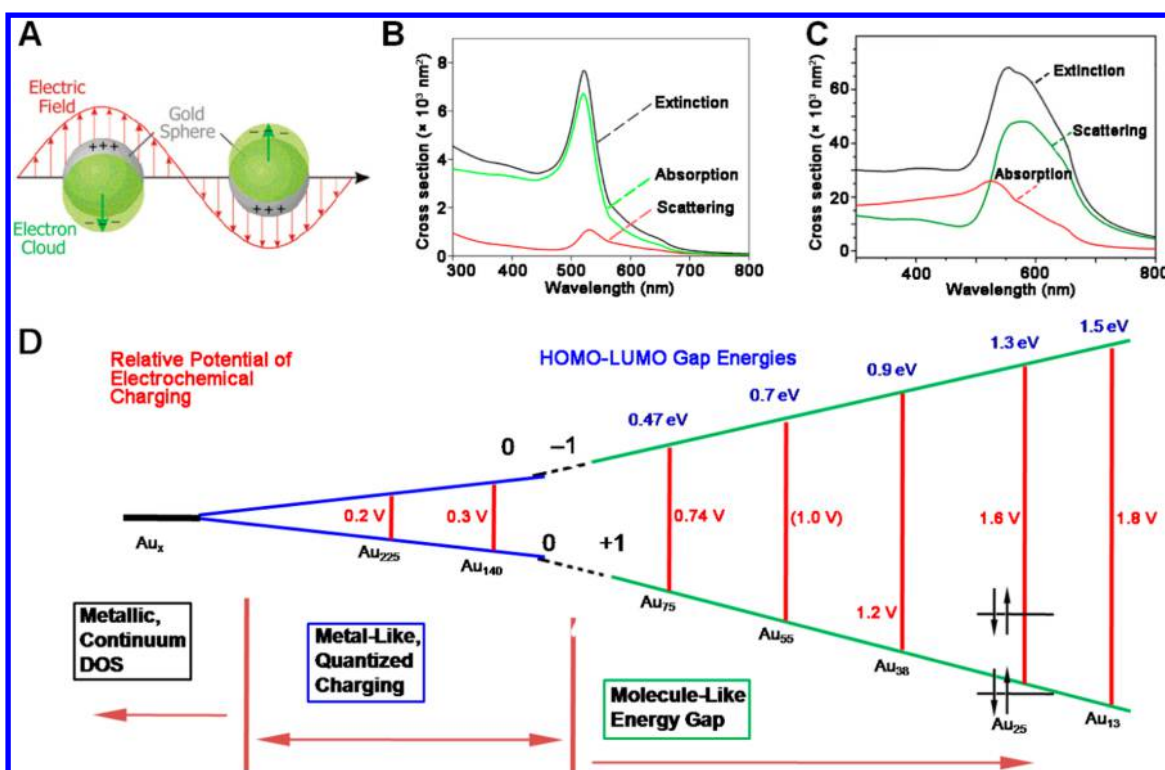


Figure 2. (A) Schematic illustration of the collective oscillation of free electrons in a Au nanosphere, which is responsible for the localized surface plasmon resonance (LSPR). (B) LSPR spectra calculated for a 50 nm Au nanosphere using the Mie theory. (C) LSPR spectra calculated for a 100 nm Au nanosphere using the Mie theory. (D) Summary of energy gaps (HOMO–LUMO gaps) and electrochemical energy gaps (the spacing between the first oxidation and the first reduction peaks) by the core size of Au nanoparticles (HOMO and LUMO stand for the highest occupied molecular orbital and the lowest unoccupied molecular orbital, respectively). (A–C) Reprinted with permission from ref 14. Copyright 2005 Materials Research Society. (D) Modified from ref 25. Copyright 2008 American Chemical Society.

the medium surrounding the nanostructure is altered, which can be employed for optical sensing. The LSPR peak position of Au nanostructures only shifts slightly when the size is changed. As shown in Figure 2B,¹⁴ Au nanospheres of 50 nm in diameter have an LSPR peak around 520 nm. The strong absorption at this wavelength (green color) gives an immediate explanation for the ruby red color (complementary to the green color) displayed by Faraday's samples of Au colloids. However, the LSPR peak shifted only to 550 nm when the Au nanospheres were enlarged to 100 nm in diameter (Figure 2C).¹⁴ For biomedical applications, we are most interested in Au nanostructures with LSPR peaks in the near-infrared region (NIR, 650–900 nm). At these wavelengths, light can readily penetrate deep into soft tissues because of the low absorption from blood and water as well as the low scattering from soft tissue.²³ To this end, we must rely on other parameters than size for appropriately tuning the LSPR peak of Au nanostructures to the NIR region: careful control of the shape or aspect ratio of nonspherical nanoparticles, or fine-tuning of the shell thickness in hollow or core–shell nanostructures.^{15,16} In these cases, even small variations in terms of corner sharpness, aspect ratio, or shell thickness can lead to large shifts in the LSPR peak position. Figure 1C shows a typical example with Au nanocages whose shell thickness decreases in samples going from left to right.¹¹ As such, the LSPR peaks of these nanocages could be tuned from 450 to 1200 nm. In addition, agglomeration of nanoparticles can lead to drastic red shifts for the LSPR peak position as the nanoparticles will interact with each other electromagnetically

when they approach one another.²⁴ More detailed discussions can be found in sections 3.2.3 and 4.1.2.

When the size of a Au nanoparticle is further reduced on a scale comparable to the Fermi wavelength of Au (approximately 0.5 nm), the band structure evolves into discrete energy levels (Figure 2D),²⁵ allowing for interactions with light through the electronic transitions between the different energy levels, resulting in strong photoluminescence properties. In general, such tiny nanoparticles behave similarly to molecular species and are often called “Au clusters” in the literature. Due to the extremely short electron Fermi wavelength and the high density of states for Au, the photoluminescence from Au clusters is highly sensitive to the cluster size.^{26,27} It has been demonstrated that once the number of Au atoms has reached 55, the clusters (roughly 1.2 nm in diameter) no longer exhibit the photoluminescence properties characteristic of a molecular system.²⁸ When the number of Au atoms is further increased to 333, the clusters (roughly 2.2 nm in diameter) start to show an LSPR peak at 520 nm as the spacing between energy states is now so minimal that the collective oscillation of free electrons instead dominates.²⁹ Taking this into account, it is not difficult to understand why Au can be considered an excellent example of a multifunctional nanomaterial whose properties can be readily engineered by tuning the size, shape, and/or structure, all without altering the basic elemental composition.

1.2. Other Properties of Gold Essential to Biomedical Applications

In addition to the aforementioned optical properties, Au also has a variety of inherent attributes that make its nanostructures

an attractive platform for biomedical applications. First, Au is one of the least reactive known metals, and can be stored under atmospheric conditions for millions of years without being tarnished or destroyed by oxidation.³⁰ In fact, Au is one of the few exceptional metals known for incredible resistance against both oxidation and corrosion. After exposure to air, not even a single atomic layer of gold oxide(s) can be detected on the surface of a Au substrate. As a result, Au is the only known elemental metal that is both colored and can maintain its unique luster indefinitely. This nonreactive and thus bioinert nature of Au therefore makes it an excellent candidate for both *in vitro* and *in vivo* applications. The low acute toxicity of Au nanomaterials has been documented by a number of *in vitro* studies, and preliminary reports have also shown favorable results for *in vivo* and clinical biocompatibility.^{13,16}

Despite its extraordinary inertness under most conditions, Au is well-known for its ability to form a relatively strong (about 184 kJ/mol) gold–thiolate (Au–S) bond with compounds containing the thiol (–SH) or disulfide group (S–S).^{31,32} This type of bond has been extensively researched in the setting of self-assembled monolayers (SAMs), wherein long-chain alkanethiols or alkyl disulfides can easily form a highly ordered molecular monolayer on the surface of a Au substrate (Figure 3).³³ This well-characterized binding has been widely

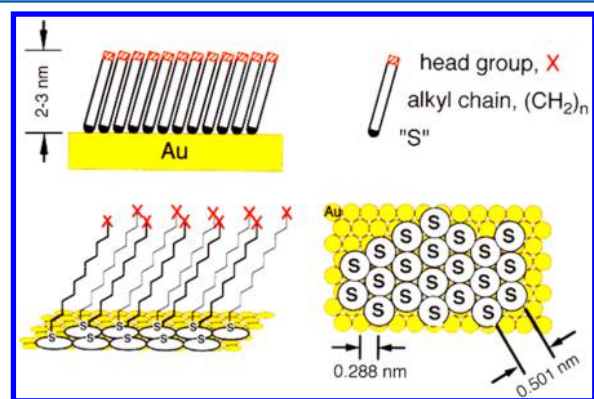


Figure 3. Schematic illustrations of a self-assembled monolayer (SAM) of alkanethiolate formed on the surface of a Au substrate. The thickness of the organic monolayer is determined by the number of methylene groups (n) in the alkyl chain, which is approximately 2.5 nm for $n = 16$. The alkyl chains extend from the surface in a nearly all-*trans* configuration and are tilted by roughly 30° from the normal to the surface to maximize the van der Waals interactions among the alkyl chains. The surface properties of the monolayer can be readily modified by varying the headgroup X. Reprinted from ref 33. Copyright 1990 American Chemical Society.

investigated to add functionality to the surface of Au nanostructures. By varying the functional group at the distal end of a thiol or disulfide molecule, we can easily generate robust, well-defined interfaces that are specifically designed to interact or remain inert within a biological system. For example, the surfaces of Au nanostructures are often derivatized with poly(ethylene glycol) (PEG) to provide biocompatible polymer layers that can help prevent nonspecific adsorption of proteins and minimize the uptake of circulating Au nanostructures by the reticuloendothelial system (RES), allowing for prolonged circulation in the bloodstream and thereby greater accumulation at the targeted diseased site.^{34,35} Gold nanostructures can also be equipped with an active targeting capability through careful surface modification procedures.³⁶ In this case, the

nanostructures are conjugated with a complementary moiety (e.g., antibodies, peptides, and folate, among others) that can strongly bind to the specific receptor typically overexpressed on the surface of a cancer cell, thus increasing the nanoparticle concentration in the desired region. The targeting moiety can be directly conjugated to the surface of a Au nanostructure, chemically coupled to the terminal end of a preattached PEG chain bearing an appropriate tail group (e.g., a carboxyl group for coupling to the amine group found in antibodies), or through click chemistry.³⁷ In addition to the use of the Au–S linkage, biological molecules can adsorb onto the surface of a Au nanostructure in a nonspecific manner, which can also be used to introduce new functionality to the nanostructure. Furthermore, because a rich variety of proteins can adsorb onto the surface of Au nanostructures during *in vitro* or *in vivo* studies, this type of binding will be an important factor to consider when examining the interaction between Au nanostructures and a biological system.³⁵ The adsorbed proteins can significantly alter the surface properties of Au nanostructures and thus their interactions with the biological system, including cellular uptake and blood circulation.³⁸

It is also worth noting that the content of Au in a sample can be easily quantified using a number of techniques such as inductively coupled plasma mass spectrometry (ICP-MS), inductively coupled plasma optical emission spectrometry (ICP-OES), and optical absorption spectroscopy. In particular, it should be noted that both AuCl_4^- salt and Au nanostructures have characteristic absorption peaks in the UV–vis–NIR region, allowing their concentrations to be readily derived based on the Beer–Lambert law once calibration curves are made.^{39,40} Finally, Au also has a number of synthetic isotopes (e.g., ¹⁹⁸Au and ¹⁹⁹Au) that can be produced and incorporated into the lattice of Au nanostructures to give them the radioactivity often sought for various biomedical applications.

1.3. Gold Nanomaterials at Work in Biomedicine

Gold has a substantial history in both biomedicine and biological studies. The first report on the use of Au compounds to treat arthritis appeared in 1934.⁴¹ It was found that Au salts could reduce inflammation and slow disease progression in patients with rheumatoid arthritis through a procedure known as “gold treatment”. In some patients, the treatment helped relieve joint pain and stiffness, reduce swelling and bone damage, and diminish the chance of joint deformity and disability. Since the 1990s, however, the clinical use of “gold treatment” has dropped significantly due to its numerous side effects and limited efficacy. In the 1950s, Au colloids were evaluated as radiotracers for sentinel lymph node biopsies in humans.⁴² In addition, Au nanoparticles have been used extensively in immunochemistry since 1971, when Faulk and Taylor reported a method that involved the conjugation of Au nanoparticles with an antibody for the direct visualization of the surface antigens of salmonellae through electron microscopy.⁴³ This application is based on the strong attenuation of an electron beam by Au due to its large atomic number. Many studies have been devoted to similar applications of Au nanoparticles (typically, conjugation with a targeting moiety such as antibody, lectin, enzyme, and aptamer, among others) in biochemistry, microbiology, immunology, cytology, and plant physiology.⁴⁴ In addition to its ability to weaken the intensity of electron beam, Au can also effectively attenuate other types of high-energy radiation such as X-rays. When Roentgen discovered X-ray radiation in 1895, he noticed that

the Au ring on his wife's finger gave greater X-ray attenuation than her bones in the X-ray image taken.⁴⁵ This was the first known demonstration of Au as a tracer or contrast agent for radiology. In recent years, many types of Au nanomaterials have been developed for such applications.¹⁶

Over the past two decades, there has been a renewed interest in applying Au nanomaterials to biological studies and biomedicine (Figure 4).^{13,15,16,36,46–49} Some of these applica-

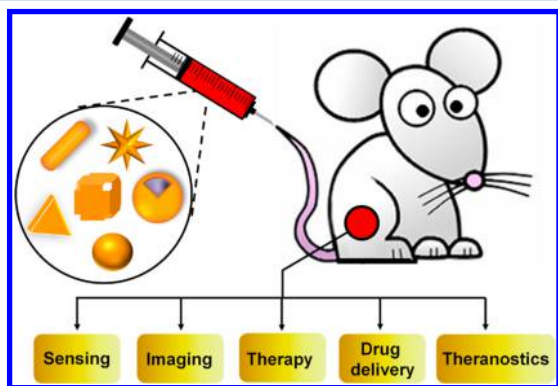


Figure 4. Summary of some biomedical applications enabled by different types of Au nanomaterials. Modified from ref 46. Copyright 2011 American Chemical Society.

tions are simply based on the notion that Au nanostructures can be readily prepared with well-controlled sizes, shapes, and surface properties. As such, one could investigate the effects of these parameters on various biological phenomena or processes, including cellular internalization, circulation, transportation, delivery, biodistribution, tumor targeting, and body clearance. On the other hand, some of these applications are built upon the unique, highly tunable optical properties of Au nanomaterials, which extend from the photoluminescence of Au clusters to the plasmonic properties of Au nanostructures. To this end, Au nanomaterials can also serve as optical probes for sensing as well as contrast agents for optical imaging. For Au clusters, their superior photostability allows them to be imaged over long periods of time with the use of laser at a high intensity. For Au nanoparticles, their absorption and scattering cross sections are typically 5–6 orders of magnitude greater than those of organic dyes, making them ideal contrast agents

for a number of newly developed imaging modalities. The LSPR peaks of Au nanostructures can be readily tuned to the NIR region to fulfill the requirement for in vivo applications while their sizes, shapes, and surface properties can all be precisely engineered for optimal tumor targeting. Significantly, the photothermal conversion capability inherent to Au nanostructures can be utilized to trigger and manage the release of drugs and thus help achieve on-demand release with high spatial and temporal resolutions. Even Au nanostructures themselves can be directly used for the ablation of tissues and killing of cancer cells owing to the photothermal effect. With these properties combined together, Au nanomaterials can serve as a multifunctional platform for biomedicine and biological studies. In a sense, each tiny Au nanostructure can be engineered to carry all the functions sought for theranostics, together with intraoperative capability.

2. CHEMICAL SYNTHESIS OF GOLD NANOMATERIALS

2.1. Gold Clusters

Gold clusters refer to molecular species containing a few to several hundred Au atoms, with their dimensions below a critical size for electronic energy quantization. According to an analysis based on the free-electron model, the critical size for Au is approximately 2 nm.⁵⁰ As a bridge between the Au atom and nanoparticles, Au clusters have received increasing attention since Marcus and Schwentner reported the first observation of photoluminescence from Au_2^+ clusters embedded in a noble-gas matrix in 1987.⁵¹ Their clusters were obtained by sputtering a Au target with an intense beam of high-energy Ar^+ ions (typically, at 10 mA and 20 keV). Later, Harbich and co-workers prepared Au_2^+ and Au_3^+ clusters using a similar method and examined their photoluminescence properties.⁵² Their measurements revealed a size dependence for the photoluminescence of Au clusters, though no quantitative relationship was established between the emission wavelength and the cluster size. Since the noble-gas matrix has a negligible impact on the photoluminescence of Au clusters, this system is particularly well-suited for deciphering the correlation between the optical properties and electronic structures of Au clusters. However, it is difficult to scale up the production of Au clusters using this approach for further exploration of their applications. As a result, solution-phase

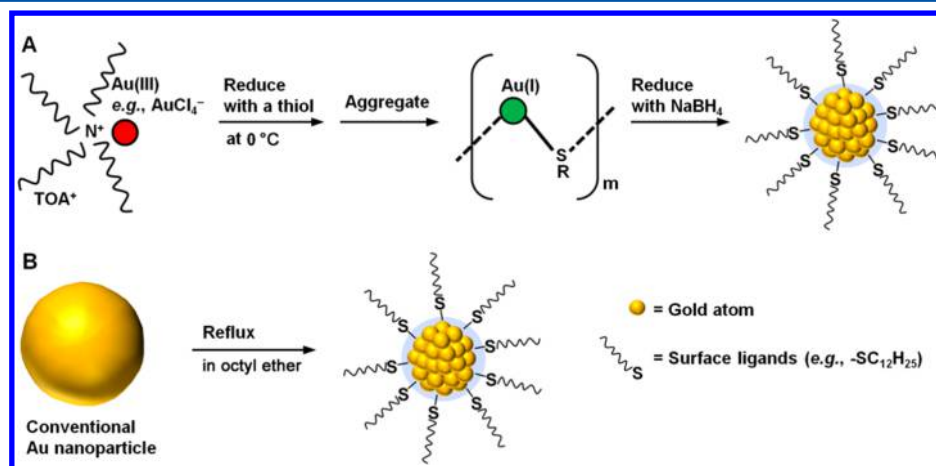


Figure 5. Schematic illustrations of two typical approaches to the synthesis of Au clusters: (A) bottom-up, and (B) top-down. (A) Modified from ref 66. Copyright 2008 American Chemical Society. (B) Modified from ref 75. Copyright 2004 American Chemical Society.

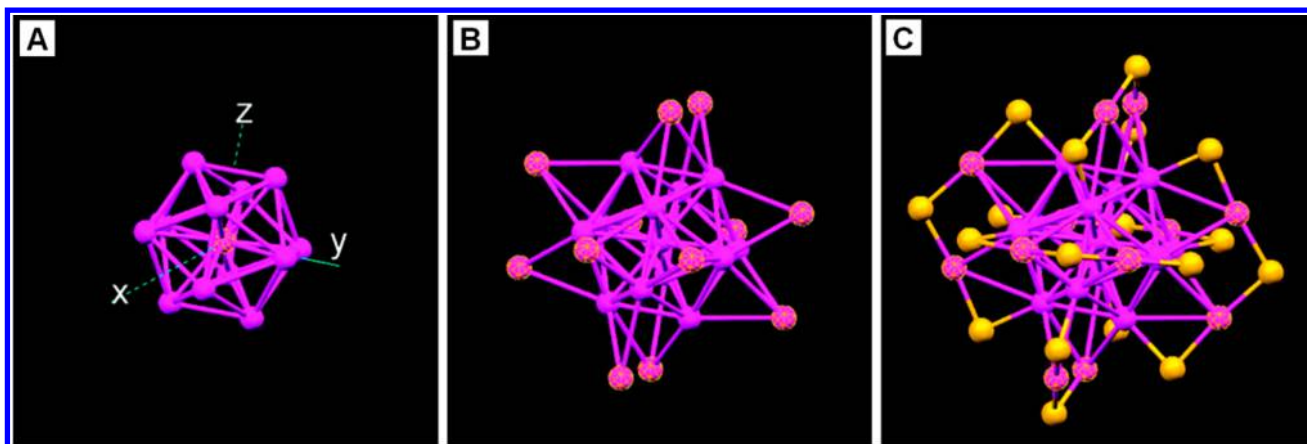


Figure 6. Crystal structure of a $\text{Au}_{25}(\text{SR})_{18}$ cluster, where “R” represents the phenylethyl group: (A) core made of 13 Au atoms, (B) Au_{13} core plus the shell containing 12 Au atoms, and (C) the whole Au_{25} cluster protected by 18 thiolate ligands (for clarity, only S atoms are shown). Color schemes: magenta (dark) for Au atoms in the core, magenta (bright) for Au atoms in the shell, and yellow for S atoms. Reprinted from ref 27. Copyright 2008 American Chemical Society.

synthesis has emerged as the prevalent route toward producing Au clusters.

In contrast to the essentially naked clusters embedded in a noble-gas matrix, the Au clusters prepared using a solution-phase method are capped and protected by ligand molecules. Although Au is widely known as an inert metal, it also has a range of coordination chemistry due to its capability to form covalent bonds with various elements.^{53,54} In particular, the covalent bond between Au and the P, N, or S element in organic compounds such as phosphines, amines, or thiols has a relatively strong binding and can cap the surface of a Au cluster with these organic molecules.⁵⁵ As such, these compounds have been widely used as capping ligands in the solution-phase syntheses of Au clusters. Many different protocols have been reported in the literature, which can be broadly classified into “bottom-up” and “top-down” approaches.^{50,56}

In the “bottom-up” approach, Au clusters are formed from atomic species. Phosphines were typically used as capping ligands in the early work and a large number of phosphine-stabilized Au clusters have been reported, including $\text{Au}_{11}(\text{PR}_3)_7\text{Cl}_3$,⁵⁷ $\text{Au}_{101}(\text{PPh}_3)_{21}\text{Cl}_5$,⁵⁸ $[\text{Au}_{13}(\text{PR}_3)_{10}\text{Cl}_2]^+$,⁵⁹ $[\text{Au}_{39}(\text{PR}_3)_{14}\text{Cl}_6]^{2+}$,⁶⁰ and $\text{Au}_{55}(\text{PR}_3)_{12}\text{Cl}_6$,⁶¹ where PR_3 and Ph represent phosphine and phenyl groups, respectively. Bimetallic clusters such as $[\text{Au}_{13}\text{Ag}_{12}(\text{PR}_3)_{10}\text{Br}_8]^+$,^{62,63} $[\text{Au}_{18}\text{Ag}_{19}(\text{PR}_3)_{12}\text{Br}_{11}]^{2+}$,⁶⁴ and $[\text{Au}_{18}\text{Ag}_{20}(\text{PR}_3)_{14}\text{Cl}_{12}]^{2+}$ ⁶⁵ have also been prepared by slightly modifying the protocol. Compared with phosphines, the interaction between Au and the S in a thiol is much stronger, making thiols better capping ligands for the synthesis of Au clusters. For this reason, more recent protocols developed for the synthesis of Au clusters rely on thiols rather than phosphines. Figure 5A shows a typical “bottom-up” process for the synthesis of Au clusters in the presence of a thiol as the capping ligand.⁶⁶ In this case, the thiol also serves as a reducing agent to bring down the oxidation state of Au from 3+ to 1+. Upon the addition of a strong reductant such as NaBH_4 , Au(I) is further reduced to Au(0) atoms. Murray and co-workers have extensively explored the use of arenethiols as capping ligands for the synthesis of Au clusters.⁶⁷ Based upon the data from transmission electron microscopy (TEM), UV–vis spectroscopy, elemental analysis, and thermogravimetric analysis (TGA), the clusters were assigned a general formula of $\text{Au}_{38}(\text{arenethiol})_{24}$. Later on, Whetten and co-workers prepared several new Au clusters with

different molecular weights by switching to benzenethiol (SPh) as a capping ligand.⁶⁸ They also prepared Au clusters with a composition of $\text{TOA}_2\text{Au}_{44}(\text{SPh})_{28}$ (here TOA represents tetraoctylammonium), verified through data from electrospray ionization mass spectrometry (ESI-MS).

Mass spectrometry involving sample preparation based upon either ESI or matrix-assisted laser desorption ionization (MALDI) has been widely used to determine the compositions of Au clusters.^{29,50} To resolve the structures of Au clusters, however, X-ray crystallography must be applied. For such analysis, the samples must be prepared with extremely high purity in order to grow single crystals from the clusters. As a result, the uniformity of Au clusters has become the most stringent criterion in determining the value of a protocol. Jin and co-workers have made remarkable progress in improving the uniformity of Au clusters.⁶⁶ By lowering the reaction temperature, it became easier to control the formation of Au(I)–SR aggregates—intermediates critical to the development of Au clusters. The product purity was also greatly enhanced and the conversion yield increased to 40–50% based on the Au content in the clusters. According to the ESI- and MALDI-MS data, most of their Au clusters were comprised of Au_{25} cores. In addition, separation methods such as polyacrylamide gel electrophoresis (PAGE) have also been explored in an effort to purify samples of Au clusters.^{69,70} When PAGE purification was applied to a sample obtained using a protocol similar to Jin’s but with a different solvent, Tsukuda and co-workers observed nine cluster species, with $\text{Au}_{25}(\text{SG})_{18}$ (SG stands for glutathione after losing the hydrogen atom from the thiol group) found to be particularly abundant among the clusters, indicating a remarkable stability for the Au_{25} core structure. This size is consistent with one of the “magic numbers” of Au atoms needed for the formation of a closed shell structure.⁷¹ They also suggested that geometric rather than electronic factors are responsible for the extraordinary stability of $\text{Au}_{25}(\text{SG})_{18}$.⁷¹

In a breakthrough, Kornberg and co-workers obtained single crystals from $\text{Au}_{102}(\text{p-MBA})_{44}$ clusters (here p-MBA stands for SPhCOOH) although their sample was not considered high purity.⁷² They obtained the first-ever crystal structure of Au clusters through X-ray crystallography. The $\text{Au}_{102}(\text{p-MBA})_{44}$ cluster is characterized by a core–shell structure. The core is comprised of 49 Au(0) atoms packed into a Marks decahedron

(MD). There are another two symmetry-equivalent rhombicododecahedral fragments of Au_{15} face-capping the Au_{49} MD under D_{5h} symmetry, forming the Au_{79} kernel. Attached to the Au_{79} kernel are 19 S–Au–S units and two S–Au–S–Au–S units, with the final cluster characterized by C_2 symmetry. In follow-up studies, the structures of $[\text{Au}_{25}(\text{SCH}_2\text{CH}_2\text{Ph})_{18}]^q$ clusters ($q = -1, 0$) were independently solved by the Jin, Murray, and Grönbeck groups.^{27,73,74} As shown in Figure 6, this cluster also has a core–shell structure, with the core and shell containing 13 and 12 Au atoms, respectively.

The “top-down” approach has also been explored as an effective route to the synthesis of Au clusters.⁷⁵ As illustrated in Figure 5B, the “top-down” approach to Au clusters typically involves two major steps, with conventional thiol- or citrate-stabilized Au nanoparticles serving as a starting material. The Au nanoparticles are dispersed in a solution containing a thiol or another capping ligand, and then refluxed and broken down into clusters. Using this approach, Jin and co-workers demonstrated the synthesis of Au_3 clusters.⁷⁵ The MALDI-MS results confirmed the formation of $\text{Au}_3(\text{SC}_{12}\text{H}_{25})_3$. Chen and co-workers systematically studied the “top-down” approach and proposed a mechanism.⁷⁶ First, the citrate on the surface of Au nanoparticles is replaced by the thiol due to the stronger binding between Au and S, and the outermost layer of atoms on the nanoparticles is loosened through sonication (or other types of agitation such as ligand-induced etching). Then, the loosened Au atoms rearrange into clusters that can stabilize and withstand the sonication. Finally, the Au clusters are released from the surface of nanoparticles into the solution where they are further protected by the thiols. As the reaction proceeds, Au nanoparticles gradually disappear while Au clusters are formed. Nie and co-workers also reported a ligand-induced etching process for the preparation of highly fluorescent, water-soluble Au clusters.⁷⁷ The Au nanoparticles were dispersed in an aqueous solution containing hyperbranched polyethylenimine (PEI). After etching was completed, the supernatant was found to contain Au clusters that exhibited strong green photoluminescence under UV irradiation. Their ESI-MS data indicated that the Au clusters mainly consisted of a Au_8 core.

Although many different protocols have been developed for the synthesis of Au clusters in the presence of alkanethiols as capping agents, the products of such reactions often suffer from low water solubility and poor biocompatibility, limiting their use in biomedical applications. To address this issue, some natural biomolecules, such as amino acids, peptides, proteins, and DNA molecules, have been directly utilized as the protective ligands for the synthesis of Au clusters using a strategy more or less similar to what was developed for the synthesis of fluorescent Ag clusters.⁷⁸ Figure 7A shows a typical procedure for the synthesis of GSH-stabilized Au clusters in an aqueous solution through a “bottom-up” approach (GSH stands for glutathione).⁷⁹ Several steps of separation and purification are typically needed in order to obtain the clusters as a pure sample. Based on the ESI-MS data, a formula of $\text{Au}_{28}(\text{SG})_{16}$ was assigned to the Au clusters by Whetten and co-workers,⁸⁰ which was consistent with the X-ray diffraction pattern from its powder sample. A later study by Tsukuda and co-workers, however, indicated that the correct formula of this cluster should be $\text{Au}_{25}(\text{SG})_{18}$.⁶⁹

As one of the most abundant plasma proteins, bovine serum albumin (BSA) is widely used in an array of applications such as sensing, self-assembly, and imaging.⁸¹ Ying and co-workers demonstrated the use of BSA as a template for the synthesis of

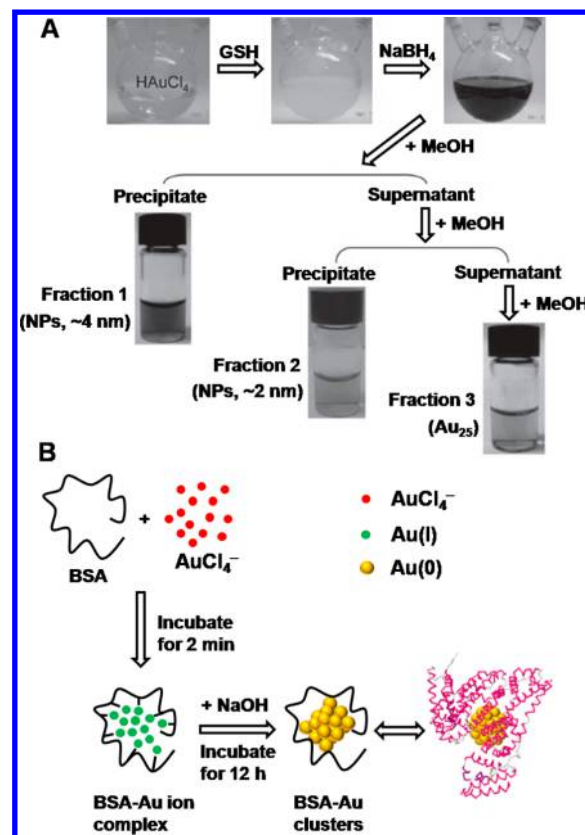


Figure 7. Illustrations showing the syntheses of Au clusters protected by peptides and proteins: (A) glutathione (GSH) and (B) bovine serum albumin (BSA). In (A), the clusters were obtained by removing Au nanoparticles of 4 and 2 nm in size through two steps of separation and purification. (A) Reprinted with permission from ref 79. Copyright 2011 Wiley-VCH. (B) Modified from ref 82. Copyright 2009 American Chemical Society.

Au clusters,⁸² similar to what was reported for the Ag clusters.⁷⁸ As shown in Figure 7B, upon the addition of Au(III) ions into an aqueous BSA solution, the protein molecules sequestered Au(III) ions and entrapped them. When the pH value was increased to 12, the reduction power of BSA was enhanced and the entrapped ions would go through progressive reduction to generate Au clusters. Based on the photoluminescence property and the spherical jellium model, the BSA-stabilized Au clusters were proposed to contain a Au_{25} core, which was consistent with the MALDI-MS data. Due to the excellent biocompatibility and abundant functional groups of BSA, this class of Au clusters remains highly promising for various applications in biomedicine.

2.2. Conventional Gold Nanoparticles

Conventional Au nanoparticles refer to polycrystalline nanostructures with a poorly defined, quasi-spherical shape. For the purposes of this article, we will refer to them simply as Au nanoparticles. These nanoparticles are typically prepared as colloidal samples by reducing HAuCl_4 in a solution phase.⁸³ After HAuCl_4 is dissolved, the solution is rapidly stirred while a reducing agent is quickly introduced to reduce AuCl_4^- ions to Au(0) atoms. As more and more Au(0) atoms are generated, the solution becomes supersaturated, causing atoms to precipitate out as nuclei in the form of subnanometer particles. To prevent the nuclei from aggregating together, a stabilizer that can bind to the Au surface must be introduced, just like the

capping ligand used in the synthesis of Au clusters. The particles produced through this method are typically characterized by a quasi-spherical or irregular shape, together with a poorly defined twinned structure. Although a large number of protocols have been reported in the literature, most of them can be considered variants of two methods originally developed by Turkevich and Brust, respectively.

The Turkevich method was pioneered by Turkevich and co-workers in 1951⁸⁴ and refined by Frens in the 1970s.⁸⁵ Figure 8

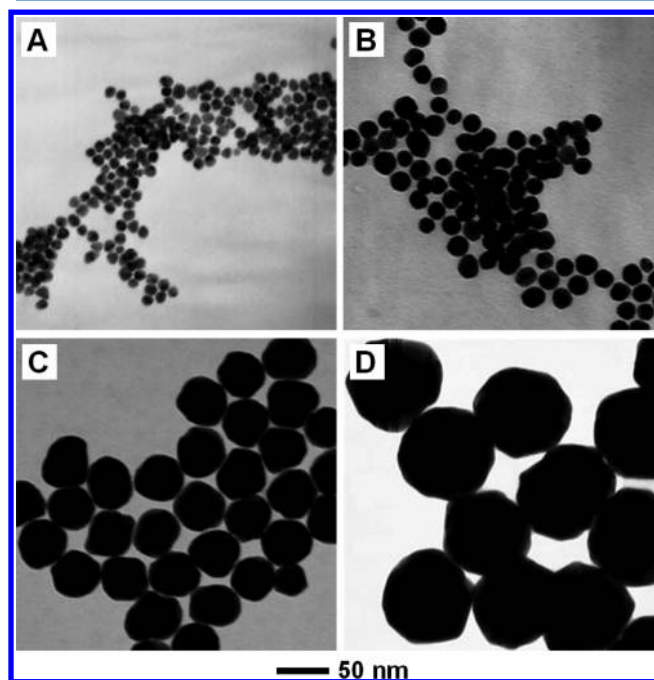


Figure 8. TEM images of four typical examples of conventional Au nanoparticles with different diameters prepared using the Turkevich method: (A) 10, (B) 20, (C) 50, and (D) 100 nm. Reprinted from ref 86. Copyright 2007 American Chemical Society.

shows TEM images of some examples of Au nanoparticles that have been prepared using this method.⁸⁶ In general, this method involves the reduction of HAuCl_4 with sodium citrate in an aqueous solution. The size of the resultant Au nanoparticles can be controlled simply by changing the molar ratio of sodium citrate to HAuCl_4 . Peng and co-workers systematically studied the growth kinetics and temporal size evolution of nanoparticles when the synthesis was conducted in boiling water.⁸⁷ Depending on the pH, the formation of nanoparticles could follow two different pathways. At a pH value below 6.2, formation of particles would follow three major steps: nucleation; random attachment to form polycrystalline, wavy nanowires; and smoothing of the nanowires via intraparticle ripening to generate individual nanoparticles. The second pathway occurs at pH higher than 6.2, which is consistent with the commonly known LaMer model for the nucleation and growth of colloidal particles. By varying the pH of the reaction solution, these authors demonstrated the synthesis of Au nanoparticles with a relatively uniform size controllable in the range of 20–40 nm.

Puntes and co-workers showed that dicarboxyacetone, acetoacetate, or acetone formed during the thermal decomposition of sodium citrate could affect the final morphology of the Au nanoparticles.⁸⁸ The sequence for introducing the reagents was also investigated to improve the size uniformity of

the Au nanoparticles prepared using the Turkevich method.⁸⁹ Traditionally, sodium citrate is rapidly injected into a hot aqueous solution of HAuCl_4 . By reversing the order (i.e., heating the sodium citrate solution, followed by the addition of HAuCl_4), Au nanoparticles with a narrower size distribution were obtained. By reversing the sequence of reagent addition, Santhanam and co-workers also obtained more uniform Au nanoparticles of 5–10 nm in size than the conventional Turkevich method.⁸⁹ The Puntes group further studied the isotopic effect on the size of Au nanoparticles by replacing H_2O with D_2O as the solvent.⁹⁰ With the replacement of H_2O by D_2O , Au nanoparticles of smaller sizes were obtained, a result that can be interpreted as the consequence of a faster reduction in the D_2O -based system. It was proposed that a complex in the form of $[\text{AuCl}_3(\text{C}_6\text{H}_5\text{O}_7)]^-$ was formed between HAuCl_4 and sodium citrate, with this complex then disproportionating into the products in a rate-limiting step.

The Brust method for the synthesis of Au nanoparticles was developed in the early 1990s by Brust and Schiffrin.⁹¹ Whereas the Turkevich method is based on an aqueous system, the Brust method involves the use of an organic solvent. In a typical synthesis, HAuCl_4 is transferred from an aqueous phase to toluene with the use of tetraoctylammonium bromide (TOAB) as a phase-transfer agent, and then reduced to Au(0) atoms by NaBH_4 . Dodecanethiol is typically added into the organic phase to serve as a capping agent. The resultant nanoparticles are much smaller in size (typically, 5–6 nm) than those prepared using the Turkevich method. Heath, Gelbart, and their co-workers further demonstrated that Au nanoparticles with sizes ranging from 1.5 to 20 nm could be readily obtained by varying the molar ratio of HAuCl_4 to the thiol.⁹²

The final size of the Au nanoparticles prepared using the Brust method is determined by the degree of Ostwald ripening, which is, in turn, largely dependent on the temperature used for the synthesis.^{93,94} The temperature at which a noticeable change in size (due to Ostwald ripening) will be observed for the Au nanoparticles is known as the evolution temperature. Zhong and co-workers found that the evolution temperature was dependent on the alkyl chain length of the thiol used as a capping agent. It was proposed that the chain length could affect the desorption and readsorption of the thiol molecules, which are two of the critical processes in controlling the reactivity of the Au nanoparticles. Miyake and co-workers also prepared Au nanoparticles with TOAB as a phase-transfer agent and in the presence of an alkanethiol as a capping agent.^{95,96} For size control, the Au nanoparticles were further aged in molten TOAB at 150–250 °C. As shown in Figure 9, the mean diameter of the nanoparticles could be tuned from 1.5 to 9.7 nm by simply adjusting the temperature used for aging.

Gold nanoparticles with a broad range of sizes can be obtained using seed-mediated growth. A typical procedure for this involves two major steps: (i) synthesis of citrate-stabilized Au nanoparticles (i.e., the seeds) using the Turkevich method and (ii) growth of the seeds into larger nanoparticles with the assistance of a surfactant such as hexadecyltrimethylammonium bromide (CTAB). In an early study,⁹⁷ the citrate-stabilized Au seeds had a diameter of approximately 3.5 nm, which were prepared by adding a strong reductant such as NaBH_4 into an aqueous HAuCl_4 solution in the presence of sodium citrate as a colloidal stabilizer. Without further cleaning, the as-obtained Au seeds were added into a growth solution containing HAuCl_4 , CTAB, and ascorbic acid (AA) for the synthesis of Au nanoparticles with diameters tunable from 5.5 to 37 nm. Liz-

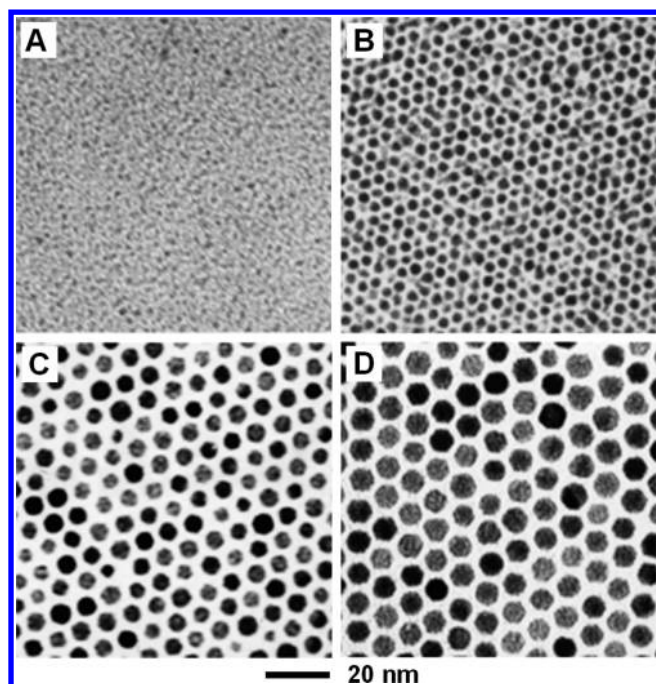


Figure 9. TEM images of four typical examples of Au nanoparticles with different diameters prepared using the Brust method: (A) 1.5, (B) 3.4, (C) 5.4, and (D) 6.8 nm. Reprinted from ref 96. Copyright 2003 American Chemical Society.

Marzán and co-workers further extended this strategy to the preparation of Au nanoparticles with sizes in the range of 12–180 nm.⁹⁸ In a typical process, the seeds were prepared using a modified Turkevich method at 35 °C, with a purification step introduced to remove most of the nonspherical particles. Despite the demonstration of control over a broad range of sizes, the products were often marred by a noticeable amount of nonspherical particles such as nanorods and nanoplates.

2.3. Gold Nanospheres

Different from the conventional nanoparticles with a quasi-spherical shape, Au nanospheres refer to nanocrystals characterized by a single-crystal structure together with a circular projection under TEM imaging. The surface of a Au nanosphere is covered by a large number of {111}, {100}, {110}, and high-index facets of very small surface areas. There is essentially no sharp corner or edge on the entire surface of the particle. In recent years, the synthesis of Au nanospheres as a pure sample and with a well-controlled size has attracted great interest due to the simplicity in modeling their optical properties.

The first attempted preparation of Au nanospheres involved the use of single-crystal Au nanorods as seeds for an overgrowth process.⁹⁹ However, the use of Au nanorods with a length greater than 20 nm makes it impossible to obtain Au nanospheres with diameters smaller than 20 nm. In 2013, our group reported a facile route to the preparation of Au nanospheres with a narrow size distribution and tunable diameters in the range of 5–30 nm (Figure 10A–C).¹⁰⁰ The first step of such a synthesis involves the preparation of Au clusters capped by CTAB, which then serve as the “initial seeds” for an overgrowth process. In the next step, an aqueous solution containing HAuCl₄, hexadecyltrimethylammonium chloride (CTAC), and AA were mixed at room temperature, followed by the introduction of a certain amount of the “initial

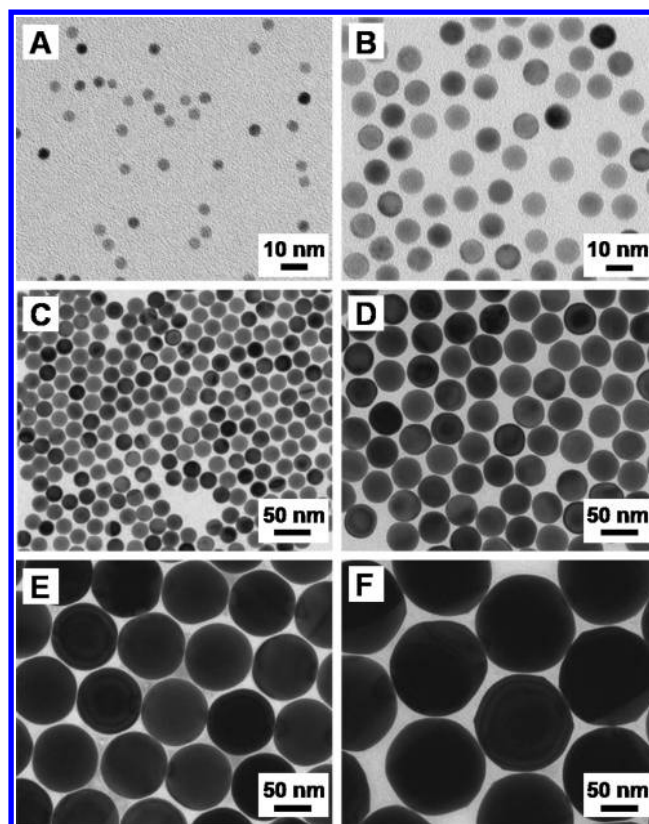


Figure 10. TEM images of single-crystal Au nanospheres with controllable diameters in the range of 5–150 nm: (A) 5, (B) 10, (C) 23, (D) 46, (E) 100, and (F) 150 nm. Reprinted with permission from ref 106. Copyright 2014 Wiley-VCH.

seeds”. The mixture turned red within a few seconds, indicating the quick formation of Au nanospheres. In comparison, the mixture of HAuCl₄, CTAC, and AA could stay colorless for several hours if no “initial seeds” were introduced. The diameter of the Au nanospheres could be easily tuned from 5 to 17 nm by simply varying the amount of the “initial seeds” added into the growth solution. The as-prepared Au nanospheres with a diameter of 10 nm could then serve as the seeds for another round of overgrowth to generate Au nanospheres with diameters in the range of 15–30 nm. In addition, the Au nanospheres could also serve as seeds for the syntheses of Au nanocrystals with many other shapes,^{101–103} as well as Au@Ag¹⁰⁴ and Au@Pd¹⁰⁵ core–shell bimetallic nanocrystals with various morphologies.

It is always difficult to avoid sharp corners or edges when the Au nanospheres grow beyond 100 nm. In a follow-up study, our group modified the overgrowth procedure and achieved the synthesis of Au nanospheres with uniform diameters up to 150 nm (Figure 10D–F).¹⁰⁶ The dropwise injection of HAuCl₄ solution using a syringe pump, the use of reducing agent at a relatively low concentration, and the absence of halide anions with strong affinity toward the Au(100) surface were all found to be critical to the formation of Au nanospheres rather than nanoscale cubes or octahedra whose surfaces are enclosed by {100} and {111} facets, respectively. The new protocol is expected to find widespread use for the preparation of Au nanospheres with precisely controlled diameters for use in elucidating the effects of particle size on an array of properties associated with Au nanomaterials, including LSPR, surface-enhanced Raman scattering (SERS), pharmacokinetics, bio-

distribution, tumor targeting, and clearance from the body. Due to their well-controlled sizes and the absence of sharp corners and edges from their surfaces, Au nanospheres can serve as a simple and well-defined system for the aforementioned evaluations.

2.4. Gold Nanorods

Different from the nanoparticles or nanospheres, Au nanorods have an anisotropic shape, with the positions of their longitudinal LSPR peaks highly sensitive to the aspect ratio.^{107–109} The synthesis of Au nanorods has been one of the most active subject areas in nanomaterials research over the past decade. A variety of methods have been developed for the formation of Au nanorods with controllable aspect ratios. Herein, we only concentrate on solution-based methods with documented reproducibility.

Early work on the synthesis of Au nanorods involved electrochemical reduction through either template-directed or templateless synthesis. Template-directed synthesis is relatively straightforward in design: Au atoms are packed inside the pores of a template and then directed to evolve into nanostructures according to the morphology of the pores. Anodic aluminum oxide (AAO) membranes have been widely explored as templates for the synthesis of Au nanorods.^{110–112} The cylindrical pores in an AAO membrane are arranged in a hexagonal array with a broad range of pore diameters (5–200 nm) available, which in turn control the diameter of resultant Au nanorods. In a typical synthesis, the AAO template is coated with a thin layer of sacrificial metal (e.g., Ag or Cu) on one side of the membrane and then used as the cathode. A salt precursor of Au(III) is reduced electrochemically inside the pores to generate Au nanorods. The as-synthesized nanorods can be released by dissolving the AAO membrane post synthesis, and a polymeric stabilizer, such as poly(vinylpyrrolidone) (PVP),¹¹³ is often added to prevent the nanorods from aggregating. Figure 11A,B shows TEM images of two typical samples of Au nanorods prepared through AAO templates. Nanorods with complex morphologies that cannot be easily synthesized using a conventional solution-based method have also been prepared using this template-directed approach. For example, nanorods comprised of multiple segments of Au and another metal (e.g., Ag,¹¹⁴ Ni,^{115,116} Cu,¹¹⁷ or Pt¹¹⁸) can be synthesized through template-directed synthesis by sequentially depositing Au and the other desired metal. Figure 11C,D shows scanning electron microscopy (SEM) images of two typical examples consisting of alternating segments of Au and Ag (or Ni). When Ni was used, the Ni segments in the nanorods could be selectively removed by etching in order to generate nanorods with well-controlled, nanoscale gaps between the Au segments.¹¹⁵

In the so-called templateless approach, Au nanorods are formed in the presence of ionic surfactants, which work as both the supporting electrolyte and shape-directing agent through the formation of micellar structures. This approach was initially reported by Wang and co-workers.¹¹⁹ In a typical process, two electrodes made of Au and Pt (for the anode and cathode, respectively) are immersed in an aqueous solution containing an ionic surfactant such as CTAB. When a current is applied, the Au anode will oxidize to generate AuBr_4^- ions, which then bind to rod-shaped CTAB micelles and migrate to the Pt cathode where they are reduced back to Au(0) atoms, thus generating Au nanorods around the micelles. Ultrasonication is often applied to dissipate the resultant nanorods away from the surface of cathode.¹²⁰ It was reported that the aspect ratio of Au

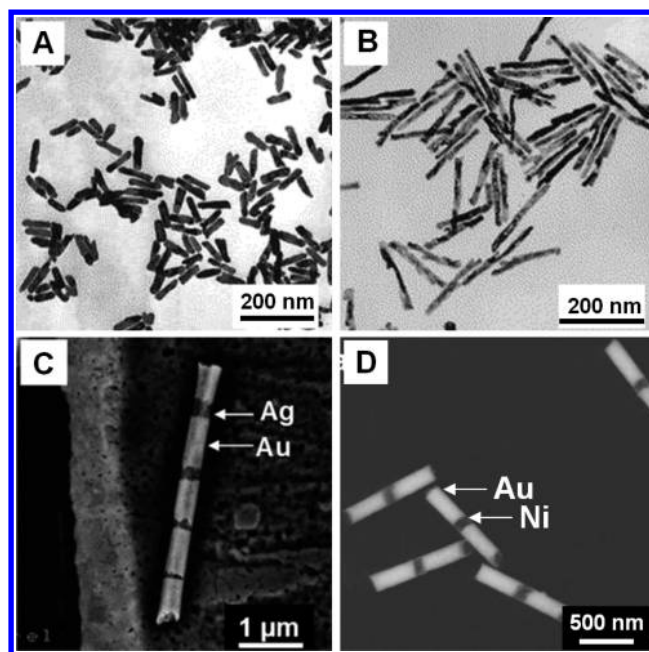


Figure 11. (A, B) TEM images of Au nanorods with aspect ratios of (A) 4.3 and (B) 12.6, respectively, that were synthesized in the channels of anodic aluminum oxide templates. (C, D) SEM images of nanorods with multiple segments comprised of (C) Au and Ag and (D) Au and Ni, which were prepared by sequentially depositing these two metals inside the channels. (A and B) Reprinted from ref 113. Copyright 2000 American Chemical Society. (C) Reprinted from ref 114. Copyright 2001 American Association for the Advancement of Science. (D) Reprinted with permission from ref 116. Copyright 2014 Nature Publishing Group.

nanorods synthesized using this method was greatly affected by the presence of a Ag electrode placed inside the electrolyte solution, which could release Ag^+ ions during the synthesis.

Seed-mediated growth has emerged as the most popular approach to the synthesis of Au nanorods, and has been widely used by many research groups due to its procedural simplicity, easily tunable control of the particle aspect ratio, high product uniformity, and flexibility for further surface modifications.¹²¹ There is not currently a consensus on the underlying mechanism that leads to the formation of these rod-shaped Au nanostructures. However, based on the general understanding in research, the formation of Au nanorods can be generally categorized into two different mechanisms, depending on whether Ag^+ ions are involved during the synthesis.^{122,123} In the absence of Ag^+ ions, the formation of Au nanorods is believed to be caused by the preferential binding of CTAB to specific crystal facets on the Au seeds, inducing the formation of nanorods. In a seed-mediated synthesis, Au(III) precursor in the solution is first reduced to Au(0) atoms, followed by its deposition on CTAB-capped seed particles. However, the deposition of new metal atoms is limited to certain regions of the seed, thus breaking the spherical symmetry as specific crystal facets begin to emerge. Due to the preferential binding of CTAB to the Au(100) surface, deposition of newly formed Au atoms onto the {100} facets is retarded. Instead, the Au atoms are deposited on the available {111} facets, resulting in elongation of the Au seed into a nanorod along the [100] direction. A second growth mechanism is proposed in the presence of Ag^+ ions. Silver ions in solution can be preferentially reduced to Ag atoms on the {110} facets of the

seed due to an underpotential deposition process. The deposition of Au atoms on these facets will then be blocked due to the strong interactions between the deposited Ag and the Br^- ions from the CTAB. As a result, the Au seed will evolve into a nanorod along the $[110]$ direction. Higher Ag^+ concentrations will lead to further deposition of Ag atoms onto the $\{110\}$ facets, resulting in the formation of nanorods with a higher aspect ratio. If the entire surface of a nanorod is completely passivated by Ag atoms, however, the growth of the nanorod will be terminated. As a result, only short nanorods (<100 nm in length) can be obtained in the presence of Ag^+ ions. For the synthesis of Au nanorods longer than 100 nm, a Ag^+ -free approach must be used. The growth of Au nanorods is, in fact, far more complicated than what we have described here. For example, Vaia and co-workers have observed a five-stage growth process for the synthesis of Au nanorods, wherein $\{250\}$ facets rather than the commonly discussed $\{110\}$, $\{100\}$, and $\{111\}$ facets were present during the late stages of growth.¹²⁴ Mulvaney and co-workers attributed the elongation of Au nanorods to the minimized surface potential at the two tips of the seed particle caused by a lower CTAB coverage density at those sites.¹²⁵ Readers who are interested in the growth mechanism of Au nanorods can find more detailed discussions from a number of reviews on this topic.^{15,122,123}

The seed-mediated route to the synthesis of Au nanorods was initially developed by Murphy and co-workers in 2001.¹²¹ A typical procedure involves two steps: synthesis of citrate-stabilized Au nanoparticles to be used as the seeds, and overgrowth of the seeds into nanorods with the assistance of a surfactant such as CTAB. The citrate-stabilized seeds were prepared with a diameter of 3–4 nm using a modified Turkevich method by quickly reducing HAuCl_4 with a strong reductant such as NaBH_4 in the presence of sodium citrate. Growth was then carried out by adding the citrate-stabilized seeds into a solution containing HAuCl_4 , CTAB, AA, and AgNO_3 . The aspect ratio could be tuned from 1 to 10 by varying the ratio of HAuCl_4 to the seeds. The Au nanorods prepared using this method typically contained a large portion of nanoparticles (up to 40–50%). Later, the same group demonstrated the synthesis of Au nanorods with aspect ratios as high as 25 using a three-step procedure, with the exclusion of AgNO_3 .^{109,126} In the new synthesis, Au nanorods formed in the first step were used as seeds for the subsequent growth, which were then further used as seeds for another round of growth. There remained a large portion of nanoparticles in the final collected product, requiring a series of centrifugation steps in order to purify the samples.

In 2003, El-Sayed and Nikoobakht greatly improved the seed-mediated route by replacing the citrate with CTAB for the synthesis of seeds.¹²⁷ They found that the aspect ratio of the resultant Au nanorods could be readily controlled by simply adjusting the Ag^+ concentration in the growth solution. Their new protocol involved two major steps: synthesis of CTAB-capped Au seeds by reducing HAuCl_4 with ice-cold NaBH_4 in the presence of CTAB, and formation of Au nanorods by adding the CTAB-stabilized Au seeds into a growth solution containing HAuCl_4 , AA, and AgNO_3 . For the preparation of Au nanorods with aspect ratios between 4.6 and 10 (corresponding to LSPR peaks located in the range of 900–1300 nm), a binary mixture of benzyldimethylhexadecyl ammonium chloride (BDAC) and CTAB was used as the surfactant. The samples prepared using this new method contained up to 99% Au nanorods, with very few leftover nanoparticles. Figure 12 shows

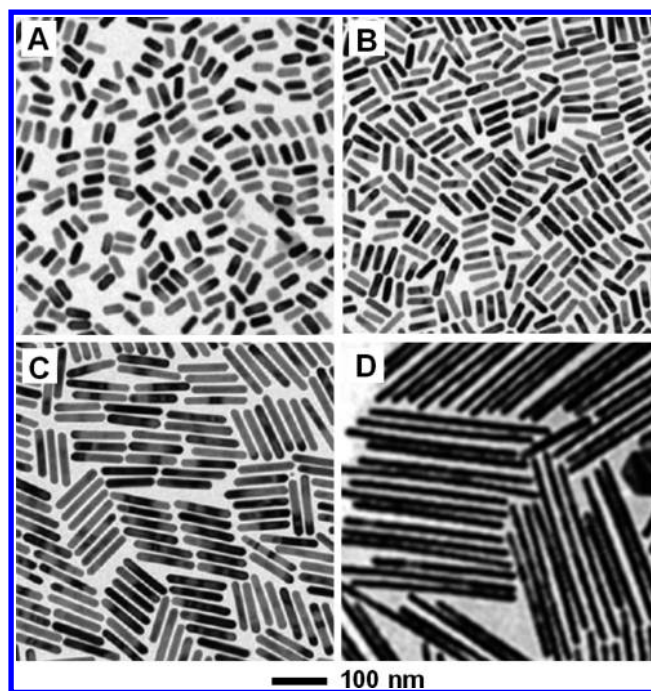


Figure 12. TEM images of Au nanorods with different aspect ratios that were synthesized using seed-mediated growth: (A) 2.6, (B) 3.9, (C) 8, and (D) 18. (A–C) Reprinted from ref 129. Copyright 2012 American Chemical Society. (D) Reprinted from ref 126. Copyright 2001 American Chemical Society.

TEM images of four typical samples of Au nanorods with different diameters and aspect ratios. Conveniently, the growth of Au nanorods could be terminated at any point during a synthesis through the addition of Na_2S at a millimolar concentration to quench any unreacted HAuCl_4 via reduction and/or stabilize the surface of Au nanorods via chemisorption.¹²⁸

Recently, Murray and co-workers reported a protocol for the synthesis of Au nanorods by introducing aromatic additives.¹²⁹ The aromatic compounds were able to modify the micellization behavior of CTAB, resulting in better control of the Au nanorod morphologies, even with the use of CTAB at half of the original concentration. For example, with the use of salicylate-based sodium salts to modify the micellar packing parameter of CTAB, Au nanorods with LSPR peaks shorter than 700 nm were obtained. By using 5-bromosalicylic acid or 2,6-dihydroxybenzoic acid as an additive, Au nanorods with LSPR peaks greater than 700 nm were obtained. Fine-tuned control over the aspect ratio from 3.9 to 4.9 was achieved for the CTAB and 5-bromosalicylic acid system by manipulating either the concentration of Ag^+ ions or the amount of seed particles involved. Uniform Au nanorods with high aspect ratios (5.9–8.5) were obtained by increasing the acidity of the growth solution without altering other parameters involved in the synthesis.

Seed-mediated growth is now able to produce Au nanorods with well-defined aspect ratios in high yields. However, procedures can prove difficult to implement and many parameters may acutely affect the synthesis, including the concentration of the seed particles, reaction temperature, pH value of the growth solution, concentration of CTAB used for the growth step, and even impurities contained in CTAB and other chemical reagents involved in the synthesis.^{108,109,130} As a

result, there is still room for improvement, and even for the development of new methods.

Photochemical reduction is another useful method for the synthesis of Au nanorods. In this approach, a precursor of Au(III) is reduced under UV light to generate Au atoms via electron transfer from AuCl_4^- ions to the capping ligand. Two stages are involved in the synthesis: aggregation of Au nuclei to generate primary particles, and aggregation of the Au particles into rod-like structures due to the preferential binding of surfactants to certain facets. Esumi and co-workers pioneered this method, reporting the first synthesis of Au nanorods with UV light (254 nm) in the presence of CTAC in 1995.¹³¹ In their synthesis, UV light reduced HAuCl_4 while CTAC served as a soft template for the anisotropic growth of Au nanorods by forming rod-shaped micelles. Yang and co-workers further improved this method with three modifications: (i) use of CTAB instead of CTAC as the shape-inducing agent, (ii) introduction of AgNO_3 into the growth solution to control the aspect ratio of Au nanorods, and (iii) addition of acetone and cyclohexane to loosen the micellar structure.¹³² Under irradiation of 254 nm UV light for 24 h, Au nanorods with aspect ratios in the range of 2.8–4.8 were obtained by increasing the amount of AgNO_3 solution (0.01 M) added from 15.8 to 31.5 μL . The Ag^+ ions were believed to affect the synthesis in the same mechanism as with the seed-mediated growth. In addition, Au nanorods with higher aspect ratios could be produced through photochemical reduction under a 300 nm UV light source.¹³³ Other methods that have been reported for the chemical syntheses of Au nanorods include bioreduction,¹³⁴ microwave-assisted reduction,^{135,136} and solvothermal reduction.¹³⁷

2.5. Gold Nanoplates

Gold nanoplates refer to plate-like nanostructures enclosed by two relatively large basal (111) planes, together with low aspect ratios. Different from an earlier report,¹³⁸ here we define the aspect ratio of a nanoplate as the ratio of thickness to edge length in order to be consistent with the notion commonly used in colloid science.¹³⁹ The nanoplates can form a triangular (Figure 13A), hexagonal (Figure 13B), or circular cross section (Figure 13C) along the direction parallel to the basal planes, and are generally known as prisms or disks. The Au nanoplates reported in the literature typically have edge lengths in the range of 40 nm to 1 μm , with thicknesses varying from 5 to 50 nm. In accordance with this two-dimensional (2D) structure, Au nanoplates exhibit tunable LSPR peaks throughout the visible and NIR regions, which are determined by the edge length, thickness, and corner sharpness.¹⁴⁰ Gold nanoplates are usually synthesized through wet chemical methods that involve the use of various surfactants. A variety of different combinations of reaction conditions, surfactants, and reducing agents have been reported, all following a similar two-stage mechanism that involves nucleation and growth. During the nucleation step, a Au precursor is reduced at a relatively slow rate to generate seeds with planar defects (e.g., lamellar twins or stacking faults). These seeds then undergo lateral growth to generate thin plates with different edge lengths.

There are a number of early reports on the observation of Au nanoplates, albeit the samples are typically marred by both low purity and yield.^{141–144} In 2002, Kotov, Liz-Marzán, and their co-workers reported a synthesis of Au nanoplates through a slow reduction approach.¹⁴¹ In their synthesis, a mild reductant (salicylic acid) was used to reduce HAuCl_4 , leading to the

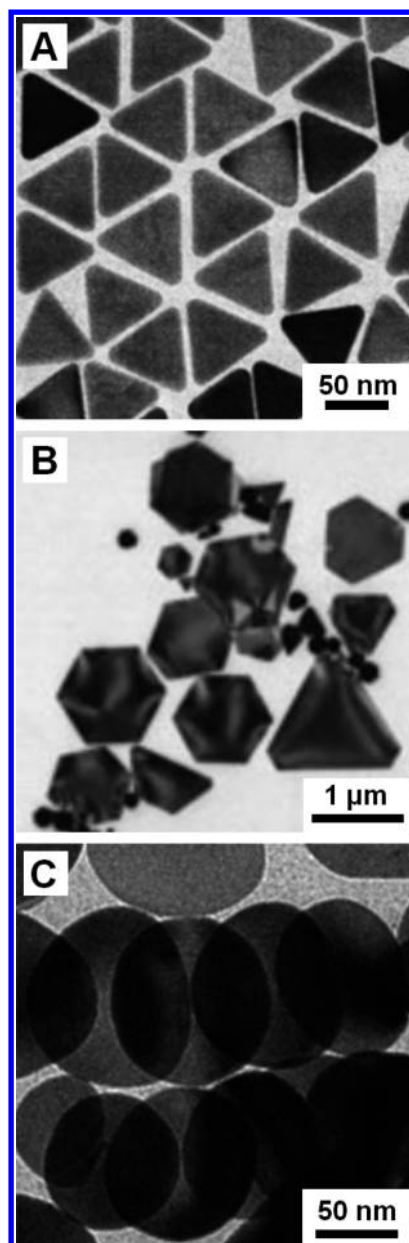


Figure 13. TEM images of Au nanoplates with different cross sections: (A) triangular, (B) hexagonal, and (C) circular. (A) Reprinted from ref 152. Copyright 2014 American Chemical Society. (B) Reprinted with permission from ref 136. Copyright 2005 Wiley-VCH. (C) Reprinted from ref 151. Copyright 2014 American Chemical Society.

formation of Au nanoplates with triangular and hexagonal shapes, with LSPR peaks around 860 nm. Since then, many different protocols have been reported. For example, Mirkin and co-workers prepared triangular Au nanoplates via seed-mediated growth originally developed for the synthesis of Au nanorods.¹⁴⁵ Their process involved two steps: preparation of Au nanoparticles through the reduction of HAuCl_4 by NaBH_4 in the presence of trisodium citrate and further growth of the Au nanoparticles into nanoplates through three sequential growth cycles in an aqueous solution containing CTAB, HAuCl_4 , AA, and NaOH. The nanoplates had an average edge length of 144 ± 30 nm, together with a uniform thickness of 7.8 ± 0.5 nm. Trisodium citrate was believed to work as a stabilizer for the seed particles in this synthesis, facilitating the

formation of stacking faults and finally leading to the growth of Au nanoplates. The reducing power of AA could be enhanced by adding NaOH to increase the pH of the solution. In a later report, the same group further increased the edge length of the Au nanoplates using the as-prepared Au nanoplates as seeds for another round of growth.¹⁴⁶ The edge length of the resulting Au nanoplates could be tuned from 100 to 300 nm while still maintaining the shape and thickness of the original Au nanoplates.

It is generally believed that the capping agent plays an important role in the formation of Au nanoplates. The capping agent can bind to a specific set of facets on the seed during the growth process, directing the deposition of Au atoms and determining the final structure of the products.¹³⁸ Hexadecyltrimethylammonium bromide is one of the most commonly used capping agents in the preparation of Au nanoplates.^{145–151} Recent studies indicated that it was the trace amount of I^- impurity contained in the commercially available CTAB that induced the formation of Au nanoplates, instead of the Br^- ions at a much higher concentration. The I^- ions preferentially bind to the Au(111) surface, blocking the deposition of Au atoms onto these facets and thus promoting the formation of Au nanoplates. Through this principle, Mirkin and co-workers reported the formation of Au nanocrystals with anisotropic shapes by varying the amount of I^- ions used in the synthesis.¹⁴⁷ Samples of CTAB from different suppliers were used in their study for the synthesis of Au nanoplates under identical reaction conditions, and Au nanocrystals with different morphologies were obtained. The morphological differences could be attributed to the variation in I^- ion concentration. When no I^- was present in the system, Au nanoparticles were obtained as the products. At a very low concentration (2.5–5 μM), a large population of nanorods was observed. Nanoplates were formed in high yields only when the I^- concentration was increased to 50 μM . Similar observations were also reported by Ha and co-workers,¹⁴⁹ in which the addition of a small amount of I^- ions (20 μM) suppressed the growth of Au along the [111] direction, facilitating the formation of triangular Au nanoplates in the presence of excessive CTAB. The Au nanoplates had an average edge length of 140 nm and a thickness of 8 nm, together with a high purity of 97%. More recently, Zhang and co-workers revealed that I^- ions contributed to the successful synthesis of Au nanoplates not only through selectively binding to the {111} facets, but also by the oxidative etching and removal of less stable nanocrystal shapes through the formation of I_3^- ions during the nucleation step.¹⁵² As such, only nuclei dominated by planar defects were formed, and uniform triangular Au nanoplates with tunable edge lengths in the range of 40–120 nm were obtained with purity >90%. However, a contradictory trend was reported by the Sastry group, in which I^- ions were found to strongly suppress the formation of nanoplates.¹⁵³ These different results suggest a pressing need to combine both kinetic controls and surface capping to induce and direct the formation of Au nanocrystals with specific shapes.

The potential toxicity of CTA^+ cations shadows the biomedical applications of Au nanoplates synthesized in the presence of CTAB. As a result, alternative synthetic approaches using biological molecules and organisms have gained increasing attention.^{154–159} To this end, Sastry and co-workers reported the synthesis of Au nanoplates using an aqueous extract from lemongrass plants, which could serve as both the reducing agent and capping agent.¹⁵⁴ According to their

explanation, Au seed particles were formed first, followed by aggregation of particles within a mixture of aldehydes and ketones, and then finally a fusion process to form nanoplates. In a related study, our group reported the use of BSA as both the reductant and stabilizer in an aqueous phase for the preparation of Au nanoplates, and systematically studied the effects of temperature, pH, BSA concentration, and ionic species on the reduction kinetics and thereby the morphology of the final products.¹⁵⁹

Poly(vinylpyrrolidone) represents another type of biocompatible material for the synthesis of Au nanoplates. The hydroxyl end group of PVP has a very mild reducing power, making it a good reductant for the formation of plate-like seeds under slow reduction. In 2006, our group reported the synthesis of both triangular and hexagonal Au nanoplates with an average edge length of 800 nm using PVP as a dual reductant and colloidal stabilizer.¹⁶⁰ In another study, the mechanism responsible for the formation of Au nanoplates was further explored.¹⁶¹ In brief, the Au atoms were directed to evolve into a structure containing a random mixture of hexagonal-close-packed (hcp) and cubic-close-packed (ccp) stacking, which was referred to as random hexagonal close-packed (rhcp) structure. The nuclei with a rhcp structure could easily evolve into plate-like seeds with vertical stacking faults, and finally grow into nanoplates. The morphology of the Au nanoplates prepared through this approach was dependent on the molecular weight of PVP, as well as the ratio between PVP and $HAuCl_4$.^{160,162}

Apart from the aforementioned methods, there are also a large number of other synthetic protocols for the preparation of Au nanoplates, including those based upon electrochemical,¹⁶³ microwave-assisted,^{136,143} ultrasound-assisted,¹⁶⁴ and photochemical-induced reductions.¹⁶⁵ However, the products of these methods are generally troubled by low nanoplate uniformity and yield.

2.6. Gold Nanoshells

The Au nanoshells reported in the literature refer to a class of core-shell nanoparticles that are typically prepared by coating colloidal particles made of a dielectric material with shells of polycrystalline Au. Figure 14 shows a schematic illustration and some typical examples. Gold nanoshells with diameters in the range of 10–400 nm have been reported, with the use of various types of cores, including silica and polymer colloidal particles,^{166–169} quantum dots (QDs),¹⁷⁰ liposomes,¹⁷¹ and iron oxide magnetic nanoparticles.^{172,173} In general, deposition of Au onto the surface of a dielectric core as a uniform, ultrathin shell using solution-phase methods is highly challenging.¹⁷⁴ Surface modification, either by attaching chelating ligands for Au(III) ions or by grafting Au nanoparticles of 1–3 nm in size through electrostatic adsorption, must be employed in order to generate nucleation sites for the deposition of Au(0) atoms.

The first attempted synthesis of Au nanoshells was reported by Haus and co-workers in 1994.¹⁷⁵ They described a one-step protocol that involved the addition of a specific amount of Na_2S into an aqueous $HAuCl_4$ solution at room temperature. After the initial formation of Au_2S nanoparticles, the subsequently introduced S^{2-} would reduce the Au_2S on the surface to Au(0), generating a polycrystalline Au shell. The resultant $Au_2S@Au$ core-shell nanoparticles showed tunable LSPR peaks in the range of 520–900 nm, as shown by their UV-vis spectra, making them attractive for biomedical purposes. However, the application of Au nanoshells prepared using this method

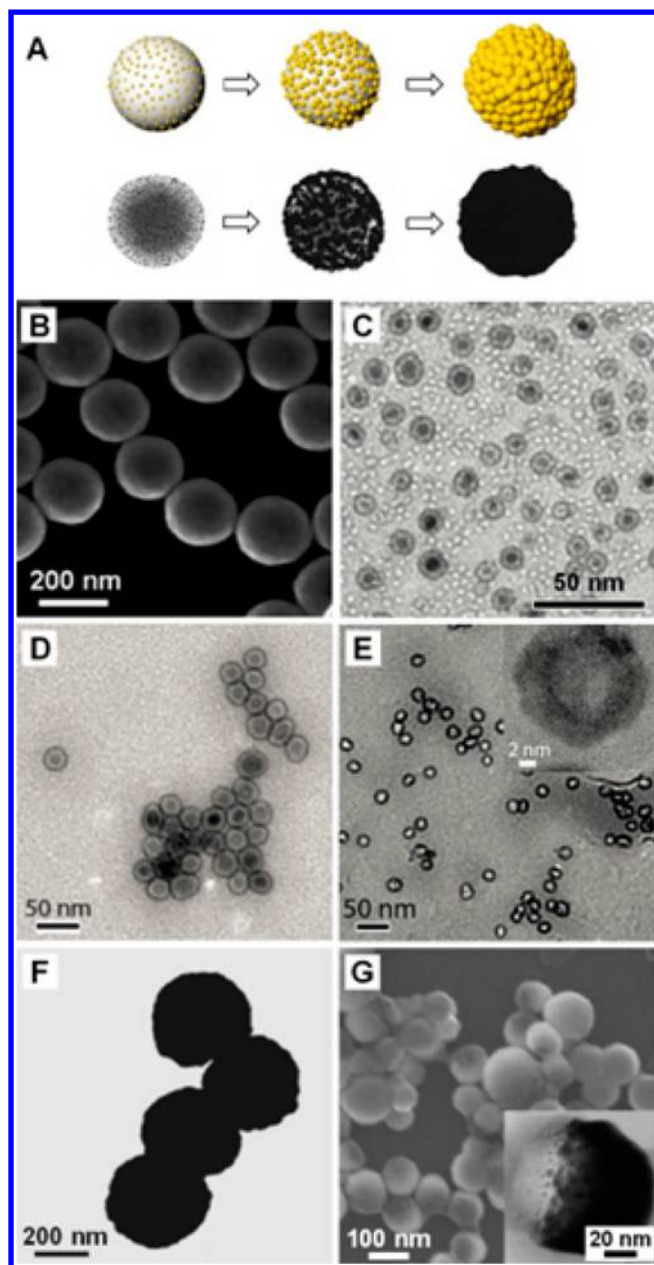


Figure 14. Gold nanoshells and half-shells synthesized by templating against different types of core materials. (A) Schematic illustration (top trace) and TEM images (bottom trace) showing changes in morphology during the deposition of Au shell on a SiO₂ colloidal sphere. Gold nanoparticles of 2–3 nm in size were attached to the surface of SiO₂ colloidal spheres before the deposition of additional Au via chemical reduction. (B) SEM image of Au nanoshells on SiO₂ cores. (C–F) TEM and HRTEM (inset) images of Au nanoshells synthesized by templating against (C) quantum dots, (D) iron oxide nanoparticles, (E) liposomes, and (F) polystyrene beads. (G) SEM and TEM (inset) images of Au half-shells synthesized with the use of poly(lactic-co-glycolic acid) (PLGA) spheres as the cores. (A) Reprinted with permission from ref 166. Copyright 1998 Elsevier. (B) Reprinted from ref 168. Copyright 2007 American Chemical Society. (C) Reprinted with permission from ref 170. Copyright 2009 Nature Publishing Group. (D) Reprinted with permission from ref 173. Copyright 2010 Nature Publishing Group. (E) Reprinted from ref 171. Copyright 2009 American Chemical Society. (F) Reprinted from ref 169. Copyright 2005 American Chemical Society. (G) Reprinted with permission from ref 178. Copyright 2008 Wiley-VCH.

remains limited due to the inability to independently control the dimensions of both the core and shell.¹⁷⁶

The Halas group improved this synthesis in 1998 by switching to SiO₂ colloidal spheres as the cores.¹⁶⁶ In a modified protocol, the nanoshells were generated by directly depositing Au nanoparticles on SiO₂ colloidal spheres, followed by the deposition of additional Au through chemical reduction. The SiO₂ colloidal spheres were, in turn, synthesized with a uniform and controllable size using the Stöber method.¹⁷⁷ The surface of the SiO₂ colloidal spheres was then functionalized with amino groups using an amino-terminated silane such as 3-aminopropyltriethoxysilane.¹⁶⁶ Due to the presence of amino groups, Au particles of 1–3 nm in size could be readily attached to the surface to act as nucleation sites for the Au(0) atoms formed in the subsequent steps. When HAuCl₄ was introduced in the presence of a mild reductant such as formaldehyde, the Au atoms produced allowed the predeposited Au particles to coalesce, generating a uniform, polycrystalline shell on the surface of each SiO₂ sphere. Depending on the size of the core and the thickness of Au coating, the nanoshells produced using this method have a typical diameter in the range of 100–400 nm, making them less desirable for most in vivo applications. These nanoshells are also plagued by a lack of a precise control over the shell thickness, uniformity, and surface smoothness. Gold atoms tended to grow around the immobilized Au nanoparticles, forming larger Au particles that only just cover the surface of the SiO₂ sphere. In fact, it was reported that such a growth process could instead result in the formation of Au nanocups as a byproduct after the SiO₂ spheres had been etched away.¹⁷⁴

Since the initial work based on SiO₂ spheres, several other types of colloidal particles have also been explored as cores for the deposition of Au nanoshells. The use of different templates can provide core–shell nanoparticles with interesting properties in addition to the LSPR features associated with the Au nanoshells, enabling a broader range of applications. To this end, the Gao group reported the use of QDs as cores to produce core–shell nanoparticles with both LSPR properties from the Au nanoshells and photoluminescence properties from the QDs.¹⁷⁰ Treatment of the surface with poly-L-histidine (PLH) was found to be critical to the success of this synthesis since the histidine group on PLH is capable of immobilizing Au(III) ions at very high packing densities, and thus serves as a soft template for the deposition of Au.¹⁷⁰ In a typical procedure, the organic-soluble QDs were coated with 1,2-distearoyl-*sn*-glycero-3-phosphoethanolamine-*N*-[carboxy-(polyethylene glycol)-2000] (DSPE-PEG₂₀₀₀-COOH) to generate a controllable gap between the Au shell and the QD core, and thereby avoid photoluminescence quenching. Poly-L-histidine was then immobilized on the surface via electrostatic interactions, followed by Au deposition initiated through a reductant such as NH₂OH. A thin layer of Au (2–3 nm) was reported to form around the QD core with a gap of 3–4.6 nm between them. The resultant QD@Au nanoshells could serve as a dual-modality imaging contrast agent because of their unique combination of photoluminescence and LSPR features. Despite the notable optical properties, application of this novel class of nanomaterials is yet to be widely explored due to complications in synthesis and the inability to easily tune particle size.¹⁷⁰ With similar PLH modification, the same group also reported the use of liposomes as dielectric cores to synthesize Au nanoshells with uniform sizes in the range of 10–70 nm and adjustable wall thicknesses.¹⁷¹ The liposomes were

first synthesized with 1,2-dimyristoyl-*sn*-glycero-3-phosphatidic acid (DMPA) and 1,2-dimyristoyl-*sn*-glycero-3-phosphocholine (DMPC) by sonication before incubation with PLH. Gold shells were then grown using a method similar to what was reported previously for the QD system.¹⁷⁰ The size of this liposome@Au nanoshell structure could be tuned from 10 to 70 nm by varying the size of liposomes serving as the templates. Because liposomes have been widely used as drug carriers, the liposome@Au nanoshells are useful as a new class of theranostic agents. The tunable LSPR features and the photothermal conversion capability of the Au nanoshells provide a simple and straightforward process to trigger drug release. In addition, the Au nanoshells around the liposomes can prevent the leakage of drugs from the liposome carriers, offering better control over the drug release profile.¹⁷¹

Magnetic iron oxide nanoparticles have also been explored as templates for the synthesis of Au nanoshells by modifying their surface with either SiO₂¹⁷² or PLH.¹⁷³ For the approach based on modification with SiO₂, the iron oxide nanoparticles were first mixed with NH₄OH and tetraethylorthosilicate (TEOS) to coat their surfaces with SiO₂ shells. This was followed by modification with 3-aminopropyltrimethoxysilane to functionalize the SiO₂ surfaces with amino groups. The surface-functionalized particles were then incubated with an aqueous solution containing HAuCl₄ and tetrakis(hydroxymethyl)-phosphonium chloride to seed the outermost surfaces with Au nanoparticles. Finally, Au shells were formed by reducing HAuCl₄ with formaldehyde in the presence of K₂CO₃.¹⁷² For the approach based on PLH coating, the iron oxide nanoparticles were subjected to a similar modification that was used for the synthesis of QD@Au nanoshells.¹⁷⁰ The iron oxide nanoparticles were sequentially modified with phospholipidpolyethylene glycol terminated in carboxylic acid (PL-PEG-COOH) and PLH to obtain a PLH-coated surface before additional Au was deposited.¹⁷³ With the encapsulation of iron oxide nanoparticles in the core, the Au nanoshells could also serve as a contrast agent for magnetic resonance imaging (MRI). Using a concept similar to Au nanoshells, particles with other morphologies (e.g., half-shells^{178,179}) and sizes up to a few micrometers^{180–183} have also been synthesized with various types of core materials to match different types of applications.

In addition to the use of dielectric cores, metal nanocrystals can also serve as cores for Au coatings to generate bimetallic core-shell nanostructures with novel properties. For example, by coating Ag nanocrystals with Au shells, Ag@Au core-shell nanocrystals were obtained with a unique combination of the excellent LSPR properties from Ag and the extraordinary stability from Au.¹⁸⁴ However, the deposition of Au on Ag in a solution phase has long been troubled by the galvanic replacement reaction between the HAuCl₄ precursor and the Ag template, which leads to the formation of Au–Ag alloyed nanoboxes or nanocages (see section 2.7).¹⁸⁵ In a recent study, Qin and co-workers solved this problem by suppressing the galvanic reaction through a parallel, faster chemical reduction reaction.¹⁸⁴ They demonstrated, for the first time, the synthesis of Ag@Au nanocubes with greatly enhanced SERS activity, together with remarkable chemical stability. In a typical synthesis, AA was used to reduce the HAuCl₄ precursor at various pH values. Since the reducing power of AA increases with pH, the reduction rate could be increased in order to suppress the reaction rate associated with galvanic replacement at pH 11.02. Similarly, the reduction rate could also be increased by switching to a much stronger reductant such as

NaBH₄. Upon addition at a greatly elevated reduction rate, the HAuCl₄ precursor would be immediately reduced to Au(0) before there was any chance to oxidize the Ag templates. By varying the amount of HAuCl₄ added, the thickness of the Au shells could be controlled to a precision of several atomic layers (Figure 15). In the presence of the Au shells, the Ag nanocubes

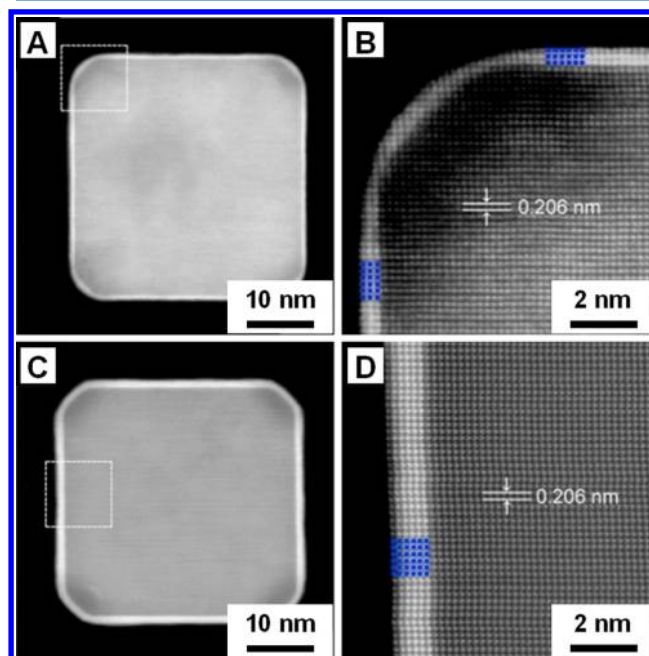


Figure 15. HAADF-STEM images of Ag@Au core-shell nanocubes with a uniform shell thickness. When the reaction is dominated by epitaxial deposition of Au rather than galvanic replacement, the thickness of the Au shell could be controlled to have three (A and B) and six (C and D) atomic layers, respectively. Reprinted from ref 184. Copyright 2014 American Chemical Society.

showed a remarkable stability against oxidation by chemicals such as aqueous H₂O₂. The ultrathin Au shells did not cause any noticeable changes to the LSPR properties of the Ag nanocubes, yet could further enhance the SERS activity of Ag nanocubes via a chemical mechanism.

2.7. Gold Nanoboxes, Nanocages, and Nanoframes

There is a class of Au nanostructures that exhibit tunable LSPR properties similar to those of Au nanoshells but have hollow interiors and/or porous walls to make them particularly useful for applications involving encapsulation, controlled release, and drug delivery. These nanostructures can be classified as nanoboxes, nanocages, and nanoframes depending on the porosity of the walls.^{11,185–188} Although such nanostructures can also be obtained from the nanoshells described in section 2.6 by selectively etching away the dielectric cores,^{189–191} it is more convenient to synthesize them via a galvanic replacement reaction between a Au(III) or Au(I) precursor and Ag nanocrystals.^{11,185,186} In this new approach, each Ag nanocube serves as a sacrificial template, around which the resultant Au atoms are deposited to generate a nanobox. Figure 16 shows a schematic illustration of the major steps involved in the formation of these hollow/porous Au nanostructures.^{185,192} The shape and dimensions of the nanobox are determined by the template while the wall thickness can be easily and precisely tuned by varying the ratio between the Au(III) or Au(I) precursor and the Ag nanocrystals. By controlling the alloying

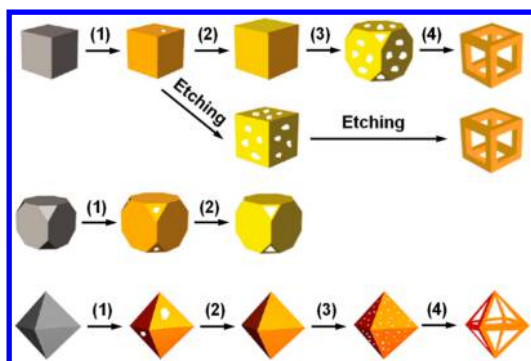
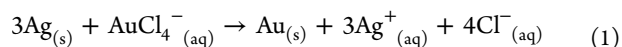


Figure 16. Schematic illustration of morphological changes involved in the galvanic replacement reaction between aqueous HAuCl_4 and a Ag nanocube with sharp corners (top trace), nanocube with truncated corners (middle trace), and octahedron (bottom trace). In all of these examples, step 1 corresponds to the initial deposition of Au on the surface of Ag nanostructures and the concurrent dissolution of Ag; step 2 corresponds to the additional deposition of Au and the alloying between Au and Ag; step 3 indicates the dealloying of the alloyed nanostructures along with the formation of porous walls on the nanostructures, and step 4 shows the further dealloying of the alloyed nanostructures and the formation of Au nanoframes. The Au content keeps increasing as the galvanic replacement reaction proceeds. The pathway indicated by “etching” corresponds to the removal of Ag from the alloyed nanostructures using an aqueous etchant such as H_2O_2 or $\text{Fe}(\text{NO}_3)_3$, and the formation of a Au nanoframe. Modified from refs 185 and 192. Copyright 2008 and 2013 American Chemical Society, respectively.

and dealloying processes involved, the walls of a nanobox can be further engineered to generate a nanocage and eventually a nanoframe.^{11,185–188,193}

The idea of using a galvanic replacement reaction to generate hollow and/or porous metal nanostructures was first conceived and demonstrated by our group in 2002, with the involvement of multiple-twinned Ag nanoparticles as the sacrificial templates.¹⁹⁴ Later, most syntheses were focused on the use of Ag nanocubes as the templates owing to their well-defined shapes and facets, as well as their broad range of controllable sizes.^{11,185,195} At the current stage of development, high quality Au nanoboxes and nanocages with edge lengths in the range of 20–200 nm can be routinely produced in relatively large quantities.^{196–200} Figure 17 shows TEM images of some representative examples. In a typical process, aqueous HAuCl_4 was titrated dropwise into an aqueous suspension of Ag nanocubes held at 90 °C. Upon contact of the two solutions, the galvanic replacement reaction will immediately take place between HAuCl_4 and Ag nanocubes according to the following equation:¹⁸⁶



Driven by the difference in electrochemical potential between $\text{AuCl}_4^{-}/\text{Au}$ (1.00 V) and Ag^{+}/Ag (0.80 V), Ag atoms are continuously oxidized and dissolved from the nanocubes, emptying the interior of the template. Simultaneously, $\text{Au}(\text{III})$ ions are reduced to generate $\text{Au}(0)$ atoms, which are epitaxially deposited on the surface of each Ag template. The LSPR peak position of the resultant Au nanostructures can be tuned continuously from the visible into the NIR region by controlling the thickness and porosity of the walls, in addition to particle size. The tuning can be precisely achieved by simply controlling the amount of HAuCl_4

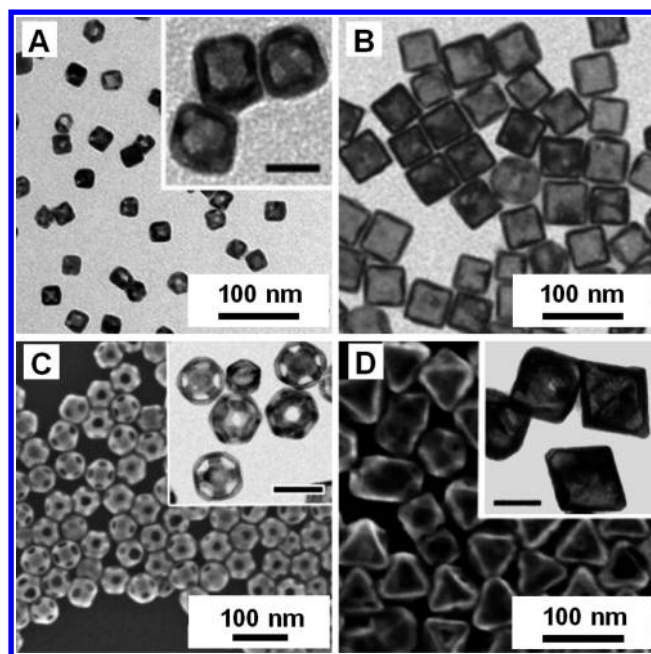


Figure 17. Electron micrographs of Au nanocages with different sizes and shapes. (A, B) TEM images of cubic Au nanocages with edge lengths of 25 and 55 nm, respectively. (C) TEM image of truncated cubic Au nanocages with an edge length of 30 nm, together with well-defined pores at the corner sites. (D) SEM and TEM (inset) images of octahedral Au nanocages with an edge length of 65 nm. The size and shape of Au nanocages are determined by the Ag templates used for the galvanic replacement reaction. The insets are the corresponding high-magnification TEM images, with the scale bars equal to 20 nm for the inset in (A) and 50 nm for the insets in (C) and (D), respectively. (A) Reprinted from ref 196. Copyright 2013 American Chemical Society. (B) Reprinted with permission from ref 200. Copyright 2010 Wiley-VCH. (C) Reprinted with permission from ref 197. Copyright 2010 Elsevier. (D) Reprinted from ref 192. Copyright 2013 American Chemical Society.

titrated into the suspension of Ag nanocubes. At the moment, the most effective method for producing Ag nanocubes is still based on the polyol method developed by our group.^{11,196,199} When the polyol method is combined with seed-mediated growth, Ag nanocubes with edge lengths in the range of 30–200 nm can be readily obtained on a scale of 1 g per batch.¹⁹⁸ Most recently, Ag nanocubes with edge lengths as short as 18 nm have also been achieved by modifying the original polyol method based upon ethylene glycol.¹⁹⁶ More detailed discussions on the synthesis of Ag nanocubes can be found in recent review articles.^{201–203}

The mechanistic details and morphological changes involved in a galvanic replacement reaction have been thoroughly investigated.^{185,195,204,205} The oxidation and dissolution of Ag tend to start from the high-energy sites on the surface of a Ag template, such as those with low PVP coverage on the side faces of a sharp cube or the {111} facets unprotected by PVP at the corner sites of a truncated cube. Newly formed $\text{Au}(0)$ atoms will then nucleate and grow on the other regions of the Ag template. With the deposition of more Au atoms, the coverage and thickness of Au gradually increases, leaving limited reactive sites for the oxidation and dissolution of Ag atoms from the interior. An alloying process also takes place along the interface of Au and Ag, facilitating the formation of hollow nanostructures with a uniform, controllable wall thickness. The as-obtained nanoboxes and nanocages are typically made

of Au–Ag alloys with various compositions. Once all pure Ag has been removed from the interior of a template, the introduction of more HAuCl_4 will lead to dealloying of Ag from the walls, transforming nanoboxes into nanocages or further increasing the porosity of nanocages. The nanocages could be made with a Au composition up to 66% by using aqueous H_2O_2 to selectively etch away Ag atoms from the alloyed walls.²⁰⁶ The transformation in morphology is also apparent by the red shift in their LSPR peak, which can be easily monitored using UV–vis–NIR spectroscopy during a synthesis. For the Au nanoboxes and nanocages derived from Ag nanocubes, their LSPR peak positions can be easily and precisely tuned from 400 nm all the way to 1200 nm. When an aqueous etchant based on $\text{Fe}(\text{NO}_3)_3$ or NH_4OH is used to selectively remove Ag from the alloyed walls, the nanocages could be transformed into nanoframes with tunable optical properties similar to those of Au nanorods.¹⁹³ In addition, Au nanoframes could be fabricated by selectively depositing Au only onto the edges of Ag decahedra or nanocubes, followed by selectively etching away the Ag templates.^{187,207} Figure 18 shows SEM and TEM images of some typical examples of Au nanoframes reported in the literature. Remarkably, their structures could be largely preserved during the preparation

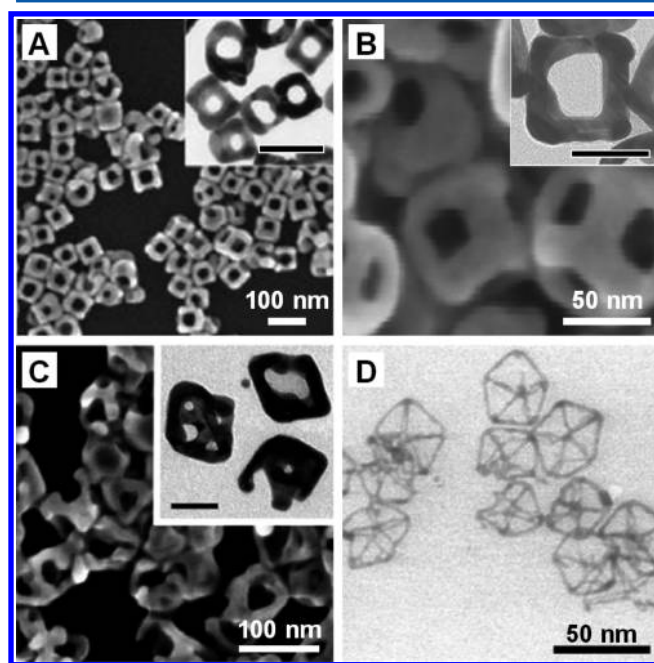


Figure 18. Electron micrographs of Au nanoframes with different sizes and shapes. (A–C) SEM and TEM (inset) images of (A) cubic nanoframes fabricated by galvanic replacement between Ag nanocubes and AuCl_2^- , (B) cubic nanoframes fabricated by galvanic replacement with Ag nanocubes and AuCl_4^- , followed by the deposition of Au and then dealloying of Ag, and (C) octahedral nanoframes prepared by galvanic replacement between Ag octahedra and AuCl_4^- . (D) TEM image of decahedral Au nanoframes prepared by depositing Au atoms onto Ag decahedra, followed by the etching of Ag templates with H_2O_2 . The insets are the corresponding high-magnification TEM images, with the scale bars equal to 100, 40, and 50 nm for the insets in (A), (B), and (C), respectively. (A) Reprinted with permission from ref 188. Copyright 2008 Springer. (B) Reprinted with permission from ref 187. Copyright 2013 Wiley-VCH. (C) Reprinted from ref 192. Copyright 2013 American Chemical Society. (D) Reprinted from ref 207. Copyright 2011 American Chemical Society.

of samples for electron microscopy, even though some of the ridges were only a few nanometers thick.

The galvanic replacement route to Au hollow nanostructures has also been explored by the Jiang, Zhang, and Li groups with the use of Co nanoparticles as templates. Hollow nanoparticles with a uniform size in the range of 30–50 nm and tunable LSPR peaks in the spectral region of 520–950 nm were obtained.^{208–211} In a typical synthesis, Co nanoparticles were prepared by reducing CoCl_2 with NaBH_4 in the presence of sodium citrate or citric acid under an inert atmosphere. After the complete decomposition of NaBH_4 , the as-prepared Co nanoparticles were subjected to galvanic replacement with HAuCl_4 . The electrochemical potentials for the redox pairs of $\text{AuCl}_4^-/\text{Au}$ (1.00 V) and Co^{2+}/Co (−0.377 V) clearly favor the reduction of AuCl_4^- by Co. Different from the synthesis involving Ag templates, the electrochemical potential of Co^{2+}/Co is so low that the Co nanoparticles are very vulnerable to oxidation by the oxygen from air. As a result, the synthesis needs to be conducted under the protection of an inert atmosphere. During the galvanic replacement reaction, a polycrystalline Au shell was formed around each Co nanoparticle. The position of the LSPR peak was determined by the ratio of its wall thickness to the inner diameter. At a fixed inner diameter, decreasing the wall thickness would cause the LSPR peak to red shift. The Co remaining inside the core of each nanoparticle could then be oxidized and etched away by the oxygen from air, leading to the formation of Au hollow nanospheres. Limited by the size of the typical Co nanoparticles, the size of the resultant hollow nanoparticles could only be tuned within a relatively narrow range.

As long as there is an enough electrochemical driving force, there is essentially no other limit to the use of galvanic replacement for the synthesis of Au hollow nanostructures. In recent years, seed-mediated growth has been explored to fabricate novel templates for the generation of Au hollow nanostructures with complex morphologies.²¹² Some delicate, multiwalled hollow structures have also been obtained by combining seed-mediated growth with galvanic replacement.^{213,214} In addition, multiwalled hollow structures could be fabricated using an approach based on Kirkendall carving, where the difference in diffusion rate between two metals was utilized.^{215,216} To facilitate the Kirkendall effect, the experiment was conducted under room temperature with the help of both PVP and CTAB. Since the experimental procedure for this type of synthesis is complicated and difficult to control at each step, it is hard to predict if such a protocol can be further extended to a larger scale in an effort to fabricate the hollow nanostructures in sufficient quantities for in vivo applications.

Another straightforward approach to the synthesis of Au hollow nanostructures is to selectively remove the dielectric cores (e.g., SiO_2 and polystyrene) used for the synthesis of Au nanoshells. Etchants such as HF or NaOH could be used to selectively remove the SiO_2 cores while preserving the Au shells.^{189–191,217,218} As detailed by van Blaaderen and co-workers, the etching could be achieved by adding HF into an as-prepared sample of $\text{SiO}_2@\text{Au}$ nanoshells to a final concentration of 2 vol %.²¹⁷ The products could be easily harvested and purified through sedimentation. As the etching process can cause aggregation for the Au hollow nanostructures, it is necessary to introduce a surfactant (such as sodium citrate) or to directly modify the surface (e.g., PEGylation).¹⁹⁰ The etching rate with HF was found to be dependent on the pH of the suspension. Further modification to this method was

made by introducing NH_4F to buffer the pH change and thus ensure a constant etching rate.²¹⁹ The etching process with NaOH could be conducted similarly by substituting HF with concentrated NaOH (3 M).¹⁹⁰ During the removal of SiO_2 cores, the LSPR peaks of the Au nanoshells would red-shift and broaden accordingly, which could be used as a parameter to monitor the extent of etching.

In general, if the coverage of Au shells is complete enough to leave only a few small pinholes on the surface, it will be difficult to etch away the SiO_2 cores. The shielding by the Au shells will drastically slow the etching reaction and possibly even prevent it from occurring. This problem was recently solved through the fabrication of hollow Au nano golf balls with controlled wall porosity.²¹⁸ As opposed to the traditional synthesis of Au nanoshells, polystyrene beads of 100 nm in diameter were first modified and attached to the surface of SiO_2 cores before the deposition of Au nanoparticle seeds. After the formation of Au shells, the polystyrene beads were dissolved by *N,N*-dimethylformamide (DMF), leaving behind a number of holes of relatively uniform size. The etchant could then readily diffuse through these holes to quickly and effectively dissolve away the SiO_2 cores.

Gold nanostructures with hollow interiors have also been prepared with templates made of other materials. However, for the same reason as with Au nanoshells, the resultant hollow structures typically possess a large size ranging from several to hundreds of micrometers, making them less favorable for most in vivo applications.^{220–225}

2.8. Other Types of Gold Nanostructures

In addition to those discussed in sections 2.1–2.7, many other types of Au nanostructures have also been reported in the literature, including those with polyhedral shapes or branched morphologies.²²⁶ While the polyhedral nanocrystals only have LSPR peaks in the visible region and are thus limited in use for biomedical applications, those with branched morphologies are optically similar to nanorods and thus well-suited for biomedical applications. In addition, the sharp corners or tips on the surfaces of a polyhedral or branched nanostructure are particularly effective for concentrating the local electric field and can thus serve as better substrates or probes for SERS-related applications.^{227–231}

2.8.1. Polyhedral Nanocrystals. There are numerous reports on the syntheses of Au nanocrystals with polyhedral shapes, including cubes, octahedra, tetrahedra, cuboctahedra, decahedra, and icosahedra.^{202,231–234} Like the shape-controlled synthesis of nanocrystals for other noble metals, significant progress has been made over the past two decades in regard to both mechanistic understanding and experimental control. For those who are interested in a more comprehensive review on this subject, please refer to some recent publications.^{202,231,232} Because of their limited use in biomedical applications (due to the need for larger amount of materials and the inability to tune the LSPR peaks to the NIR region), here we only briefly discuss a few typical examples (see Figure 19 for some representative images).^{235,236}

In 2004, the Yang group modified the polyol method developed for Ag nanocrystals and demonstrated the synthesis of Au tetrahedra, cubes, octahedra, and icosahedra as a mixture.²³⁴ In this procedure, ethylene glycol was used as both the reductant and solvent, with PVP serving as a colloidal stabilizer. By varying the concentrations of HAuCl_4 precursor and AgNO_3 additive, the yield of each individual shape could be

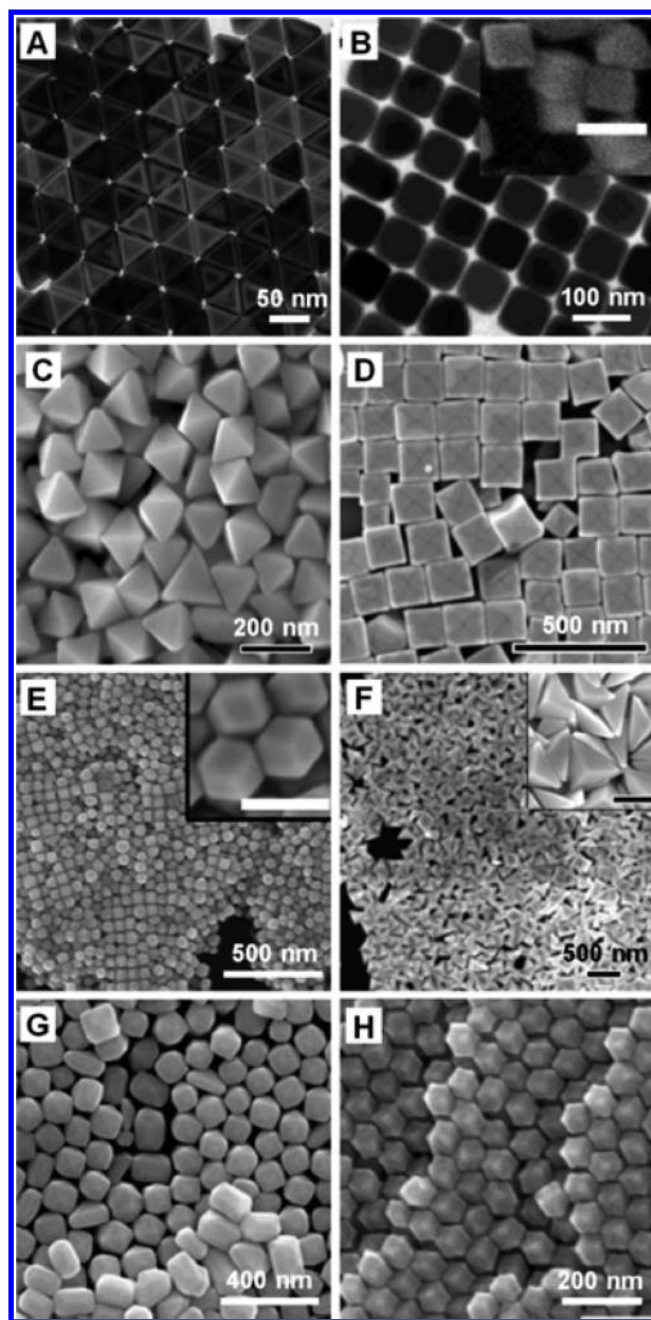


Figure 19. (A, B) TEM images of Au nanostructures with two different shapes: (A) tetrahedra and (B) nanocubes (with SEM in the inset), respectively. (C–H) SEM images of Au nanostructures with different shapes: (C) octahedra, (D) concave nanocubes, (E) rhombic dodecahedra, (F) obtuse triangular bipyramids, (G) tetrahedra, and (H) rhombic dodecahedra. The insets are the corresponding high-magnification SEM images, with the scale bars equal to 100 nm. (A) Reprinted with permission from ref 233. Copyright 2014 Wiley-VCH. (B) Reprinted from ref 239. Copyright 2004 American Chemical Society. (C and H) Reprinted from ref 99. Copyright 2008 American Chemical Society. (D) Reprinted from ref 241. Copyright 2010 American Chemical Society. (E and F) Reprinted from ref 235. Copyright 2011 American Chemical Society. (G) Reprinted from ref 236. Copyright 2009 American Chemical Society.

manipulated. Song and co-workers later modified the polyol method by replacing ethylene glycol with 1,5-pentanediol, and demonstrated the synthesis of Au octahedra, truncated octahedra, cuboctahedra, and cubes with sizes around 100

nm.^{237,238} The seed-mediated approach has also been applied to the synthesis of Au polyhedral nanocrystals. To this end, Murphy and co-workers demonstrated the synthesis of Au cubes in high purity by modifying their procedure for the synthesis of Au nanorods.²³⁹ Interestingly, Au nanorods could also serve as the seeds to generate octahedra by replacing the CTAB with PVP.²⁴⁰ Aside from these polyhedra, Au nanocrystals with concave surfaces and possessing high-index facets have been reported. For example, Mirkin and co-workers prepared Au cubes with concave surfaces by partially substituting the CTAB with CTAC.²⁴¹ The size of the concaved cubes could be tuned from 38 to 270 nm with a high purity approaching 95%. In this case, the concavity of the cubes was controlled by varying the concentration of Br⁻ ions present in the reaction solution.

2.8.2. Nanostructures with Branched Arms. Gold nanostructures with branched arms (e.g., multipods, stars, flowers, and sea urchins; see Figure 20 for four typical

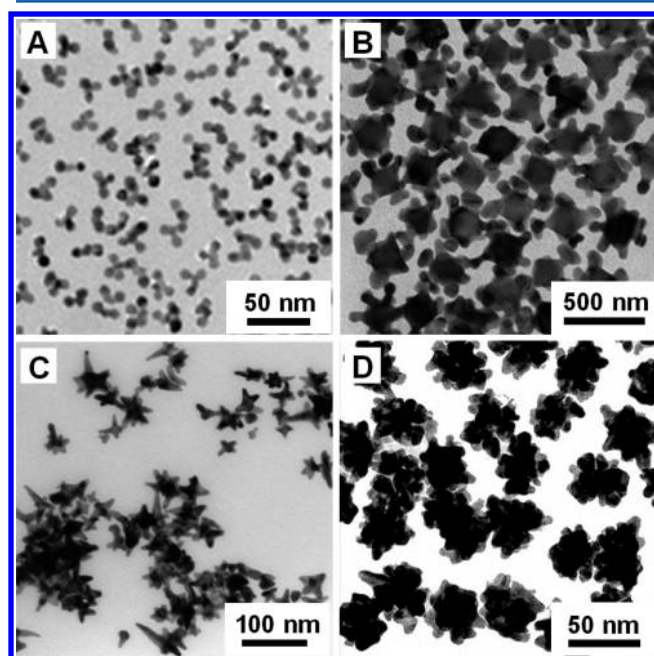


Figure 20. TEM images of Au nanostructures with branched arms in different configurations: (A) tripods, (B) hexapods, (C) stars, and (D) sea urchins. (A) Reprinted from ref 243. Copyright 2014 American Chemical Society. (B) Reprinted from ref 263. Copyright 2004 American Chemical Society. (C) Reprinted from ref 245. Copyright 2014 American Chemical Society. (D) Reprinted from ref 264. Copyright 2008 American Chemical Society.




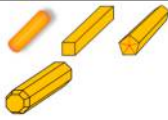
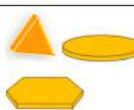




examples) are inherently anisotropic in structure and therefore characterized by tunable optical properties similar to those of Au nanorods.^{228,242–246} However, their syntheses are more diverse and challenging when compared with what has been achieved for Au nanorods. Unlike the synthesis of Au nanorods, anisotropic growth must be initiated from multiple sites of a seed and then maintained in order to generate multiple, branched arms with controlled lengths. Two different mechanisms are typically involved in the formation of Au nanostructures with branched arms: (i) site-selective deposition of Au atom on a single seed particle (either introduced or formed through self-nucleation) with the assistance of a capping agent, and (ii) aggregation or oriented attachment of many seed particles formed through self-nucleation, followed

by their growth.²⁴⁷ Both mechanisms involve anisotropic growth that is more or less similar to the case of Au nanorods. The capping agent and colloidal stabilizer play a pivotal role as they determine the site selectivity and degree of aggregation. The reaction temperature should be kept relatively low as high temperatures will lead to the formation of more thermodynamically favored shapes, such as the Wulff polyhedra.²⁴⁸ Depending on the preparation methods, each individual nanostructure can be considered as either a mono- or polycrystalline particle, with the possible involvement of twin defects or stacking faults. For those with a monocrystalline structure, the branched arms are epitaxially grown from different but equivalent facets of a single-crystal seed. In comparison, a polycrystalline structure often involves the growth of branched arms from polycrystalline seeds or aggregates of multiple seeds during the growth process.²⁴⁶ In addition, the type of reductant also plays an important role in the synthesis of Au nanostructure with branched arms.

Both seed-mediated growth and one-pot syntheses have been employed for generating Au nanostructures with branched arms. The seed-mediated approach typically offers better control over the morphology, crystallinity, and size distribution of the final product as it can use different reaction conditions to best fit the requirements needed for optimal nucleation or growth. With the introduction of seeds, secondary nucleation can be avoided to facilitate the site-selective deposition of the newly formed atoms. The first attempt was reported by Carroll and co-workers in 2003, in which Ag nanoplates were used as seeds to generate single-crystal Au multipods.²⁴⁶ In a typical process, HAuCl₄ was reduced by AA in the presence of Ag nanoplates, NaOH, and CTAB. The final products were a mixture of monopod, bipods, tripods, and tetrapods, with a yield of about 60% for the morphology with branched arms. In this synthesis, NaOH was believed to be responsible for accelerating the reduction of Au(III), inducing anisotropic growth on the seeds. The role of Ag nanoplates, however, remains unclear as they should be entirely or partially dissolved to release Ag⁺ ions into the reaction solution due to the galvanic replacement prior to the introduction of AA.

Murphy and co-workers demonstrated the synthesis of a set of Au nanoparticles with branched arms, including tetrapods, by modifying the seeded growth method developed for Au nanorods.²³⁹ Using a similar protocol, Au nanostructures with branched arms were prepared with overall dimensions in the range of 70–300 nm and a polycrystalline structure by starting with either mono- or polycrystalline Au nanoparticles as the seeds.^{242,246,249–251} It was shown that the concentrations of surfactants and other additives played a critical role in these syntheses as they could alter the deposition rates of Au onto different crystallographic facets in addition to initiating the anisotropic growth. Like the synthesis of Au nanorods, CTAB and AgNO₃ are often used (as the surfactant and additive, respectively) to induce and facilitate anisotropic growth of the seeds.^{16,127,228,252,253} They appear to work in a similar way as described in section 2.4 for the synthesis of Au nanorods. Specifically, the Br⁻ ions from CTAB have been shown to play a critical role in the formation of Au nanoparticles with branched arms.^{193,195} At an intermediate concentration of 0.01 M for the Br⁻ ions, Au nanoparticles with branched arms could be obtained with purity close to 100%.²³⁹ Surfactants other than CTAB were also shown to induce the formation of branched structures. For example, when the CTAB in a synthesis was replaced by sodium dodecyl sulfate (SDS), Au

Table 1. Summary of the Syntheses and LSPR Properties of Different Types of Au Nanostructures

Au nanostructures	Schematic drawing	LSPR peak positions	Size range	Methods of Synthesis	References
Clusters			<2 nm	"Bottom-up" and "Top-down"	26–29, 57–77, 79, 80, 82, 275, 279, 280
Conventional particles		520–650 nm	1.5–180 nm	Turkevich method and Brust method	84–98
Spheres		520–650 nm	5–150 nm	Seed-mediated growth	99–103, 106
Rods		600–1800 nm, for the longitudinal mode	20 nm to several μ m	Electrochemical reduction, seed-mediated growth, photochemical reduction, bioreduction, microwave-assisted reduction, solvothermal reduction	108–137
Plates, prisms, and disks		700–1300 nm, for the in-plane mode	40–1000 nm (edge length) and 5–50 nm (thickness)	Electrochemical reduction, microwave-assisted reduction, ultrasound-assisted reduction, photo-induced reduction	138, 140–165
Shells		520–900 nm	10–400 nm	Template-directed synthesis	166–175, 178–184
Boxes, cages, frames, and related hollow structures		400–1200 nm	20–200 nm (edge length)	Galvanic replacement reaction	186–200, 205–218, 220, 222–225
Polyhedra		560–1000 nm	20–270 nm	Polyol process, seed-mediated growth	233–241
Structures with branched arms		550–800 nm	45–300 nm	Seed-mediated growth, one-pot synthesis	227–230, 239, 242–254, 256–270

nanoparticles with branched arms could be made with an overall size as small as 40 nm by employing citrate-stabilized nanoparticles as seeds.²⁵⁴ The surface diffusion of the deposited atoms can play an important role in controlling the formation of anisotropic structures through a site-selective-deposition mechanism, as was demonstrated in the synthesis of Pd octapods.²⁵⁵ In addition, the reducing agent can affect the formation of Au nanoparticles with branched arms because of its direct impact on the reaction kinetics. For example, Au nanostructures with thin thorns were obtained when NH_2OH was used as a reducing agent in the presence of AgNO_3 and citrate-stabilized Au nanoparticles. No additional stabilizer or capping agent was involved.²⁵⁶ Similarly, hydroxylamine sulfate, a salt of NH_2OH with sulfuric acid, could also be used to generate Au nanoparticles with branched arms.²⁵⁷

In a later study, Liz-Marzán and co-workers reported the synthesis of Au nanostructures with branched arms using DMF as a reductant and PVP as a stabilizer.^{258,259} This protocol has

found great application for its relative simplicity and high product purity (approaching 100%). By varying the concentration of seeds, the overall size of the resultant Au nanostructures with branched arms could be tuned from 45 to 160 nm without sacrificing particle uniformity. Using a similar approach, spines were also grown on the surface of Au nanowires to generate the so-called thorny nanowires.²⁶⁰ As expected, it was difficult to control the number of branched arms presented on each seed. In a modified procedure, our group demonstrated the synthesis of Au hexapods using PVP-protected, single-crystal Au octahedra as the seeds.²⁶¹ By optimizing the experimental conditions, only one arm was selectively grown to a specific length from each corner of an octahedral seed, allowing for a precise control over both the number of arms and their length.

One-pot syntheses have also been explored to prepare Au nanostructures with branched arms. The synthesis could follow one of the two aforementioned mechanisms, yielding either

mono- or polycrystalline nanostructures. In one example, AA was used to directly reduce HAuCl_4 without any additional stabilizer or capping agent to generate a mixture of mono- and polycrystalline Au nanostructures with branched arms in an aqueous system under ambient conditions.²⁶² This synthesis followed the site-selective-deposition mechanism. After the initial formation of Au nanocrystals with a cuboctahedral or icosahedral shape, the preferential addition of Au atoms to the {111} facets leads to the formation of star-shaped nanostructures. In another example, the HAuCl_4 precursor was reduced by a mixture of sodium citrate and H_2O_2 in the presence of bis(*p*-sulfonatophenyl)phenylphosphine dipotassium dehydrate (BSPP) to generate Au nanostructures with branched arms at a purity of >90%.²⁶³ However, this synthesis suffered from a nonuniform number of arms grown from particle to particle. The one-pot approach has also been used to obtain Au nanostructures with morphology resembling a sea urchin, flower, or raspberry.^{247,264–268} Such a synthesis tends to involve the aggregation of initially formed Au nanoparticles, followed by their growth from the surface of an aggregate. In a typical synthesis described by Chang and co-workers, Au sea urchins were obtained by reducing HAuCl_4 with sodium citrate, followed by the addition of NaCl.²⁶⁸ After the initial reduction of HAuCl_4 and primary nucleation, the Au nanoparticles began to aggregate upon the addition of NaCl to form particles with multiple sites for further anisotropic growth into branched arms. Another interesting synthesis involved the use of *N*-2-hydroxyethylpiperazine-*N*-2-ethanesulfonic acid (HEPES), a so-called “green chemical” because of its barely noticeable toxicity and wide use in cell biology, to serve as both the reducing agent and surfactant.²⁶⁹ By varying the concentrations of HAuCl_4 and HEPES, Au nanoparticles with one to eight arms, together with “nanoflowers”, were obtained at a purity as high as 90%.^{247,270} As detailed by Wang and co-workers, the concentration of HEPES had to be kept at a low level to facilitate the aggregation of primary Au nanoparticles and then induce the formation of nanoflowers with a large number of arms.²⁴⁷ The use of HEPES at high concentrations effectively prevents the aggregation of primary Au nanoparticles, resulting in the formation of Au nanostars instead.²⁴⁴ In addition to colloidal stabilizers, capping agents with a strong binding to the Au surface could also be used to prepare nanostructures with branched arms by inducing anisotropic growth for the nanoparticle seeds. To this end, thiol-based capping agents have been used to induce the formation of polycrystalline nanoscale Au sea urchins through chemisorption on the surface of a seed.²⁶⁶

Although there are a number of protocols for the syntheses of Au nanostructures with branched arms, the mechanism underlying the anisotropic growth of the arms or tips is yet to be fully elucidated. As a result, it remains challenging to finely control the yield, size, number of arms, length of the arms, and sharpness of the tips. In general, the success of such a synthesis critically depends on the use of a proper capping agent or stabilizer to selectively minimize the interfacial free energies of different crystal facets or to control the degree of particle aggregation. Table 1 shows the summary of the syntheses and LSPR properties of different Au nanostructures.

2.9. Postsynthesis Surface Modification

The as-prepared Au nanostructures typically possess surface ligands such as citrate, CTAB, and PVP, among others. In most cases, these surface ligands inherited from the syntheses do not

meet the requirements for a specific biomedical application. As a result, postsynthesis surface modification is needed to appropriately adapt the Au nanostructures for a specific biomedical application. Surface modification can change the properties of Au nanostructures in several ways. First, surface modification can serve to endow water solubility to the otherwise hydrophobic Au nanostructures. For example, Rotello and co-workers used 11-mercaptoundecanoic acid (11-MUA) to partially replace the surface-bound octanethiol ligand on 2 nm Au nanoparticles using the Brust method.²⁷¹ As a result, the hydrophobic Au nanoparticles were successfully transferred into an aqueous system. Second, surface modification can help improve the colloidal stability of Au nanostructures. For Au nanoparticles stabilized with citrate ions, they tend to aggregate under the biological conditions, while a surface coating of PEG molecules can alleviate this problem through the additional stability brought by the steric repulsion between PEG chains.²⁷² In addition, surface modification with PEG can prevent protein binding during in vivo applications, thus minimizing the clearance of Au nanostructures by the immune system and improving the biodistribution of such nanomaterials.^{273,274} Finally, some surface modifications can bring entirely new properties to the Au nanostructures. For example, Chen and co-workers prepared dodecanethiol-capped Au_{11} clusters by reacting $\text{Au}_{11}\text{Cl}_3(\text{PPh}_3)_7$ clusters with dodecanethiol.²⁷⁵ Despite the same Au_{11} core, photoluminescence was only observed from the dodecanethiol-stabilized clusters. By replacing the original surface ligand with Raman active ones, Au-based SERS probes could be fabricated.^{276,277} Surface modifications with polymeric ligands could lead to the aggregation of Au nanoparticles, and their LSPR properties could thus be manipulated.²⁷⁸

Ligand exchange is by far the most widely used method for the surface modification of Au nanostructures, which is based on the formation of a strong Au–S bond between the Au surface and a thiolate ligand, replacing the originally bound ligands.²⁴ The ligand exchange can be realized by simply incubating the desired thiolate molecules with the Au nanostructures. This exchange method can also be used to replace the originally bound thiolate ligands with other thiols, which was developed by Murray and co-workers under the name of “place exchange”.²⁷⁹ There exists an equilibrium between the surface-bound ligands and the free ones in the solution. As a result, the degree of ligand exchange on the surface of Au nanostructures is controlled by the ratio of the new ligands relative to the old ones, as well as the reaction temperature and time. A mixed composition can be obtained for the surface of Au nanostructures by introducing two or more thiolate ligands for the exchange process, and the ratio of each component can be tuned by varying the feeding ratio of the different ligands. Commonly used thiolate ligands include small molecules (e.g., mercapto acids,²⁷¹ peptides²⁸⁰), biomacromolecules (e.g., thiolated DNA²⁸¹), and polymers (e.g., thiolated PEG²⁸²). In one example, Tsukuda and co-workers reported the ligand exchange between the as-synthesized phosphine-stabilized Au_{11} clusters and GSH. The Au_{11} clusters were observed to change their size after ligand exchange to become GSH-capped Au_{25} clusters. They attributed the formation of $\text{Au}_{25}(\text{SG})_{18}$ clusters to the extraordinarily high stability associated with the “magic number” of 25.²⁸⁰ Mirkin and co-workers prepared Au nanoparticles covered by mercaptoalkyloligonucleotide through ligand exchange for the citrate-stabilized nanoparticles, and used them as probes in

colorimetric detection of polynucleotide.²⁸³ Petri-Fink and co-workers reported the replacement of surface CTAB on Au nanorods by thiolated PEG. They found that the CTAB molecules could not be replaced completely with a one-step ligand exchange process, and the remaining CTAB on the surface of Au nanorods could only be further removed through the addition of ethanol.²⁸⁴ The two-step ligand exchange process was able to provide Au nanorods free of CTAB, accomplishing complete detoxification. Cao and co-workers developed a dual interaction ligand based on thiolated Tween derivatives (TD) for replacing the original alkanethiolate ligands on the surface of Au nanostructures.²⁸⁵ The TD ligands were observed to bind to Au surface more strongly because of a dual interaction including both the formation of the covalent Au–S bond and the hydrophobic interactions between the remaining alkanethiol ligands with the hydrophobic chains in the TD ligands.

It is worth mentioning that a secondary tethering of molecules to the thiolate ligands is possible either through covalent conjugation (e.g., amine–carboxylate coupling,²⁸⁶ or click chemistry^{37,287}) or noncovalent interactions (e.g., electrostatic interactions,^{288,289} or hydrophobic interactions²⁹⁰). For example, Astruc, Hosmane, and co-workers demonstrated the preparation of dendritic PEGylated Au nanoparticle–carborane assemblies through click chemistry between azido-terminated Au nanoparticles and a mixture of carborane alkyne and PEG alkyne.²⁸⁷ Such Au nanostructures may find application in boron neutron capture therapy (BNCT) due to the presence of carboranes. Rotello and co-workers reported the preparation of a Au–enzyme conjugated structure via electrostatic interactions between negatively charged β -galactosidase and positively charged trimethylammonium PEGylated Au nanoparticles.²⁸⁹ Upon the addition of toluene and 1,2,4-trichlorobenzene, microcapsules composed of nanoparticle–enzyme conjugates were formed. The secondary tethering of Au nanostructures is often used in sensing, drug loading, and improving the biodistribution of such nanomaterials.

In addition to ligand exchange, there are other approaches to surface modification. For example, SiO₂ coating on Au nanostructures can improve their hydrophilicity and biocompatibility. The coating can be realized using the Stöber method through the hydrolysis and condensation of silicon alkoxides (e.g., TEOS) in alcohol solvents (e.g., ethanol) in the presence of water and a small amount of base (e.g., NH₄OH) serving as a catalyst.^{291,292} The SiO₂ shell is able to protect the underlying Au nanostructures from aggregation in the biological environment. Furthermore, the surface of SiO₂ shell can be further functionalized for targeting purposes.²⁹³ The porous structure in the SiO₂ shell is particularly useful for applications such as drug delivery.^{294,295}

For detailed discussions on the surface modification of Au nanostructures, readers can refer to some recent reviews on this topic.^{296–298}

3. OPTICAL PROPERTIES OF GOLD NANOMATERIALS

3.1. Photoluminescence

Luminescence is a process that involves the electronic transition between two different energy levels and thus the emission of electromagnetic radiation. Depending on the means of excitation, luminescence can be classified into many different categories, including photo-, chemo-, and electroluminescence, among others. Photoluminescence is a result of light absorption

where the emission can be described as either fluorescence or phosphorescence depending on the relaxation mechanism (singlet–singlet versus triplet–singlet) and thus the emission lifetime (nanoseconds to microseconds versus milliseconds). Fluorescence has found widespread use in both analytical chemistry and biomedicine owing to the following attractive features: (i) ease of sample preparation; (ii) easy detection; (iii) high selectivity; (iv) high sensitivity (down to the single-molecule level).

The size of a Au nanostructure has a large impact on its photoluminescence properties. When the size of a Au nanostructure decreases to approximately 2 nm, the spatial confinement of free electrons by the nanostructure results in discrete, size-dependent energy levels, and thus tunable photoluminescence.^{25,299–301} In general, the valence electrons in a piece of metal can be considered as free electrons (i.e., they are not tied to any particular atoms) while the core electrons are confined to individual atoms. The photoluminescence emitted by a Au cluster can be described using a free-electron model (based on the assumption that the valence electrons can travel freely through the cluster due to the negligible interactions between the valence electrons and the nuclei), suggesting that the emission arises primarily from intraband (sp–sp) rather than interband (sp–d) transitions.³⁰² In comparison, the photoluminescence from Au nanostructures or bulk Au can be assigned to radioactive recombination following interband electronic transitions between the d and sp bands.³⁰²

In general, the number of Au atoms in each cluster,^{26,76,77,82,300,303–307} the aggregation state of the clusters,³⁰⁸ and the type of capping ligand can all impact the photoluminescence emitted from a sample of Au clusters.³⁰⁹ Ying and co-workers reported the use of BSA as a matrix to prepare fluorescent Au clusters with a remarkable quantum yield of 6%.⁸² Spectroscopy studies further confirmed that the photoluminescence originated from the Au clusters rather than BSA. As shown in Figure 21A, the Au clusters displayed an emission peak at 640 nm, implying the presence of Au₂₅ clusters according to the spherical jellium model, which was supported by the data from MALDI-MS. In another study, Xie and co-workers demonstrated that the strong luminescence from Au(0)@Au(I)–thiolate clusters could be explained using a mechanism based on aggregation-induced emission (AIE).³⁰⁸ As shown in Figure 21B, nonluminescent oligomeric Au(0)@Au(I)–thiolate clusters could emit strong photoluminescence once the clusters had been induced to aggregate. The wavelength and intensity of the photoluminescence were largely determined by the degree of aggregation. This method was further used to develop highly luminescent Au nanostructures with a quantum yield up to 15%.

Jin and co-workers examined the photoluminescence properties of [Au₂₅(SR)₁₈]^q (where *q* indicates the charge state of the cluster) and found that the capping ligand, –SR, played a major role in enhancing the photoluminescence of Au clusters, as shown in Figure 21C,D.³⁰⁹ The surface capping ligand can affect the photoluminescence in two different ways: (i) charge transfer from the ligand to S and then Au through the Au–S bond and (ii) direct donation of electrons from other electron-rich atoms or groups in the ligand to Au. Recently, it was found that the type of solvent could also affect the optical properties of Au clusters.³⁰⁸ It was demonstrated that any change to the chemical environment could induce electronic energy splitting

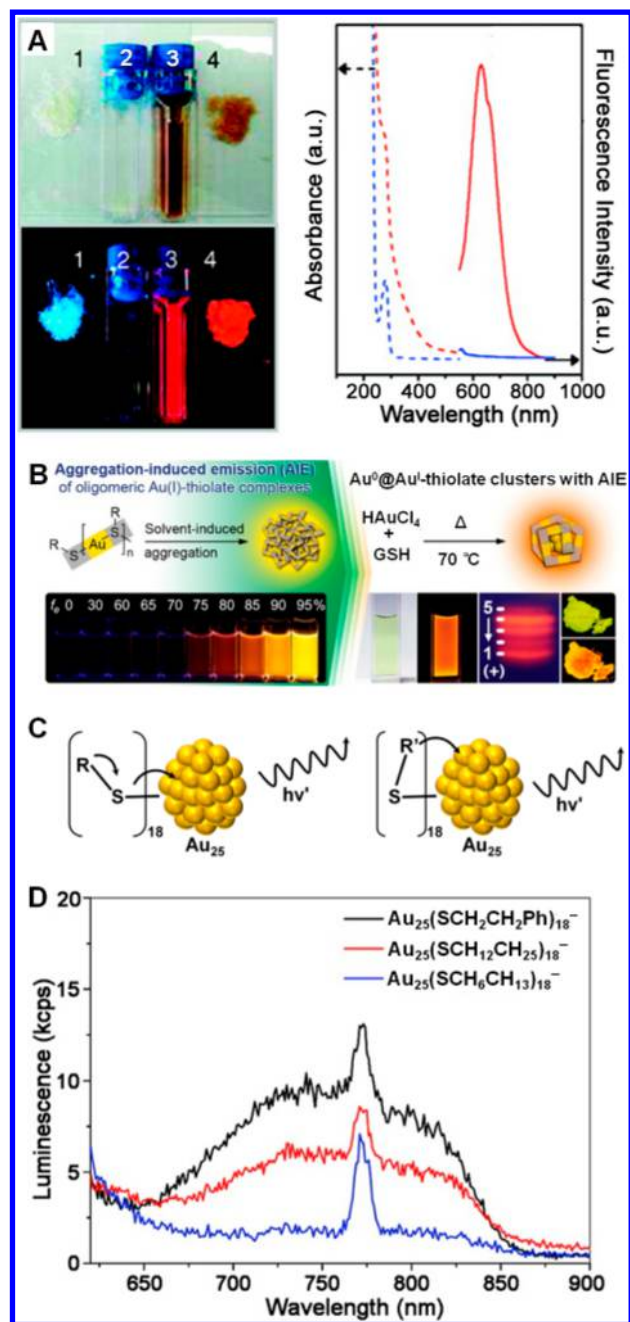


Figure 21. Photoluminescence properties of Au clusters. (A) Photographs of bovine serum albumin (BSA) powder (1) and aqueous solution (2), and BSA-stabilized Au clusters in an aqueous solution (3) and as a powder sample (4) under exposure to visible (top) and UV light (bottom). The right panel shows optical absorption (dashed lines) and emission (solid lines, $\lambda_{\text{ex}} = 470$ nm) spectra for aqueous solutions of BSA (blue) and BSA-stabilized Au clusters (red). (B) Schematic illustration showing the strong photoluminescence through an aggregation-induced emission mechanism. (C) Schematic illustration showing how the surface ligand can influence the photoluminescence properties of Au clusters. (D) Photoluminescence spectra of Au clusters protected by different types of ligands (Ph stands for phenyl group). (A) Reprinted from ref 82. Copyright 2009 American Chemical Society. (B) Reprinted from ref 308. Copyright 2012 American Chemical Society. (C and D) Reprinted from ref 309. Copyright 2010 American Chemical Society.

and charge redistribution on the surface of a Au cluster, resulting in variations to the photoluminescence.

Gold nanostructures with a variety of shapes or morphologies, including conventional particles,³¹⁰ rods,³¹¹ plates,³¹² shells,³¹³ cages,³¹⁴ and stars,³¹⁵ have all been reported with photoluminescence properties. For the conventional particles, a decrease in grain size not only increases grain boundary scattering but also results in the quantum confinement effect (i.e., the appearance of discrete energy levels).^{316–319} Figure 22A shows the emission spectrum recorded from conventional

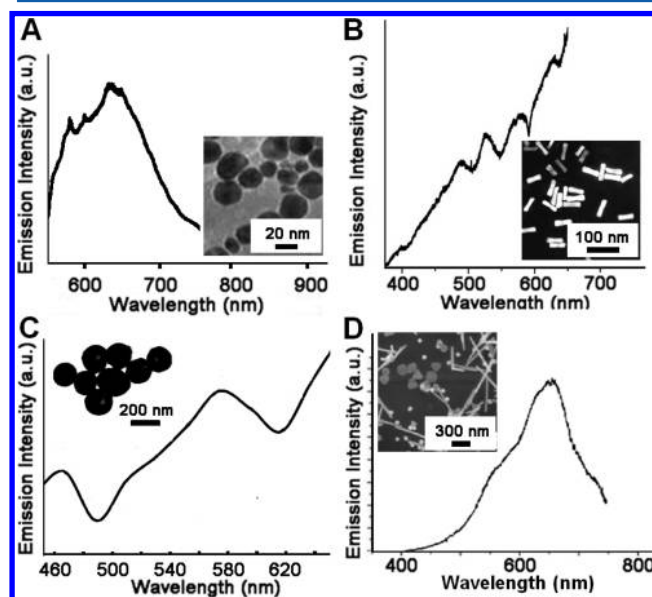


Figure 22. Photoluminescence properties of Au nanostructures with different shapes: (A) SPPL emission spectrum of the conventional Au nanoparticles (SPPL stands for single-photon photoluminescence), (B) TPPL emission spectrum of Au nanorods (TPPL represents two-photon photoluminescence), (C) TPPL emission spectrum of Au nanoshells, and (D) TPPL emission spectrum of Au nanoplates. Each inset shows a typical TEM or SEM image of the corresponding sample. (A) Reprinted with permission from ref 310. Copyright 2012 Royal Society of Chemistry. (B) Reprinted with permission from ref 311. Copyright 2005 National Academy of Sciences, U.S.A. (C) Reprinted with permission from ref 313. Copyright 2011 IOP Publishing. (D) Reprinted with permission from ref 312. Copyright 2006 American Institute of Physics.

Au nanoparticles (see the inset for a TEM image).³¹⁹ These polycrystalline particles had an average diameter of approximately 20 nm, and each particle was composed of multiple grains, each as small as 1 nm. The particles showed strong absorption and emission with peaks at 540 and 650 nm, respectively. Compared to bulk Au, the photoluminescence quantum yield of Au nanoparticles can be enhanced by millions-fold due to the enhancement of the local electromagnetic field on the surface (by several orders of magnitude) and coupling with the LSPR.^{320–322}

Depending on the excitation scheme, photoluminescence can be classified as single-, two-, and three-photon photoluminescence, respectively, abbreviated as SPPL, TPPL, and 3PPL. In TPPL, the electron is excited by two photons of half the energy relative to the photon in SPPL. Similarly, 3PPL involves the absorption of three photons with one-third of the energy for the photon in SPPL. As a linear optical property, SPPL involves the polarization of a material as a linear function of the electric field strength. On the contrary, TPPL and 3PPL are nonlinear optical properties where the induced polarization

depends on the applied electric field in a nonlinear manner. For example, the emission intensity of TPPL is proportional to the square of the intensity of the excitation light source while the emission intensity of 3PPL depends on the excitation light intensity to the third power.

El-Sayed and co-workers were among the first to study the photoluminescence properties of Au nanorods. They discovered that Au nanorods with an aspect ratio of 2.0–5.4 had a photoluminescence quantum yield over 1 million times higher than that of bulk Au.^{320,323} The quantum yield was found to increase quadratically with the length for Au nanorods of the same width, while the peak wavelength increased linearly. The emission was assigned to the radioactive recombination following interband electronic transitions between the d and sp bands. Figure 22B shows a typical TPPL spectrum recorded from Au nanorods (see the inset for a TEM image).³¹¹ The TPPL signal from a single Au nanorod was found to be 58 times stronger than that from a single rhodamine 6G (R6G) molecule. Figure 22C shows a typical TPPL spectrum of Au nanoshells with the inset giving a TEM image.³¹³ Okamoto and co-workers investigated the TPPL properties of individual Au nanoplates using an apertured scanning near-field optical microscope.³¹² Figure 22D shows the TPPL spectrum recorded from one triangular Au nanoplate (see the inset for a TEM image of the sample). The Au nanoplate showed much stronger TPPL than a single Au nanorod contained in the same sample. The TPPL signal of the Au nanoplates is strongly dependent on the polarization and wavelength of the incident light. Again, the coupling with LSPR was believed to be the primary reason for the enhancement in TPPL signal intensity. In principle, the TPPL from Au nanoparticles can be manipulated by engineering both the size and shape.

Through a collaboration, the Cheng and Xia groups investigated the nonlinear optical properties of Au nanocages (see Figure 23A for a typical UV–vis–NIR extinction spectrum) using a multimodal multiphoton microscope.^{314,324} It was found that the Au nanocages showed TPPL properties similar to other types of Au nanostructures such as nanorods (Figure 23B). In addition, the Au nanocages displayed strong 3PPL because of the unique Au–Ag alloy composition. Figure 23C shows a typical 3PPL spectrum recorded from the Au nanocages. When excited with a femtosecond laser at 1290 nm, a third harmonic generation (THG) peak was observed at 430 nm, together with a broad 3PPL peak in the visible region. Unlike TPPL that involves the use of an excitation wavelength overlapping with the LSPR peak of Au nanocages, the use of a much longer excitation wavelength in 3PPL could greatly reduce the level of phototoxicity arising from the cavitation effect and completely eliminate the autofluorescence background when applied to ex vivo tissue imaging.

3.2. Localized Surface Plasmon Resonance

As discussed in section 3.1, the electronic structures of Au clusters are characterized by discrete energy levels. The situation differs in the case of nanoparticles due to the drastic increase in the number of Au atoms and thereby the decrease and eventual disappearance of the spacing between adjacent energy levels. Upon irradiation by light, the free electrons in a Au nanoparticle will undergo collective oscillation due to the presence of an oscillating electromagnetic field. This optical phenomenon is commonly known as LSPR.

3.2.1. The Basics. Although Michael Faraday wondered about the bright red appearance of his sample of Au colloids

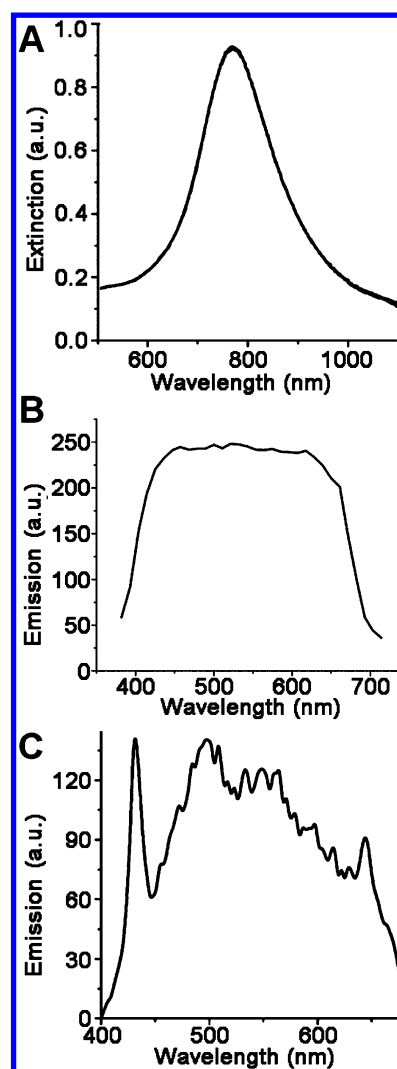


Figure 23. (A) UV–vis extinction, (B) TPPL (TPPL stands for two-photon photoluminescence), and (C) 3PPL (3PPL represents three-photon photoluminescence) spectra recorded from aqueous suspensions of Au–Ag alloy nanocages with an edge length of about 50 nm. (A and B) Reprinted from ref 324. Copyright 2010 American Chemical Society. (C) Reprinted with permission from ref 314. Copyright 2010 Wiley-VCH.

and suspected that “a mere variation in the size of its particles gives rise to a variety of colors”, there was no established theory at the time for understanding or explaining the phenomenon he observed in 1856.⁹ In retrospect, Faraday could have potentially solved the mystery using an early form of the Maxwell equations published around 1861. However, a theory was not proposed until 1908 when Gustav Mie derived the first-ever solutions to the Maxwell equations for small particles with a spherical shape, which offered a clear explanation for the fascinating ruby red color displayed by Au colloids.¹³ It is now well-established that the optical properties of a small particle made of Au (and other materials) can always be computed using the Maxwell equations in an analytical or numerical format depending on the geometric shape of the particle.³²⁵

For a metal nanoparticle, its optical properties are dominated by the collective oscillations of free electrons contained in the particle. Under the irradiation of light, the free electrons are driven by the alternating electric field to collectively oscillate at an eigenfrequency (ω_p) relative to the lattice of positive ions.

For a bulk metal with infinite sizes in all three dimensions, the ω_p can be derived as $\omega_p = (Ne^2/\epsilon_0 m_e)^{1/2}$ using the Drude model, where N is the number density of free electrons; e and m_e are the charge and effective mass of an electron.^{326,327} In practice, we have to evaluate an object that is confined by finite dimensions and surrounded by a medium with a specific dielectric constant. Since the light impinging on a metal surface can only penetrate to a certain depth (<50 nm for Au and Ag), only the free electrons on the surface of a metallic object will contribute to the plasmon resonance. For a metal–vacuum interface, application of the boundary condition results in a surface plasmon mode of frequency $\omega_p/(2)^{1/2}$, where this plasmon mode represents a longitudinal surface charge density wave along the metal surface. When the collective oscillations of free electrons are further confined to a finite volume (e.g., within a metal nanoparticle), we will obtain a new plasmon mode, which is commonly referred to as LSPR. When vacuum is taken as the surrounding medium, the resonant frequency becomes $\omega_p/(3)^{1/2}$.³²⁵ When the surrounding medium is no longer a vacuum, the resonant frequency will be determined by the dielectric constants of both the metal and the surrounding medium. For a spherical system, the analytical solutions are commonly referred to as the Mie theory.

3.2.2. The Mie Theory. When a light source with intensity of I_0 passes through a colloidal suspension of spherical particles (with a radius of r) over a distance of l , its intensity will drop to I and the degree of attenuation can be expressed as $\log(I_0/I) = \mu_{\text{ext}} l M_p$, where μ_{ext} is the molar extinction coefficient ($\text{L mol}^{-1} \text{cm}^{-1}$) of the colloidal suspension, l is the light path length (cm), and M_p is the molar particle concentration (mol L^{-1}). The molar extinction coefficient is correlated to the extinction cross section (C_{ext}) of an individual particle by $\mu_{\text{ext}} = N_A C_{\text{ext}}$, where N_A is the Avogadro constant. When suspended in a homogeneous medium, the C_{ext} of a spherical particle with a radius much smaller than the wavelength (λ) of incident light can be calculated using the Mie theory:³²⁸

$$C_{\text{ext}} = \frac{24\pi^2 r^3 \epsilon_m^{3/2}}{\lambda} \frac{\epsilon_i}{(\epsilon_r + 2\epsilon_m)^2 + \epsilon_i^2} \quad (2)$$

While the surrounding medium is characterized by a dielectric constant of ϵ_m , the dielectric constant (ϵ) of the metal has to be expressed as a complex number with a real part ϵ_r and an imaginary part ϵ_i . From eq 2, it can be seen that C_{ext} is dependent on the particle size, as well as the dielectric constants of both the medium and the metal. The real part of the dielectric constant for the metal determines the position of the resonance peak because C_{ext} reaches a maximum (i.e., when resonance occurs) at $\epsilon_r = -2\epsilon_m$. The imaginary part of the dielectric constant of the metal, on the other hand, determines the width of the resonance peak.

The extinction of light can be divided into two parts: absorption and scattering. Scattering is an elastic process that changes the direction of incident light without changing its frequency. On the other hand, the absorption of incident light involves the conversion of photons into heat (i.e., phonons, or vibrations of the crystal lattice). Similar to extinction, the optical cross sections for both scattering and absorption will reach their maximum values simultaneously at the resonant frequency. Specifically, the absorption and scattering cross sections (C_{abs} and C_{sca}) of a spherical particle and their relationships to C_{ext} can be expressed as the following:^{325,327}

$$C_{\text{ext}} = C_{\text{abs}} + C_{\text{sca}} \quad (3)$$

$$C_{\text{abs}} = 4\pi k r^3 \text{Im} \left[\frac{\epsilon - \epsilon_m}{\epsilon + 2\epsilon_m} \right] \quad (4)$$

$$C_{\text{sca}} = \frac{8\pi}{3} k^4 r^6 \left| \frac{\epsilon - \epsilon_m}{\epsilon + 2\epsilon_m} \right|^2 \quad (5)$$

where k is the wavevector of light in the medium ($k = 2\pi/\lambda$). It can be seen that both the C_{abs} and C_{sca} increase with larger particle sizes. While the C_{abs} increases at a slower rate that is proportional to r^3 or the volume of the particle (V), the C_{sca} increases at a faster rate proportional to r^6 or V^2 . As shown in Figure 24A, the ratio of C_{sca} to C_{abs} increases quickly as a

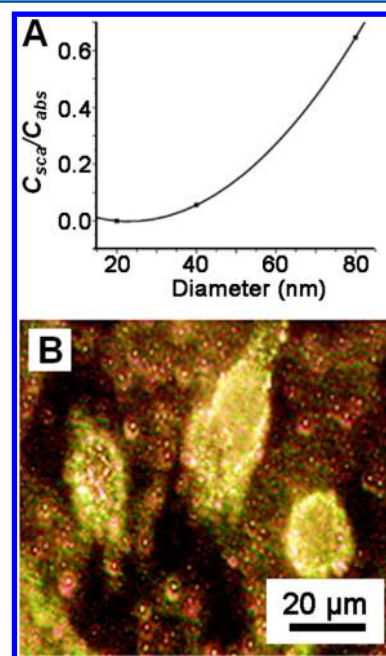


Figure 24. (A) Plot showing the variation of the ratio of scattering cross section to absorption cross section ($C_{\text{sca}}/C_{\text{abs}}$) as a function of the diameter of Au nanospheres. (B) Dark-field microscopy image of HSC cancer cells after incubation with anti-EGFR antibody-conjugated Au nanoparticles. (A) Reprinted from ref 329. Copyright 2006 American Chemical Society. (B) Reprinted from ref 331. Copyright 2005 American Chemical Society.

function of particle size, indicating that C_{sca} will contribute more to C_{ext} for large particles than for small particles of the same composition.³²⁹ Comparing to conventional organic dyes, whose scattering could be largely neglected, the absorption and scattering cross sections of Au nanoparticles with a size in the range of 10–100 nm can be stronger by more than 5 orders of magnitude. As a result, the presence of Au nanoparticles can be readily detected using conventional optical microscopy. Figure 24B shows optical micrographs of cells whose surfaces had been decorated with Au nanoparticles. The images can be captured using reflectance confocal microscopy³³⁰ and dark-field microscopy,³³¹ respectively. More discussion with regard to the optical imaging of Au nanoparticles based on their elastic light scattering can be found in section 4.2.2.

Mie theory only holds under the following assumptions: (i) the dielectric constants of both the nanoparticle and the surrounding medium are homogeneous and can be described

by their bulk dielectric functions,³³² (ii) the size of the nanoparticle is much smaller relative to the wavelength of incident light ($2a \ll \lambda$) so only dipolar oscillation needs to be considered,^{332,333} and (iii) the local electric field of light in the nanoparticle is uniform and constant so as to ignore the retardation effect.³³² In the case of Au, these assumptions only hold for spheres smaller than 20 nm in diameter.³³² For Au spheres larger than 20 nm in diameter, the retardation effect can no longer be neglected and will give rise to oscillation modes in higher orders and at lower frequencies.

Under the same assumptions, analytical solutions have been derived for a number of systems, including spherical particles, concentric core–shell spherical particles, spheroids, and cylinders with an infinite length.¹² For other geometric shapes and boundary conditions, only numerical solutions can be obtained through computational simulation. The most popular method for calculating the LSPR spectra of nanoparticles with an arbitrary shape or a complex structure, as well as their aggregates, is based on the discrete dipole approximation (DDA).^{334,335} In this method, the nanoparticle is divided into an array of point dipoles, each of which can interact with the electric field induced by the incident light and other point dipoles. Other approaches, including the finite-difference time-domain (FDTD) method^{336,337} and boundary element method (BEM),³³⁸ have also been developed and used in the biomedical community.

3.2.3. Tuning Resonance Peaks into the Near-Infrared Region.

In general, a strong resonance peak in the NIR region is desirable for biomedical applications due to the high transparency of soft tissues in this region.^{339,340} This requirement can be readily met by nanostructures made of Au, Ag, Cu, and their alloys, whereas those comprised of other metals are limited by resonance peaks that occur only in the UV region and/or are too chemically reactive in air.³⁴¹ Since Cu nanostructures are unstable when exposed to air, and both Cu and Ag ions are potentially toxic to biological systems,^{342–344} nanostructures based on Au are considered the best choice for biomedical applications. As a critical prerequisite, one has to find a reliable way to tune the resonance peaks of Au-based nanostructures into the NIR region.

Based on the Mie theory (Figure 25A), the LSPR peaks of 5 and 70 nm Au spheres are positioned around 520 and 530 nm, respectively, indicating a red shift of less than 15 nm in wavelength for an increase of 65 nm in diameter. As discussed above, increasing the size of Au nanospheres does cause red shift to the LSPR peak and increases the strength of scattering (C_{sca}) relative to absorption (C_{abs}). However, it is impossible to tune the LSPR peak of Au nanospheres into the range of 700–900 nm while maintaining their diameters below 100 nm. In fact, as shown in Figure 25B, the LSPR peak position is still below 700 nm for a Au nanosphere with a diameter increased up to 150 nm.³⁴⁵

The shape, morphology, or structure of a nanoparticle is a more effective means for shifting the LSPR peak position than changing the size, as these parameters can change the boundary conditions that govern the Maxwell equations.^{346,347} To this end, Au-based nanostructures with a number of nonspherical shapes or complex structures have been developed and have all been shown to possess highly tunable LSPR peaks in the NIR region. Notable examples include nanorods, nanoplates, nanoshells, nanoboxes, nanocages, and nanostructures with branched arms. Their LSPR spectra can be analytically

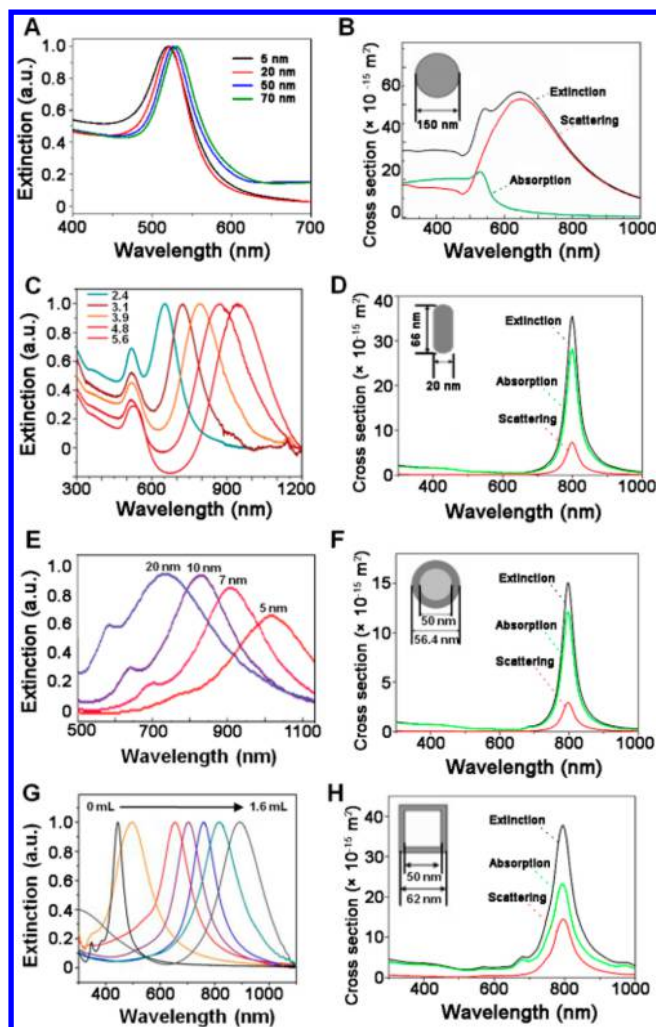


Figure 25. Comparison of four typical types of widely used Au nanostructures and their LSPR properties. The experimental UV–vis–NIR spectra in the left panels indicate the feasibility to tune the LSPR peak for (A) nanospheres with different diameters, (C) nanorods with different aspect ratios, (E) nanoshells with different shell thicknesses, and (G) nanocages prepared by titrating with different volumes of HAuCl_4 solution. The calculated LSPR spectra in the right panels compare the ratios of scattering to absorption for (B) nanospheres, (D) nanorods, (F) nanoshells, and (H) nanocages. The inset in each spectrum gives dimensions of the corresponding nanostructure used for modeling. (A) The spectrum was recorded by X. Yang in the Department of Biomedical Engineering, Georgia Institute of Technology. (B) Reprinted from ref 345. Copyright 2009 American Chemical Society. (C) Reprinted from ref 353. Copyright 2006 American Chemical Society. (D, F, and H) Reprinted with permission from ref 107. Copyright 2006 Royal Society of Chemistry. (E) Reprinted with permission from ref 166. Copyright 1998 Elsevier. (G) Reprinted with permission from ref 11. Copyright 2007 Nature Publishing Group.

calculated using the Mie theory (for those with spherical symmetry) or numerically simulated using the DDA method.

Among those Au nanostructures with LSPR peaks in the NIR region, nanorods have been studied most extensively.^{348–352} When a nanosphere is elongated along one direction into a nanorod, the free electrons can oscillate along two distinctive directions parallel to the short and long axes of the rod, respectively. As a result, the LSPR peak splits into two modes: a transverse mode that remains at the original position associated

with the nanosphere, and a longitudinal mode which can be tuned into the NIR region.³⁴⁹ The LSPR of a nanorod can be described using the Gan theory.^{350,351}

$$C_{\text{ext}} = \frac{2\pi N V \epsilon_m^{3/2}}{3\lambda} \sum_j \frac{(1/P_j^2) \epsilon_2}{\left(\epsilon_1 + \frac{1-P_j}{P_j} \epsilon_m\right)^2 + \epsilon_2^2} \quad (6)$$

where P_j ($j = A, B, C$) are the depolarization factors of the nanorod along the (A) longitudinal and (B, C) transverse directions, and are given by

$$P_A = \frac{1 - e^2}{e^2} \left[\frac{1}{2e} \ln \left(\frac{1+e}{1-e} \right) - 1 \right] \quad (7)$$

$$P_B = P_C = \frac{1 - P_A}{2} \quad (8)$$

Here e is the rod ellipticity, defined as $e = (1 - \xi^{-2})^{1/2}$, and ξ is the aspect ratio of the nanorod (ratio of length to diameter). Since the transverse direction shares the same circular cross section profile as a sphere, the transverse peak position is not highly sensitive to the change in diameter for the nanorod. To tune the longitudinal peak into the NIR region, one can simply increase the aspect ratio of the nanorod (Figure 25C).³⁵³ El-Sayed and co-workers observed a linear relationship between the longitudinal LSPR peak position and the aspect ratio:³⁵¹

$$\lambda_{\text{max}} = 95\xi + 420 \quad (9)$$

This linear relationship provides a useful guidance for tuning the LSPR peak of Au nanorods.

Another approach to tuning the LSPR peak of Au nanostructures into the NIR region is based on the formation of a core-shell or hollow structure.^{328,347} In 1989, Neeves and Birnboim proposed and studied the LSPR properties of a new class of nanostructures comprised of a thin metal shell around a nonmetal core.³⁵⁴ According to their theoretical analysis, the LSPR peak position of such nanostructures could be enhanced and tuned over a broad range by controlling the shell thickness. Later studies by Halas and co-workers on the Au nanoshells provided an experimental system to validate the theoretical predictions.^{355,356} By varying the wall thickness of the Au shells and thus altering the ratio of shell thickness to particle diameter, the LSPR peaks could be tuned from the visible to the NIR region.³⁵⁷ As shown in Figure 25E, the LSPR peak position was red-shifted from below 700 nm to approximately 1000 nm when the shell thickness was reduced from 20 to 5 nm for the Au nanoshells deposited on SiO₂ spheres of 120 nm in diameter.¹⁶⁶

Nordlander, Halas, and co-workers developed a theory known as “plasmon hybridization”, an electromagnetic analogue of the molecular orbital theory, to help explain the LSPR properties of Au nanoshells.³⁵⁸ According to this theory, the plasmon resonance of a Au nanoshell can be viewed as a product of the coupling between the plasmon resonance of a Au solid nanosphere and that of a nanocavity. Due to the finite thickness of a Au nanoshell, the plasmons of the nanosphere and nanocavity can interact with each other, and the coupling strength is determined by the shell thickness. This interaction results in the splitting of the plasmon resonance into two new modes, namely, the symmetrically coupled “bonding” plasmon with a lower energy and the asymmetrically coupled “antibonding” plasmon with a higher energy. What is observed in the optical spectrum of Au nanoshells corresponds to the low

energy, “bonding” plasmon. Due to the strong plasmon damping of Au at wavelengths below 600 nm, the antibonding plasmon cannot be resolved in the optical spectrum.³⁵⁹ When the shell thickness is reduced, a stronger interaction between the plasmons of the nanosphere and nanocavity will result in a wider splitting between the “bonding” and “antibonding” plasmons, or a further downshift for the energy of the “bonding” plasmon, corresponding to a red shift for the LSPR peak of the Au nanoshell. Based on the concept of Au nanoshells, our group developed Au nanoboxes and nanocages with hollow interiors and/or porous walls.¹⁸⁶ Significantly, the nanoboxes and nanocages could be easily prepared using a galvanic replacement reaction between Ag nanocrystals and HAuCl₄ in an aqueous medium.¹⁹⁵ As shown in Figure 25G, by controlling the amount of HAuCl₄ titrated into an aqueous suspension of Ag nanocrystals, the LSPR peaks of the resultant nanostructures could be precisely tuned from around 400 nm all the way into the NIR region by varying the wall thickness relative to the overall dimensions. Experimentally, the titration process allows a simpler and tighter control over the morphology and LSPR property of the resultant nanostructures, allowing for a close match with the wavelength of laser used for optical imaging and photothermal therapy (PTT).^{360–362}

Besides the LSPR peak position, the $C_{\text{abs}}/C_{\text{sca}}$ ratio of Au nanostructures also needs to be tuned to best fit the specific biomedical application. For applications involving photothermal conversion, they require a large extinction cross section, together with a high $C_{\text{abs}}/C_{\text{sca}}$ ratio. The simulated LSPR spectra of a Au nanosphere, nanorod, nanoshell, and nanocage were plotted in parts B, D, F, and H, respectively, of Figure 25 with the extinction cross section being broken down into absorption and scattering components. The LSPR peaks of a Au nanorod, nanoshell, and nanocage were centered at 800 nm, while the LSPR peak of a Au nanosphere was positioned at 650 nm. Although the 100 nm Au nanosphere has the largest extinction cross section, it shows a broad main LSPR peak with the scattering component accounting for more than 70% of the total extinction (Figure 25B).³⁴⁵ This type of nanostructure is not ideal for biomedical applications due to its large dimensions, regardless of the LSPR peak position. As shown in Figure 25D,F,H, the other three kinds of Au nanostructure are comparable in size (about 60 nm in at least one of the dimensions), and all have a high $C_{\text{abs}}/C_{\text{sca}}$ ratio.¹⁰⁷ However, the Au nanoshell has a smaller extinction cross section, which is only about half those of the Au nanorod and nanocage. Moreover, it is worth mentioning that the widely used Au nanoshells typically have a diameter above 100 nm, with their $C_{\text{abs}}/C_{\text{sca}}$ ratios quickly decreasing to a level less than 1/5.³²⁹ As such, both Au nanorods and nanocages seem to be better choices than Au nanoshells for most biomedical applications.

In addition to the aforementioned nanostructures, Au nanoplates^{138,363–365} and nanostructures with branched arms^{228,232} have also been demonstrated with tunable LSPR peaks in the NIR region. The positions of their LSPR peaks are typically determined by their geometric parameters such as edge length, arm length, and sharpness of the corners or tips.

3.2.4. Measuring the Optical Cross Sections. Either theoretical calculation or numerical simulation can be employed to obtain the extinction, absorption, and scattering cross sections of Au nanostructures. Experimentally, it is far more challenging to measure these optical parameters. In general, the extinction spectra of Au nanostructures can be recorded using a

conventional UV–vis–NIR spectrometer. The extinction coefficient can be derived from the particle concentration of a suspension and the extinction measured using a conventional UV–vis–NIR spectrometer. In general, the Beer–Lambert law holds for suspensions of Au nanoparticles at a molar particle concentration of ~ 10 nM to ensure an optical density in the range of 0.1–1. Given that the concentration of Au nanoparticles can be calculated using the elemental content determined by ICP–MS in conjunction with the physical dimensions obtained by electron microscopy, one can obtain both the optical extinction coefficients and extinction cross sections at different wavelengths.³⁶⁶ When combined with the computationally derived ratio between the scattering and absorption cross sections, the extinction cross section can then be separated into the two components responsible for scattering and absorption, respectively.

A commonly adopted, reliable method for directly measuring the scattering and absorption properties of a colloidal suspension is based on the double-integrating sphere (DIS) system along with an inverse adding–doubling (IAD) algorithm.^{367,368} The DIS–IAD approach only requires a small amount of sample and can handle conditions where absorption is strong. A DIS apparatus contains two integrating spherical chambers with a thin slide of sample sandwiched between them. Each spherical chamber has three ports located at 0° (entry port), 180° (exit port), and 90° (detector port). The sphere diameter and port size are chosen by taking into account a balance between detection sensitivity (for which a small sphere is more desirable) and the ratio of port size to the sphere inner surface area (for which a large sphere and a small port are more desirable to maximize the active sphere area). The sphere on the side of the light source is called the reflectance sphere, while the one on the other side is called the transmittance sphere. The inner surfaces of both spheres are coated with a highly reflective material (e.g., polytetrafluoroethylene or PTFE) which has a reflectivity of more than 98.5% around 800 nm.³⁶⁹ For wavelengths around 800 nm, silicon photodetectors can be used. A collimated laser beam comes through the entry port of the reflectance sphere and strikes the sample at a normal incidence angle. The backward and forward scattered light are collected by the reflectance and transmittance spheres, respectively, and diffusely reflected onto the detectors. A baffle can be used inside each sphere to prevent direct illumination of light scattered from the sample. The collimated (i.e., unscattered) transmitted light through the sample will go through the exit port of the transmittance sphere. The major drawback of this method is the limited apparatus availability and special algorithm for data analysis.

Photoacoustic (PA) imaging offers a simple tool for measuring the absorption cross section of Au nanostructures suspended in a liquid. Since the detected PA signal is directly proportional to the molar absorption coefficient (μ_{abs}) of the absorber involved, the molar absorption coefficient of Au nanostructures can be derived by benchmarking against a dye (with a known molecular absorption coefficient) solution and then converted to the cross section by taking into consideration the Avogadro constant (N_A): $\mu_{\text{abs}} = N_A C_{\text{abs}}$. Using this technique, Xia, Wang, and their co-workers quantitatively measured and compared the absorption cross sections of Au nanorods (44 nm \times 19.8 nm), nanocages (with two different outer edge lengths of 32 and 45 nm), and nanoshells (150 nm in diameter). The absorption cross section of the Au nanocages was found to have the largest absolute value relative to the

nanorods and nanoshells. When comparing the ratio of absorption to extinction, the Au nanocages showed a value (0.82 and 1.0 for the 45 and 32 nm nanocages) similar to that (0.87) of the Au nanorods, while all of those values were much higher than that (0.056) of the Au nanoshells. The major drawback of this method is the need for a specialized apparatus that may not be accessible to all researchers.

In a recent study, our group demonstrated the fabrication of a simple optofluidic device (Figure 26A) for measuring the

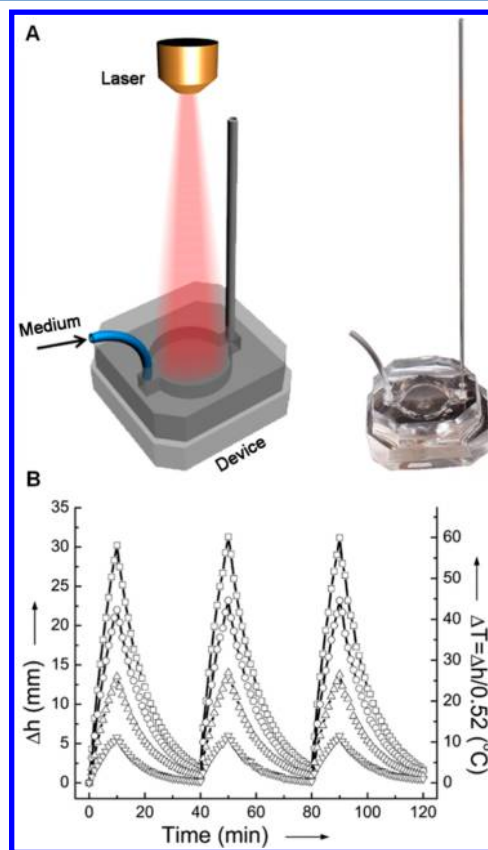


Figure 26. (A) Schematic illustration and photograph of a plasmon-assisted optofluidic (PAOF) system that can be used to measure the photothermal conversion efficiency of Au nanostructures. (B) Plots showing the rise in height (Δh) and increase in temperature (ΔT) upon irradiation as a function of time for four samples of Au nanocages with different concentrations: 1.0×10^9 (▽), 2.5×10^9 (△), 5.0×10^9 (○), and 1.0×10^{10} (□) particles/mL (from bottom to top). Both Δh and ΔT showed a good reproducibility between different cycles of laser irradiation. For each cycle of laser irradiation, the suspension of Au nanocages was irradiated for 10 min and then allowed to cool down for 30 min. Reprinted with permission from ref 370. Copyright 2013 Wiley-VCH.

absorption cross section of Au nanostructures.³⁷⁰ This system contains a diode laser as the light source, an aqueous suspension of Au nanostructures as the photothermal transducer, and a simple microfluidic device for measuring the volumetric expansion of the suspension under photothermal heating. Depending on the type of Au nanostructures suspended in the medium and the particle concentration, the fluid can be driven to move up a capillary tube by as much as 30.5 mm. By benchmarking against an organic dye with a known molecular absorption coefficient, this device could be used to quickly measure the photothermal conversion efficiency of a sample of Au nanostructures as well as their absorption

Table 2. Summary of Extinction, Adsorption, and Scattering Cross Sections of Different Types of Au Nanostructures^a

shape	size	$\sigma_e (\times 10^{-15} \text{ m}^2)$		$\sigma_a (\times 10^{-15} \text{ m}^2)$		$\sigma_s (\times 10^{-15} \text{ m}^2)$		ref
		calcd	exptl	calcd	exptl	calcd	exptl	
nanospheres	$D = 150 \text{ nm}$	99.96	145 ± 14.76	5.73				345
	$D = 20 \text{ nm}$			0.31		0.002		329
	$D = 40 \text{ nm}$			2.93		0.18		329
	$D = 80 \text{ nm}$			18.2		12.31		329
nanorods	$44.0 \times 19.8 \text{ nm}$	2.15	2.16 ± 0.02	1.83	1.87 ± 0.23			345
	$56 \times 17 \text{ nm}$				3.5 ± 0.3			370
nanoshells	$D_{\text{core}} = 80 \text{ nm}$			59.1		5.03		329
	$T = 30 \text{ nm}$							
	$D_{\text{core}} = 100 \text{ nm}$			18.8		40.7		329
nanocages	$E = 32 \text{ nm}$	6.39	2.99 ± 0.04	6.02	3.05 ± 0.12			345
	$T = 5.8 \text{ nm}$							
	$E = 45 \text{ nm}$	19.88	7.26 ± 0.06	16.26	5.96 ± 0.25			345
	$T = 4.0 \text{ nm}$							
	$E = 45 \text{ nm}$				18.4 ± 1.3			370
	$T = 5 \text{ nm}$							

^a σ_e , σ_a , and σ_s represent the extinction, adsorption, and scattering cross sections, respectively. D , E , and T stand for diameter, edge length, and thickness, respectively. "calcd" and "exptl" are the abbreviations of calculated and experimental results, respectively.

cross section (Figure 26B). For example, the Au nanocages with an outer edge length of 45 nm and wall thickness of 5 nm were measured to have an absorption cross section of $18.4 \times 10^{-15} \text{ m}^2$ at a concentration of 1.0×10^{10} particles/mL, whereas the Au nanorods with dimensions of $56 \text{ nm} \times 17 \text{ nm}$ were found to have an absorption cross section of $3.5 \times 10^{-15} \text{ m}^2$. Although such a device still needs to be improved in terms of heat insulation and accuracy, the simple design makes it straightforward and easy to implement and use.

Table 2 shows the summary of extinction, adsorption, and scattering cross sections of different types of Au nanostructures.

3.3. Surface-Enhanced Raman Scattering

In an inelastic light scattering process, the scattered light shows a shift in frequency relative to the incident light (either higher or lower), indicating an energy transfer between the incident photons and chemical bonds in the molecules or materials involved. The gained or lost energy and thereby the shift in frequency is determined by the chemical bonds. This phenomenon was first discovered by C. V. Raman and K. S. Krishnan in liquids, and was named Raman scattering.³⁷¹

Surface-enhanced Raman scattering refers to an optical phenomenon by which the Raman scattering cross section can be increased by more than 6 orders in magnitude when the probe molecules are deposited on a roughened metal surface.^{17,18,372–376} This phenomenon was first observed by Fleischmann in 1974 for pyridine molecules adsorbed on the surface of an electrochemically roughened Ag electrode,³⁷⁷ and a plausible mechanism was independently proposed in 1977 by Van Duyne³⁷⁸ and Creighton.³⁷⁹ In such a process, the extremely small cross section (typically, 10^{-31} – 10^{-29} cm^2 per molecule) of Raman scattering can be drastically augmented to enable the use of Raman spectroscopy as a routine technique for ultrasensitive detection.³⁸⁰ This technique has found widespread use in both analytical chemistry and life sciences owing to the unique advantages provided by Raman spectroscopy, including (i) ease of sample preparation, (ii) availability of characteristic peaks for label-free "fingerprinting" of an analyte, (iii) narrow peak width for multiplexing, (iv) good

stability toward photobleaching, and (v) excitation by a single wavelength laser.^{380–382}

The extraordinary enhancement can arise from two different mechanisms of chemical and electromagnetic origins, respectively.^{383–385} The chemical mechanism leads to enhancement through charge transfer between the lowest unoccupied molecular orbital (LUMO) or the highest occupied molecular orbital (HOMO) of analyte molecules and the Fermi energy level of the metal substrate.^{385–387} The chemical enhancement factor is typically on an order below 10^2 , and it varies depending on the types of analyte and substrate involved, as well as the locations on the substrate. The electromagnetic mechanism is generally believed to be the predominant contributor to SERS, which accounts for an enhancement factor ranging from 10^6 to 10^8 .^{17,372} This kind of enhancement is associated with the LSPR of the metal substrate. The collective oscillations of free electrons in a metal substrate can enhance the intensity of the local electric field by a factor of 2–4 orders of magnitude in the vicinity of the metal surface (less than 5 nm from the surface),³⁸⁸ leading to a tremendous enhancement of the Raman scattering cross section.

The relationship between the Raman signal intensity and the local electromagnetic field strength can be understood using a simple model based on a metal nanosphere. The analytical solution for the magnitude of the electromagnetic field outside the nanosphere (E_{out}) can be calculated according to the following equation:

$$E_{\text{out}}(x, y, z) = E_0 \hat{z} - \alpha E_0 \left[\frac{\hat{z}}{d^3} - \frac{3z}{d^5} (x\hat{x} + y\hat{y} + z\hat{z}) \right] \quad (10)$$

where x , y , and z are the usual Cartesian coordinates; d is the radial distance; \hat{x} , \hat{y} , and \hat{z} are the Cartesian unit vectors; and α is the metal polarizability, which is expressed as

$$\alpha = gr^3 \quad (11)$$

Here r is the radius of the sphere and g is defined as

$$g = \frac{\epsilon_{\text{in}} - \epsilon_{\text{out}}}{\epsilon_{\text{in}} + 2\epsilon_{\text{out}}} \quad (12)$$

in which ϵ_{in} is the dielectric constant of the metal nanoparticle, and ϵ_{out} is the dielectric constant of the surrounding medium.^{17,372} The intensity of Raman scattering is linearly proportional to the field intensity of incident light, E_0 .^{2,389} Given that the field intensity is augmented at the surface of the particle, the Raman intensity is therefore related to the absolute square of E_{out} at the surface (i.e., $d = r$). Combining eqs 10–12, the absolute square of E_{out} for a small metal sphere can be expressed by

$$|E_{\text{out}}|^2 = E_0^2 [1 - g^2 + 3 \cos^2 \theta (2 \operatorname{Re}(g) + |g|^2)] \quad (13)$$

in which θ is the angle between the incident field vector and the position vector of the molecule on the surface. Equation 13 gives a general expression for the enhancement of the incident field, which induces an oscillating dipole in the molecule adsorbed on the surface, followed by the radiation of the dipole. In addition to this, the emission of radiation from the dipole may also be enhanced, which adds to the complexity of the enhanced emission intensity calculation. A first-order approximation can be applied to estimate the enhancement factor, which is similar to eq 13 except evaluated at the Raman–Stokes shifted frequency only. Under this approximation, the following expression can be derived:

$$\text{EF} = \frac{|E_{\text{out}}|^2 |E'_{\text{out}}|^2}{|E_0|^4} = 4 |g|^2 |g'|^2 \quad (14)$$

where the primed symbols refer to the field evaluated at the frequency of scattered photons. This expression is defined as the theoretical SERS electromagnetic enhancement factor. In the case of a small Stokes shift, both g and g' are at approximately the same wavelength, and the enhancement factor scales as g^4 , which is commonly referred to as E^4 enhancement or the fourth power of field enhancement at the surface of the nanoparticle. Assuming $|g|$ is approximately 10 for a small sphere in this model, the magnitude of the SERS electromagnetic enhancement will be around 10^4 .^{17,372} The electromagnetic enhancement is closely related to the morphology (both size and shape) of the metal substrate, as well as the type of metal involved. As such, different SERS substrates are expected to show distinct performances.

Noble metals, such as Au and Ag, are the most widely used materials for SERS substrates due to their broad and intense LSPR peaks in the visible and NIR regions. In addition, Ag is much more efficient than Au at enhancing Raman signals as Au has a strong plasmon damping below 600 nm, which largely limits the use of Au substrates to the NIR region.³⁵⁹ In spite of this, Au is chemically more stable than Ag, with both higher biocompatibility and lower toxicity, making Au nanostructures ideal SERS substrates for various biomedical applications. The size and shape of Au nanostructures can be maneuvered in a controllable fashion to optimize their performance in various SERS-based devices.

Many studies have been carried out, both theoretically and experimentally, to study the relationship between the SERS activity and the size and shape of Au nanostructures. As a general trend, the SERS activity increases with particle size. This can be explained by considering the fact that the intensity of the local electromagnetic field generated by LSPRs is directly proportional to the number of electrons excited and thus the size of the nanostructures.³⁸¹ Zhong and co-workers reported on the size dependence of SERS activity for *p*-MBA adsorbed onto the surface of Au nanoparticles with sizes in the range of

30–90 nm.⁸⁶ They found that SERS signals could only be detected from the *p*-MBA molecules adsorbed on Au nanoparticles with diameters larger than 50 nm, and the intensity monotonically increased with particle size. Similarly, Chen and co-workers reported an increase in the SERS enhancement factor from 10^2 to 10^5 for 2-naphthalenethiol adsorbed on Au nanoparticles as the average particle size was increased from 13.7 to 62.1 nm,³⁹⁰ which is consistent with the observations of Kneipp and co-workers.³⁹¹

The shape of Au nanostructures is another key parameter that can affect the SERS activity.³⁹² It has been demonstrated that the local electromagnetic fields are not homogeneously distributed on the surface of an anisotropic nanostructure, giving rise to highly concentrated fields in several specific regions and leading to extraordinarily strong SERS enhancement at these sites. El-Sayed and co-workers reported the SERS enhancement factors on the order of 10^4 – 10^5 for CTAB molecules immobilized on the surface of Au nanorods, while no such enhancement was observed for the same molecules supported on Au nanospheres with similar dimensions (Figure 27A,B).^{120,393} Our group studied the distinctive SERS behavior of Au nanocages and found that the SERS intensity was dependent on the elemental composition of the Au–Ag bimetallic nanocages, which could be attributed to the plasmon damping associated with Au. The SERS detection was sensitive enough to be used for monitoring the conformational changes associated with the alkyl chains of thiolate molecules adsorbed on Au nanocages during a photothermal heating process (Figure 27C,D).^{394,395} For Au nanostars containing sharp apexes on the surface, their electromagnetic fields could be concentrated on the tips. As a result, this type of Au nanomaterial has been reported to exhibit much greater SERS enhancement than that of Au nanospheres similar in size.^{396,397}

Besides size and shape, SERS activity is also strongly dependent on the distance between two Au nanoparticles. When two Au nanoparticles approach each other, the electromagnetic field inside the gap between the particles can be greatly enhanced due to the coupling of their plasmon resonances.³⁹⁸ The gap region is commonly known as the “hot spot” due to the extraordinarily large SERS enhancement factor, typically 10^3 – 10^4 times greater than those of individual nanoparticles.³⁹⁹ To this end, Van Duyne and co-workers have fabricated dimers and trimers of Au nanoparticles and then encapsulated them in SiO_2 shells. These structures were referred to as nanoantennas.⁴⁰⁰ On average, a SERS enhancement factor of 10^8 was derived from the measurements of 30 individual nanoantennas. It was also found that the enhancement factors did not correlate with the aggregation state, indicating that one hot spot between two particles was adequate and the “extra” particle did not contribute significantly to the SERS signal. They did observe a dependency of the SERS intensity on interparticle distance, which showed roughly 2 orders of magnitude decrease when the interparticle gap was varied from 0 to 1 nm.

Yin and co-workers investigated the SERS properties of Au nanoshells obtained at different stages of a synthesis (Figure 27E,F).⁴⁰¹ Only weak Raman signals were detected for the discrete Au nanoparticles that were initially immobilized on the surface of SiO_2 spheres in the early stage of a synthesis. As the seed particles grew in size, dipole coupling was enhanced due to the decrease in interparticle distance, leading to the formation of “hot spots” and thereby strong Raman signals. A decrease in

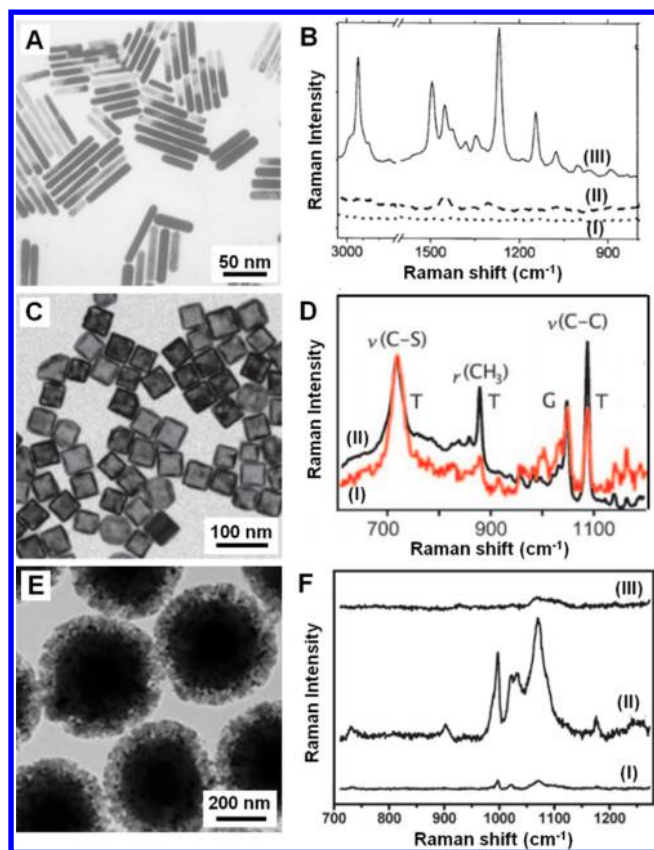


Figure 27. (A) TEM image of CTAB-capped Au nanorods and (B) their SERS spectrum (trace III) recorded in solution phase, in comparison with the spectra recorded from CTAB-coated Au nanospheres in solution phase (trace I) and pure CTAB solution (trace II). (C) TEM image and (D) SERS spectra of Au nanocages functionalized with 1-dodecanethiolate (1-DDT). The Au nanocages were suspended in water and excited with lasers of 514 (trace I) and 785 nm (trace II) in wavelength for 120 s. No apparent difference was observed from the two spectra, suggesting the self-assembled monolayer of 1-DDT was not reversibly damaged during the photothermal process. (E) TEM image of Au nanoshells prepared after 12 cycles of Au deposition on a SiO_2 sphere and (F) SERS spectra of thiophenol adsorbed on the initial SiO_2 spheres seeded with Au nanoparticles (trace I), Au nanoshells prepared after 12 cycles of seeded growth (trace II), and Au nanoshells obtained after 22 cycles of seeded growth (trace III). (A) Reprinted from ref 120. Copyright 1997 American Chemical Society. (B) Reprinted with permission from ref 393. Copyright 2002 Elsevier. (C and D) Reprinted with permission from ref 394. Copyright 2009 Wiley-VCH. (E and F) Reprinted with permission from ref 401. Copyright 2010 Wiley-VCH.

Raman intensity was observed when the Au shell grew to completion, likely due to the disappearance of “hot spots” and the reduction in surface area caused by the smoothing effect. Halas and co-workers demonstrated the fabrication of Au particles with a “meatball-like” morphology through the controlled reduction of HAuCl_4 by AA in an aqueous solution with the use of gum arabic as a stabilizer.⁴⁰² The “meatball-like” particles of Au showed a stable and reproducible SERS enhancement factor of 10^6 – 10^7 for individual particles. They also created “hot spots” using these particles by forming close-packed arrays through self-assembly, and found that the enhancement factor could be further increased to $\sim 10^8$. These extremely high enhancement factors associated with

“hot spots” make it possible to detect single molecules by means of SERS.^{403,404}

As discussed above, Ag nanostructures always outperform their Au counterparts for both LSPR- and SERS-related applications. However, Ag is chemically less stable than Au, making it difficult to use Ag nanostructures for biomedical applications. Coating the surface of a Ag nanostructure with an ultrathin layer of Au can greatly improve the chemical stability and biocompatibility of the nanostructure without compromising its high performance for LSPR and SERS. Interestingly, the $\text{Ag}@Au_{nL}$ ($n = 3$ or 6) nanocubes were recently shown to exhibit even greater SERS activity in comparison to the original Ag nanocubes.¹⁸⁴ Theoretical calculations and experimental measurements both indicated that the Ag and $\text{Ag}@Au_{nL}$ had essentially identical LSPR features. The improved SERS activity was therefore attributed to a much stronger binding affinity toward the thiol-based SERS probe molecules with the Au surface, generating a greater chemical enhancement factor through the charge transfer between the Au surface and the surface-bound probe molecules.

Despite its many unique advantages, the scope of SERS applications still faces prominent challenges, such as low substrate preparation reproducibility and difficulties in handling the small sample volumes. To compensate for these drawbacks, droplet-based, flow-through SERS measurements have been recently developed. Readers who are interested in this new design can refer to some recent review articles on the topic.^{405,406}

4. BIOMEDICAL APPLICATIONS OF GOLD NANOMATERIALS

4.1. Optical Sensing

As discussed in section 3, Au nanostructures exhibit a variety of tunable optical properties, including photoluminescence, LSPR, and SERS. All of these optical properties can be used to develop various types of sensors for the detection of metal ions, small molecules, DNA, and proteins by taking advantage of the high sensitivity of these properties to the environment surrounding the Au nanostructures, as well as the particle aggregation states.

4.1.1. Sensing Based on the Photoluminescence of Gold Clusters. Fluorescent Au clusters are excellent optical probes for the detection of biological species owing to their large Stokes shifts, low toxicity, and high emission efficiency. Compared to organic dyes, conjugate oligomers/polymers, and semiconductor quantum dots, Au clusters are superior in terms of photostability and biocompatibility, while the photoluminescence of Au clusters can be readily tuned from the visible to the NIR region. Recently, various types of sensors have been developed based on fluorescent Au clusters for the detection of proteins,^{407–411} metal ions,^{412–414} glucose,⁴¹⁵ and other types of small molecules.^{416,417}

The “turn off” detection scheme refers to an approach that involves a decrease in signal intensity in the presence of analyte molecules. Since the photoluminescence properties of Au clusters are determined by both the ligand shell and the core, the luminescence intensity can drop through two different means: interaction with the ligand shell, or destruction of the core. When the ligand shell on a Au cluster is perturbed by analyte molecules through either covalent bonding or physical adsorption, the photoluminescence from the Au cluster tends to drop significantly. Depending on the type of ligand used to

protect the fluorescent Au clusters, it is feasible to detect different types of analyte molecules. For example, horseradish peroxidase (HRP) has been used as a protecting ligand for the synthesis of fluorescent Au clusters, allowing the Au clusters to detect H_2O_2 .⁴¹⁷ It was found that the photoluminescence of HRP-capped Au clusters was quenched quantitatively by H_2O_2 . To validate the role of HRP in H_2O_2 -induced quenching, BSA-stabilized Au clusters were used as a control. While the addition of H_2O_2 induced a significant decline in photoluminescence intensity for the HRP-stabilized Au cluster, in the case of BSA-stabilized Au clusters, the photoluminescence intensity only showed a negligible change. These results indicate that the photoluminescence quenching by H_2O_2 is related to the activity of the HRP enzyme. Based on this “turn off” strategy, a limit of detection (LOD) as low as 30 nM was reported for H_2O_2 in a concentration range of 100 nM–100 μM .

Proteases represent a major class of enzymes that catalyze the hydrolysis of peptide bonds to break down proteins into smaller pieces in a process known as proteolysis.⁴⁰⁷ To this end, protein-stabilized fluorescent Au clusters can serve as probes for the detection of proteases. In the presence of proteases, the protein shell around each Au cluster will be broken down and the photoluminescence will be effectively quenched by the O_2 from ambient air (Figure 28A,B). By simply changing the protein substrates surrounding the Au clusters, this assay could be easily adapted for the detection of different proteases. With BSA-stabilized fluorescent Au clusters, the LOD for proteinase K reached 1 ng mL^{-1} . Based on the selective interactions with ligands, many small molecules and heavy metal ions can also be detected through the principle of quenching photoluminescence from the Au clusters.^{415,417}

Some molecules or ions are able to dissolve the cores of fluorescent Au clusters and thus cause the photoluminescence to diminish. Such changes can be used for their detection. For example, cyanide (CN^-) is one of the most toxic anions in the environment, and is well documented as a toxin because of its strong binding to α_3 cytochromes and inhibition of the electron transport chain in mitochondria.⁴¹⁸ The uptake of CN^- can directly lead to the death of an adult human within several minutes even at a low concentration of 1 mg L^{-1} in the blood by depressing the central nervous system.⁴¹⁹ It was demonstrated that BSA-stabilized Au clusters could be dissolved by CN^- to generate a stable complex of $\text{Au}(\text{CN})_2^-$ via strong coordination bonding, in a process known as the Elsner reaction (Figure 28C,D).^{420,421} Due to the dissolution of Au clusters in the presence of CN^- ions, there would be a significant drop in photoluminescence intensity. With BSA-stabilized Au clusters, the LOD for CN^- was as low as 0.2 μM , which is 14 times lower than the maximum level of CN^- in drinking water recommended by the World Health Organization (WHO).⁴²²

The “turn on” detection scheme involves an increase in photoluminescence intensity in the presence of analyte molecules. In this case, the increase in photoluminescence intensity is usually caused by the interactions between the analyte molecules and the protecting ligands or inhibitors adsorbed onto the surface of Au clusters. It was found that GSH could significantly and selectively enhance the photoluminescence intensity of histidine-stabilized Au clusters.⁴²³ In the presence of GSH, the quantum yield of Au clusters could reach levels above 10% without other thiolate molecules impacting the photoluminescence. Based on this “turn on”

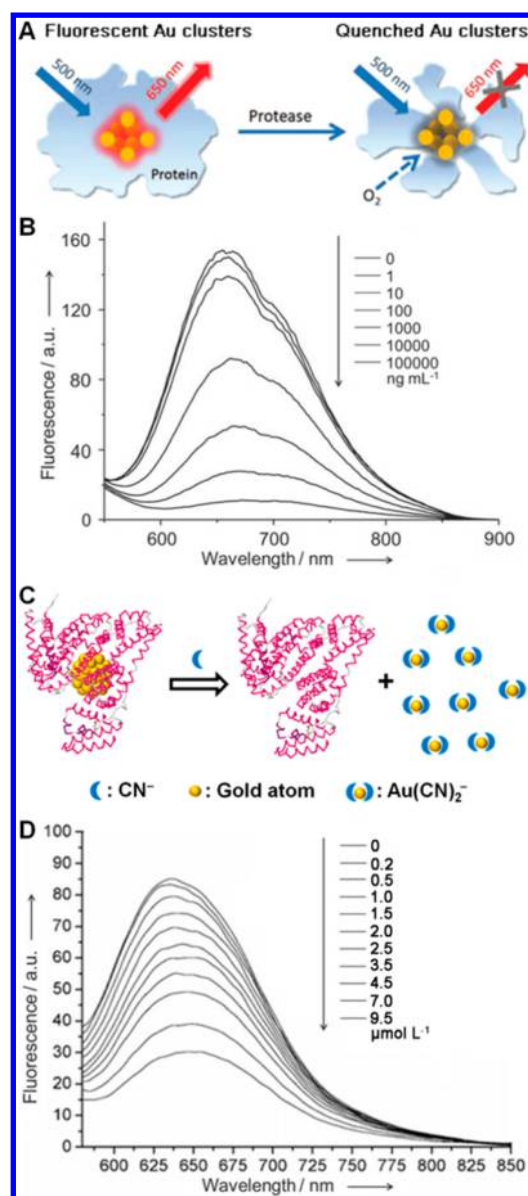


Figure 28. Optical sensing based on the photoluminescence of Au clusters for the detection of protease (A and B) and CN^- (C and D). (A and C) Schematic illustrations of the mechanisms for the detection of protease and CN^- , respectively. (B and D) Photoluminescence of Au clusters upon the addition of protease and CN^- , respectively, with various concentrations. (A and B) Reprinted with permission from ref 407. Copyright 2012 Wiley-VCH. (C and D) Reprinted with permission from ref 422. Copyright 2010 Wiley-VCH.

strategy, a LOD of 0.2 μM was demonstrated for GSH in the detection range of 150–1200 μM .

Due to the metallophilic Hg^{2+} –Au interaction,^{424–427} Hg^{2+} ions are capable of efficiently quenching the photoluminescence from Au clusters. In the presence of a biological thiol, however, the photoluminescence of Au clusters will be recovered because of a stronger interaction between the biological thiol and Hg^{2+} ions. Different biological thiols, such as cysteine, glutathione, and homocysteine, have all been detected, with LODs of 8.3, 9.4, and 14.9 nM, respectively.⁴²⁸

Although the sensors based on the photoluminescence of Au clusters have good selectivity and sensitivity, they tend to suffer from the following disadvantages owing to the use of Au clusters: (i) it is hard to reduce the cost of such a sensor due to

the high price of Au and the involvement of a photoluminescence spectrometer, and (ii) it is not easy to make the sensor portable as it tends to need a photoluminescence spectrometer to read out the signals.

4.1.2. Sensing Based on Localized Surface Plasmon Resonance. The LSPR of Au nanostructures can change as a result of variations to parameters such as the local refractive index and the aggregating state (Figure 29). When the surface of Au nanostructures is covered by analyte molecules through chemical or physical adsorption, the local refractive index will

change, resulting in shifts for the LSPR peak position. In terms of aggregation, a suspension of Au nanoparticles would appear red when the interparticle distance is substantially greater than the average particle diameter. As the interparticle distance decreases to a scale less than the average particle diameter, the color will change from red to blue.⁴²⁹ This phenomenon arises from the coupling between the LSPR modes of individual Au nanoparticles, and it can be used to design and fabricate colorimetric sensors. To this end, Au nanostructures with different shapes have been utilized as the sensing components for colorimetric detection of various types of analytes, including DNA,^{283,430,431} metal ions,^{432–441} small molecules,^{442–448} and proteins.^{449,450}

Typically, after the addition of analyte molecules, the Au nanoparticles will aggregate and the LSPR peak will shift to longer wavelengths, known as the “red shift”. In the presence of certain molecules or ions, an aggregation of Au nanoparticles can also be broken down into individual nanoparticles. In this case, the LSPR peak of the colloidal suspension will be “blue-shifted” to shorter wavelengths. For both cases, there will be an obvious color change in the suspension of Au nanoparticles, which can be used for the colorimetric detection.

Red shift can be used as a “label-free” approach to sensing, in which there is no need to modify the surface of the Au nanoparticles. For example, it was found that unfolded single-stranded DNAs (ssDNAs) could be adsorbed onto the surface of citrate-protected Au nanoparticles and enhance their stability against salt-induced aggregation, whereas folded ssDNAs and double-stranded DNAs (dsDNAs) could not.^{451,452} Rothberg and co-workers suggested a mechanism where unfolded ssDNAs could uncoil sufficiently to expose their bases while folded ssDNAs (or dsDNAs) could not.⁴⁵¹ Therefore, folded ssDNAs (or dsDNAs) would not adsorb onto the surface due to the repulsion between the charged phosphate backbone of folded ssDNAs (or dsDNAs) and the citrate ions on the surface of Au nanoparticles. On the contrary, the negative charge on the backbone of unfolded ssDNAs was sufficiently distant from citrate ions due to the flexibility of unfolded ssDNAs. Thus, the van der Waals forces allowed the ssDNAs to attach to the surface of Au nanoparticles. After the addition of unfolded, complementary target ssDNAs, the concentration of unfolded ssDNAs would drop and the Au nanoparticles could no longer be stabilized in the presence of salt at a high concentration. The Au nanoparticles would aggregate, causing an obvious color change from red to blue, which could be readily resolved by the naked eye. Based on this colorimetric assay, a LOD of 100 fmol was reported for ssDNAs without any special instrumentation.⁴⁵¹ This detection platform also works for aptamers, which are nucleic acids with strong affinity toward specific molecules and can be obtained through a combinatorial selection process known as systematic evolution of ligands by exponential enrichment (SELEX). By replacing unfolded ssDNAs with other probes, such as aptamers, such “label-free” assays can also be used for the detection of proteins,^{453,454} adenosine triphosphate (ATP),⁴⁵⁴ cocaine,⁴⁴⁷ adenosine,⁴⁵⁴ and metal ions.⁴⁵⁵

In a “labeled” detection strategy, the surface of Au nanoparticles has to be modified with specific ligands in an effort to achieve both selectivity and sensitivity. After the introduction of analyte molecules, the Au nanoparticles will quickly aggregate due to the interactions between the analyte molecules and the ligands conjugated to the surface of Au nanoparticles. When functionalized with a mercaptoalkyloligo-

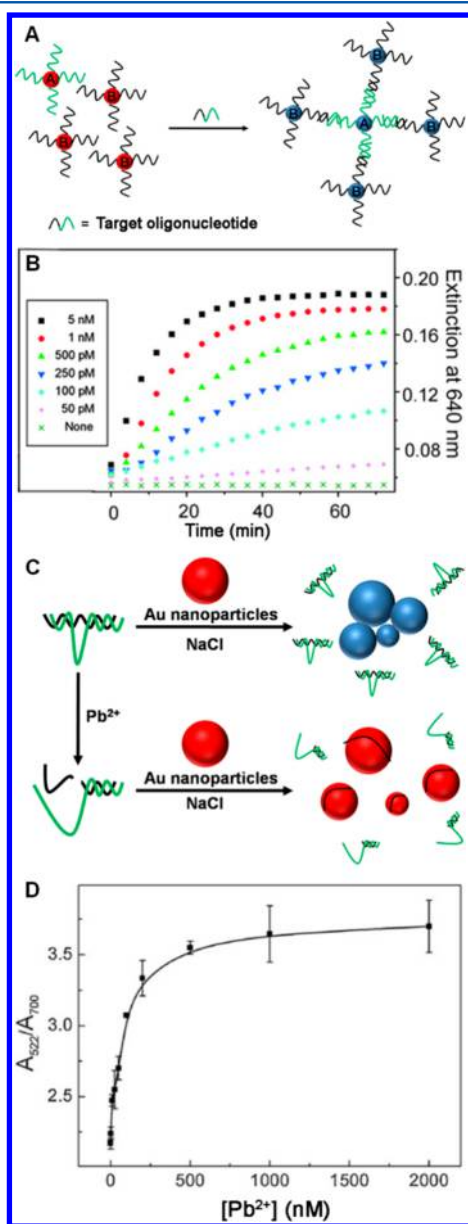


Figure 29. Schematic illustration showing mechanisms for the colorimetric detection of (A) oligonucleotides and (C) Pb^{2+} ions. (B) Plots showing changes to the extinction at 640 nm as a function of time when the target oligonucleotides with different concentrations were introduced to induce aggregation for the Au nanoparticles. (D) Calibration curve for the colorimetric detection of Pb^{2+} ions at pH 7.2 based on the absorbance at 522 and 700 nm (A_{522}/A_{700}). (A and B) Reprinted from ref 430. Copyright 2000 American Chemical Society. (C and D) Reprinted with permission from ref 435. Copyright 2008 Wiley-VCH.

nucleotide, for example, Au nanoparticles have been utilized for the selective colorimetric detection of polynucleotides.^{430,283} As the analysis starts with a network of Au nanoparticles, the color of the suspension changes from red to blue. The networks are denatured with sharp transition temperatures, allowing for the differentiation of analytes with mismatched sequences. This technique can be used for the detection of single base pair mismatches. A LOD of 10 fmol has been reported for ssDNA.²⁸³ By modifying the surface of Au nanoparticles with different probes, such a “labeled” assay can also be used for the detection of proteins,⁴⁵⁴ small molecules,⁴⁵⁶ and ionic species.^{456,457}

Similarly, both “label free” and “labeled” strategies can be employed for the detection of analyte molecules based on the “blue shift” of LSPR. For example, after the formation of a DNA duplex with the complementary DNA strands, aptamers would not be able to protect the Au nanoparticles from aggregation when subjected to salts at a high concentration. In the presence of analyte molecules or ions, the aptamers will fold and the complementary, unfolded ssDNAs will be released. As such, Au nanoparticles can be protected by the released unfolded ssDNAs and the aggregation of Au nanoparticles will be broken into individual Au nanoparticles. The suspension of Au nanoparticles will then change color from blue to red. Using different DNA strands and aptamers, various types of molecules and ions can be detected based on this “blue-shift” approach.^{226,443–445,450,458}

Another detection platform involves the use of DNazymes, which are DNA molecules capable of catalyzing chemical reactions. The first DNzyme was discovered in 1994,⁴⁵⁹ and various DNazymes with high specificity toward metal ions such as Pb^{2+} , Cu^{2+} , and Zn^{2+} have been obtained through a combinatorial biology approach known as *in vitro* selection. Typically, a DNzyme consists of an enzyme strand and a substrate strand. The substrate strand can be hydrolytically cleaved at the scissile ribonucleic acid adenosine (rA) to break down the DNzyme into several unfolded ssDNAs. In the presence of a DNzyme, the Au nanoparticles functionalized with ssDNA complementary to the DNzyme will aggregate into a network. After the addition of analyte ions such as Pb^{2+} and Cu^{2+} ,^{435–439} the DNzyme will be fragmented and break down the network of Au nanoparticles. As a result, the LSPR of the Au nanoparticles will blue-shift and the color of the suspension will change from blue to red. A LOD of 0.3 μM was demonstrated for Pb^{2+} ions. This method was also applied to detect the presence of Pb^{2+} in leaded paints, including those containing 0.5% Pb^{2+} ions, which represents the upper limit allowed by the U.S. Environmental Protection Agency (EPA).⁴³⁹ Using different types of aptamers and DNazymes, such a “labeled” assay can also be applied to the detection of many other types of molecules or ions.⁴⁴⁰

Although the detection based on such colorimetric sensors is relatively simple and many different target molecules or ions can be detected by changing the probes, colorimetric sensors tend to suffer from the following disadvantages: (i) the high materials cost due to the involvement of both Au and nucleic acids, and (ii) a lower sensitivity of colorimetric compared to those based on the photoluminescence.

4.1.3. Sensing Based on Surface-Enhanced Raman Scattering. Compared with sensors based on photoluminescence, detection based on SERS shows even higher sensitivity. Both label-free and Raman reporter assays have been explored for SERS-based detection. In a label-free assay, the analyte

molecules can be identified according to a pattern of their SERS peaks.^{460–464} The SERS substrates can be individual Au nanostructures or their aggregates, which tend to offer a stronger Raman enhancement than individual nanostructures due to the formation of hot spots. In one demonstration, El-Sayed and co-workers have explored the use of Au nanorods functionalized with anti-EGFR for the detection of cancer cells (Figure 30).⁴⁶¹ It was found that the Raman signals from

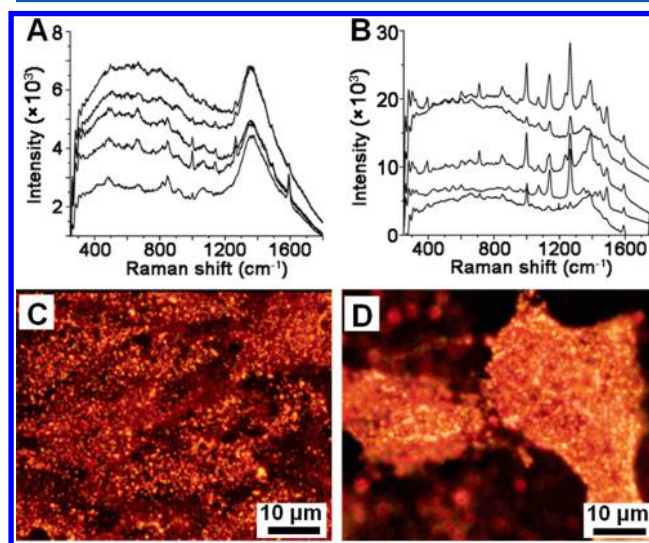


Figure 30. Detection of cancer cells based on SERS properties of immune-labeled Au nanorods. SERS spectra of different cell lines incubated with Au nanorods conjugated with anti-EGFR antibody: (A) normal HaCaT cells and (B) HSC cancer cells. Raman spectra from five cells for each cell line are shown in (A) and (B). Dark-field images of anti-EGFR antibody conjugated Au nanorods on normal HaCat cells and HSC cancer cells are shown in (C) and (D), respectively. Note that cancer cells in (D) show stronger, sharper, and better resolved SERS signals than normal cells in (C) due to the specific binding of immune-labeled Au nanorods with receptors on the cancer cell surface, suggesting that SERS may serve as a clinical diagnostic tool. Reprinted from ref 461. Copyright 2007 American Chemical Society.

CTAB and anti-EGFR were greatly enhanced after the Au nanorods had been attached to the surface of cancer cells. Due to the strong affinity of anti-EGFR toward the receptors on cancer cells, such a SERS-based assay can be used to reveal the molecular information about cancer cells and thus differentiate cancer cells from normal cells. Later on, Liz-Marzán and co-workers demonstrated that Au nanostars could be used to detect various types of analytes at a zeptomolar detection limit through the use of a sandwich structure between a Au film and Au nanostars using the label-free strategy.⁴⁶⁴

By attaching Raman active molecules to the surface of Au nanoparticles, SERS tags can be obtained, which have been widely used for Raman reporter assays. After further coated with a protective shell and conjugated with a recognition ligand, the SERS tags can be fabricated with good biostability, biocompatibility, and specific binding capability.^{277,465–470} Due to the unique Raman signatures and the high detection sensitivity, SERS tags can be used for more complicated, ultrasensitive detection of multiple biomolecules in the format of multiplexing.⁴⁷¹ To this end, antigen identification was first demonstrated with different SERS tags.⁴⁷² The SERS tags modified with different antibodies and Raman reporters were

attached to different antigen molecules through the specific, strong interaction between the antibody and antigen. As such, the antigen molecules can be detected from the different SERS signals using the sandwich immunoassay format. In addition, SERS tags can be employed for tumor detection and biodistribution analysis in live animals.^{277,473}

Again, although the sensors based on SERS have superb selectivity and sensitivity, their scope of use is limited by the high cost of Au and the requirement of a Raman spectrometer. In addition, it is still difficult to apply SERS to quantitative analysis because of the variance in the SERS enhancement factor across different regions of the same substrate, as well as differences between substrates.

4.1.4. Sensing Based on Photoluminescence Quenching. Gold nanostructures can be used as acceptors to construct a Förster resonant energy transfer (FRET) system by simply attaching organic chromophores (i.e., the donors) to their surfaces. In such a system, the Au nanostructure can serve as an excellent photoluminescence quencher for the FRET-based assay due to its extraordinarily high molar extinction coefficient and broad energy bandwidth. To this end, Murray and co-workers developed a nanosensor for the detection of various metal ions based on the FRET between Au nanoparticles and $[\text{Ru}(\text{bpy})_3]^{2+}$.⁴⁷⁴ It was found that the photoluminescence from $[\text{Ru}(\text{bpy})_3]^{2+}$ could be efficiently quenched by Au nanoparticles functionalized with *N*-(2-mercaptopropionyl)glycine (tiopronin) due to the electrostatic attraction between tiopronin and $[\text{Ru}(\text{bpy})_3]^{2+}$. The photoluminescence from $[\text{Ru}(\text{bpy})_3]^{2+}$ could be restored after the addition of various electrolytes to trigger the aggregation and sedimentation of Au nanoparticles. Such a FRET-based assay can also be utilized for the detection of other types of ionic species.

In a different approach, our group demonstrated the fabrication of an enzyme-sensitive probe that was composed of a Au nanocage and dye molecules linked together through an enzyme-cleavable peptide (Figure 31).⁴⁷⁵ The photoluminescence from the dye molecules was efficiently quenched through the FRET effect. In the presence of a protease, however, the peptide would be cleaved and the photoluminescence would be recovered from the release of dye molecules from the surface of Au nanocages. It is feasible to choose different combinations of peptide linkers and dyes to construct probes well-suited for in vivo determination of enzyme activities due to the optical tunability of Au nanocages in the NIR region.

To better control the FRET process, a nanosensor for the detection of DNA strands with single-base mismatch was developed based on a hybrid material that was comprised of ssDNAs, Au nanoparticles, and fluorophores.⁴⁷⁶ Through a distance-dependent process, the photoluminescence from the hybrid material could be increased by a factor of several thousand after the binding of complementary ssDNAs. Based on this nanosensor, the ability to detect single-base mismatches could be increased by 8-fold compared to other types of molecular sensors.⁴⁷⁶ In another study, Dulkeith and co-workers found that the photoluminescence from dye molecules could be efficiently quenched when they were attached to the surface of Au nanoparticles with different sizes via a thioether linker.⁴⁷⁷ The quenching was caused not only by an increase in the nonradiative rate but also by a drastic decrease in the radiative rate of the dye. They further investigated the quantum yield of Cy5 molecules attached to the surface of Au nanoparticles via an ssDNA spacer to control the distance between the Cy5 molecules and the Au surface.⁴⁷⁸ The distance

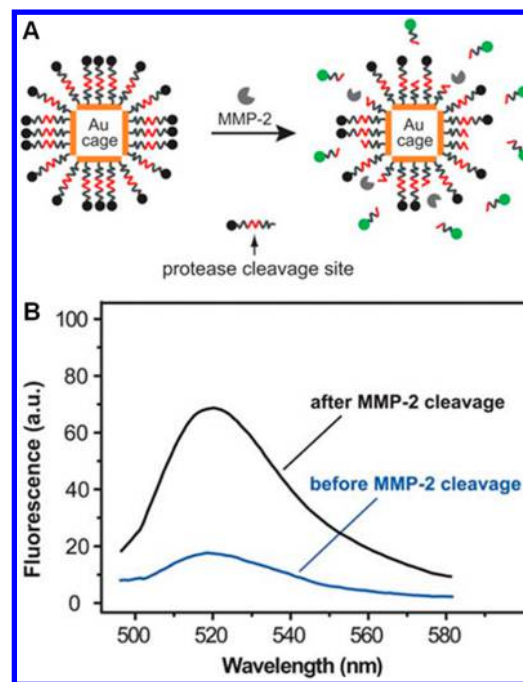


Figure 31. (A) Schematic illustration of a dual optical probe composed of a Au nanocage conjugated with dye molecule through a peptide specific to metalloprotease-2 (MMP-2) that can be activated by an enzyme. (B) Photoluminescence spectra of Au nanocages with absorption at 770 nm conjugated with fluorescein isothiocyanate (FITC) through a MMP-2 specific peptide GKGPLGVRGC (termed FITC-GKGPLGVRGC-cage770) before and after incubation with 1 U (72 ng mL^{-1}) MMP-2 at 37°C for 3 h. Reprinted with permission from ref 475. Copyright 2011 Royal Society of Chemistry.

dependent quantum efficiency was almost exclusively governed by the radiative rate.

Based on the capability of Au nanoparticles to quench photoluminescence, many different types of sensors have been constructed for the sensitive detection of proteins,⁴⁷⁹ DNA,⁴⁸⁰ metal ions,^{481–484} and small molecules.⁴⁸⁵ Table 3 shows the comparison of four different sensing platforms based on Au nanomaterials discussed in section 4.1.

4.2. Optical Imaging

4.2.1. Imaging Based on Photoluminescence. As discussed in section 3.1, Au clusters show excellent photoluminescence properties due to the quantum confinement effect. Compared to traditional organic dyes and semiconductor quantum dots, Au is a more bioinert material and Au clusters demonstrate more stable photoluminescence. In addition, the excitation and emission peaks of Au clusters can be readily tuned from the UV to the NIR region, making Au clusters an excellent choice of probes for optical imaging.^{261,486–489}

Cellular imaging based on Au clusters tends to suffer from their low uptake by the cell. This issue can be addressed through proper surface modification. For example, Au clusters conjugated with a cell-penetrating peptide using a ligand-exchange approach have been prepared and evaluated as an optical probe for cellular imaging. Prior to functionalization with a peptide known as SV40 nuclear-localization signal (NLS), the Au clusters were unable to enter the cell efficiently.⁴⁸⁸ In contrast, the NLS-conjugated Au clusters were distributed throughout both the cytoplasm and nucleus. Several other targeting ligands have also been utilized to functionalize Au clusters for cellular imaging.^{488,489} Streptavidin

Table 3. Comparison of Different Sensing Platforms Based on Au Nanomaterials

sensing platform	Au nanomaterials	analytes	detection limit	disadvantages
photoluminescence (PL)	clusters	protein, ^{407–411} ions, ^{412–414,422,424–427} small molecules ^{415–417,423,428}	nM–pM	high cost, not portable
LSPR	colloidal nanoparticles	DNA, ^{283,430,431,451,452} ions, ^{432–441,455,457} small molecules, ^{442–448,454,456} protein ^{449,450,458}	μ M–pM	lower sensitivity compared to PL
SERS	colloidal nanoparticles, nanorods, nanoshells, nanostars	cancer cells, ⁴⁶¹ ions, ⁴⁶⁹ protein, ⁴⁷¹ tumor, ^{277,473} small molecules ^{464,465,472}	single molecule	high cost, not quantitative
PL quenching	colloidal nanoparticles	ions, ^{474,481–484} protein, ^{475,479} DNA, ^{476,480} small molecules ⁴⁸⁵	nM–pM	high cost, not portable

was found to improve the cellular uptake of Au clusters relative to both PEG- and BSA-covered samples.⁴⁹⁰ Folic acid and insulin could also improve the cellular uptake and thus improve cellular imaging with Au clusters.^{491,492} Compared to single-photon excitation, TPPL is advantageous due to its deeper penetration into biological tissues and the reduced phototoxicity from radiation in the NIR region. To this end, Nienhaus and co-workers used D-penicillamine as a capping ligand to synthesize Au clusters with a TPPL quantum yield of 1.3%.⁴⁹³ They further studied the internalization of these Au clusters by live HeLa cells using two-photon confocal microscopy (Figure 32A,B).

Besides cellular imaging, Au clusters have also been explored for in vivo studies. He, Wang, and co-workers reported the first demonstration of in vivo photoluminescence imaging with BSA-stabilized Au clusters.⁴⁹⁴ The photoluminescence signal from the Au clusters in living organisms can be distinguished from the background by spectroscopy. The high photostability and low toxicity of Au clusters are particularly attractive for in vivo imaging. Recently, Zheng and co-workers used GSH-stabilized Au clusters for in vivo NIR photoluminescence imaging.⁴⁹⁵ They also studied the distribution and body clearance of Au clusters by directly monitoring changes to the intensities of photoluminescence signals. It was found that the renal clearance of GSH-stabilized Au clusters (~ 2.5 nm in size) was more than 10 and 100 times faster than that of GSH-stabilized Au nanoparticles with average diameters of 6 and 12 nm, respectively.

As discussed in section 3.1, the photoluminescence emitted from Au nanostructures via interband transitions can be enhanced by many orders of magnitude in the presence of plasmon resonance. Accordingly, a number of imaging modalities based on the photoluminescence from Au nanostructures have been reported in the literature. These imaging modalities can be divided into three major categories involving single-, two-, and three-photon excitation, respectively. In SPPL imaging, the Au nanostructures have to be excited by UV or visible light. Chen and co-workers used Au nanocubes for cell imaging through single-photon excitation, and reported a photoluminescence quantum yield of 4%.⁴⁹⁶ Human liver cancer cells (QGY) and human embryo kidney cells (293T) were imaged using Au nanocubes at an excitation wavelength of 544 nm. The relatively low power density (50 μ W) involved in single-photon excitation helped keep the phototoxicity at a manageable level. However, due to the strong absorption and scattering of UV or visible light by blood and tissues, SPPL imaging cannot be readily applied to in vivo applications.

To address this issue, TPPL imaging was developed, which relies on the use of a NIR laser for excitation (Figure 32C–F). Due to the quadratic dependence of the TPPL intensity on the

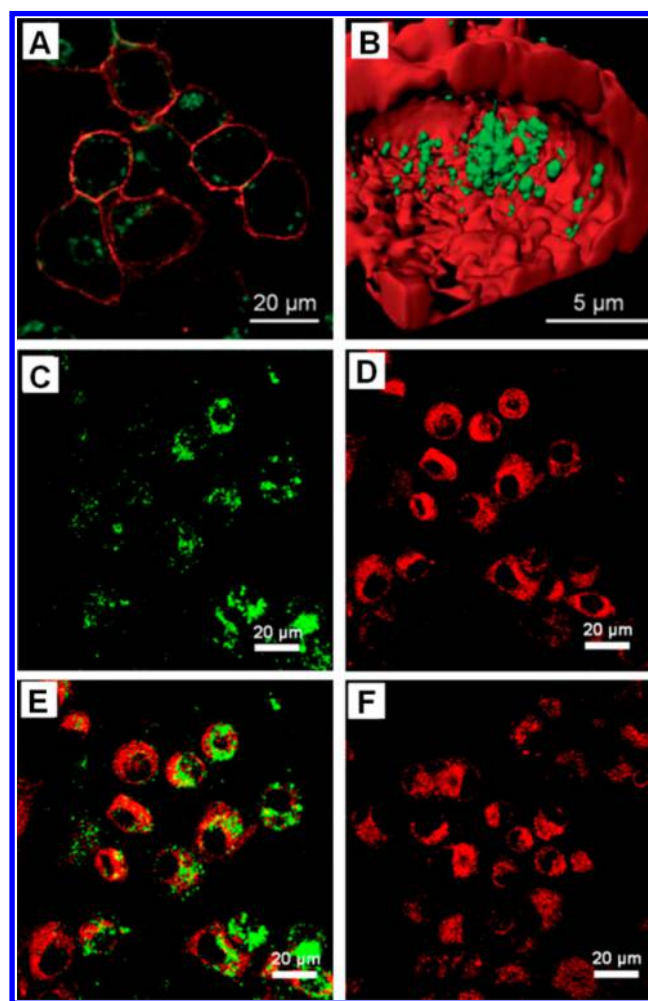


Figure 32. (A) Confocal optical micrograph of HeLa cells after incubation with D-penicillamine (DPA)-stabilized Au clusters for 2 h and (B) cross section from a 3D image reconstruction, showing the internalized DPA-stabilized Au clusters. Membranes were stained with the red dye DiD and the images were taken by two-photon excitation at 810 nm. (C–E) Confocal optical micrographs of U87MGwtEGFR cells after incubation for 3 h with 0.02 nM anti-EGFR-conjugated Au nanocages and 5 μ g mL⁻¹ FM4-64 dye: (C) photoluminescence from Au nanocages (false color), (D) red photoluminescence from FM4-64, and (E) superimposition of (C) and (D). (F) Confocal optical micrographs (superimposed images) of U87MGwtEGFR cells after incubation with PEGylated Au nanocages and FM4-64 for 3 h. (A and B) Reprinted with permission from ref 493. Copyright 2011 Royal Society of Chemistry. (C–F) Reprinted from ref 324. Copyright 2010 American Chemical Society.

power of excitation light, a pulsed femtosecond laser with a relatively high power density is required in order to generate

sufficiently strong signals. Compared to SPPL, TPPL has several advantages: (i) it has a nonlinear dependence on the excitation intensity and can be resolved in the axial direction to provide three-dimensional (3D) spatial resolution, (ii) it is excited with a NIR laser, ensuring a deep penetration into soft tissue, and (iii) the signals can be spectrally separated from tissue autofluorescence.³¹¹ Two-photon photoluminescence is commonly used in the study of cellular uptake of nanoparticles, as well as in the tracking of cells both *in vitro* and *in vivo*. Besides qualitative imaging, a quantitative estimate of the concentration of Au nanomaterials can be made based on the intensity of two-photon signals, greatly extending the scope of application for this technique. To this end, our group analyzed the uptake of PEGylated Au nanocages conjugated with anti-EGFR antibodies by U87MGwtEGFR cells using TPPL (Figure 32C–F).³²⁴ The nanocages with an average edge length of 45 nm and an LSPR peak at 795 nm were excited using a two-photon scheme by a Ti:sapphire laser centered at 800 nm. The data collected through TPPL correlated well with what was obtained from ICP-MS analysis, and it was shown that the anti-EGFR-conjugated Au nanocages were attached to the surface of the cells through antibody–antigen interactions. The surface-bound nanocages were then internalized into the cells via receptor-mediated endocytosis. The cellular uptake of the Au nanocages was found to depend on many parameters, including the number of surface-bound anti-EGFR per nanocage, the size of the nanocages, the incubation time, and the temperature used for cell cultures.

In a later study, our group also reported the tracking of human mesenchymal stem cells (hMSCs) both *in vitro* and *in vivo* using TPPL microscopy with Au nanocages as the probes (Figure 33).⁴⁹⁷ It was revealed that PEGylated Au nanocages could remain in the cells for up to 28 days during culturing, and the capability of hMSCs to differentiate into different cell lineages was not affected by the labeling of Au nanocages. As the initially labeled cells divided, the Au nanocages were separated into the daughter cells, leading to a linear decrease of TPPL intensity. The homing of hMSCs labeled with Au nanocages to the tumor region could be effectively monitored in the ear of a tumor-bearing mouse using TPPL microscopy. These demonstrations confirmed the viable use of Au nanocages for long-term tracking of hMSCs. One potential issue about TPPL is that the laser excitation wavelength of TPPL overlaps with the LSPR peak of Au nanomaterials, causing photothermal conversion to occur during TPPL imaging. Thermal degradation tends to take place in the Au nanomaterials under these circumstances, and the hyperthermia effect induced by the photothermal heating could lead to potential toxicity of the cells during the imaging process. Additionally, the quantum yield of TPPL is always much lower than that of SPPL. When applied to *ex vivo* tissue imaging, the excitation source used can also result in a strong background due to the involvement of autofluorescence.

Three-photon photoluminescence can address the problems of both photothermal toxicity and autofluorescence of TPPL by switching to an excitation source with a much longer wavelength. During 3PPL imaging, the NIR excitation wavelength is shifted away from the plasmon resonance peak of Au nanostructures, and the absorbed photons are more effectively used for the generation of luminescence. As a result, much less thermal energy is produced during a 3PPL process. In a collaboration, our group and the Cheng group compared the 3PPL and TPPL of Au nanocages for cellular imaging.³¹⁴ As

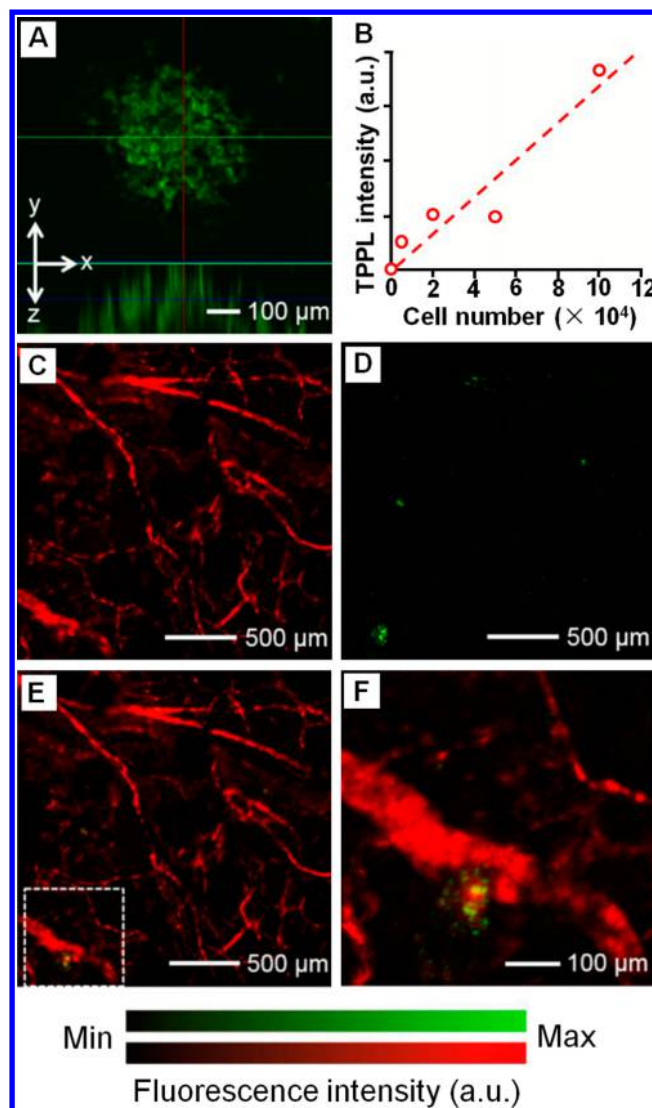


Figure 33. (A) Typical two-photon projection image showing the Au nanocages-labeled hMSCs subcutaneously injected into a mouse ear. (B) Calibration curve for the two-photon intensity as a function of the number of hMSCs labeled with Au nanocages. (C–E) Confocal optical micrographs showing (C) blood vessels in a U87 brain tumor model, (D) hMSCs labeled with Au nanocages that homed to the tumor region, and (E) a superimposed image. (F) Enlarged view showing the area boxed by white dotted lines in (E). Reprinted with permission from ref 497. Copyright 2013 Ivyspring International Publisher.

shown in Figure 34, the Au nanocages could be imaged using both TPPL and 3PPL with the same initial level of intensity. After a repetitive raster scanning of the cells with 760 nm laser for 90 s in TPPL, membrane blebbing was observed (Figure 34C), together with a reduced TPPL intensity from nanocages. In contrast, no plasma membrane damage was observed during 3PPL, and the signal intensity remained constant throughout the scan with 1290 nm laser for 90 s (Figure 34D). Different from TPPL, there is no autofluorescence in a 3PPL process (Figure 34E,F), making it feasible to map the distribution of Au nanocages in a tissue during *ex vivo* imaging. Apart from the aforementioned advantages, 3PPL suffers from a low quantum yield due to the involvement of a three-photon process. As a result, a compromise between penetration depth, photothermal toxicity, and signal intensity has to be made when choosing the

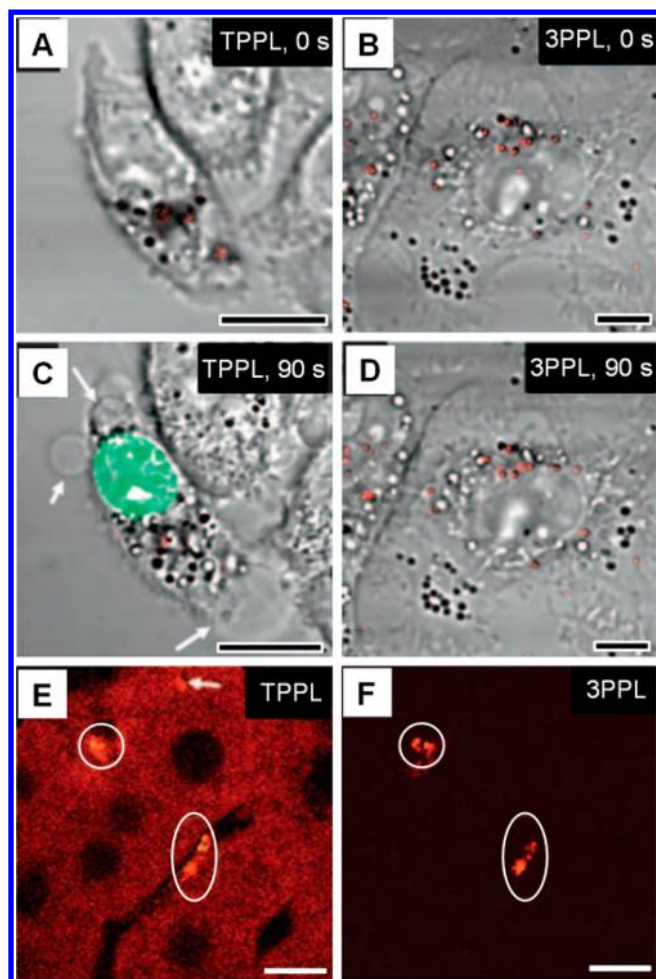


Figure 34. Comparison of two- and three-photon photoluminescence (TPPL and 3PPL) imaging of Au nanocages in (A–D) KB cells and (E and F) a piece of liver tissue. (A) TPPL image and (B) 3PPL image of Au nanocages (red dots) in KB cells before laser scanning. (C) TPPL image of the same cell as in (A) after scanning with a 760 nm femtosecond laser for 90 s. After scanning, membrane blebbing (indicated by arrows) and compromised membrane integrity were observed as indicated by ethidium bromide labeling (green). (D) 3PPL image of the same cell as in (B) after scanning with a 1290 nm femtosecond laser for 90 s. (E) TPPL image of Au nanocages (indicated by white circles) in a piece of liver tissue, with the strong autofluorescence from the tissue indicated by the white arrow. (F) 3PPL image taken from the same region as in (E). The scale bar in each image corresponds to 10 μm . Reprinted with permission from ref 314. Copyright 2010 Wiley-VCH.

best method of excitation for photoluminescence imaging with Au nanomaterials.

4.2.2. Imaging Based on Elastic Light Scattering. Along with the increase in size, the scattering cross section of a Au nanostructure will steadily increase regardless of its shape.³²⁷ In general, the light scattered by a Au nanoparticle could be more than 1 million times stronger in intensity than the light emitted by a fluorescent dye.^{329,498,499} It is an attractive concept to use the elastically scattered light for optical imaging as it can be detected and quantified more easily than the light being absorbed.

Dark-field optical microscopy can be utilized to image Au nanoparticles by recording the elastically scattered light.³³¹ In this case, single-particle detection capability has been

demonstrated with Au nanorods, nanoboxes, and nanocages, even though their scattering cross sections were not optimized.⁵⁰⁰ In 2005, for example, El-Sayed and co-workers demonstrated the capability to directly image individual anti-EGFR-conjugated Au nanoparticles with dark-field microscopy.³³¹ In that work, a halogen lamp (the same as for bright-field imaging) was used as a source of white light. By selectively blocking the central area of the illumination, only the scattered light from the sample was collected. As shown in Figure 24B, the Au nanoparticles conjugated with anti-EGFR appeared as bright spots in the image due to their strong scattering cross sections. By quantifying the signal intensities for different samples, the targeting efficiency of the Au nanoparticles toward different types of cancer cells and noncancerous cells could be compared with and benchmarked against their nontargeted counterparts. It was shown that the anti-EGFR-conjugated Au nanoparticles had an affinity 600% greater toward the cancer cells than the noncancerous cells. Another interesting observation was the apparent aggregation of the Au nanoparticles as indicated by the shoulder peaks on their UV–vis spectra. This aggregation was believed to arise from the endocytosis of the nanoparticles but was also affected by the surface capping agent and the salinity of the medium. Given that the scattering cross section of Au nanoparticles reaches its maximum at the wavelength of its LSPR peak, the scattered light could also be color coded by employing Au nanoparticles with different LSPR peak positions. To this end, Irudayaraj and co-workers utilized this strategy to map the distribution of biomarkers on cell surface.⁵⁰¹ In their study, three types of biomarkers (CD44, CD24, and CD49f) were simultaneously tracked with three kinds of Au nanorods, each with different aspect ratios. In general, this imaging modality is only suitable for in vitro studies as the absorption and scattering from tissues will result in undesired attenuation for an in vivo experiment, resulting in low resolution and a poor signal-to-noise ratio (SNR).⁵⁰²

When light propagates through a sample, it will be scattered into different directions and its phase will be altered. As a noninvasive imaging modality, optical coherence tomography (OCT) utilizes the changes in phase and intensity from the elastically scattered light for 3D imaging with micrometer resolution.⁵⁰³ Due to its high spatial resolution, OCT can be utilized to image tissues at the cellular level with reasonable SNR. During imaging, the light reflected from the sample is combined with the light from a reference arm to generate interference. If the reflected light cannot cancel the light from the reference arm due to a coherent process, a bright spot will be created in the image.⁵⁰⁴

In a collaboration, our group and the Li group demonstrated the potential of using Au nanocages as a new class of OCT contrast enhancement agents in a phantom study.³⁶⁰ In this work, the gelatin phantom was prepared containing 1 nM Au nanocages (with LSPR peak tuned to 800 nm) in one region, and employed TiO_2 powders to mimic the background scattering of soft tissues. Imaging analysis showed greater light attenuation from the region containing Au nanocages. In a related study, West and co-workers demonstrated the use of Au nanoshells as contrast agents for in vivo imaging with OCT.⁵⁰⁵ The Au nanoshells were synthesized with a uniform diameter of about 143 nm, with a corresponding LSPR peak at 800 nm. Based on Mie theory, the Au nanoshells were calculated to have a scattering cross section approximately 33% of the total extinction cross section at 800 nm. This allows the Au

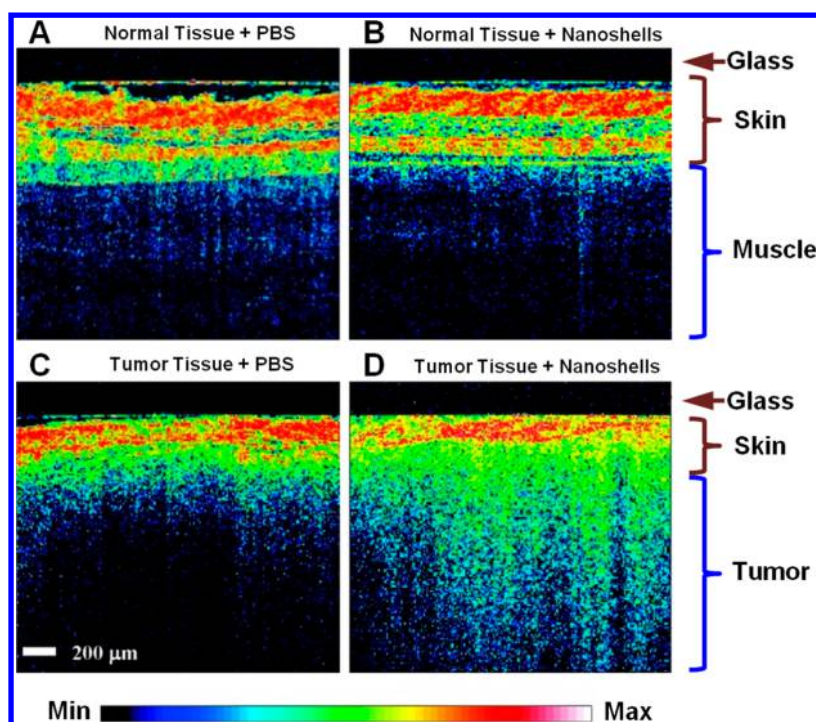


Figure 35. Demonstration of Au nanoshells as contrast agents for optical coherence tomography (OCT): (A and B) OCT images taken from normal muscle tissue beneath the skin on a mouse model systemically injected with PBS and Au nanoshells, respectively. (C and D) OCT images from tumor tissue beneath the skin on a mouse model systemically injected with PBS and nanoshells, respectively. The glass layer is shown as a dark, nonscattering layer with a thickness of 200 μm . Reprinted from ref 505. Copyright 2007 American Chemical Society.

nanoshells to scatter a large portion of light, making them a good candidate for OCT contrast enhancement. After PEGylation, the Au nanoshells were intravenously injected into mice bearing CT-26 murine colon carcinoma. After 20 h of passive targeting, images were captured using a commercial OCT system, with axial and transverse resolutions of about 10 and 15 μm , respectively. The images in Figure 35 indicate that even though the skin of the mice gave the strongest signal across all the experimental and control groups, the tumor showed an elevated level of OCT signal, with an increase of 53% in intensity. The ability to use OCT imaging for guided PTT was also demonstrated in the same study. Along the same line, Au nanorods have been demonstrated for OCT contrast enhancement using phantom samples and in vivo studies.^{506,507}

Because OCT depends on an interference process for the detection of signals, the depth of imaging resolution (hundreds of micrometers) is even less than that which can be achieved through fluorescence imaging, and is therefore highly dependent on the type of tissue being imaged.⁵⁰³ This technique has found clinical uses in ophthalmology for directly examining fundus oculi. Yet for other types of tissue or organs, the light needs to transmit through the skin before reaching the lesion, thus making it unfavorable for most applications.

4.2.3. Imaging Based on Inelastic Light Scattering. As discussed in section 3.3, Raman scattering can give specific information on the analyte molecule involved. As a result, Raman scattering spectra can serve as “fingerprints” with characteristic peaks for the identification of molecular species by their functional groups.

With the use of a commercial Raman confocal microscope, Raman spectra can be recorded from different locations of a sample and then organized in the 2D or 3D format to generate a Raman image.^{508,509} The drawback of this technique is a long

acquisition time of several seconds for a single Raman spectrum or pixel, and thus the requirement of several hours for obtaining a single image.⁵¹⁰ In addition to the improvements made for the design of the imaging system, SERS has also been explored to address this issue.⁴⁶⁸ As discussed in section 3.3, the introduction of Au nanoparticles can enhance the intensity of Raman signals by many orders of magnitude, making it feasible for the detection of Raman signals with higher sensitivity, thus requiring shorter acquisition time.

In 2002, Feld and co-workers reported the use of SERS for imaging live cells with the assistance of 60 nm Au nanoparticles.⁵¹¹ In that study, differentiated intestinal epithelial cells HT29 were cultured on a glass cover slide, and then incubated with Au nanoparticles for 24 h. With a focal point size of 1 μm , SERS spectra with good SNR were obtained at a rate of 1 s/pixel. It was argued that the SERS imaging technique could open up new opportunities for the early detection of diseases, as it can monitor the chemical changes in a cell. However, since the Au nanoparticles were not evenly distributed throughout the cell, the SERS image could not be correlated with the spatial distribution of molecular species. In similar studies, Abrahamsson and co-workers⁵¹² and Smith and co-workers⁵¹³ also used SERS imaging to map R6G introduced into lymphocytes and G292 human osteosarcoma cells, respectively, with the assistance of 60 nm Au nanoparticles.

It was demonstrated that SERS imaging could also be utilized for the monitoring of therapeutic drugs in live cells. With the introduction of a new instrument design, SERS images can be acquired at a high enough speed to enable the real-time tracking of Au nanoparticles in live cells.^{514–518} In 2008, Kawata and co-workers developed the slit-scanning Raman microscope for imaging live cells.⁵¹⁴ Using the same technique, they also investigated the endocytosis process of 50 nm Au

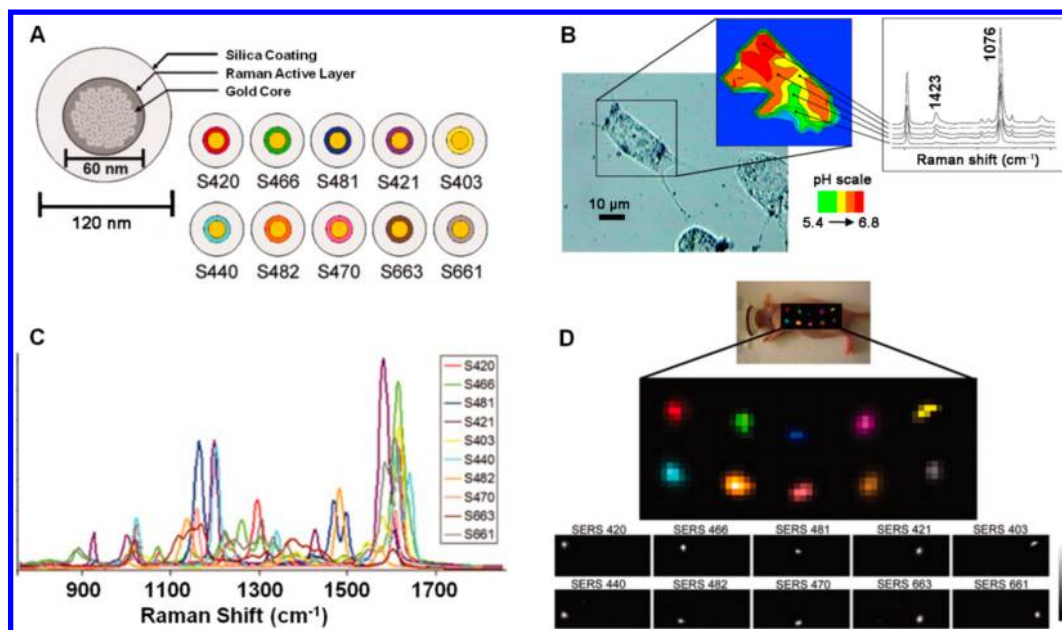


Figure 36. Use of Au nanoparticles for SERS imaging. (A) Schematic illustration of SERS tags based on 60 nm Au nanoparticles, whose surfaces were derivatized with different Raman active molecules, followed by coating with a SiO₂ shell. The name of each SERS nanoparticle is shown on the right. (B) Imaging and mapping of pH values across an individual living cell using 4-mercaptobenzoic acid (*p*-MBA) covered Au nanoparticles as the SERS probe. Left panel shows a bright-field image of an NIH/3T3 cell after 4.5 h incubation with the *p*-MBA-covered Au nanoparticles. Middle panel shows a pH map of the cell. The value at each pixel is derived from the ratio of the SERS peaks at 1423 and 1076 cm⁻¹ and displayed as a false color plot. Right panel shows the SERS spectra recorded from the probes located in the endosomal compartments with different pHs. (C) SERS spectra of all 10 SERS tags, with each spectrum being assigned a color corresponding to its Raman active molecule as shown in (A). (D) Multiplexing of 10 different SERS tags in vivo. Different colors are assigned to each SERS tag. The below panels show separate channels of each injected SERS tags. Grayscale bar to the right indicates the Raman intensity, with white representing the maximum intensity and black representing no intensity. (A, C, and D) Reprinted with permission from ref 521. Copyright 2009 National Academy of Sciences, U.S.A. (B) Reprinted from ref 520. Copyright 2007 American Chemical Society.

nanoparticles by macrophage and tracked the movement of particles with high spatial and temporal resolutions.^{497,519} When illuminated with a 785 nm laser in a continuous wave (CW) mode at a power density of 15 mW/μm², SERS signals with reasonable SNR could be obtained within the first 2.5 min. After incubation for 30 min, they observed that the Au nanoparticles attached to the cell surface had begun to enter the cell. The Au nanoparticles can also be conjugated with functional groups to serve as molecular probes. To this end, Kneipp and co-workers explored the use of aggregates assembled from *p*-MBA-coated Au nanoparticles for pH sensing over a broad range.⁵²⁰ As shown in Figure 36B, the local pH value could be readily derived from the ratio of peak intensities for the 1423 and 1076 cm⁻¹ bands of *p*-MBA.

Probes based on Au nanoparticles were also developed for in vivo imaging with tumor targeting capability. In 2008, Nie and co-workers reported a novel SERS contrast agent with tumor targeting capability that is suitable for in vivo cancer diagnosis.²⁷⁷ When the surfaces of PEGylated Au nanoparticles (60 nm in diameter) were further derivatized with malachite green, they served as a good contrast agent for SERS imaging. These nanoparticles were called nanotags by the authors. The SERS signals were strong enough to be detected using a Raman spectrometer when the nanotags were subcutaneously injected into the flank of a nude mouse. They also conjugated the nanotags with an EGFR-antibody fragment to specifically target anti-EGFR, which is overexpressed on multiple types of cancer cells. The in vivo targeting capability was demonstrated in a nude mouse model bearing human head-and-neck squamous cell carcinoma (Tu686). Both SERS imaging and ICP-MS

analysis indicate that tumor accumulation of the targeting nanoparticles could be enhanced by 10-fold relative to the nontargeting counterpart 5 h postinjection. Gambhir and co-workers later demonstrated multiplexed imaging of SERS nanotags in live mice.^{521,522} In their approach, different kinds of SERS tags based on small molecules were first attached to the surface of Au nanoparticles, followed by SiO₂ coating and PEGylation (Figure 36A,C). The distributions of different types of nanotags could be monitored by SERS imaging in vivo and distinguished from each other by their unique spectral fingerprints (Figure 36 D). Gold nanoparticles with different shapes have also been explored as contrast agents for both in vitro and in vivo SERS imaging.^{461,521,523–525} However, further study is needed to improve the reproducibility of SERS imaging. It is also necessary to optimize the size of the nanoparticles to improve in vivo tumor targeting efficiency without compromising the SERS activity.

4.2.4. Imaging Based on Photothermal Conversion.

When light is absorbed by a molecule or material, the photons can pass their energy to electrons in the molecule or material to excite those electrons to higher energy levels. Following excitation, the electrons will quickly relax down to their ground state either through radiative decay and emit photons, or through nonradiative decay and release heat through electron–phonon and phonon–phonon couplings.⁵²⁶ Accordingly, photoluminescence or photothermal heating will be observed. When the local environment of a constrained size is rapidly heated up and the accumulated heat cannot quickly dissipate, thermoelastic expansion and explosive vaporization will occur, accompanied by the generation of photoacoustic (PA)

waves.⁵²⁷ In general, fast heat generation and a large gradient in temperature both facilitate the generation of PA waves.⁵²⁷ As a result, a pulsed or chopped laser is typically used for imaging based on the PA phenomenon.

Photoacoustic imaging shares the advantages of both optical and ultrasonic modalities, and has emerged as a versatile imaging modality for various kinds of biomedical applications.^{528–531} Ultrasonic imaging typically suffers from poor resolution, due to the relatively low intensity of an ultrasound source compared to that of a laser. With the use of a highly focused laser as the excitation source, the resolution can become compatible with an optical system. The scattering effect of ultrasound is 2–3 orders of magnitude weaker than that of light, so ultrasound can offer a higher resolution in deep tissue imaging than optical modalities.⁵²⁸ The acoustic signals can then be directly collected and converted into an image as in photoacoustic microscopy (PAM) or reconstructed with an inverse algorithm as in photoacoustic tomography (PAT). The imaging depth can be pushed up to tens of millimeters, with a spatial resolution ranging from submicrometer to millimeter.^{528–531} With these benefits, PA imaging is a promising technique that can bridge the resolution and penetration gaps between optical imaging and conventional radiological medical imaging.

Photoacoustic imaging is most powerful in resolving the vascular structures in tissues due to the strong absorption associated with both hemoglobin and deoxyhemoglobin in the red blood cells. Most tumor tissues (except for melanoma) and normal tissues do not possess the adequate contrast to be differentiated through PA imaging as they do not have distinguishable absorption features beyond the vascular structures embedded in them.^{528–531} For such cases, an exogenous contrast agent must be introduced to increase the absorption at specific locations.

With highly tunable LSPR peak positions, large absorption cross sections, and excellent passive targeting capability, Au nanoparticles can effectively convert the energy harvested from light into heat and thus serve as a class of superb contrast agents for PA imaging.^{328,357,531} In an early study, Oraevsky and co-workers explored the use of Au nanoparticles as a contrast agent for PA imaging using a gelatin phantom and an optoacoustic tomography system (later known as PAT).⁵³² They assessed the contrast enhancement by 40 nm Au nanoparticles, which were conjugated with Herceptin to target SK-BR-3 breast cancer cells. The targeted cells showed a brighter spot in the image, indicating contrast enhancement. The in vivo contrast enhancement was then demonstrated using Au nanoshells as an intravascular contrast agent for PAT.⁵³³ The Au nanoshells were synthesized with an average diameter of 135 nm, and a LSPR peak tuned to 800 nm. After PEGylation, three shots of Au nanoshells were sequentially administered into Sprague–Dawley rats via tail vein injection. The distribution of Au nanoshells in the rat cortical blood vessels was directly imaged at different intervals of time. The circulation dynamics were recorded as changes to the absorption readout on the image. The nanoshells were shown to enhance the PA contrast by 63% following the three sequential injections, improving the sensitivity of cortical blood volume measurements. In a later study, our group worked with Wang and co-workers to demonstrate the use of Au nanocages as an intravascular contrast agent for the PA imaging of a rat's cerebral cortex.⁵³⁴ A peak value of 81% was obtained for the enhancement at 2 h postinjection relative to a blank control.

Another use of Au nanostructures and PA imaging is in cancer diagnosis. Working with Wang and co-workers, our group compared the passive and active targeting of melanoma by Au nanocages using PA imaging.⁵³⁵ We quantitatively assessed the contrast enhancement in B16 melanomas by functionalizing Au nanocages of 46 nm in edge length with succinimidyl propionyl PEG disulfide and thiol-mPEG, followed by [Nle⁴,D-Phe⁷]- α -melanocyte-stimulating hormone or [Nle⁴,D-Phe⁷]- α -MSH, a short peptide that can selectively bind to α -MSH receptors on the surface of melanoma cells. Figure 37 shows superimposed PA images collected with

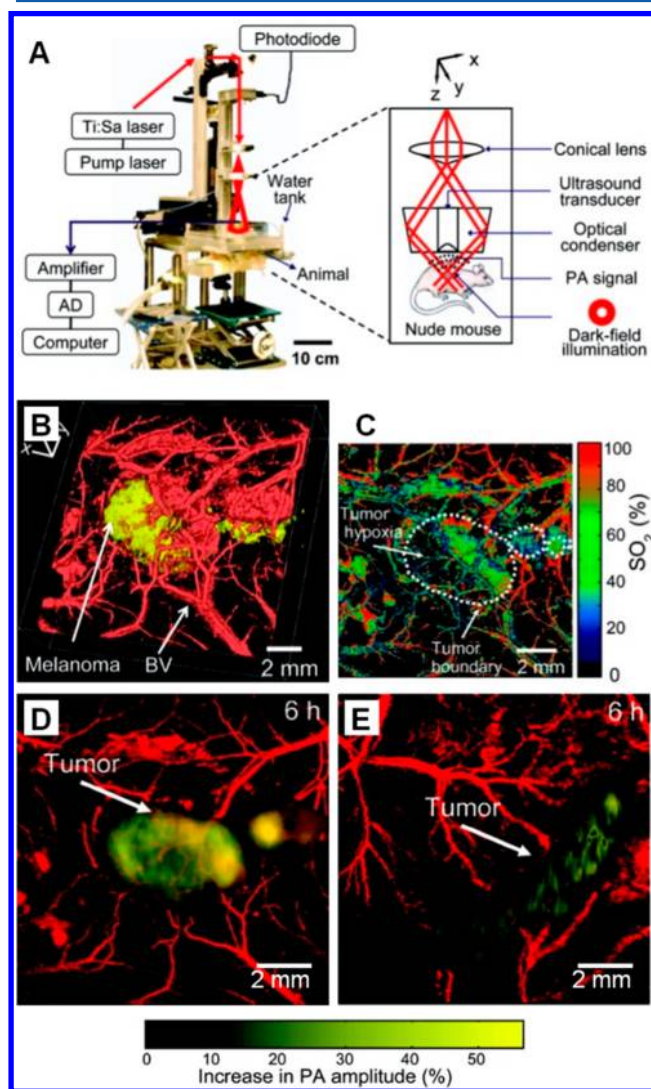


Figure 37. (A) Illustration of a photoacoustic (PA) microscope. (B) Noninvasive volumetric morphological PA images of B16 melanoma (yellow) and its surrounding blood vessels (red). BV, blood vessels. (C) PA maximum amplitude projection (MAP) mapping of hemoglobin oxygen saturation (SO_2) of blood vessels surrounding the melanoma. The white dotted line shows the tumor boundary. (D, E) PA coronal MAP images of B16 melanomas at 6 h post the intravenous injection of 100 μ L of 10 nM Au nanocages covered with [Nle⁴,D-Phe⁷]- α -MSH and PEG, respectively. Color schemes: red for blood vessels and yellow for the increase in PA amplitude. The melanoma and the surrounding vasculatures were imaged with lasers at 778 nm (ultrasonic frequency = 10 MHz) and 570 nm (ultrasonic frequency = 50 MHz), respectively. Reprinted from ref 535. Copyright 2010 American Chemical Society.

illumination at 778 and 570 nm for resolving the Au nanocages and vasculatures, respectively. At 6 h postinjection, the melanoma was clearly visualized by comparing the patterns with the control images of melanoma and its surrounding microvasculatures acquired before the injection of Au nanocages. Quantitative comparison of the enhancement data suggests that the signal enhancement from active targeting was approximately 300% higher than that from the passive targeting at 6 h postinjection. This result confirms that the surface functional group can indeed have a significant impact on the accumulation of Au nanocages in melanoma.

The position of sentinel lymph node (SLN) can also be readily resolved using PAT when the contrast is enhanced by Au nanostructures. Cancer cells will normally be found in SLN in the early stage of metastasis after they have penetrated through the base membrane. Detecting the metastatic cancer cells in the lymph nodes, especially in the SLN, provides important information for cancer diagnostics and therapy. Since Au nanostructures are removed from the tissue through lymph drainage, they will accumulate in the SLN. Working with Wang and co-workers, our group demonstrated the use of Au nanocages for mapping the position of SLN by PAT.^{536,537} Compared to existing methods, a combination of Au nanostructures and PA imaging offers high sensitivity, high spatial resolution, together with adequate imaging depth for human use. In a typical study, the PA signal could be detected within 5 min after the injection of Au nanocages, and a clear image of SLN could be resolved after 28 min. The signal would continue to increase and could last for up to several hours, which is ideal for diagnostic purposes. By covering the SLN with chicken breasts of various thicknesses, an imaging depth up to 33 mm was demonstrated, larger than the depth of SLN in humans (~12 mm), without compromising the quality of the image. In a later study, the functional groups on the surface of Au nanocages were found to influence their transport kinetics and detection sensitivity.⁵³⁷ Similar results were obtained when Au nanorods and nanobeacons were used for the detection of SLN.^{538,539}

4.3. Other Imaging Modalities

Besides optical imaging, Au nanostructures have also been explored as contrast agents for radiological imaging modalities such as X-ray computed tomography (X-ray CT),^{45,540,541} positron emission tomography (PET),^{542–545} and Cerenkov luminescence imaging.^{151,546} As the most widely used medical imaging modalities in the clinics, both X-ray CT and PET scanners are easily accessible. PET is also commonly used for molecular imaging that visualizes cellular functions and biological processes at a molecular level with specially designed contrast agents.⁵⁴⁷ Cerenkov luminescence imaging, on the other hand, is an emerging technique that tracks the distribution of radionuclides by detecting their radioluminescence.⁵⁴⁸ Although these modalities tend to suffer from a lower resolution than most optical imaging techniques, they all offer deeper penetration depth for whole-organism imaging. They can also be integrated with one another for multimodality imaging.^{549–552} To this end, by combining the morphological and quantitative data acquired from an anatomical imaging modality such as X-ray CT and a molecular imaging modality such as PET, it is possible to obtain a better overview of the biodistribution, targeted accumulation, and clearance behavior of Au nanostructures, even allowing for accurate imaging-guided surgery. These imaging techniques are of critical

importance to translational research in bringing nanomedicine from benchtop to bedside.

4.3.1. X-ray CT Imaging. X-ray CT is one of the most widely used modalities for medical imaging in the hospital. It can be used to obtain complementary anatomical information for diagnostics in a cost-effective fashion. For conventional X-ray CT, however, the contrast between different types of soft tissues is negligible, and a good contrast can only be achieved between hard and soft tissues when no contrast agent is applied.⁵⁵³ As a result, conventional X-ray CT cannot be used alone to differentiate cancerous from normal tissues, rendering it essentially useless for the early stage detection of cancer or cancer metastasis. Various types of contrast agents, most of which are iodine-based compounds, have been developed to address this technical issue in terms of contrast.⁵⁵³ Most of them, however, do not have targeting capabilities, resulting in contrast enhancement largely reliant on perfusion.

Given that the attenuation of X-rays by tissue depends on the electron densities and thus atomic numbers of chemical elements present in the tissue, Au can provide a strong contrast relative to most of the naturally occurring elements found in the body.⁵¹⁶ As expected, the presence of Au nanostructures can greatly enhance X-ray attenuation, creating high contrast on the CT image. At the clinically used X-ray energy, Au nanostructures, regardless of their sizes and shapes, have a mass attenuation coefficient 2.7 times greater relative to the conventional iodine-based compounds, as well as other advantages such as prolonged presence in the circulation, lower renal toxicity, and well-established surface chemistry for the conjugation of targeting ligands.^{540,551,554} All these attributes make Au nanostructures promising contrast agents for clinical X-ray CT applications.

The first demonstration of X-ray contrast enhancement by Au can be traced back to the X-ray image taken by Wilhelm Roentgen, in which the Au ring on his wife's finger showed a greater X-ray attenuation than her bones.⁴⁵ However, only when broken down into small, injectable pieces, such as nanoparticles, can Au be used as a contrast agent for X-ray CT imaging in terms of diagnosis. In 2004, Smilowitz and co-workers demonstrated the first in vivo contrast enhancement with citrate-stabilized Au clusters of 1.9 nm in size.^{555,556} Upon injection of the Au clusters, blood vessels thinner than 100 μm could be clearly distinguished from the surrounding tissues. With a prolonged circulation time and slower renal clearance, such clusters offer a longer imaging time compared to conventional iodine-based compounds. Even without the use of any targeting ligand, the Au clusters still provided excellent passive targeting efficacy and selective contrast enhancement, with tumor-to-muscle concentration ratios of 3.4 at 15 min and 9.6 at 24 h postinjection.⁵³² Following this work, Au nanoparticles with different surface functional groups have also been employed to investigate their contrast enhancement, biodistribution, and resolution of the vasculature structure in tumor models.^{557,558} The effect of particle size on the contrast enhancement was also investigated.⁵⁵⁹ In general, the contrast enhancement is proportional to the total amount of Au accumulated within a certain volume of tissue, regardless of the size or shape of the nanoparticles. However, it was shown that greater enhancement was achieved with Au nanoparticles smaller in size, possibly due to a higher surface area and thus enhanced scattering from the surface of a particle.

Gold nanostructures with different shapes and a variety of surface functional groups have been evaluated for enhancing

the contrast of X-ray CT imaging. These nanostructures have been employed as a blood-pool contrast agent, as well as contrast agents with targeting capabilities toward cancer cells.^{43,560–562} Because of the low sensitivity of X-ray CT, however, it is necessary to use the Au nanostructures at a high dosage in order to generate sufficient contrast enhancement. The focus of current research has shifted toward the demonstration of multimodal contrast agents, radiosensitization, combined radiotherapy, and additional contrast enhancement with the use of spectrum CT.^{540,561,563,564}

4.3.2. PET Imaging. As the most commonly used modality for molecular imaging, PET can be employed to collect quantitative information about the expression of molecular species on a biological target.^{565,566} PET has been a standard tool for the evaluation of biodistribution and pharmacokinetics of Au nanostructures, as well as other types of nanomaterials. It can be used to obtain valuable information about cellular function and can give insight into the molecular processes of a living organism, enabling diagnosis even before any anatomical change is observed. This modality is more sensitive in detecting small lesions than X-ray CT, offering better contrast and serving as a more reliable diagnostic tool.

As opposed to X-ray CT, all nuclear imaging modalities require the functionalization of Au nanostructures with a radionuclide prior to their introduction into a living organism. A typical approach is to chelate or covalently attach the radionuclide to the surface of Au nanostructures. Depending on the chelator and radionuclide used, the radio-labeled Au nanostructures can be imaged by either PET or single photon emission tomography (SPECT). A broad range of studies have been conducted using this approach to evaluate the biodistribution, tumor targeting efficacy, and pharmacokinetics of Au nanostructures with a variety of sizes and shapes.^{542–545,567–572} In a study conducted by our group, a chelator, 1,4,7,10-tetraazacyclododecane-1,4,7,10-tetraacetic acid (DOTA), was covalently linked to PEGylated Au nanocages to immobilize ^{64}Cu .⁵⁴⁵ As shown in Figure 38, this method could be used to trace the biodistribution of Au nanocages and to quantify the tumor uptake of Au nanocages with gamma counting. However, such applications do not rely on the intrinsic properties of Au or Au nanostructures, and so are not extensively discussed in this article. In general, this approach suffers from a number of problems such as undesired alterations to the surface properties of Au nanostructures and possible detachment of the radionuclides during in vivo studies.⁵⁷³ When deattachment occurs, it leads to biased results on biodistribution and pharmacokinetics, as well as higher background signals.

Recently, there has been an emerging trend to incorporate the radionuclide directly into the lattice of Au nanostructures for improved labeling stability. To this end, ^{64}Cu atoms were successfully incorporated into the lattice of Au nanoparticles to enable the particles with PET imaging capabilities. Specifically, Liu and co-workers synthesized CuAu alloyed nanoparticles of 9.4 ± 1.2 nm in diameter by directly reducing copper(II) acetylacetonate ($\text{Cu}(\text{acac})_2$), $^{64}\text{CuCl}_2$, and HAuCl_4 in the presence of oleylamine.⁵⁷⁴ The same group also reported the synthesis of much smaller CuAu nanoparticles with an average diameter of 2.5 ± 0.8 nm.⁵⁷⁵ Compared to their larger counterparts, when coated with PEG (MW ≈ 350 Da) the small particles showed superior clearance properties, with 36.2% and 40.8% of the injected dose cleared from feces and urine, respectively, 48 h postinjection. This demonstration

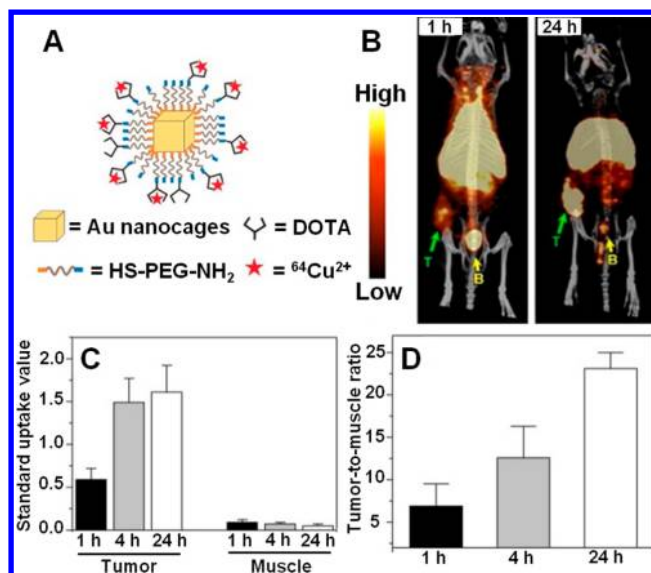


Figure 38. (A) Schematic illustration of Au nanocages (AuNCs) labeled with ^{64}Cu through a technique based on DOTA. (B) PET/CT images showing the tumor targeting ability of the 30 nm ^{64}Cu -DOTA-PEG-AuNCs in a mouse model bearing an EMT-6 tumor at 1 and 24 h post intravenous injection (100 μCi per mouse). “T” and “B” indicate tumor and bladder, respectively. (C) Standardized uptake values (SUV) measured at different time points in both tumor and muscle regions obtained from PET/CT images. (D) Tumor-to-muscle SUV ratios corresponding to the data shown in panel (C). Reprinted from ref 545. Copyright 2012 American Chemical Society.

helps address the clearance issue faced by many nanomaterials, demonstrating that smaller particles are better suited for in vivo application. However, the involvement of radioactive $^{64}\text{CuCl}_2$ makes it difficult to synthesize Au nanostructures with other shapes. An alternative approach is to add the radioactive ^{64}Cu by deposition after the Au nanostructures have been synthesized.^{573,576} As demonstrated by Chen and co-workers, ^{64}Cu could be deposited on the surface of various types of PEG-stabilized Au nanostructures to enable their use for PET imaging (Figure 39). In a typical synthesis, a trace amount of ^{64}Cu was introduced into a suspension of PEG-stabilized Au nanostructures and reduced by hydrazine in the presence of poly(acrylic acid). To compare with a conventional labeling technique based on DOTA, both ^{64}Cu -coated and ^{64}Cu -chelated Au nanoparticles with a diameter of 80 nm were introduced into a mouse model and the signals from bladder and urine were evaluated. As shown in Figure 39A, negligible signals were detected in both bladder and urine for the mice injected with ^{64}Cu -coated Au nanoparticles, whereas a significant signal was detected for their counterparts using the conventional chelating technique. These results confirm the possible release of $^{64}\text{Cu}^{2+}$ ions or ^{64}Cu -chelated polymer chains from the nanoparticles labeled using the chelating method. The authors then demonstrated the capability to modify the surface of Au nanorods (8.0 nm \times 25.1 nm) and coat them with ^{64}Cu for tumor targeting and imaging-guided photothermal therapy (Figure 39B).

A major limitation of PET imaging is its low resolution (>1 mm) as compared to optical imaging modalities. This limitation can be largely attributed to the current instrument design, as well as the underlying physics. PET can be complemented through a combination of techniques with X-ray CT or MRI.^{549,566}

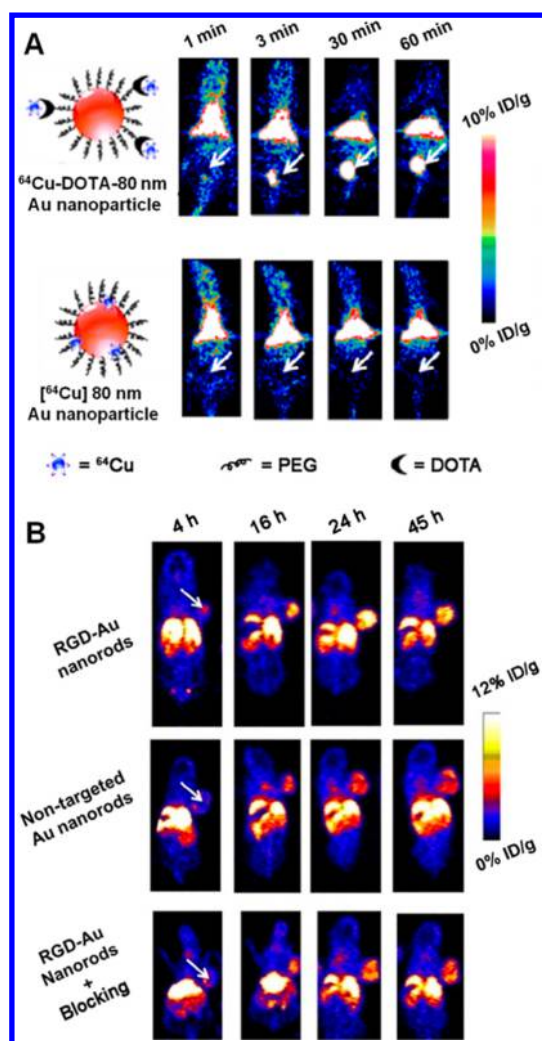


Figure 39. (A) Whole-body coronal PET images of ^{64}Cu -DOTA-80 nm Au nanoparticles (upper) and ^{64}Cu -coated 80 nm Au nanoparticles (lower) in mouse model at 1, 3, 30, and 60 min after intravenous injection (150 μCi per mouse, $n = 3$ per group; arrow, bladder area). (B) Whole-body coronal PET images of RGD- ^{64}Cu coated Au nanorods (upper), nontargeting ^{64}Cu -coated Au nanorods (middle), and RGD- ^{64}Cu -coated Au nanorods + blocking (lower) in a U87MG tumor-bearing mouse model at 4, 16, 24, and 45 h post intravenous injection (150 μCi per mouse, $n = 3$ per group; arrow, tumor area). Reprinted from ref 573. Copyright 2014 American Chemical Society.

4.3.3. Cerenkov Luminescence Imaging. Cerenkov luminescence refers to the optical radiation emitted by charged elementary particles traveling at a speed greater than the phase velocity of light in a dielectric medium.⁵⁷⁷ Although this phenomenon was predicted and validated by physicists more than one century ago, it only started to find use in biomedical imaging in recent years. Most of the β emitters, including the PET isotopes, commonly used in clinics or biomedical research meet the requirement for emitting Cerenkov luminescence due to the generation of electrons or positrons with a high kinetic energy through β -decay.⁵⁷⁷ Since the wavelengths of the luminescence are typically located in the visible spectrum, one can conveniently monitor and analyze the accumulation and biodistribution of radionuclides by optical means. As such, the equipment for Cerenkov luminescence imaging is generally more accessible than a PET scanner, enabling a broader range of applications.

For Au nanostructures, they can be endowed with Cerenkov luminescence capabilities through the introduction of a radioactive isotope such as ^{198}Au . This isotope shares the same chemical properties as nonradioactive ^{197}Au , with no impact on the synthesis and properties of the Au nanostructures. In 2006, Kannan and co-workers reported the first synthesis of ^{198}Au -doped nanostructures stabilized by starch or gum arabic using an aqueous system.⁵⁷⁸ The synthetic method was straightforward, and only a small portion of the nonradioactive precursor ($\text{H}^{197}\text{AuCl}_4$) needed to be substituted with the radioactive compound ($\text{H}^{198}\text{AuCl}_4$). Zheng and co-workers later synthesized Au nanoparticles (2.6 ± 0.3 nm in size) capable of emitting NIR light and thus suitable for SPECT imaging by reducing a mixture of $\text{H}^{197}\text{AuCl}_4$ and $\text{H}^{198}\text{AuCl}_4$ with GSH.⁵⁷⁹

In 2013, our group demonstrated the use of Cerenkov luminescence imaging for studying both the biodistribution and tumor targeting efficacy of PEGylated Au nanocages.⁵⁴⁶ The isotope ^{198}Au was introduced into the crystal lattice of Au nanocages by mixing $\text{H}^{198}\text{AuCl}_4$ with $\text{H}^{197}\text{AuCl}_4$ at a well-controlled ratio before they were used for a galvanic replacement reaction with Ag nanocubes (Figure 40A). The ^{198}Au -doped Au nanocages showed the same morphology as traditional Au nanocages, shown by the TEM image in Figure 40B. The radioactive nanocages showed good chemical stability, with no dissociation of ^{198}Au from the particles. For Au nanocages with an edge length of 33 nm, the in vivo biodistribution showed an apparent passive tumor targeting effect, with $15.3 \pm 2.9\%$ of the injected dose (ID) accumulating in the tumor 24 h postinjection, as measured by a gamma counter. As shown in Figure 40C, the accumulation of Au nanocages in tumors and other major organs can be readily visualized and quantified using Cerenkov luminescence imaging. In a follow-up study, the capability of this approach was further extended to prepare radioactive, ^{198}Au -doped Au nanostructures with other shapes (e.g., spheres, disks, and rods) for a systematic comparison of the biodistribution and tumor targeting efficacy (Figure 40D).¹⁵¹ It was found that the Au nanospheres possessed significantly improved circulation compared to other shapes, with 24.8% and 10.4% ID/g remaining in circulation at 6 and 24 h postinjection, respectively. As expected, all of the four types of Au nanostructures showed significant clearance by the major mononuclear phagocyte system (MPS) organs, with 34.9–63.4% ID/g accumulating in the liver at 24 h postinjection. The accumulation in the spleen was much lower for Au nanospheres (5% ID/g at 24 h postinjection) than the other three samples (>40% ID/g at 24 h postinjection). In the same study, the effect of shape on the intratumoral distribution of the Au nanostructures was also investigated. From the autoradiography images of tumor sections, the nanospheres and nanodisks were found to have a heterogeneous distribution in the tumor, in contrast with the homogeneous distribution for nanocages and nanorods.

A potential limitation to this labeling method is that ^{198}Au is not a widely accessible radionuclide and its production needs special facilities. An alternative approach was explored to substitute ^{198}Au with ^{64}Cu , which is a more accessible radionuclide. In a study reported by Chen and co-workers, ^{64}Cu -doped Au nanoparticles were investigated for their Cerenkov luminescence imaging capability.⁵⁷⁶ A strong emission peak in the region of 695–770 nm was observed in addition to the emission peaks in the blue and UV regions,

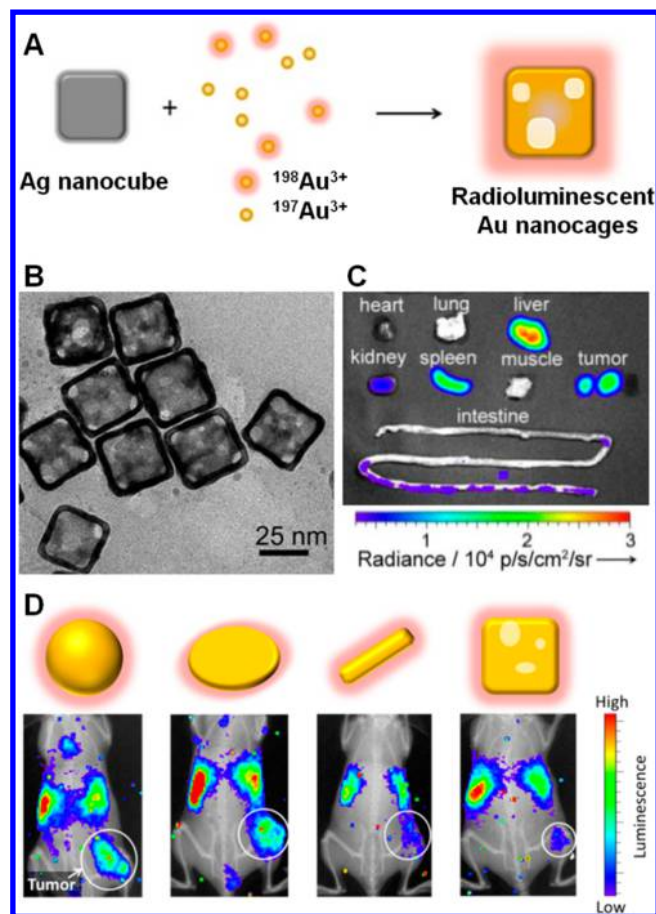


Figure 40. (A) Schematic illustration showing the synthesis of radioactive Au nanocages by directly incorporating ^{198}Au into the crystal lattice. (B) TEM image of ^{198}Au -doped Au nanocages, which was taken after the ^{198}Au -labeled sample was set to decay for 1 month. (C) Cerenkov luminescence image showing the distribution of 33 nm PEGylated ^{198}Au -doped Au nanocages in major organs of a mouse at 48 h post intravenous administration. (D) Cerenkov luminescence images for comparing the biodistributions and tumor targeting properties of ^{198}Au -doped Au nanostructures with different shapes in mice bearing EMT-6 tumor at 24 h postinjection. (A–C) Reprinted from ref 546. Copyright 2013 American Chemical Society. (D) Reprinted from ref 151. Copyright 2014 American Chemical Society.

which are intrinsic to the Cerenkov luminescence of ^{64}Cu . The difference from ^{198}Au can be explained through the Cerenkov resonance energy transfer (CRET) effect, which retains part of the energy from Cerenkov radiation and converts it to photoluminescence at a longer wavelength. The PET signal was observed to have a linear correlation with the total luminescence signal and NIR signal from CRET, supporting the argument based on CRET.

Apart from the use of different types of scanners, Cerenkov luminescence and PET imaging share the same limitations imposed by the need for radioactive isotopes that require specialized production facilities. In addition, Cerenkov luminescence imaging is limited by poor tissue penetration as most of the emitted light falls into the UV and visible regions and is thus strongly scattered and attenuated by surrounding tissue.⁵⁷⁷

4.4. Drug Delivery

As discussed in section 2, Au nanostructures with different sizes and shapes can be readily synthesized using a variety of

methods. Through surface modification, these nanostructures can be rendered hydrophilic or hydrophobic, as well as positively or negatively charged. Due to their ease of preparation and surface modification, bioinert property, and photothermal capability, Au nanostructures are emerging as a new class of platform materials for drug delivery and related applications. As opposed to nanoparticles made of biodegradable polymers, the photothermal conversion inherent to Au nanostructures can be triggered to control the release of the drugs.

Like other systems, two major steps are involved in the application of Au nanostructures to drug delivery: drug loading and controlled release. The first step is to load the drug molecules either onto the surface or into the interior of Au nanostructures.

4.4.1. Drug Loading. A variety of methods have been developed for loading different types of drugs onto the surface of Au nanostructures, including direct conjugation via the Au–S or Au–N linkage,⁵⁸⁰ grafting to the capping ligand,⁵⁸¹ and adsorption by means of electrostatic interactions,⁵⁸² van der Waals forces,⁵⁸³ and hydrogen bonding.⁵⁸⁴ Figure 41A shows a brief summary of these methods. Most of these methods can also be used to functionalize the surface of Au nanostructures (see section 2.9). Due to the strong affinity between Au and S or N,⁵⁵ the most direct way to load a drug onto the surface of Au nanostructures is to incorporate the –SH or –NH₂ group into a drug molecule. To this end, a highly efficient vector was developed with PEGylated Au nanoparticles for the delivery of silicon phthalocyanine (Pc),^{580,585} which is a hydrophobic drug currently under clinical evaluation for photodynamic therapy (PDT). The use of PEGylated Au nanoparticles can dramatically improve the delivery efficacy of the drug. With the aid of Au nanoparticles, it was demonstrated by Burda and co-workers that the time for maximum drug accumulation in the target tumor could be shortened from 2 days to less than 2 h relative to free silicon phthalocyanine 4 (Pc 4).⁵⁸⁰ The same group also investigated the effect of the linker between the drug and the surface of Au nanoparticles on the drug delivery efficiency and PDT efficacy. Different from that of amido-bound silicon phthalocyanine, it was found that the thiol-bound silicon phthalocyanine was barely released from the Au nanoparticles over a course of 24 h due to a stronger interaction between Au and S.⁵⁸⁶ In general, the labile Au–N bond allows for more efficient drug release into the cancer cells for improved PDT when compared with the system involving the Au–S bond. This observation highlights the importance of paying close attention to the linker between drug molecules and the surface of Au nanoparticles.

Drugs can also be loaded onto the surfaces of Au nanoparticles by directly grafting the drugs to the capping ligands. Based on an esterification reaction, the chemotherapeutic drug paclitaxel was attached to 4-mercapto-phenol using a flexible hexaethylene glycol as the linker. Through Au–S linkage, the drug was further attached to the surface of Au nanoparticles. Thermogravimetric analysis revealed that the molar ratio of drug molecules to Au nanoparticles was 70.⁵⁸⁷ Mirkin and co-workers also combined DNA-stabilized Au nanoparticles with a Pt(IV) prodrug to obtain a single agent for drug delivery.⁵⁸⁸ Based on the amidation reaction, a prodrug terminated in the carboxyl group was connected to the amido group of DNA strands, which also served as a capping ligand for the Au nanoparticles. The inactive Pt(IV) prodrug could be internalized by cells and reduced to release cisplatin, which then

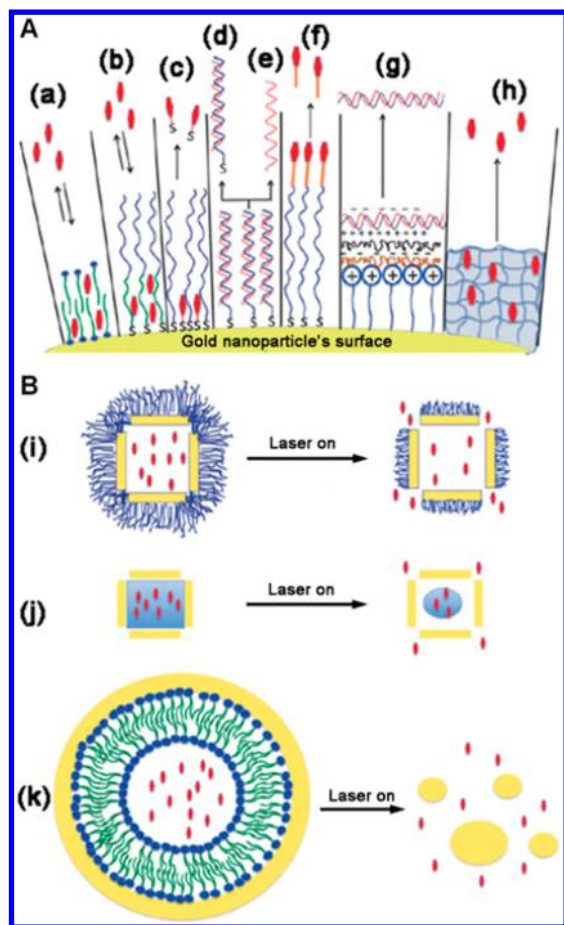


Figure 41. (A) Schematic illustration showing different strategies for releasing drugs from the surfaces of solid Au nanoparticles. Diffusion-driven release in a surfactant bilayer (a) and an amphiphilic layer (b), controlled release based on breakage of Au–S bond (c and d), denaturation of DNA duplex (e), breakage of a cleavable linker by light (f), dissociation of the layer-by-layer structure due to the pH change (g), and conformation change of thermosensitive, cross-linked polymer (h). (B) Two examples of drug release from the interiors of hollow Au nanoparticles: exterior surface of a Au nanocage functionalized with a thermoresponsive polymer brush (i, laser irradiation will induce local heating via photothermal conversion, causing the thermosensitive polymer to collapse and thus release the caged drug molecules); interior of a Au nanocage loaded with a phase-change material containing the drug (j, laser irradiation will melt the phase-change material and thus release the drug). (k) The interior of a liposome is loaded with a drug and then covered with a Au shell; when the Au shell is destructed upon light irradiation due to photothermal effect, the encapsulated drug will be released. Reprinted with permission from ref 16. Copyright 2012 Royal Society of Chemistry.

entered the nucleus and formed 1,2-d(GpG) intrastrand cross-links with DNA. Compared with cisplatin, the Pt(IV) prodrug immobilized on Au nanoparticles was found to be more effective in killing cancer cells.

Electrostatic interaction is another effective means for loading a drug onto the surface of Au nanoparticles. In one demonstration, CTAB-stabilized Au nanorods were utilized as a platform for the delivery of small interfering RNA (siRNA) and single-stranded RNA (ssRNA).^{589,590} Because of the strong electrostatic interaction between CTAB-stabilized Au nanorods (positively charged) and nucleic acid (negatively charged), the nucleic acid molecules could be readily immobilized on the surface of Au nanorods. The resultant system caused gene

silencing with no observed cytotoxicity to the cells as shown by the reduction in expression of some key proteins. In another approach, layer-by-layer (LbL) assembly based on electrostatic interactions between positively and negatively charged species was utilized to add multiple layers of polymers onto the surface of a nanoparticle.^{582,591–594} The LbL method is simple and versatile, and various types of charged molecules can be incorporated. In a typical process, charge-reversed polyelectrolytes such as PEI and poly(allylamine hydrochloride)–citraconic anhydride (PAH–Cit) were used to functionalize Au nanoparticles for the delivery of drugs such as siRNA.⁵⁸² The use of functionalized Au nanoparticles improved the expression efficiency of enhanced green fluorescent protein (EGFP), and showed much lower toxicity toward cell proliferation. Compared to commercial Lipofectamine 2000, the system based on Au nanoparticles also showed better knockdown efficiency.⁵⁸² The functionalized Au nanoparticles could protect siRNA against enzymatic degradation at a vector to RNA mass ratio of 2.5:1 and above. Using this carrier, the uptake of siRNA by HeLa cells could be significantly improved relative to PEI, which is an efficient polycationic transfection reagent. Due to the simplicity and efficiency of the LbL approach, many other polyelectrolytes have also been used for the functionalization of Au nanoparticles for drug delivery.^{592,593}

van der Waals forces are weak interactions, which exist widely between atoms or molecules. Using van der Waals forces, different drug molecules can be readily adsorbed onto the capping ligands on Au nanoparticles. For example, Murphy and co-workers explored the use of CTAB-stabilized Au nanorods as a platform for the delivery of 1-naphthol, which is a model hydrophobic drug.⁵⁹⁵ The bilayer of CTAB provides a ~ 3 nm thick hydrophobic layer that can be used to sequester 1-naphthol from an aqueous solution. The adsorption isotherm of 1-naphthol onto the CTAB bilayer can be fitted to a Langmuir model. The maximum number of adsorbed 1-naphthol molecules was found to be 14.6×10^3 molecules per Au nanorod with an equilibrium binding constant of 1.97×10^4 M⁻¹ at room temperature. Doxorubicin (Dox) has also been loaded onto the surface of Au nanoparticles through the van der Waals forces between Dox and DNA strands attached to Au surface.⁵⁶⁴ The loading efficiency of Dox could reach 615 ± 34 Dox molecules per Au nanoparticle of about 12.7 nm in size.

Hydrogen bonding has also been employed for the loading and delivery of DNA or RNA using oligonucleotide-functionalized Au nanoparticles. To this end, Mirkin and co-workers designed oligonucleotide-modified Au nanoparticles for gene delivery based on the hydrogen bonding between the target mRNA and the complementary DNA strand.⁵⁹⁶ The Au nanoparticles modified with complementary DNA have a larger affinity constant toward the target mRNA than their unmodified oligonucleotide counterparts. As such, the DNA-modified Au nanoparticles are less susceptible to degradation by nuclease activity, exhibiting greater than 99% cellular uptake while showing no cytotoxicity. Furthermore, the same group demonstrated that RNA-modified Au nanoparticles required no help from a transfection agent to enter cells, resulting in an uptake of RNA-modified Au nanoparticles up to 99%.⁵⁸⁴ In the presence of 10% serum, the RNA-modified Au nanoparticles showed a half-life 6 times longer than the free RNA duplexes, indicating that the Au nanoparticles could prevent the RNA from degradation in an extracellular context. Based on hydrogen bonding, different types of DNA and RNA can be

loaded onto the surfaces of Au nanoparticles to enable tunable gene knockdown.

Despite their extensive use for drug delivery, solid Au nanoparticles may face challenges such as low efficiency of loading and poor colloidal stability. Compared with the solid counterparts, Au hollow nanostructures seem to be better suited for drug delivery as the drugs can be loaded in the interiors to increase the loading efficacy and help prevent the drugs from being released prior to use. To this end, Au nanocages are emerging as a new tool for drug delivery applications (Figure 41B).^{597–600} Since Au nanocages are characterized by hollow interiors and porous walls, drug molecules can be readily loaded inside their cavities. To both prevent drug leakage and engineer a controlled release, the surface of the Au nanocages can be further modified with a temperature-sensitive polymer such as poly(*N*-isopropylacrylamide) (pNIPAAm) that changes configuration in response to small variations in temperature.^{597,599} When the temperature is below the low critical solution temperature (LCST), the polymer will be hydrophilic and soluble in water. Thus, the polymer chains will be in an extended conformation to seal the pores of the Au nanocages and thus prevent the leakage of drug molecules. Upon heating to a temperature above LCST, the polymer chains will collapse, opening the pores on the nanocage and allowing the drugs to diffuse out. The heating can be achieved with a pulsed laser or high-intensity focused ultrasound (HIFU) to manage the drug release profile.

Phase-change materials (PCMs) have also started to emerge as a novel system for drug delivery.⁶⁰¹ By combining Au nanocages with a PCM of a melting point around 38–39 °C, our group has demonstrated a versatile system for the delivery of R6G and Dox (Figure 41B).^{598,600} To improve their targeting efficacy, the surface of the Au nanocages was further modified with SV119, a small-molecule ligand capable of specifically binding to the sigma-2 receptor overexpressed on various types of cancer cells.⁶⁰⁰ The SV119-functionalized Au nanocages could selectively target breast cancer stem cells (CSCs), while the non-CSCs showed essentially no uptake of the SV119-modified Au nanocages. In a different study, Gao and co-workers demonstrated that they could load fluorophore molecules into the interior of Au nanoshells.¹⁷¹ The fluorophore molecules were initially loaded into liposomes, which were then derivatized with PLH and further coated with Au nanoshells. As a result, the fluorophore molecules were sealed inside the Au nanoshells. In another work, spherical hollow Au nanoparticles with a diameter of 40 nm were also used as a platform for the delivery of Dox.²¹¹ It was found that Dox molecules could be loaded onto both the outer and inner surfaces of each hollow particle with loading efficacy as high as 63% Dox by weight ($\sim 1.7 \mu\text{g}$ of Dox/ μg of Au).

4.4.2. Controlled Release. Once the Au nanoparticles loaded with a drug have been delivered to the tumor and further into cancer cells, it becomes critical to trigger and manage the release of drug molecules. In early studies, Au nanoparticles simply served as a carrier for the drug molecules. The release of the drugs was achieved using thermally activated desorption and diffusion, without making use of the unique properties associated with Au nanomaterials. To this end, Au nanoparticles functionalized with *N*-diazoniumdiolate were directly used for the delivery and controlled release of NO. It was found that *N*-diazoniumdiolate underwent both thermal and proton-driven dissociation to achieve the release of NO. The loading capacity and release profile could be tuned by

using *N*-diazoniumdiolates synthesized with different amines.^{602,603} In other studies, amphiphilic molecules were commonly used for the functionalization of Au nanoparticles to generate hydrophobic pockets on the particle surface for the loading of hydrophobic drugs.⁶⁰⁴ It was demonstrated that the hydrophobic drugs could be released into cells through membrane-mediated diffusion without the uptake of the Au-based vehicles. As shown in Figure 42A,C,E, Burda and co-

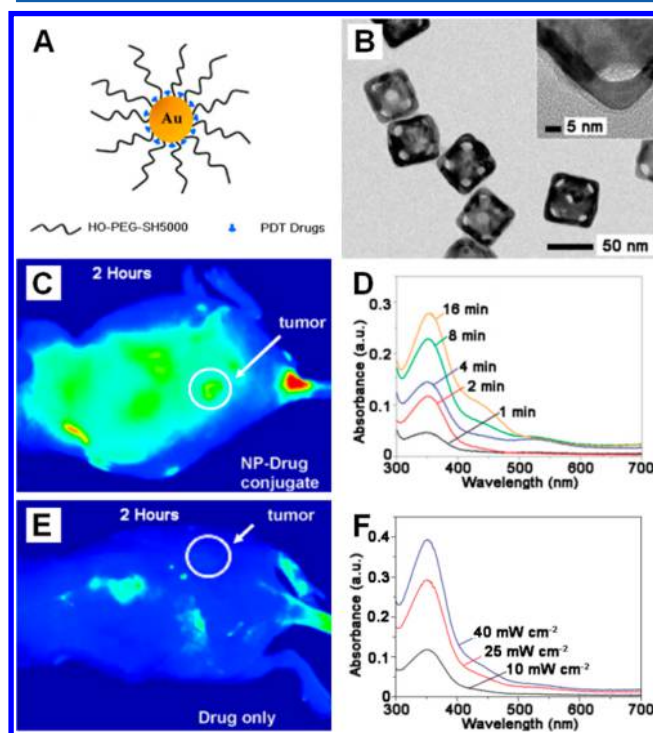


Figure 42. Gold nanostructures used as drug carriers for in vivo (left column) and in vitro (right column) applications. (A) Schematic of a Au nanoparticle used for the conjugation and delivery of a PDT drug. (C) Photoluminescence image of a tumor-bearing mouse after being injected with the Au nanoparticle–Pc 4 conjugates in normal saline (0.9% NaCl, pH 7.2) at 120 min post intravenous tail injection. For comparison, a mouse that only received a Pc 4 formulation without the use of Au nanoparticles is shown in (E). (B) TEM image of Au nanocages whose surfaces were covered by a polymer brush of pNIPAAm-co-pAAm with a low critical solution temperature of 39 °C. (D) Absorption spectra of alizarin–PEG released from copolymer-covered Au nanocages upon exposure to a pulsed NIR laser at a power density of 10 mW cm^{−2} for 1, 2, 4, 8, and 16 min. (F) Absorption spectra of alizarin–PEG released from copolymer-covered Au nanocages upon exposure to a pulsed NIR laser at different power densities of 10, 25, and 40 mW cm^{−2} for 2 min. (A, C, and E) Reprinted from ref 580. Copyright 2008 American Chemical Society. (B, D, and F) Reprinted with permission from ref 597. Copyright 2009 Nature Publishing Group.

workers applied a drug delivery system based on Au nanoparticles for in vivo applications.⁵⁸⁰ It was found that the release of drug molecules from the surface of Au nanoparticles was a diffusion-driven process. Smart drug delivery systems based on Au nanoparticles have also been developed through the use of photosensitive chemical bonds. The photosensitive chemical bonds can be broken under the irradiation of light, triggering the release of payloads. For example, Au nanoparticles have been reported for photocontrolled release of anticancer drugs such as 5-fluorouracil (5-FU) by conjugating

the drug to the nanoparticle surface through a photoresponsive *o*-nitrobenzyl (ONB) linkage.⁶⁰⁵ The ONB group has long-term stability under exposure to ambient light in biological environments. However, it undergoes photolytic cleavage when exposed to UV light at 365 nm, allowing for controlled release of the anticancer drug.

As discussed in section 3.2, Au nanomaterials are capable of absorbing light and converting it into heat because of their LSPR properties. The released heat can lead to a local temperature rise in the vicinity of the nanostructure, sufficient to even break the linkage between the drug molecule and Au surface. Based on this mechanism, Au nanorods have been used for the controlled release of DNA via the photothermal cleavage of the Au–S bond.⁶⁰⁶ Depending on the laser system used, the Au nanorods might also change their shape or morphology during the drug release process. For example, El-Sayed and co-workers found that the Au nanorods evolved into quasi-spherical nanoparticles when they were irradiated with a femtosecond laser ($\lambda = 1064$ nm, 150 mJ/pulse) for 2 min. In this case, it was suggested that the photoinduced reshaping of Au nanorods and the dissociation of Au–S bond was responsible for the release of the immobilized DNA.⁶⁰⁷ It should be emphasized that the rapid bond dissociation was not the result of a pure heating process. Instead, it was initiated by the photoexcited electrons in the Au nanoparticles, possibly through coupling to the vibration modes of the Au–S bond. In a related study, Li and co-workers reported the *in vivo* delivery of siRNA based on hollow Au nanoparticles.⁶⁰⁸ Upon irradiation with a NIR laser, release of siRNA was achieved in a controllable fashion. They suggested that the NIR-laser-triggered siRNA release was due to the breakage of Au–S bonds as a result of the local temperature elevation. They also found that the hollow Au nanoparticles showed better *in vivo* targeting efficiency after functionalization with folic acid.

Besides the aforementioned drug release mechanism involving Au–S bond breakage, the heat generated through the photothermal conversion of Au nanostructures can also be used for the controlled release of DNA by breaking the hydrogen bonds between two complementary oligonucleotide strands. Stoeger, de la Fuente, and co-workers reported the *in vivo* delivery of siRNA with Au nanoparticles functionalized with complementary DNA strands.⁶⁰⁹ Based on the photothermal effect, the hybridized oligonucleotide strands melted and siRNAs were released by breaking the hydrogen bonds. To improve the tumor targeting efficacy, a RGD peptide was used to modify the surface of Au nanoparticles. It was found that the siRNA delivery system based on RGD-functionalized Au nanoparticles could lead to successful suppression of tumor cell proliferation and reduce the tumor size. Branda and co-workers also investigated the controlled release of DNA from the surface of Au nanoparticles based on the photothermal effect.⁶¹⁰ They reported a rapid release of DNA strands in a solution containing 200 mM NaOAc and 10 mM Mg(OAc)₂ under the irradiation of a 532 nm laser at 100 mW. The morphology of the Au nanoparticles remained the same before and after laser irradiation. According to their study, both the thermal denaturation of double-strand DNA and thermolysis of the Au–S bond contributed to the release, with the former being a major factor. A combination of the two release approaches could compensate for the commonly seen drawbacks of decreased particle stability in thermolysis and slow release rate for thermal denaturation, both of which should be

taken into consideration in designing novel DNA delivery systems based on Au nanostructures.

Temperature-responsive polymers are polymers capable of changing their conformations in response to temperature variations, and can be integrated with Au nanostructures to fabricate smart drug delivery systems by taking advantage of photothermal heating. To this end, our group demonstrated a controlled release system based on Au nanocages (Figure 42B,D,F).^{597–600} In this system, a thermal-responsive polymer, pNIPAAm, was introduced to seal the pores on the surfaces of the nanocages and thus encapsulate the dye molecules loaded into the interiors.^{597,599} When the temperature rises beyond the LCST of pNIPAAm, the polymer undergoes a phase transition from hydrophilic to hydrophobic, accompanied by the collapsing of the polymer chains. As such, the pores on the surfaces of Au nanocages are opened and allow the drugs to diffuse out. Specifically, upon exposure to a pulsed NIR laser at a power density of 10 mW cm^{−2} (Figure 42D,F) or HIFU at a power density of 10 W, the dye molecules inside the Au nanocages were released in a controlled fashion.

We also loaded R6G molecules into Au nanocages using a PCM with a melting point of 38–39 °C.^{598,600} After the suspension of cargo-loaded nanocages was heated to 40 °C or exposed to HIFU, the R6G molecules encapsulated could be released due to the melting of PCM. These studies clearly demonstrate that Au nanostructures can not only act as carriers for the drugs, but also serve as transducers to trigger the release of drugs in a delivery system.^{611,612}

4.4.3. Multidrug Resistance. Multidrug resistance (MDR) is a condition under which cancer cells become insensitive to the chemotherapy.^{613–615} The tumor is usually comprised of mixed populations of malignant cells, some of which are drug-sensitive while others are not (i.e., drug-resistant). Chemotherapy can only kill the drug-sensitive cells, leaving behind an increased proportion of drug-resistant cells. When the tumor begins to grow again, chemotherapy will fail simply because the remaining tumor cells are no longer responsive to the anticancer drugs.

A number of traits have been identified for MDR (Figure 43A), including increased efflux pumping of drugs by the overexpressed ATP-binding cassette (ABC) transporters, reduced intracellular accumulation of drugs by non-ABC drug transporters, blocked apoptosis, repair of drug-induced DNA damage, metabolic modification, and detoxification by drug-metabolizing enzymes.^{613,614,616} Among these, the overexpression of P-glycoprotein, a member of the ABC superfamily, has been recognized as one of the most common causes of MDR.

A general strategy for overcoming MDR is to co-deliver two different types of drugs, with one inhibiting the ABC transporters and the other for actual killing of cancer cells. As a result, it is necessary to develop a platform for the delivery of multiple drugs. The drug delivery system based on LbL assembly has been proven to be an effective approach to multidrug delivery.^{617,618} The colloidal stability of such a system increases with the number of adsorbed layers, with the surface and biological properties determined by the outmost layer over the Au nanoparticles.⁶¹⁹ Hexadecyltrimethylammonium bromide, a commonly used surfactant in the synthesis of Au nanorods, can serve as an MDR inhibitor.⁶²⁰ For this reason, CTAB-stabilized Au nanorods have shown great potential as a multidrug delivery system for overcoming MDR.

Nucleus targeting is another effective strategy for overcoming MDR. If Au nanoparticles can be functionalized to enable

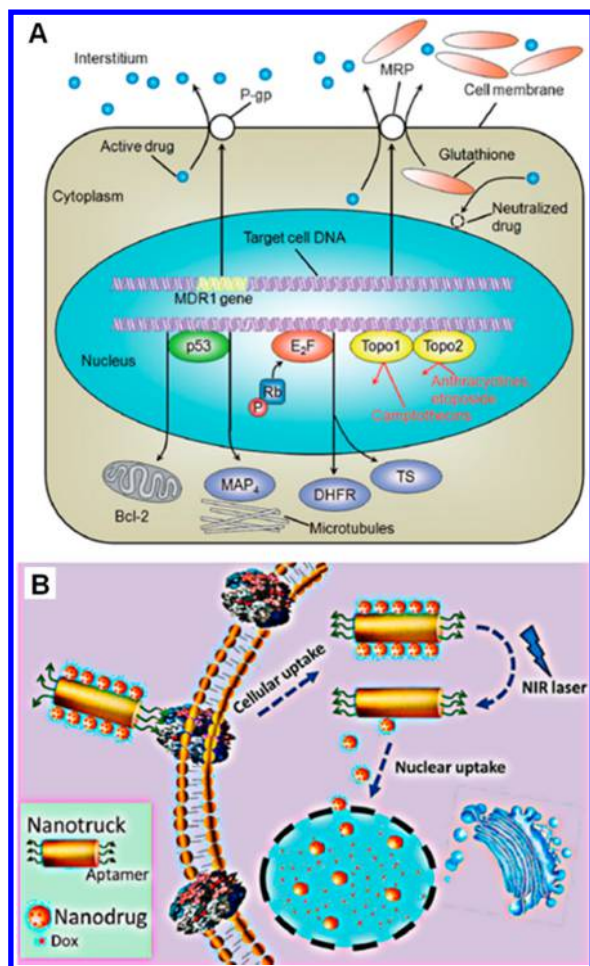


Figure 43. (A) Mechanisms of multidrug resistance (MDR) in cancer cells: drug efflux caused by multidrug resistance protein (MRP) (e.g., P-glycoprotein or P-gp), down-regulation of the sensitivity to drug by the tumor suppressor protein p53, reduction in sensitivity to methotrexate and fluorouracil by phosphorylation of the retinoblastoma protein (Rb), and production of resistance to camptothecins through down-regulation expression or mutations in topoisomerases (Topo). (B) Schematic illustration of a cell-targeted, photocontrolled nuclear-uptake nanodrug delivery system for cancer therapy. (A) Reprinted with permission from ref 613. Copyright 2014 Wiley-VCH. (B) Reprinted from ref 621. Copyright 2015 American Chemical Society.

intracellular release of anticancer drugs, they can be used to address the MDR issue by completely bypassing P-glycoprotein. Figure 43B demonstrates a report by Tan and co-workers, in which drug-loaded Au nanoparticles were assembled on the side faces of Au nanorods through DNA hybridization.⁶²¹ When functionalized with a cell-type-specific internalizing aptamer, the Au nanorods efficiently accumulated around the nucleus. Upon irradiation with a NIR laser, the drug-loaded Au nanoparticles would be released due to photothermal heating and uptake by the nucleus, inside which Dox molecules would be further released to effectively kill the cancer cell.

4.5. Cancer Therapy

In addition to their use as carriers or vectors for the delivery of drugs or genetic materials for effective treatment, Au nanostructures themselves can be directly used as cancer therapeutic agents. To this end, the therapeutic effects of Au

nanostructures can be divided into three major categories: (i) denaturing of proteins through hyperthermia induced by photothermal heating with the use of a CW laser, (ii) disruption of cell membranes through cavitation induced by an ultrafast laser, and (iii) apoptosis and necrosis caused by the reactive oxygen species (ROS) produced under light or X-ray irradiation. The first two mechanisms are responsible for PTT, whereas the third one leads to PDT and radiotherapy.

4.5.1. Photothermal Therapy. PTT relies on the use of hyperthermia to kill tumor cells. Hyperthermia is a condition under which cells are subject to a temperature in the range of 41–47 °C for tens of minutes. Such a condition will cause irreversible damage to the cells due to denaturing of proteins and/or destruction of cell membranes.⁶²² A variety of heating methods, including those based on lasers,^{623,624} microwaves,^{625,626} and ultrasound,⁶²⁷ have been applied to achieve PTT. Compared to healthy cells, tumor cells are more prone to destruction at an elevated temperature due to their poor blood supply. A critical issue that hampers the clinical application of PTT lies in nonspecific heating, which will destroy malignant tissues as well as healthy ones. Nanomaterials can be used to address this issue. Specifically, Au nanostructures can absorb electromagnetic energy and convert it into heat through the photothermal effect, making them suitable agents for PTT.^{231,628} With their ability to accumulate at the tumor site through passive targeting⁶²⁹ and/or active targeting enabled by ligands,¹⁶ Au nanostructures have much higher tumor specificity for PTT compared to the traditional heating methods. The accumulation of Au nanostructures at the desired site will lead to selective heating of target cells upon laser irradiation, minimizing potential damage to the surrounding, healthy tissue during a treatment.

Compared to organic dyes, which have also been explored as photothermal agents for PTT,^{630,631} Au nanostructures offer a number of distinctive advantages: (i) higher stability against photobleaching, (ii) better targeting capability due to their nanoscale sizes, and (iii) much greater absorption cross sections and thus higher photothermal conversion efficiency.^{632,633} In addition, Au nanostructures can serve as contrast agents for various imaging techniques, making it possible to achieve imaging-guided therapy. The high photothermal conversion efficiency of Au nanostructures minimizes the required particle dosage for PTT. This makes Au a more attractive choice as a hyperthermia-inducing agent over magnetic nanomaterials, which are also known to induce hyperthermia under an alternating magnetic field, but require a relatively high dose for effective treatment (10–100 mg/mm³ tumor).⁶³⁴ It is worth emphasizing that Au nanostructures with strong absorption in the NIR region (including nanorods, nanoshells, nanocages, and nanostars) are particularly well-suited for PTT, owing to the penetration depth of lasers at such wavelengths.

Halas and West reported the use of Au nanoshells for PTT in 2003, in which PEGylated Au nanoshells (10 nm thick) on SiO₂ spheres (110 nm in diameter) were used as photothermal agents for both in vitro and in vivo ablation of tumor tissues.⁶³³ After PTT treatment using nanoshells, tumor-bearing mice appeared healthy and tumor free for more than 90 days, while the control animals only showed a survival time of 6–19 days.⁶³⁵ The PEG coating on the surface of Au nanomaterials could help to extend their blood circulation time in vivo, leading to their better accumulation at the tumor site. Bhatia and co-workers reported a long blood circulation time of 17 h after intravenous injection for PEGylated Au nanorods, and a

tumor accumulation of 7% ID/g was observed 72 h postinjection.⁶³⁶ Tumor-bearing mice showed a prolonged survival time from 33 to 50 days after PTT treatment using these Au nanorods. Similarly, our group reported a tumor uptake value of 5.7% ID/g for PEGylated Au nanocages at 96 h post intravenous injection.⁶³⁷ Upon irradiating with a CW laser ($\lambda = 808$ nm, at a power density of 0.7 W/cm^2) for 10 min, the tumors with Au nanocages showed a rapid rise in temperature to over 50°C , indicating an effective photothermal ablation of the tumors (Figure 44). Enhancement in treatment selectivity could be realized through the introduction of active targeting by functionalizing the surface of Au nanomaterials with targeting moieties (e.g., small molecule, antibody, and peptide).^{638–643} To this end, West and Halas demonstrated the selective photothermal ablation of SKBR3 breast cancer cells using anti-HER2-conjugated Au nanorods in 2005.⁶³⁸ In a related report, Li and co-workers demonstrated the effective photothermal ablation of melanoma tumors using hollow Au nanospheres conjugated with melanocyte-simulating hormone (MSH).⁶⁴⁰

To help the clearance of Au nanomaterials after PTT, aggregates of small Au nanoparticles were explored as novel photothermal agents. For example, Nie and co-workers reported the use of amphiphilic plasmonic micelle-like nanoparticles (APMNs), comprised of Au nanoparticles and amphiphilic block copolymers, as a NIR-absorbing photothermal agent for PTT.⁶⁴⁴ The controlled assembly of Au nanoparticles was accompanied by a red shift of the LSPR peak to the NIR region because of the plasmonic coupling between discrete Au particles, facilitating the photothermal ablation of tumor tissues. After PTT treatment, APMNs could readily dissociate into individual nanoparticles, facilitating the clearance process.

The aforementioned PTT studies all relied on a CW laser, which provides a steady rise in temperature upon irradiation, leading to local hyperthermia. On the other hand, when pulse laser irradiation is used for PTT with Au nanomaterials, a second cell killing mechanism comes into play alongside the normal hyperthermia. Under pulse laser irradiation, a high photon density is present, and the repetitive absorption of photons by Au nanomaterials can exceed the rate of heat dissipation, leading to an extremely rapid rise in local temperature (i.e., superheating). Under such conditions, a phenomenon termed cavitation effect could take place.^{504,645,646} The cavitation in cells was shown to cause the perforation of plasma membranes, leading to an influx of extracellular Ca^{2+} , and finally causing cell death. Wei, Cheng, and co-workers reported that folate-conjugated Au nanorods targeted to cancer cell surfaces were able to produce severe cell membrane damage upon pulse laser irradiation at 765 nm.⁶⁴⁷ They observed that photoinduced damage to the cell plasma membrane resulted in a rapid increase in intracellular Ca^{2+} concentration, followed by the degradation of the actin network and the production of severe membrane blebs. Interestingly, this enhanced cell killing performance is only observed for Au nanorods attached to the cell surface, and not for the internalized nanorods. In principle, Au nanomaterials targeted to other cell-surface biomarkers are expected to produce similar membrane-compromising effects, offering a new route for the design of novel Au-based PTT agents for cancer therapy.

In spite of the progress made in research on using Au nanomaterials as photothermal agents for PTT, there still remain some complications that have to be resolved before this noninvasive therapeutic method can find clinical application.

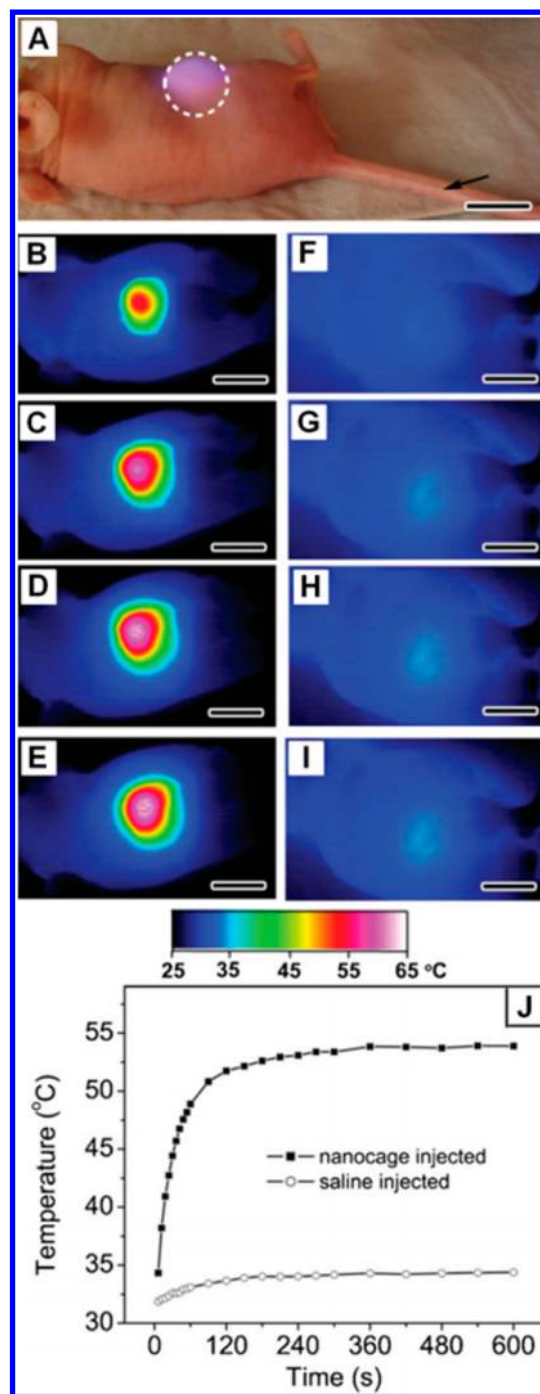


Figure 44. (A) Photograph of a tumor-bearing mouse under photothermal treatment. Typically, $100 \mu\text{L}$ of PEGylated Au nanocages with a concentration of 9×10^{12} particles/mL or saline was injected intravenously through the tail vein as indicated by an arrow. At 72 h postinjection, the tumor on the right flank was irradiated by an 808 nm laser at a power density of 0.7 W cm^{-2} with a beam size indicated by the dashed circle. Thermographic images of (B–E) nanocage-injected and (F–I) saline-injected mice at different time points: (B, F) 1, (C, G) 3, (D, H) 5, and (E, I) 10 min. (J) Plots of average temperature within the tumor regions as a function of laser irradiation time. All the scale bars are 1 cm. Reprinted with permission from ref ⁶³⁷. Copyright 2010 Wiley-VCH.

First, the laser power used in most cases (typically in the range of W/cm^2 scale) for Au nanostructure-mediated PTT are far exceed the skin tolerance threshold of $\sim 0.33 \text{ W/cm}^2$ at 808 nm

set by the American National Standards Institute (ANSI).⁶⁴⁸ As a result, efforts should be put on increasing the efficiency of energy conversion during PTT and thus reducing the laser dose required for effective treatment. Second, although the penetration depth of PTT has been greatly improved through the use of NIR lasers, it still needs to be further refined in order to reach deep-buried tumors. This issue renders PTT less attractive than magnetic hyperthermia, for which there is no limitation on the penetration depth from the alternating magnetic field.⁶⁴⁹ Third, the cell killing mechanism of PTT with Au nanomaterials needs to be systematically investigated. Finally, the high cost of Au may remain a major limitation to the real-world applications of these nanomaterials.

4.5.2. Photodynamic Therapy. Photodynamic therapy (PDT) damages or kills cells through the use of singlet oxygen ($^1\text{O}_2$) generated photochemically. Upon light irradiation at some specific wavelengths, a light-sensitizing agent (or photosensitizer) can convert endogenous O_2 to $^1\text{O}_2$ to induce cell apoptosis and necrosis.⁶⁵⁰ Similar to PTT, PDT can provide a localized treatment, meaning that the cell killing is limited to the region where photosensitizers are located, with limited damage to the surrounding tissue. As a result, PDT offers better selectivity and thus fewer side effects compared to conventional chemotherapy. One major issue with PDT is the poor hydrophilicity of commonly used photosensitizers (e.g., phthalocyanines and porphyrins), which makes it challenging to deliver them to the target site for treatment.⁶⁵⁰ A transport carrier is required to increase the water solubility of the photosensitizers for more effective PDT. Gold nanomaterials have therefore received attention as carriers for PDT photosensitizers. In an early study, Russell and co-workers demonstrated the use of Pc-conjugated Au nanoparticles as photosensitizers for PDT.⁶⁵¹ The Pc-conjugated Au nanoparticles showed improved solubility in polar solvents, and the quantum yield of $^1\text{O}_2$ was reported to increase by 50%. The in vitro and in vivo PDT performances of these Pc-conjugated Au nanoparticles were investigated in their later studies.^{652,653} Importantly, the Pc-conjugated Au nanoparticles showed better selectivity for tumor targeting, with a higher ratio of Pc accumulated in tumor to skin (5.5), compared to that of free Pc molecules (2.3). Tumor growth was significantly retarded after PDT treatment with the Pc-conjugated Au nanoparticles, and the mechanism of photodamage to the tumor cells during PDT was found to be through the destruction of vasculature by $^1\text{O}_2$.

Instead of acting as delivery vehicles for organic photosensitizers, Au nanomaterials themselves were recently shown to sensitize the production of singlet oxygen through irradiation with light.^{654–656} Upon excitation of Au nanomaterials by light, an energy transfer from the electrons at excited states to molecular oxygen could take place, leading to the generation of ROS. Compared to the organic PDT photosensitizers that require UV or visible light for activation, photosensitizers based on Au nanomaterials could be activated with NIR light, leading to greater penetration depth for the treatment. In addition, Au nanomaterials are much more stable than organic dyes, which tend to undergo self-destruction upon irradiation with light. Importantly, the elimination of organic photosensitizers in Au-sensitized PDT can potentially reduce undesired side effects during a treatment. In a recent study, Hwang and co-workers demonstrated the destruction of melanoma in mice through PDT using Au nanorods as photosensitizers.⁶⁵⁷ The PDT effect enabled by Au nanorods was confirmed in vitro by the generation of a high level of ROS. Upon irradiation by NIR

light at 915 nm ($130 \text{ mW}/\text{cm}^2$), the tumors were completely destroyed and the tumor growth rate was dramatically slowed post treatment. It was also reported that the activation of PTT or PDT could be selectively controlled by tuning the NIR excitation wavelengths. Other types of Au nanomaterials, including conventional nanoparticles,⁶⁵⁵ nanoshells,⁶⁵⁸ nanocages,⁶⁵⁹ and nanoechinus,⁶⁶⁰ have all been reported as photosensitizers for PDT.

4.5.3. X-ray Radiotherapy. Radiotherapy is based on the use of high-energy radiation to damage or kill cancer cells, thus slowing down or even prohibiting the growth of a tumor.⁶⁶¹ The radiation commonly used for this purpose include X-rays, γ rays, electron beams, and protons, with X-ray radiotherapy being the most intensively studied. X-ray radiotherapy damages or kills cancer cells by generating photoelectrons and Auger electrons, which then cause the ionization of water and formation of reactive free radicals. Through the extraction of hydrogen atoms from ribose sugars, the free radicals can cleave polynucleotide backbones and thus damage the DNA in mitochondria and nuclei.^{662,663} Similar to PTT and PDT, X-ray radiotherapy is a method for localized treatment that only affects the area under irradiation. The X-ray used for radiotherapy, however, provides much deeper penetration than the NIR light used to trigger PTT and PDT.

The main challenge with X-ray radiotherapy is the lack of selectivity, meaning that both cancerous and normal cells in the path of X-rays will be killed indiscriminately. To address this issue, radiosensitizers made of heavy elements with high atomic numbers can be used to absorb and thus concentrate the X-rays in the area where the radiosensitizers are located. To this end, various types of radiosensitizers have been developed.⁶⁶⁴ Owing to their high density, large energy absorption coefficient, and low toxicity, Au nanomaterials have been demonstrated as radiosensitizers for X-ray radiotherapy.^{555,665–668} The dose of X-rays deposited at the tumor site can be further enhanced through passive and/or active targeting. As such, the differentiation between cancerous and healthy tissue is made possible, allowing for better dose localization at the tumor site. Hainfeld and co-workers demonstrated the enhancement of X-ray radiotherapy with 1.9 nm Au clusters.⁵⁵⁵ A high dose of Au clusters (2.7 g of Au/kg of mice body weight) was intravenously injected into tumor-bearing mice prior to therapeutic treatment. The experimental results clearly indicate that the mice treated with Au nanoparticles and X-ray irradiation showed a prolonged survival time compared to those treated with only X-rays or Au nanoparticles alone. After treatment, the small Au nanoparticles could be readily cleared through the kidney, minimizing the potential side effects due to Au accumulation inside the body. Similar results were reported by Chien and co-workers, who examined the use of 20 nm Au nanoparticles as radiosensitizers for X-ray radiotherapy.⁶⁶⁶

Since X-ray radiotherapy damages and kills a cell by targeting the DNA, the internalization of radiosensitizers can have a profound impact on the overall therapeutic performance. For Au-based radiosensitizers, modifying the surfaces with a cell-targeting ligand can greatly improve the cellular uptake and thereby the treatment efficiency. To this end, Xing and co-workers modified the surface of 10.8 nm Au nanoparticles with thioglucose (Glu) to substantially increase their uptake by a breast-cancer cell line (MCF-7).⁶⁶⁹ A benign breast-cancer cell line (MCF-10A) was used as a control in their study. When irradiated with 200 kVp X-ray, the killing of MCF-7 cells in the presence of Glu-conjugated Au nanoparticles was enhanced

relative to the MCF-10A cells. This observation indicates that the Glu–Au nanoparticles only entered the malignant cancer cells and enhanced their radiation sensitivity, rather than the benign cells, which can be potentially used to achieve targeted cancer treatment.

In addition to X-ray radiotherapy, microparticles of radioactive Au can also be embedded in solid tumors, radiating away and killing cancer cells in a method known as brachytherapy, which has been around for several decades. Readers interested in brachytherapy can find more detailed discussions from the review on this topic.⁶⁷⁰

4.5.4. Combined Therapy. Treatment of cancer using a single type of therapy often does not provide satisfactory outcomes. As a result, combined therapy, which involves two or more types of therapies simultaneously, has been explored in recent years to improve the therapeutic efficacy. Among them, a combination of PTT with chemotherapy has been intensively studied,^{211,570,576,671–682} primarily due to the fact that the heat released during PTT can also be directly used to control the release of drug molecules. In addition, hyperthermia can compensate for the reduced therapeutic effect due to the development of drug resistance, which is a commonly encountered issue in conventional chemotherapy.

As discussed in section 4.2.4, upon electromagnetic irradiation, Au nanomaterials are able to absorb and then convert the optical energy into heat. By taking advantage of the rise in temperature during a photothermal process, remotely controlled drug release can be achieved. Furthermore, it was established that the cell membrane permeability could be greatly enhanced when the environmental temperature was increased from 37 to 43 °C, thereby facilitating the cellular uptake of nanoparticles.^{683–685} As a result, the hyperthermia condition produced by optical irradiation of Au nanomaterials can enhance the delivery of drugs during a therapeutic process.

Dox is a DNA intercalating agent and topoisomerase II inhibitor, and a commonly used anticancer drug. Li and co-workers fabricated Dox-loaded hollow Au nanospheres (Dox–AuHSs) and tested them for the destruction of MDA-MB-231 melanoma cells.²¹¹ The loading capacity of Dox was estimated to be around 63% (or 1.7 μg of Dox/ μg of Au) due to the binding of Dox to both the inner and outer surfaces of AuHSs. Upon irradiation with NIR light, the Dox–AuHSs were able to provide enhanced cell killing performance (with 86.4% of cells being killed) compared to free Dox (77.4%) or the irradiation of drug-free AuHSs (40.6%). The enhancement in cell killing was attributed to a combination of both photothermal ablation and the cytotoxicity of the released Dox molecules. The tumor ablation performance of the Dox–AuHSs was later evaluated by the same group on a mouse tumor model.^{570,672} The experimental results clearly showed that the combined therapy provided more effective, synergistic tumor suppression than any single type of therapy. It is worth pointing out that a lower dose of Dox was required in the combined therapy, which could minimize the toxic side effects of the drug while maintaining the satisfied treatment result.

The hyperthermia induced by PTT can cause dilation of blood vessels at the tumor site and thus increase oxygenation of the tumor. The increased oxygen level can lead to increased tumor damage in PDT and radiotherapy through the generation of more ROS, justifying the increased efficacy of PDT–PTT and radiation–PTT combined therapy.^{658,686–688} In a recent report, Nie and co-workers fabricated a multifunctional therapeutic platform based on photosensitizer (Ce6)–

loaded plasmonic vesicular assemblies of Au nanoparticles (termed Ce6-loaded Au vesicles) for the combined PTT–PDT treatment of tumor-bearing mice.⁶⁸⁸ The Au vesicles showed strong absorption in the NIR range of 650–800 nm, and a 671 nm CW laser was used to excite the multifunction therapeutic platform. The enhanced therapeutic efficacy of Ce6-loaded Au vesicles, as compared to either PTT or PDT alone or their sum together, was confirmed both in vitro and in vivo, due to the synergistic effect (Figure 45). A triple therapeutic system with the combination of PTT, PDT, and chemotherapy using Au nanomaterials has also been reported.⁶⁸⁹

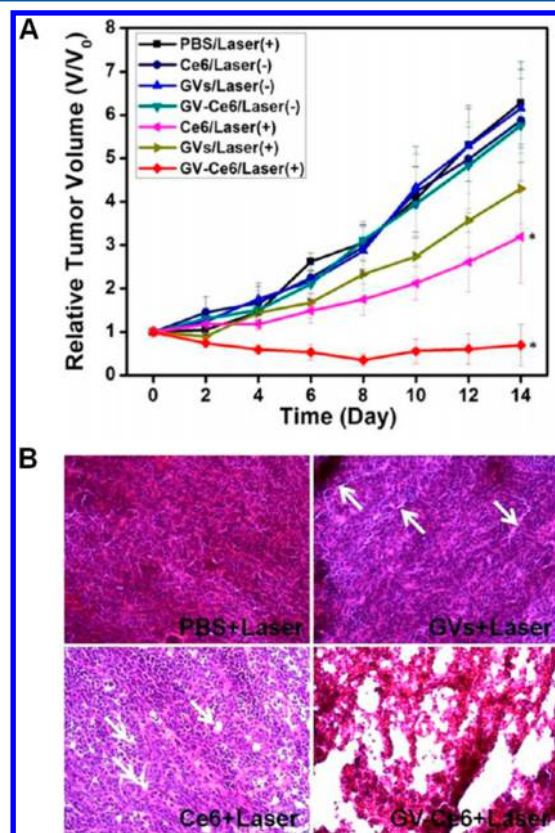


Figure 45. (A) Tumor growth curves of different groups of tumor-bearing mice after photothermal-only treatment (Au vesicles, GVs, with laser irradiation), photodynamic-only treatment (Ce6 with laser irradiation), a combined treatment with both GV–Ce6 and laser irradiation, and no effective treatment (other groups). Tumor volumes were normalized to their initial values. Error bars represent the standard deviations of four to six mice per group. Asterisk indicates $P < 0.05$. (B) Tumor sections with H&E stain collected from different groups of mice 14 days post treatment. Arrows indicate the sporadic necrotic areas. Reprinted from ref 688. Copyright 2013 American Chemical Society.

However, one common barrier that limits the use of combined therapy lies in the biodistribution of Au nanomaterials. At the current stage of development, most of the Au nanomaterials administrated through systematic injection are taken up by RES and only a small portion can navigate to the target site to fulfill their function. In addition, the distribution of Au nanomaterials within a tumor is not homogeneous, which hampers the diffusion of heat and/or ROS throughout the tumor during treatment. A detailed discussion on this issue can be found in section 5.

5. PHARMACOKINETICS, BIODISTRIBUTION, TUMOR TARGETING, AND ISSUES

5.1. In Vitro versus in Vivo Applications

In vitro applications are primarily concerned about the interactions between Au nanostructures and cells, which include the uptake of nanostructures by a cell and their subsequent delivery to various compartments within the cell.⁶¹³ Understanding the in vitro delivery of Au nanostructures is a critical step toward their successful application in vivo. In general, the Au nanostructures used as theranostic agents have to be evaluated in vitro at the cellular level before they are further tested in vivo with tissues, organs, and animals. Only with an adequate understanding of the cellular responses can the properties of Au nanostructures be effectively engineered and optimized for in vivo applications in terms of drug delivery, imaging contrast enhancement, and therapy.

Different from in vitro applications that typically involve one specific type of cell, in vivo applications have to deal with many different types of cell lines involved in the transportation of nanostructures from the site of administration to the target lesion. Upon entering the body, the nanostructures need to reach the target site and be selectively accumulated before any diagnosis or treatment can be conducted. To this end, a number of issues need to be addressed, including the avoidance or suppression of immune responses, and the selectivity and efficiency in terms of targeting, biodistribution, biodegradation, clearance, and toxicity. From the perspective of toxicity, the nanostructures should be constructed from biocompatible and biodegradable materials; they should be selectively accumulated at the diseased site while maintaining low concentrations in healthy tissues or organs; and they should be cleared from the body within a reasonable period of time. For Au-based theranostic agents, it remains challenging to satisfy all of these requirements while using the nanomaterials at a minimum dosage in order to reduce their potential adverse impacts.³⁸

5.2. Pharmacokinetics

Pharmacokinetics is a measure of the proportion of externally administered nanostructures remaining in the circulation system as a function of time postinjection. The goal in studying the pharmacokinetics of Au nanostructures is to optimize their physical properties so they can be preferentially accumulated at the disease site while minimizing their concentrations in healthy tissues or organs. Typically, the Au nanostructures with a longer circulation half-life would exhibit higher accumulation in the tumor as a result of significant reduction in clearance by the MPS.⁶¹³

The surface functional group on Au nanostructures is a major parameter that determines their pharmacokinetics. Modifying the surface of a nanostructure will cause changes to its hydrodynamic size, surface charge, and reactivity, all of which can affect their half-life in the circulation system.^{575,690} Generally, a positive charge on the nanostructures will lead to high systemic toxicity because of complications such as hemolysis and platelet aggregation, resulting in faster clearance of such nanostructures from the bloodstream by the MPS. Negatively charged Au nanostructures have a longer circulation half-life than positively charged counterparts, while neutral nanostructures have the longest circulation half-life.^{691,692} For this reason, PEGylation has been widely used for surface modification to increase the circulation half-life of Au

nanostructures. For PEGylated Au nanostructures, it has been demonstrated that their circulation half-life increases as the length of PEG chains increases.²⁸²

The coverage density of PEG chains is a critical parameter in determining the efficiency of PEGylation. To this end, our group demonstrated four complementary methods for quantifying the coverage density of PEG chains on various types of Au nanostructures using a model system based on HS-PEG-NH₂ with different molecular weights.⁶⁹³ These methods take advantage of reactions with fluorescamine and ninhydrin, as well as labeling with fluorescein isothiocyanate (FITC) and Cu²⁺ ions. The first two methods use the conventional amine assay to measure the number of unreacted HS-PEG-NH₂ molecules left behind in the solution after incubation with the Au nanostructures. The other two methods involve coupling between the terminal -NH₂ groups of adsorbed -S-PEG-NH₂ chains and FITC or a ligand for Cu²⁺ ion, and thus pertain to the “active” -NH₂ groups on the surface of a Au nanostructure. Through this method, it was found that the coverage density decreased as the length of PEG chains increased. The initial capping ligand on the Au nanostructures played a pivotal role in determining both the efficiency and kinetics of the ligand exchange process. A stronger binding affinity of the initial capping ligand toward the Au surface would reduce the PEGylation efficiency by slowing down the ligand exchange kinetics. For the four different types of Au nanostructures and capping ligands examined, the PEGylation efficiency decreased in the order citrate-capped nanoparticles > PVP-capped nanocages ≈ CTAC-capped nanoparticles ≫ CTAB-capped nanorods. This study provides a set of useful guidelines for the PEGylation of Au nanostructures in an effort to improve their in vivo delivery.

The physical dimensions of Au nanostructures can also affect their pharmacokinetics.⁶⁹⁴ For nanostructures with a size smaller than 6 nm, they will be rapidly filtered out and cleared by the kidneys, while those larger than 200 nm will be rapidly retained by spleen. Chan and co-workers found that the clearance of small particles was much slower than that of large particles with the particle size range from 15 to 100 nm and the circulation half-life could be improved by decreasing particle size at a given length of PEG.⁶⁹⁵ For example, the circulation half-life of 15 nm Au nanoparticles coated with 5 kDa PEG was roughly 4.4 times longer than that of 100 nm Au nanoparticles covered by the same PEG.

5.3. Biodistribution and Tumor Targeting

The biodistribution of Au nanostructures refers to their disseminations into different types of tissues, organs, and systems, typically including blood, liver, spleen, muscle, heart, lung, kidneys, intestines, and the immune system.⁶¹³ Of particular interest is the MPS that involves organs such as liver, spleen, and bone marrow that are rich in phagocytic cells (e.g., macrophages, Kupffer cells, and monocytes) capable of engulfing and digesting particulate materials. One of the physiological functions of the MPS is to actively capture and eliminate viruses and other small objects from the circulation system. Studies have shown that the MPS is responsible for the clearance of most nanostructures larger than 10 nm, regardless of their shape, morphology, and surface chemistry.⁶⁹⁶

When Au nanostructures enter the plasma, opsonization will occur immediately on their surface, and once coated with opsonins, the Au nanostructures will be covered by a protein corona to make them more visible to the phagocytic cells in the

MPS.³⁸ Depending on the charge and hydrophobicity of Au nanostructures, opsonization can occur within minutes.^{691,697–699} It has been shown that charged nanostructures tend to be covered by proteins more rapidly than those with a neutral surface.³⁸ Upon opsonization, the Au nanostructures will be rapidly uptaken by the phagocytic cells in the MPS. Therefore, the fate of Au nanostructures in plasma is mainly determined by their surface properties in conjunction with opsonization.⁷⁰⁰ The liver plays a most important role in Au clearance from the plasma due to its abundance of Kupffer cells, whose function is to eliminate foreign substances through phagocytosis. This is critical for Au nanostructures larger than 6 nm in size, which cannot undergo renal clearance.^{690,696} Once processed by Kupffer cells and phagocytic cells, the Au nanostructures sequester in the MPS organs. Therefore, a large proportion of Au nanostructures concentrate in the liver and other MPS organs, which could potentially induce long-term toxicity. The spleen has a blood filtration system based on a tight reticular mesh (about 200 nm in width) comprised of interendothelial cells. Nanostructures larger than 200 nm are thus preferentially retained by spleen.⁷⁰¹

Owing to their relatively large sizes, most of the nanostructures cannot go through the tight junctions (with a gap of ~ 0.4 nm) between endothelial cells on normal vascular linings.⁷⁰² However, the walls of blood vessels inside a tumor are leaky, allowing nanostructures with the right dimensions to pass through.^{703,704} The insufficient drainage also facilitates the accumulation of nanostructures inside the tumor due to the largely absent and/or dysfunctional lymphatic system. This phenomenon has been known as the enhanced permeability and retention (EPR) effect, which serves as a basis for the passive targeting of tumor.^{629,705} The size of nanostructures plays the most important role in EPR-based tumor targeting. Only nanostructures with a size smaller than the gap between adjacent endothelial cells can be extravasated from the vasculature. Once extravasated, the transport of nanostructures in the tumor tissues is a diffusion-mediated process. The nanostructures extravasated into the tumor interstitium can also move back into the blood vessels through the gaps in vascular walls and then be cleared by the MPS. In general, nanostructures with dimensions in the range of 30–200 nm show better retention by the tissue resistance, shifting the equilibrium toward extravasation and leading to enhancement in tumor accumulation.^{706,707}

Taking into account both the MPS uptake and EPR effect, the tumor accumulation of Au nanostructures is most significantly affected by their physical dimensions.^{457,659,672,708} Chan and co-workers have systematically investigated the tumor targeting capability of Au nanoparticles with different sizes and functionalized with PEG.²⁸² The amount of nanoparticles accumulated inside the tumor was quantified as the area under the curve (AUC) by measuring both percent injected dose per gram over time and particle mass per gram over time. It was found that Au nanoparticles of 60 nm in diameter had the greatest AUC at 26.47% ID h/g as compared to other samples of Au nanoparticles with diameters of 20, 40, 80, and 100 nm.

The surface properties of Au nanostructures, including functional groups and charges, may affect the efficiency of extravasation and retention in the tumor tissues as these properties can influence the hydrodynamic size, circulation half-life, and “stealth” capability.^{546,692,709–711} To this end, surface modification such as PEGylation is widely used to reduce

opsonization and thereby increase the circulation half-life of Au nanostructures. As a consequence of lower opsonization, the PEGylated nanostructures are less recognized by phagocytic cells and tend to accumulate in tumors more effectively, known as the “stealth” property.⁶¹³ However, it was recently demonstrated that nanoparticles can be targeted by the immune system through the development of antibodies.^{712,713} For instance, up to 25% patients were shown to develop anti-PEG antibodies after treatment with PEGylated nanoparticles. Thus, the opsonization process may be more complicated than simple protein adsorption, affecting the tumor targeting efficacy of PEGylated Au nanostructures. The shape or morphology of Au nanostructures can also affect their accumulation inside a tumor as they follow different patterns in moving toward the surface of the vascular wall and extravasating into the tumor (see Figure 46 for some typical examples).^{151,546,710,714,715} Therefore, the biodistribution of Au nanostructures is a combined result of many different tissues, organs, and systems, including the MPS, the immune system, and the tumor tissue, and their recognition and interaction with the nanostructures.

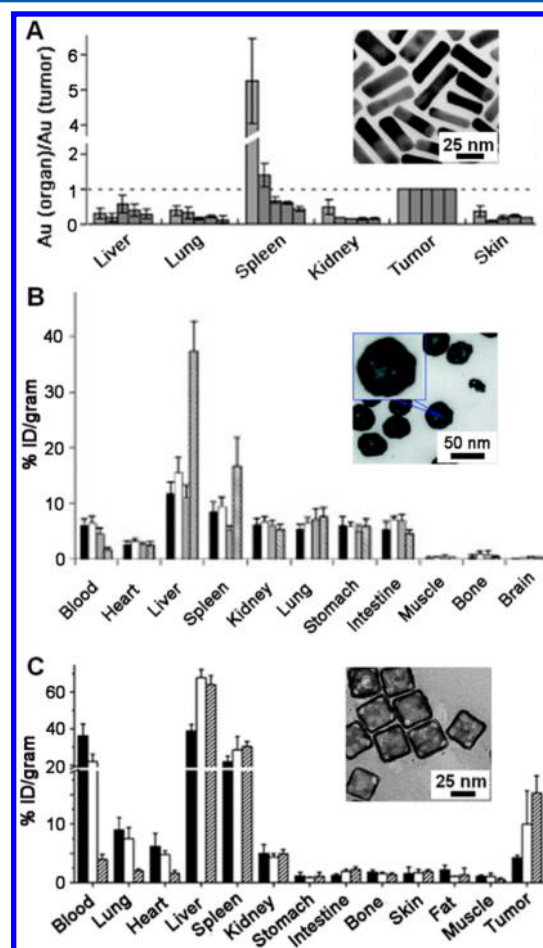


Figure 46. TEM images of Au nanostructures with different shapes and their representative biodistribution data: (A) nanorods, (B) nanoshells, and (C) nanocages. (A) Reprinted with permission from refs 710 and 714. Copyright 2009 Elsevier and copyright 2003 Royal Society of Chemistry, respectively. (B) Reprinted with permission from refs 211 and 672. Copyright 2010 American Chemical Society and copyright 2012 Elsevier, respectively. (C) Reprinted from ref 546. Copyright 2013 American Chemical Society.

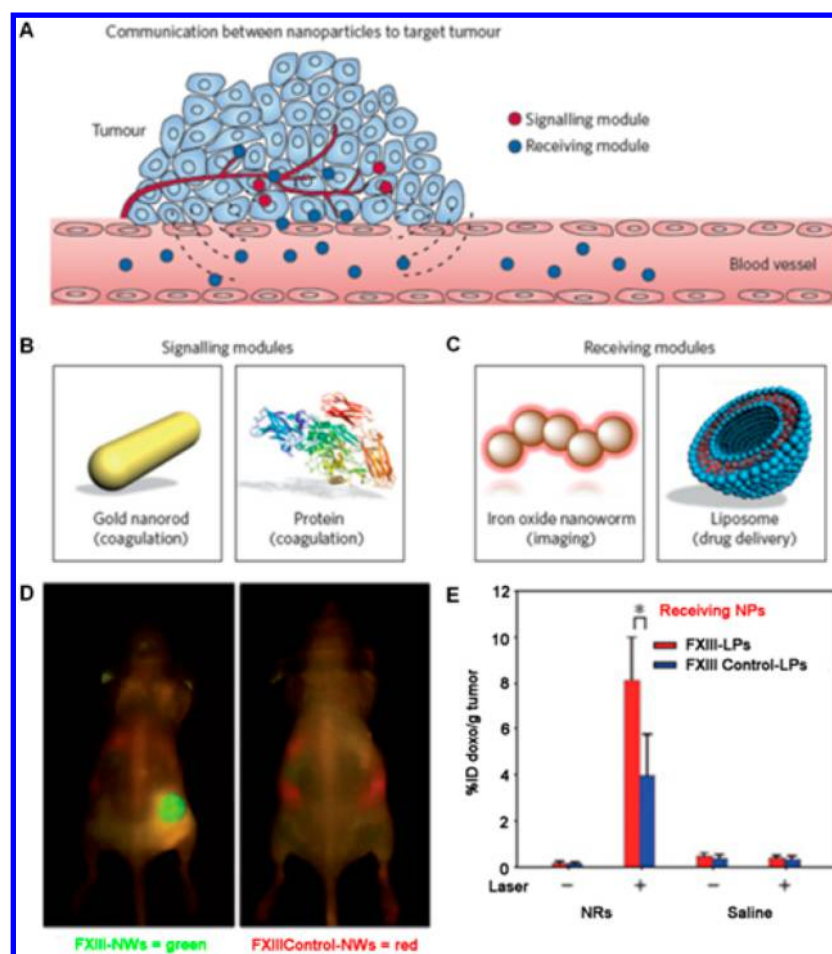


Figure 47. Schematic illustrations showing (A) how the signaling module (red) can broadcast the tumor location to the receiving module (blue) in the circulation. (B) The two types of signaling modules: a Au nanorod that initiates coagulation upon NIR laser irradiation and an engineered tumor-targeted human protein tissue factor that activates coagulation upon binding to the tumor receptors. (C) The two types of receiving modules: an iron oxide nanoworm designed for magnetic resonance imaging and a drug-loaded liposome (LP) as an example of a therapeutic agent. (D) Overlaid fluorescence reflectance image of mice with targeted and untargeted receiving nanoparticles. At 24 h postirradiation, fluorescence imaging revealed the distributions of coagulation-targeted (FXIII-NWs, green) and untargeted (FXIIIControl-NWs, red) receiving nanoparticles (FXIII and NWs stand for the coagulation transglutaminase factor XIII and nanoworm, respectively). (E) Quantification of doxorubicin-loaded LPs in irradiated and contralateral unirradiated tumors. At 96 h postinjection of signaling nanoparticles, mice were dissected and the fluorescence of doxorubicin of each tumor homogenate in acidic ethanol was measured to quantify the homing of receiving nanoparticles. (Asterisk indicates $P = 0.021$, unpaired, two-sided t -test, $n = 4$; error bar = standard deviation). (A–C) Reprinted with permission from ref 727. Copyright 2011 Nature Publishing Group. (D and E) Reprinted with permission from ref 726. Copyright 2011 Nature Publishing Group.

Various types of ligands such as small molecules,⁷¹⁶ peptides,^{570,572} antibodies or antibody fragments,^{674,717} and nucleic acids⁷¹⁸ have been employed to functionalize the surfaces of Au nanostructures in an effort to improve their tumor targeting efficiency. Different from passive targeting that is solely based on the EPR effect, the new targeting mechanism involves molecular recognition and is thus commonly known as “active targeting”. Active targeting can be achieved in two different ways, via cellular and vascular targeting, respectively. Currently, the improvement in tumor accumulation achieved through active cellular targeting is still under debate.^{719,720} It is believed that the accumulation of nanostructures in a tumor is dominated by the passive process. Even without using any targeting ligand, it is always possible to increase the accumulation of Au nanostructures in a tumor by engineering their size, shape, and surface chemistry. Only after the Au nanostructures have extravasated from the vasculature can the retention and uptake of nanostructures by cancer cells be augmented as a result of receptor-mediated endocytosis.⁷²¹

Some experimental results suggest that active cellular targeting could increase both tumor accumulation and cellular uptake,^{722–724} but these results are likely caused by the discrepancy in surface properties of the particles, nonuniformity of tumor models, and the variance of targeting ligands.³⁸ On the other hand, it has been argued that active cellular targeting would anchor nanostructures to tumor cells next to the leaky vessels, decreasing the efficiency of diffusion and tumor accumulation. Therefore, the coverage density of targeting ligands on the surface of a Au nanostructure must be optimized and controlled. Alternatively, active vascular targeting has shown promise as a means for tumor targeting.⁷²⁵ By targeting and killing the endothelial cells of the tumor vessels, tumor cells can be eradicated due to the lack of oxygen and nutrients. In this case, the targeting ligand is of critical importance as the targeting is no longer determined by the EPR effect, but by the binding affinity of the ligand toward blood vessels.

Recently, some other methods have also been developed to improve the targeting efficacy of Au nanostructures.^{726,727} It

was demonstrated that the plasmonic nanobubbles, generated from the NIR irradiation of Au nanoparticles, could adhere and form transient pores on the plasma membrane.^{728,729} As a result, the cellular uptake of drugs will be greatly enhanced due to a higher flux of diffusion. A new strategy containing “signaling” and “receiving” modules that communicate through endogenous signaling cascades has been proposed for improving tumor targeting efficiency (Figure 47).^{726,727} In this case, an engineered human protein was conjugated to PEGylated Au nanorods and employed as the “signaling” module. After delivery to the tumor site through passive targeting and irradiation with a NIR laser, coagulation was initiated via the photothermal effect. The heat released from the irradiated Au nanorods caused damage to the blood vessels inside the tumor, activating both the extrinsic and intrinsic coagulation pathways. By binding to receptors on the surface of tumor cells, the truncated tumor-targeted human protein tissue factor can also activate the extrinsic coagulation pathway. Iron oxide nanoparticles (an MRI imaging contrast agent) and drug-loaded liposomes (a therapeutic agent) have been used as the “receiving” modules. Their surfaces were functionalized with a peptide that can target the coagulation cascade and serve either as direct targets for fibrin or as substrates for factor XIII (a specific coagulation-cascade enzyme). In comparison with plain liposomes, the accumulation of Dox in a tumor could be enhanced by 40 times when loaded inside liposomes functionalized with factor XIII.

5.4. Toxicity and Clearance Issues

Despite advancements in using Au nanomaterials for in vivo imaging and therapy, a number of issues remain to be addressed before these applications can be translated into the clinics. These issues can either hamper the efficacy/efficiency or cause adverse effects. First, it is always critical to have a tight control over the surface properties of Au nanomaterials as they can affect the biodistribution, targeting efficiency, and toxicity of the nanomaterials. As discussed above, prolonged circulation of nanostructures can be achieved through PEGylation. However, PEGylation with large PEG molecules (e.g., PEG₅₀₀₀) will increase the hydrodynamic diameter of Au nanostructures and drastically alter their biodistribution and pharmacokinetics. The introduction of a targeting ligand onto the surface will compromise their stealth property, increasing the hydrophobicity and thus associated protein adsorption. There is always a compromise between the stealth and targeting properties that requires a proper degree of surface modification in order to optimize both the targeting efficiency and biodistribution profile. Second, the tumor targeting efficiency of Au nanomaterials tends to be compromised by their accumulation in major organs. A large dose is often needed, which may potentially harm these organs. In addition, the penetration of Au nanomaterials into tumors and their intratumoral distribution may not always favor the treatment as the penetration depth is generally shallow and homogeneous distribution is often hard to achieve, thus making the local concentration of Au nanostructures lower than what is required. Here we would like to emphasize two well-recognized issues that have yet to be fully addressed: the long-term toxicity of Au nanomaterials and their elimination from the body.

5.4.1. Long-Term Toxicity. Although Au colloids are drunk by people as a dietary supplement to rejuvenate their health condition, a clinical trial is still needed to validate their actual health benefits and identify the long-term adverse effects.

Though the toxicity of Au nanoparticles has been studied both in vitro and in vivo, most of these studies only focus on the acute toxicity that occurs within weeks, while a systematic study of the long-term (longer than 1 year) toxicity of Au nanoparticles is still missing.^{730–734} This can be potentially attributed to two reasons: (i) the hazardous side effects are most likely to show up in the first few days to weeks after administration of treatment and thus fall into the acute time frame, while long-term side effects could be comparatively insignificant relative to the acute toxicity and the control group, and (ii) the investment needed to feed the laboratory animals for months to years is expensive and uneconomical given the limited data generated.

In the short-term approach, the Au nanoparticles are first synthesized with controlled size and shape, followed by various means of characterization. Then, surface modification is carried out to endow the nanoparticles with prolonged circulation and targeting capabilities. The nanoparticles are subsequently subjected to in vitro assessment for their cytotoxicity prior to in vivo studies of their pharmacokinetics, biodistribution, and degradation. A histology examination is also normally carried out to evaluate the toxicity. A similar procedure can also be employed for a long-term study, but with an extended period of time for the examination. The current, albeit limited, data suggests that Au nanoparticles are not toxic in the long term. For instance, Hainfeld and co-workers studied the X-ray contrast and radiotherapy enhancement with Au clusters 1.9 nm in diameter, and found an enhanced survival rate after a year with no apparent adverse effect being observed.^{555,556} They also evaluated Au nanoparticles of larger sizes (4, 13, and 100 nm) for their toxicity up to 6 months.⁷³⁵ Studies from other groups indicate that the Au nanoparticles tended to accumulate in the major organs for the period of time being evaluated without effective excretion.^{709,736,737} However, the nanoparticles were not found to exert any adverse impact on the animals during the time frame (a few weeks to a year), in spite of major differences in biodistribution.

Several factors have been identified to affect the overall in vivo toxicity, such as size, shape, surface chemistry, surface charge, and the presence of surfactant.^{730–734} Although these factors affect the acute toxicity in critical ways, they are less important for the long-term toxicity, as the Au nanoparticles will be processed by different types of phagocytic cells before long-term accumulation. These factors may have an impact on the long-term toxicity of Au nanoparticles by changing their biodistribution profile. Recent clinical trials also demonstrated that even when acute toxicities were not observed, most patients would still suffer a controllable fever alongside various types of adverse events such as lymphopenia, hypoalbuminemia, hypokalemia, hypophosphatemia, hyperbilirubinemia, and increased aminotransferase.⁷³⁸

5.4.2. Clearance from the Body. As recommended by the U.S. Food and Drug Administration (FDA), pharmaceutical drugs should be eliminated via metabolism or excretion processes within a reasonable period of time in order to reduce accumulation and potential side effects. To meet this requirement, the mechanism of clearance for Au nanoparticles has been an active subject of research.⁶¹³ Two aspects of clearance need to be addressed separately: the clearance from the bloodstream and from the body, respectively. Clearance from the blood pool is more frequently studied as it determines the efficacy of lesion targeting and the removal via different mechanisms, in conjunction with the pharmacokinetics and

biodistribution studies discussed above.⁶¹³ The blood clearance property will directly impact the effectiveness of a nanomaterial-based medicine and its toxicity. On the other hand, clearance from the body addresses the amount of nanomaterials eliminated from the body by urine and bile while either during clearance or after they have been cleared from the blood pool. In this review, we call the removal of nanoparticles from body by hepatic cells biliary clearance to differentiate it from the blood clearance process. The elimination of Au nanomaterials from the body is less well studied as Au cannot be digested by enzymes within the body.^{739,740} This is one of the major barriers that limits the clinical use of most Au-based agents. To make Au nanomaterials clearable, we need a better understanding of the details involved in both renal and biliary clearance.

Renal clearance is a natural mechanism for the human body to eliminate undesired small particles and molecular wastes through kidneys. The process involves multiple steps, including glomerular filtration, tubular secretion, and reabsorption.⁶¹³ When nanoparticles circulate through the glomerular capillary bed, they can enter the proximal tubule through the porous glomerular capillary wall via physical filtration or electrostatic interaction.⁷⁴¹ They may also be resorbed before ultimately being eliminated from the body.⁶¹³ The size and surface properties of the particles that can be processed by the kidney are limited by biological features of the organ. When the nanoparticles are filtered out, they need to pass through a capillary wall comprised of fenestrated endothelium, glomerular basement membrane (GBM), and foot processes of glomerular epithelial cells bridged by slit diaphragms.⁷⁴¹ These features have been characterized to have a pore size of about 43 nm for the slit and about 500 nm between the GBM. Since the nanoparticles need to pass through multiple layers of cell before the drainage, the functional pore size is typically on the scale of 5 nm.^{741,742} This also indicates that the filtration of nanoparticles is highly size-dependent; nanoparticles larger than the threshold can only accumulate in the kidney with little chance of being eliminated without further processing.⁶¹³ In 2007, Choi and co-workers confirmed this size dependence by observing the renal clearance of PEGylated QDs with different hydrodynamic diameters.⁷⁴³ It was observed that nanoparticles with a hydrodynamic diameter less than 6 nm were rapidly cleared, while those larger than 8 nm could not be easily filtered out. The renal clearance properties of the intermediate ones between 6 and 8 nm were affected by both their hydrodynamic diameter and their surface charge. Because of the electrostatic interaction between particles and the glomerular capillary wall, negatively charged particles fixed within the capillary wall, resulting in a reduced renal clearance compared to their positively charged counterparts.

In order to make Au nanomaterials renal clearable, they need either to be engineered with a hydrodynamic diameter smaller than 6 nm or be biodegradable. Since Au is generally not biodegradable, reducing the size seems to be the most effective way to promote clearance. For example, Au clusters of 1.9 nm in diameter used to enhance X-ray contrast could still be effectively cleared.^{555,556,744} The highest tissue concentration in the kidneys was found to be at a level of $10.60 \pm 0.2\%$ at 15 min postinjection, indicating that kidneys were the primary sites for their clearance. A total of $77.5 \pm 0.4\%$ of the injected Au clusters was found to be cleared from the body after 5 h.^{555,556} Tillement and co-workers studied radioactive-labeled, dithiolated polyaminocarboxylate-coated Au nanoparticles of

2.4 ± 0.5 nm in core size and 6.6 ± 1.8 nm in hydrodynamic diameter.⁷⁴⁵ The particles were found to be rapidly cleared, with a cumulative dose of about 70% of the total injected Au being found in urine within 72 h. This result was also confirmed using SPECT imaging by comparing the signals recorded from kidneys and bladder. Luminescent Au clusters with a hydrodynamic diameter of 2.2 nm were also found to have good renal clearance as compared to their larger counterparts (6.3 and 13.0 nm in hydrodynamic diameter).⁷⁴⁴ As shown in Figure 48, the small luminescent Au nanoparticles had an

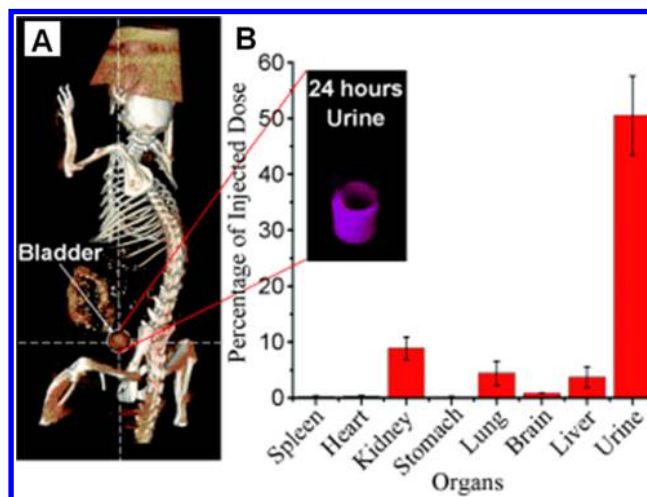


Figure 48. Renal clearance of luminescent Au nanoparticles. (A) X-ray CT image of a mouse injected with luminescent Au nanoparticles at 30 min postinjection and (B) biodistribution of luminescent Au nanoparticles measured by ICP-MS at 24 h postinjection. The inset shows a photoluminescence image of the collected urine, confirming the presence of luminescent Au nanoparticles 24 h postinjection. The excreted Au nanoparticles still maintain their photoluminescence properties, indicating a direct renal clearance with little change in their structure. Reprinted with permission from ref 744. Copyright 2011 Wiley-VCH.

effective renal clearance, with about 50% of the total injected Au eliminated via urine within 24 h, while the larger ones were much less effectively cleared. It also showed that the ratio between the amounts of Au accumulated in kidneys and liver was a good indicator for the renal clearance of Au nanoparticles.⁷⁴⁴ For Au clusters with only tens to hundreds of Au atoms, their hydrodynamic diameters are usually below the threshold for renal clearance. However, the surface chemistry of clusters is difficult to alter, so their clearance property is largely determined by the surface stabilizer.⁷⁴⁶ Protein adsorption and aggregation can greatly affect the biodistribution and thus the clearance properties of these clusters. A recent study by Zheng and co-workers compared the effects of different surface chemistries based on zwitterionic and PEG coatings.⁷⁴⁷ Despite their comparable clearance through liver and kidneys, the PEGylated nanoparticles showed a higher passive tumor targeting with slower metabolism kinetics.

It is still unrealistic to achieve effective renal clearance for the more widely used Au nanospheres, nanorods, nanocages, and nanoshells. Nevertheless, large Au nanoparticles are often desired for many applications because of unique properties such as LSPR, SERS, and passive targeting capability that arise only at certain particle sizes. Alternative approaches are needed to fabricate Au nanostructures that are more biodegradable and

thus more easily cleared from the body. One general idea is to assemble Au nanoparticles smaller than the threshold for renal clearance into large structures, which can be broken apart once their theranostic role is no longer needed.⁶¹³ Nanoparticle–liposome composites (Au-coated liposomes) were first introduced to address this problem.⁶¹¹ These composites demonstrated degradation into small fragments *in vitro*. However, to date, there is no convincing *in vivo* data to support this hypothesis. In another report, Sokolov and co-workers developed a novel kind of aggregate made of sub-5-nm Au nanoparticles and PLA(2K)-*b*-PEG(10K)-*b*-PLA(2K).⁷⁴⁸ When the pH was lower than 5, the aggregate would disassemble, releasing subunits of 4.3 nm hydrodynamic diameters. Still, this work lacked sufficient data to demonstrate the effectiveness of this mechanism *in vivo*. This could be because the acidic environment needed for breaking down the assembled structures does not typically exist in circulation or major organs compared to the intracellular environment. However, the nanoparticles uptaken and processed by cells are rarely excreted back into circulation. Recently, Chan and co-workers demonstrated biodegradable Au “core–satellite” superstructures connected by DNA linkers that could achieve reasonable renal clearance with good tumor targeting abilities.⁷⁴⁹ By controlling the ratio between the core and satellite particles, various kinds of Au superstructures could be assembled with different morphologies. Up to 15% of the injected dose from the smallest satellites particles (3 nm) was found excreted into urine by 48 h.

As part of the RES that is abundant in Kupffer cells (the phagocytic cells) and reticular connective tissue, the liver can actively capture and eliminate foreign particulate materials.⁶¹¹ The important role of Kupffer cells was widely emphasized for the clearance of nanoparticles from the bloodstream, as they are the cells that can actively capture and process particulate materials in the liver. However, Kupffer cells are not actively involved in the process of hepatic clearance of Au nanoparticles from the body because Au can hardly be broken down by the catabolic mechanism and will ultimately accumulate in Kupffer cells. The capture, catabolism, and excretion of Au nanoparticles are carried out by the hepatocytes, which naturally process and excrete waste via the biliary system.⁶¹³ In a few cases where the Au nanoparticles are somewhat biliary clearable, the dose eliminated via bile is much lower than the dose that is eliminated through urine.⁷⁴⁵ The core size of the Au nanoparticles may also play a certain role as the smaller ones tended to show slightly better clearance via bile.⁷³⁵ A recent study by Liu and co-workers demonstrated the synthesis of ⁶⁴Cu-incorporated Au–Cu alloyed clusters of 2.5 ± 0.8 nm.⁵⁷⁵ It was found that up to 38.4% of the injected dose was found in feces, and the clearance number was not sensitive to the length of the PEG chains. This value was much higher than what was reported for Au clusters with a similar size. A possible explanation is that the alloyed core could be more easily broken down and processed by the hepatocytes. In spite of the evidence that Au nanoparticles can be processed and eliminated by the hepatic process, a detailed mechanism remains elusive. To our knowledge, no study has been reported with regard to the possible difference in distribution between Kupffer cells and hepatocytes for the Au nanoparticles after long-term accumulation.

Compared to the renal clearance, biliary clearance involves a more complicated mechanism and is normally associated with RES. It is also a less effective and more time-consuming process

than the renal clearance. Since biliary clearance is an active process, the handling of a large amount of exotic materials can also result in further side effects. As a result, biliary clearance should not be a primary targeting mechanism for the elimination of Au nanomaterials.

6. CONCLUDING REMARKS

The extensive research into Au nanomaterials over the past few decades has demonstrated a myriad of unique capabilities for a rich variety of biomedical applications. Many advances were enabled by the remarkable progress in both understanding and controlling the chemical synthesis of Au nanomaterials. Only two decades ago, Au nanoparticles could only be prepared through primarily the Turkevich and Brust methods. Although nanoparticles prepared using these methods were often claimed as “uniform”, it was difficult to identify two particles from such a sample that simply shared the same size and/or shape, to say nothing of the diversity in terms of twin structure. Thanks to the efforts from many research groups, it is now feasible to synthesize Au nanomaterials as more uniform samples and with better-controlled sizes, shapes, morphologies, and structures through a large number of solution-phase methods. Notable examples include Au clusters, nanospheres, nanorods, nanoplates, nanoshells, nanoboxes, nanocages, nanoframes, and nanostars, as briefly reviewed in section 2. It is now far easier to engineer the optical properties of Au nanomaterials in an effort to explore different types of biomedical applications, including the tuning of their photoluminescence or LSPR peaks to the transparent window for soft tissues in the NIR region. As discussed in sections 2 and 3, it is an impressive accomplishment to be able to process the same, simple element of Au into so many different types of nanomaterials with tunable and controllable properties ranging from photoluminescence to photothermal conversion, scattering, and surface-enhanced spectroscopy.

Owing to their inherent bioinertness and tunable optical properties, Au nanomaterials have shown tremendous promise in a wide variety of biomedical applications, including sensing, imaging, diagnostics, drug delivery, gene delivery, and cancer treatment. As opposed to other types of nanomaterials commonly used in nanomedicine, including liposomes, polymersomes, polymer nanoparticles, and metal oxide nanoparticles, each Au nanoparticle can individually serve as a multifunctional platform for an array of theranostic applications.¹⁶ The involvement of only a single element for the differently purposed nanomaterials also makes it straightforward to develop a universal, robust chemistry to control their surface properties for attaining high sensitivity and selectivity toward sensing/imaging, as well as good biocompatibility and targeting capability toward cancer theranostics. Recent clinical trials involving Au nanomaterials have begun to pave the road toward their ultimate implementation in both cancer diagnostics and treatment.^{738,750}

Despite the large number of reports on the successful demonstration of Au nanomaterials for cancer theranostics and other biomedical applications, several issues are still yet to be addressed. First, at the current stage of development, a high dose of Au nanomaterials is often needed because of their relatively poor accumulation (typically below 10%) in the tumor. Besides the potentially harmful impacts on healthy tissue and organs, the use of a large amount of Au can substantially increase the cost of a treatment. Second, Au nanomaterials larger than 8 nm in physical dimensions are not

easily cleared from the body as they cannot be broken down into smaller pieces through existing enzymatic reactions in the body. After introduction into the body, they will quickly accumulate in healthy organs such as liver and spleen, which may result in potential adverse effects and long-term toxicity.

Since Au is one of the scarcest precious metals in the Earth's crust, we must also keep in mind the sustainability of the material. The viability of using Au nanomaterials as a drug carrier for cancer treatment is in fact still under debate. As predicted by WHO, cancer cases are expected to surge 57% worldwide in the next 20 years, with new cancer cases rising from an estimated 14 million annually in 2012 to 22 million. According to the literature, the loading efficacy of Dox was about 2.68×10^{-2} g of Dox/g of Au for solid Au nanospheres of 12.7 nm in size⁵⁶⁴ or 1.7 g of Dox/g of Au for hollow Au nanoparticles with a size of 43 nm.²¹¹ When used in combination with other anticancer drugs, the most commonly used dosage of Dox is 40–60 mg/m² for intravenous injection every 21–28 days. If solid Au nanospheres of 12.7 nm in size are used for the delivery of this amount of Dox, 2.67 g of Au will be needed for each patient every 21–28 days, which amounts to approximately 766.189 tons/year in terms of expected worldwide demand in 2032. When Au hollow nanoparticles are used, the demand for this particular application will be much lower, at about 12.078 tons/year. According to the data released by the U.S. Geological Survey (USGS), the world Au production in 2012 was only 2700 tons. Given that the majority of Au is used as either reserve currency or for the jewelry business, the annual demand of Au for the delivery of anticancer drugs alone would not be an insignificant number, to say nothing of the demands for other theranostic applications. Needless to say, the large demand of Au nanomaterials for biomedical applications may have significant impacts on the existing applications of Au and their market shares. For each of the biomedical applications reviewed in this article (as well as those to be demonstrated in the future), we must ask ourselves whether Au is absolutely necessary before we push the technology toward any clinical or commercial use. For most of the applications reviewed in this article, it appears like that Au can be replaced by other functional materials without sacrificing the performance. For example, considering their good biocompatibility, high catalytic activity, excellent magnetic properties, and straightforward procedures for both synthesis and surface modification, iron oxide nanoparticles have a potential to replace Au nanomaterials in applications related to imaging, controlled release, drug delivery, and photothermal cancer therapy.⁷⁵¹ Readers who are interested in this class of nanomaterials can find more detailed discussions from a number of review articles.^{752–754} In this regard, what has already been reported for Au nanomaterials can serve as a good starting point for those who aim to develop more practical materials for nanomedicine.

AUTHOR INFORMATION

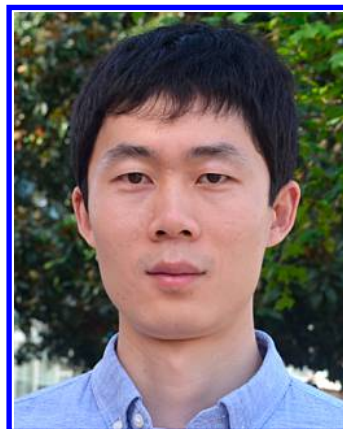
Corresponding Author

*E-mail: younan.xia@bme.gatech.edu.

Notes

The authors declare no competing financial interest.

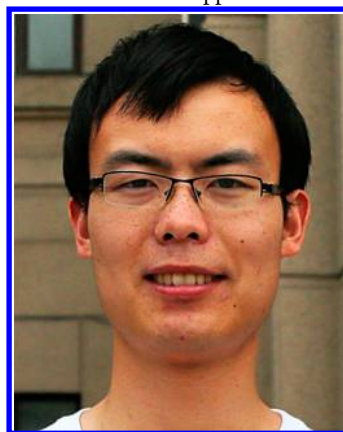
Biographies



Xuan Yang received his B.S. degree in chemistry from the University of Science and Technology of China in 2008, and a Ph.D. degree in analytical chemistry from the University of Chinese Academy of Sciences in 2013. He joined the Xia group in February 2014. His research interests include the development of novel nanomaterials for applications in controlled drug release and electrocatalysis.



Miaoxin Yang received his B.S. in pharmacy from Shanghai Jiaotong University in 2006, M.S. in chemistry from Nanyang Technological University in 2009, and M.S. in biomedical engineering from Washington University in St. Louis in 2011. After working for Philips Electronics as a research scientist for two years, he joined the Xia group in 2013 to pursue a Ph.D. degree in chemistry and biochemistry at Georgia Tech. His research interests include the development of novel nanomaterials for biomedical applications.



Bo Pang received his B.E. in mechanical engineering (2010) and B.S. in chemistry (2011) from Peking University, China. He is currently pursuing his Ph.D. degree in biomedical engineering in the joint Ph.D.

program by Georgia Tech/Emory/Peking University under the supervision of Profs. Qiushi Ren and Younan Xia. His research interests focus on the use of gold nanocages for cancer therapy and nanoparticle-based contrast agents for nuclear imaging.



Madeline Vara received her B.A. in chemistry from Wellesley College in 2010. She then worked for Nano Terra, Inc. based out of Cambridge, MA, until 2013, focusing on a variety of nano- and microtechnology-based products and design applications. Currently, she is pursuing a Ph.D. degree in chemistry and biochemistry at Georgia Tech under Prof. Younan Xia. Her research interests focus on the synthetic design of metal and metal oxide nanocrystals, and their applications in energy and catalytic processes.



Younan Xia studied at the University of Science and Technology of China (B.S. in 1987) and University of Pennsylvania (M.S. in 1993), and received his Ph.D. from Harvard in 1996 (with George Whitesides). He started as an assistant professor at the University of Washington (Seattle) in 1997, and was promoted to associated professor and professor in 2002 and 2004, respectively. He joined the Department of Biomedical Engineering at Washington University in St. Louis in 2007 as the James M. McKelvey Professor. In early 2012, he moved to Georgia Tech to take the position of Brock Family Chair and GRA Eminent Scholar in Nanomedicine. His research interests include nanomaterials, biomaterials, nanomedicine, and regenerative medicine.

ACKNOWLEDGMENTS

This work was supported in part by a grant from NCI (1R01 CA138527), an NIH Director's Pioneer Award (DP1 OD000798), and startup funds from Washington University in St. Louis and the Georgia Institute of Technology. We are grateful to our coworkers and collaborators for their invaluable contributions to this research project.

REFERENCES

- (1) Gray, T.; Mann, N. *The Elements: A Visual Exploration of Every Known Atom in the Universe*; Black Dog & Leventhal Publishers, Inc.: New York, 2012.
- (2) Prior, E. How much gold is there in the world? *BBC News* April 1, 2013. <http://www.bbc.com/news/magazine-21969100>.
- (3) Savage, N. Resources: Mine, All Mine! *Nature* **2013**, 495, S2–S3.
- (4) Tilling, R. I.; Gottfried, D.; Rowe, J. J. Gold Abundance in Igneous Rocks: Bearing on Gold Mineralization. *Econ. Geol. Bull. Soc. Econ. Geol.* **1973**, 68, 168–186.
- (5) A History of the World-Episode 25—Gold Coin of Croesus. BBC British Museum.
- (6) Nutting, J.; Nuttall, J. L. The Malleability of Gold. *Gold Bull.* **1977**, 10, 2–8.
- (7) Yannopoulos, J. C. *The Extractive Metallurgy of Gold*; Van Nostrand Reinhold: New York, 1991.
- (8) <http://www.vam.ac.uk/>.
- (9) Faraday, M. The Bakerian Lecture: Experimental Relations of Gold (and Other Metals) to Light. *Philos. Trans. R. Soc. London* **1857**, 147, 145–181.
- (10) <http://www.rigb.org/>.
- (11) Skrabalak, S. E.; Au, L.; Li, X.; Xia, Y. Facile Synthesis of Ag Nanocubes and Au Nanocages. *Nat. Protoc.* **2007**, 2, 2182–2190.
- (12) Mie, G. Beiträge zur Optik Trüber Medien, Speziell Kolloidaler Metallösungen. *Ann. Phys.* **1908**, 330, 377–445.
- (13) Cobley, C. M.; Chen, J.; Cho, E. C.; Wang, L. V.; Xia, Y. Gold Nanostructures: a Class of Multifunctional Materials for Biomedical Applications. *Chem. Soc. Rev.* **2011**, 40, 44–56.
- (14) Xia, Y.; Halas, N. J. Shape-Controlled Synthesis and Surface Plasmonic Properties of Metal Nanostructures. *MRS Bull.* **2005**, 30, 338–348.
- (15) Huang, X.; Neretina, S.; El-Sayed, M. A. Gold Nanorods: From Synthesis and Properties to Biological and Biomedical Applications. *Adv. Mater.* **2009**, 21, 4880–4910.
- (16) Dreaden, E. C.; Alkilany, A. M.; Huang, X.; Murphy, C. J.; El-Sayed, M. A. The Golden Age: Gold Nanoparticles for Biomedicine. *Chem. Soc. Rev.* **2012**, 41, 2740–2779.
- (17) Willets, K. A.; Van Duyne, R. P. Localized Surface Plasmon Resonance Spectroscopy and Sensing. *Annu. Rev. Phys. Chem.* **2007**, 58, 267–297.
- (18) Stiles, P. L.; Dieringer, J. A.; Shah, N. C.; Van Duyne, R. P. Surface-Enhanced Raman Spectroscopy. *Annu. Rev. Anal. Chem.* **2008**, 1, 601–626.
- (19) Campion, A.; Kambhampati, P. Surface-Enhanced Raman Scattering. *Chem. Soc. Rev.* **1998**, 27, 241–250.
- (20) Qian, X.-M.; Nie, S. M. Single-Molecule and Single-Nanoparticle SERS: From Fundamental Mechanisms to Biomedical Applications. *Chem. Soc. Rev.* **2008**, 37, 912–920.
- (21) Aslan, K.; Gryczynski, I.; Malicka, J.; Matveeva, E.; Lakowicz, J. R.; Geddes, C. D. Metal-Enhanced Fluorescence: An Emerging Tool in Biotechnology. *Curr. Opin. Biotechnol.* **2005**, 16, 55–62.
- (22) Lakowicz, J. R. Radiative Decay Engineering: Biophysical and Biomedical Applications. *Anal. Biochem.* **2001**, 298, 1–24.
- (23) Weissleder, R. A Clearer Vision for *in Vivo* Imaging. *Nat. Biotechnol.* **2001**, 19, 316–317.
- (24) Daniel, M.-C.; Astruc, D. Gold Nanoparticles: Assembly, Supramolecular Chemistry, Quantum-Size-Related Properties, and Applications toward Biology, Catalysis, and Nanotechnology. *Chem. Rev.* **2004**, 104, 293–346.
- (25) Murray, R. W. Nanoelectrochemistry: Metal Nanoparticles, Nanoelectrodes, and Nanopores. *Chem. Rev.* **2008**, 108, 2688–2720.
- (26) Zheng, J.; Zhang, C.; Dickson, R. M. Highly Fluorescent, Water-Soluble, Size-Tunable Gold Quantum Dots. *Phys. Rev. Lett.* **2004**, 93, 077402.
- (27) Zhu, M.; Aikens, C. M.; Hollander, F. J.; Schatz, G. C.; Jin, R. Correlating the Crystal Structure of a Thiol-Protected Au₂₅ Cluster and Optical Properties. *J. Am. Chem. Soc.* **2008**, 130, 5883–5885.
- (28) Schmid, G.; Liu, Y.-P.; Schumann, M.; Raschke, T.; Radehaus, C. Quasi One-Dimensional Arrangements of Au₅₅(PPh₃)₁₂Cl₆ Clusters

and their Electrical Properties at Room Temperature. *Nano Lett.* **2001**, *1*, 405–407.

(29) Qian, H.; Zhu, Y.; Jin, R. Atomically Precise Gold Nanocrystal Molecules with Surface Plasmon Resonance. *Proc. Natl. Acad. Sci. U. S. A.* **2012**, *109*, 696–700.

(30) Puddephatt, R. J. *The Chemistry of Gold*; Elsevier Scientific: Amsterdam, 1978.

(31) Ulman, A. Formation and Structure of Self-Assembled Monolayers. *Chem. Rev.* **1996**, *96*, 1533–1554.

(32) Love, J. C.; Estroff, L. A.; Kriebel, J. K.; Nuzzo, R. G.; Whitesides, G. M. Self-Assembled Monolayers of Thiolates on Metals as a Form of Nanotechnology. *Chem. Rev.* **2005**, *105*, 1103–1169.

(33) Whitesides, G. M.; Laibinis, P. E. Wet Chemical Approaches to the Characterization of Organic Surfaces: Self-Assembled Monolayers, Wetting, and the Physical–Organic Chemistry of the Solid–Liquid Interface. *Langmuir* **1990**, *6*, 87–96.

(34) Jokerst, J. V.; Lobovkina, T.; Zare, R. N.; Gambhir, S. S. Nanoparticle PEGylation for Imaging and Therapy. *Nanomedicine* **2011**, *6*, 715–728.

(35) Lane, L. A.; Qian, X.; Smith, A. M.; Nie, S. Physical Chemistry of Nanomedicine: Understanding the Complex Behaviors of Nanoparticles. *Annu. Rev. Phys. Chem.* **2015**, *66*, 521–547.

(36) Ghosh, P.; Han, G.; De, M.; Kim, C. K.; Rotello, V. M. Gold Nanoparticles in Delivery Applications. *Adv. Drug Delivery Rev.* **2008**, *60*, 1307–1315.

(37) Gole, A.; Murphy, C. J. Azide-Derivatized Gold Nanorods: Functional Materials for “Click” Chemistry. *Langmuir* **2008**, *24*, 266–272.

(38) Nie, S. Understanding and Overcoming Major Barriers in Cancer Nanomedicine. *Nanomedicine* **2010**, *5*, 523–528.

(39) Cho, E. C.; Zhang, Q.; Xia, Y. The Effect of Sedimentation and Diffusion on Cellular Uptake of Gold Nanoparticles. *Nat. Nanotechnol.* **2011**, *6*, 385–391.

(40) Cho, E. C.; Zhang, Y.; Cai, X.; Moran, C. M.; Wang, L. V.; Xia, Y. Quantitative Analysis of the Fate of Gold Nanocages *in Vitro* and *in Vivo* after Uptake by U87-MG Tumor Cells. *Angew. Chem., Int. Ed.* **2013**, *52*, 1152–1155.

(41) Forestier, J. Rheumatoid Arthritis and its Treatment by Gold Salts. *Lancet* **1934**, *224*, 646–648.

(42) Sherman, A. I.; Ter-Pogossian, M. Lymph-Node Concentration of Radioactive Colloidal Gold Following Interstitial Injection. *Cancer* **1953**, *6*, 1238–1240.

(43) Faulk, W. P.; Taylor, G. M. An Immunocolloid Method for the Electron Microscope. *Immunochemistry* **1971**, *8*, 1081–1083.

(44) Dykman, L. A.; Khlebtsov, N. G. Gold Nanoparticles in Biology and Medicine: Recent Advances and Prospects. *Acta Nat.* **2011**, *3*, 34–55.

(45) Popovtzer, R.; Agrawal, A.; Kotov, N. A.; Popovtzer, A.; Balter, J.; Carey, T. E.; Kopelman, R. Targeted Gold Nanoparticles Enable Molecular CT Imaging of Cancer. *Nano Lett.* **2008**, *8*, 4593–4596.

(46) Xia, Y.; Li, W.; Cogley, C. M.; Chen, J.; Xia, X.; Zhang, Q.; Yang, M.; Cho, E. C.; Brown, P. K. Gold Nanocages: From Synthesis to Theranostic Applications. *Acc. Chem. Res.* **2011**, *44*, 914–924.

(47) Bardhan, R.; Lal, S.; Joshi, A.; Halas, N. J. Theranostic Nanoshells: From Probe Design to Imaging and Treatment of Cancer. *Acc. Chem. Res.* **2011**, *44*, 936–946.

(48) Alkilany, A. M.; Thompson, L. B.; Boulos, S. P.; Sisco, P. N.; Murphy, C. J. Gold Nanorods: Their Potential for Photothermal Therapeutics and Drug Delivery, Tempered by the Complexity of their Biological Interactions. *Adv. Drug Delivery Rev.* **2012**, *64*, 190–199.

(49) Shang, L.; Dong, S.; Nienhaus, G. U. Ultra-Small Fluorescent Metal Nanoclusters: Synthesis and Biological Applications. *Nano Today* **2011**, *6*, 401–418.

(50) Jin, R. Quantum Sized, Thiolate-Protected Gold Nanoclusters. *Nanoscale* **2010**, *2*, 343–362.

(51) Markus, R.; Schwentner, N. *Physics and Chemistry of Small Clusters*; Springer-Verlag: Berlin, 1987; pp 611–616.

(52) Fedrigo, S.; Harbich, W.; Buttet, J. Optical Response of Ag₂, Ag₃, Au₂, and Au₃ in Argon Matrices. *J. Chem. Phys.* **1993**, *99*, 5712–5717.

(53) Häkkinen, H. The Gold–Sulfur Interface at the Nanoscale. *Nat. Chem.* **2012**, *4*, 443–455.

(54) Freeman, R. G.; Grabar, K. C.; Allison, K. J.; Bright, R. M.; Davis, J. A.; Guthrie, A. P.; Hommer, M. B.; Jackson, M. A.; Smith, P. C.; Walter, D. G.; Natan, M. J. Self-Assembled Metal Colloid Monolayers: An Approach to SERS Substrates. *Science* **1995**, *267*, 1629–1632.

(55) Maity, P.; Xie, S.; Yamauchi, M.; Tsukuda, T. Stabilized Gold Clusters: From Isolation toward Controlled Synthesis. *Nanoscale* **2012**, *4*, 4027–4037.

(56) Lu, Y.; Chen, W. Sub-Nanometre Sized Metal Clusters: From Synthetic Challenges to the Unique Property Discoveries. *Chem. Soc. Rev.* **2012**, *41*, 3594–3623.

(57) Bellon, P.; Manassero, M.; Sansoni, M. Crystal and Molecular Structure of Tri-iodoheptakis(tri-*p*-fluorophenylphosphine)-Undecagold. *J. Chem. Soc., Dalton Trans.* **1972**, 1481–1487.

(58) Weare, W. W.; Reed, S. M.; Warner, M. G.; Hutchison, J. E. Improved Synthesis of Small ($d_{\text{CORE}} \approx 1.5$ nm) Phosphine-Stabilized Gold Nanoparticles. *J. Am. Chem. Soc.* **2000**, *122*, 12890–12891.

(59) Briant, C. E.; Theobald, B. R. C.; White, J. W.; Bell, L. K.; Mingos, D. M. P.; Welch, A. J. Synthesis and X-Ray Structural Characterization of the Centred Icosahedral Gold Cluster Compound [Au₁₃(PMe₂Ph)₁₀Cl₂](PF₆)₃; the Realization of a Theoretical Prediction. *J. Chem. Soc., Chem. Commun.* **1981**, 201–202.

(60) Teo, B. K.; Shi, X.; Zhang, H. Pure Gold Cluster of 1:9:9:1:9:9:1 Layered Structure: A Novel 39-Metal-Atom Cluster [(Ph₃P)₁₄Au₃₉Cl₆]Cl₂ with an Interstitial Gold Atom in a Hexagonal Antiprismatic Cage. *J. Am. Chem. Soc.* **1992**, *114*, 2743–2745.

(61) Schmid, G.; Pfeil, R.; Boese, R.; Bandermann, F.; Meyer, S.; Calis, G. H. M.; van der Velden, J. W. A. Au₅₅[P(C₆H₅)₃]₁₂Cl₆ — ein Goldcluster Ungewöhnlicher Größe. *Chem. Ber.* **1981**, *114*, 3634–3642.

(62) Teo, B. K.; Zhang, H.; Kean, Y.; Dang, H.; Shi, X. Binary Icosahedral Clusters: Atom and Electron Counting Rules. *J. Chem. Phys.* **1993**, *99*, 2929–2941.

(63) Teo, B. K.; Shi, X.; Zhang, H. Cluster of Clusters. Structure of a Novel Gold–Silver Cluster [(Ph₃P)₁₀Au₁₃Ag₁₂Br₈](SbF₆) Containing an exact Staggered-Eclipsed-Staggered Metal Configuration. Evidence of Icosahedral Units as Building Blocks. *J. Am. Chem. Soc.* **1991**, *113*, 4329–4331.

(64) Teo, B. K.; Hong, M. C.; Zhang, H.; Huang, D. B. Cluster of Clusters: Structure of the 37-Atom Cluster [(*p*-Tol₃P)₁₂Au₁₈Ag₁₉Br₁₁]²⁺. *Angew. Chem., Int. Ed. Engl.* **1987**, *26*, 897–900.

(65) Teo, B. K.; Shi, X.; Zhang, H. Clusters of Clusters. 25. Synthesis and Structure of a New [Gold–Silver]-38-Metal-Atom Cluster [(Ph₃P)₁₄Au₁₈Ag₂₀Cl₁₂]Cl₂ and its Implications with Regard to Intracavity Chemistry on Metal Cluster Surfaces. *Inorg. Chem.* **1993**, *32*, 3987–3988.

(66) Zhu, M.; Lanni, E.; Garg, N.; Bier, M. E.; Jin, R. Kinetically Controlled, High-Yield Synthesis of Au₂₅ Clusters. *J. Am. Chem. Soc.* **2008**, *130*, 1138–1139.

(67) Hostetler, M. J.; Wingate, J. E.; Zhong, C.-J.; Harris, J. E.; Vachet, R. W.; Clark, M. R.; Londono, J. D.; Green, S. J.; Stokes, J. J.; Wignall, G. D.; Glish, G. L.; Porter, M. D.; Evans, N. D.; Murray, R. W. Alkanethiolate Gold Cluster Molecules with Core Diameters from 1.5 to 5.2 nm: Core and Monolayer Properties as a Function of Core Size. *Langmuir* **1998**, *14*, 17–30.

(68) Price, R. C.; Whetten, R. L. All-Aromatic, Nanometer-Scale, Gold-Cluster Thiolate Complexes. *J. Am. Chem. Soc.* **2005**, *127*, 13750–13751.

(69) Negishi, Y.; Nobusada, K.; Tsukuda, T. Glutathione-Protected Gold Clusters Revisited: Bridging the Gap between Gold(I)–Thiolate Complexes and Thiolate–Protected Gold Nanocrystals. *J. Am. Chem. Soc.* **2005**, *127*, 5261–5270.

(70) Negishi, Y.; Takasugi, Y.; Sato, S.; Yao, H.; Kimura, K.; Tsukuda, T. Kinetic Stabilization of Growing Clusters by Passivation with Thiolates. *J. Phys. Chem. B* **2006**, *110*, 12218–12221.

- (71) Negishi, Y.; Chaki, N. K.; Shichibu, Y.; Whetten, R. L.; Tsukuda, T. Origin of Magic Stability of Thiolated Gold Clusters: A Case Study on $\text{Au}_{25}(\text{SC}_6\text{H}_{13})_{18}$. *J. Am. Chem. Soc.* **2007**, *129*, 11322–11323.
- (72) Jadzinsky, P. D.; Calero, G.; Ackerson, C. J.; Bushnell, D. A.; Kornberg, R. D. Structure of a Thiol Monolayer–Protected Gold Nanoparticle at 1.1 Å Resolution. *Science* **2007**, *318*, 430–433.
- (73) Heaven, M. W.; Dass, A.; White, P. S.; Holt, K. M.; Murray, R. W. Crystal Structure of the Gold Nanoparticle $[\text{N}(\text{C}_6\text{H}_{17})_4]\text{Au}_{25}(\text{SCH}_2\text{CH}_2\text{Ph})_{18}$. *J. Am. Chem. Soc.* **2008**, *130*, 3754–3755.
- (74) Akola, J.; Walter, M.; Whetten, R. L.; Häkkinen, H.; Grönbeck, H. On the Structure of Thiolate-Protected Au_{25} . *J. Am. Chem. Soc.* **2008**, *130*, 3756–3757.
- (75) Jin, R.; Egusa, S.; Scherer, N. F. Thermally-Induced Formation of Atomic Au Clusters and Conversion into Nanocubes. *J. Am. Chem. Soc.* **2004**, *126*, 9900–9901.
- (76) Zhou, R.; Shi, M.; Chen, X.; Wang, M.; Chen, H. Atomically Monodispersed and Fluorescent Sub-Nanometer Gold Clusters Created by Biomolecule-Assisted Etching of Nanometer-Sized Gold Particles and Rods. *Chem. - Eur. J.* **2009**, *15*, 4944–4951.
- (77) Duan, H.; Nie, S. Etching Colloidal Gold Nanocrystals with Hyperbranched and Multivalent Polymers: A New Route to Fluorescent and Water-Soluble Atomic Clusters. *J. Am. Chem. Soc.* **2007**, *129*, 2412–2413.
- (78) Zheng, J.; Dickson, R. M. Individual Water-Soluble Dendrimer–Encapsulated Silver Nanodot Fluorescence. *J. Am. Chem. Soc.* **2002**, *124*, 13982–13983.
- (79) Wu, Z.; Chen, J.; Jin, R. One-Pot Synthesis of $\text{Au}_{25}(\text{SG})_{18}$ 2- and 4-nm Gold Nanoparticles and Comparison of their Size-Dependent Properties. *Adv. Funct. Mater.* **2011**, *21*, 177–183.
- (80) Schaaff, T. G.; Knight, G.; Shafigullin, M. N.; Borkman, R. F.; Whetten, R. L. Isolation and Selected Properties of a 10.4 kDa Gold:Glutathione Cluster Compound. *J. Phys. Chem. B* **1998**, *102*, 10643–10646.
- (81) Tkachenko, A. G.; Xie, H.; Coleman, D.; Glomm, W.; Ryan, J.; Anderson, M. F.; Franzen, S.; Feldheim, D. L. Multifunctional Gold Nanoparticle–Peptide Complexes for Nuclear Targeting. *J. Am. Chem. Soc.* **2003**, *125*, 4700–4701.
- (82) Xie, J.; Zheng, Y.; Ying, J. Y. Protein-Directed Synthesis of Highly Fluorescent Gold Nanoclusters. *J. Am. Chem. Soc.* **2009**, *131*, 888–889.
- (83) Hayat, M. A. *Colloidal Gold: Principles, Methods, and Applications*; Harcourt Brace Jovanovich Publishers: San Diego, CA, USA, 1989.
- (84) Turkevich, J.; Stevenson, P. C.; Hillier, J. Nucleation and Growth Process in the Synthesis of Colloidal Gold. *Discuss. Faraday Soc.* **1951**, *11*, 55–80.
- (85) Frens, G. Particle Size and Sol Stability in Metal Colloids. *Kolloid Z. Z. Polym.* **1972**, *250*, 736–741.
- (86) Njoki, P. N.; Lim, I. -I. S.; Mott, D.; Park, H.-Y.; Khan, B.; Mishra, S.; Sujakumar, R.; Luo, J.; Zhong, C.-J. Size Correlation of Optical and Spectroscopic Properties for Gold Nanoparticles. *J. Phys. Chem. C* **2007**, *111*, 14664–14669.
- (87) Ji, X.; Song, X.; Li, J.; Bai, Y.; Yang, W.; Peng, X. Size Control of Gold Nanocrystals in Citrate Reduction: The Third Role of Citrate. *J. Am. Chem. Soc.* **2007**, *129*, 13939–13948.
- (88) Ojea-Jiménez, I.; Bastús, N. G.; Puentes, V. Influence of the Sequence of the Reagents Addition in the Citrate-Mediated Synthesis of Gold Nanoparticles. *J. Phys. Chem. C* **2011**, *115*, 15752–15757.
- (89) Sivaraman, S. K.; Kumar, S.; Santhanam, V. Monodisperse Sub-10 nm Gold Nanoparticles by Reversing the Order of Addition in Turkevich Method — the Role of Chloroauric Acid. *J. Colloid Interface Sci.* **2011**, *361*, 543–547.
- (90) Ojea-Jiménez, I.; Romero, F. M.; Bastús, N. G.; Puentes, V. Small Gold Nanoparticles Synthesized with Sodium Citrate and Heavy Water: Insights into the Reaction Mechanism. *J. Phys. Chem. C* **2010**, *114*, 1800–1804.
- (91) Brust, M.; Walker, M.; Bethell, D.; Schiffrin, D. J.; Whyman, R. Synthesis of Thiol-Derivatised Gold Nanoparticles in a Two-Phase Liquid-Liquid System. *J. Chem. Soc., Chem. Commun.* **1994**, 801–802.
- (92) Leff, D. V.; Ohara, P. C.; Heath, J. R.; Gelbart, W. M. Thermodynamic Control of Gold Nanocrystal Size: Experiment and Theory. *J. Phys. Chem.* **1995**, *99*, 7036–7041.
- (93) Maye, M. M.; Zheng, W.; Leibowitz, F. L.; Ly, N. K.; Zhong, C.-J. Heating-Induced Evolution of Thiolate–Encapsulated Gold Nanoparticles: A Strategy for Size and Shape Manipulation. *Langmuir* **2000**, *16*, 490–497.
- (94) Maye, M. M.; Zhong, C.-J. Manipulating Core-Shell Reactivities for Processing Nanoparticle Size and Shapes. *J. Mater. Chem.* **2000**, *10*, 1895–1901.
- (95) Teranishi, T.; Hasegawa, S.; Shimizu, T.; Miyake, M. Heat-Induced Size Evolution of Gold Nanoparticles in the Solid State. *Adv. Mater.* **2001**, *13*, 1699–1701.
- (96) Shimizu, T.; Teranishi, T.; Hasegawa, S.; Miyake, M. Size Evolution of Alkanethiol–Protected Gold Nanoparticles by Heat Treatment in the Solid State. *J. Phys. Chem. B* **2003**, *107*, 2719–2724.
- (97) Jana, N. R.; Gearheart, L.; Murphy, C. J. Seeding Growth for Size Control of 5–40 nm Diameter Gold Nanoparticles. *Langmuir* **2001**, *17*, 6782–6786.
- (98) Rodríguez-Fernández, J.; Pérez-Juste, J.; García de Abajo, F. J.; Liz-Marzán, L. M. Seeded Growth of Submicron Au Colloids with Quadrupole Plasmon Resonance Modes. *Langmuir* **2006**, *22*, 7007–7010.
- (99) Niu, W.; Zheng, S.; Wang, D.; Liu, X.; Li, H.; Han, S.; Chen, J.; Tang, Z.; Xu, G. Selective Synthesis of Single-Crystalline Rhombic Dodecahedral, Octahedra, and Cubic Gold Nanocrystals. *J. Am. Chem. Soc.* **2009**, *131*, 697–703.
- (100) Zheng, Y.; Ma, Y.; Zeng, J.; Zhong, X.; Jin, M.; Li, Z.-Y.; Xia, Y. Seed-Mediated Synthesis of Single-Crystal Gold Nanospheres with Controlled Diameters in the Range 5–30 nm and their Self-Assembly upon Dilution. *Chem. - Asian J.* **2013**, *8*, 792–799.
- (101) Eguchi, M.; Mitsui, D.; Wu, H.-L.; Sato, R.; Teranishi, T. Simple Reductant Concentration-Dependent Shape Control of Polyhedral Gold Nanoparticles and their Plasmonic Properties. *Langmuir* **2012**, *28*, 9021–9026.
- (102) Lee, Y.-J.; Schade, N. B.; Sun, L.; Fan, J. A.; Bae, D. R.; Mariscal, M. M.; Lee, G.; Capasso, F.; Sacanna, S.; Manoharan, V. N.; Yi, G.-R. Ultrasoft, Highly Spherical Monocrystalline Gold Particles for Precision Plasmonics. *ACS Nano* **2013**, *7*, 11064–11070.
- (103) O'Brien, M. N.; Jones, M. R.; Brown, K. A.; Mirkin, C. A. Universal Noble Metal Nanoparticle Seeds Realized through Iterative Reductive Growth and Oxidative Dissolution Reactions. *J. Am. Chem. Soc.* **2014**, *136*, 7603–7606.
- (104) Ma, Y.; Li, W.; Cho, E. C.; Li, Z.; Yu, T.; Zeng, J.; Xie, Z.; Xia, Y. Au@Ag Core-Shell Nanocubes with Finely Tuned and Well-Controlled Sizes, Shell Thicknesses, and Optical Properties. *ACS Nano* **2010**, *4*, 6725–6734.
- (105) Li, J.; Zheng, Y.; Zeng, J.; Xia, Y. Controlling the Size and Morphology of Au@Pd Core-Shell Nanocrystals by Manipulating the Kinetics of Seeded Growth. *Chem. - Eur. J.* **2012**, *18*, 8150–8156.
- (106) Zheng, Y.; Zhong, X.; Li, Z.; Xia, Y. Successive, Seed-Mediated Growth for the Synthesis of Single-Crystal Gold Nanospheres with Uniform Diameters Controlled in the Range of 5–150 nm. *Part. Part. Syst. Charact.* **2014**, *31*, 266–273.
- (107) Hu, M.; Chen, J.; Li, Z.-Y.; Au, L.; Hartland, G. V.; Li, X.; Marquez, M.; Xia, Y. Gold Nanostructures: Engineering their Plasmonic Properties for Biomedical Applications. *Chem. Soc. Rev.* **2006**, *35*, 1084–1094.
- (108) Murphy, C. J.; Sau, T. K.; Gole, A. M.; Orendorff, C. J.; Gao, J.; Gou, L.; Hunyadi, S. E.; Li, T. Anisotropic Metal Nanoparticles: Synthesis, Assembly, and Optical Applications. *J. Phys. Chem. B* **2005**, *109*, 13857–13870.
- (109) Gole, A.; Murphy, C. J. Seed-Mediated Synthesis of Gold Nanorods: Role of the Size and Nature of the Seed. *Chem. Mater.* **2004**, *16*, 3633–3640.
- (110) Martin, C. R. Membrane-Based Synthesis of Nanomaterials. *Chem. Mater.* **1996**, *8*, 1739–1746.
- (111) Hornyak, G. L.; Patrissi, C. J.; Martin, C. R. Fabrication, Characterization, and Optical Properties of Gold Nanoparticle/Porous

Alumina Composites: The Nonscattering Maxwell-Garnett Limit. *J. Phys. Chem. B* **1997**, *101*, 1548–1555.

(112) Hurst, S. J.; Payne, E. K.; Qin, L.; Mirkin, C. A. Multisegmented One-Dimensional Nanorods Prepared by Hard-Template Synthetic Methods. *Angew. Chem., Int. Ed.* **2006**, *45*, 2672–2692.

(113) van der Zande, B. M. I.; Böhmer, M. R.; Fokkink, L. G. J.; Schönenberger, C. Colloidal Dispersions of Gold Rods: Synthesis and Optical Properties. *Langmuir* **2000**, *16*, 451–458.

(114) Nicewarner-Peña, S. R.; Freeman, R. G.; Reiss, B. D.; He, L.; Peña, D. J.; Walton, I. D.; Cromer, R.; Keating, C. D.; Natan, M. J. Submicrometer Metallic Barcodes. *Science* **2001**, *294*, 137–141.

(115) Banholzer, M. J.; Qin, L.; Millstone, J. E.; Osberg, K. D.; Mirkin, C. A. On-Wire Lithography: Synthesis, Encoding and Biological Applications. *Nat. Protoc.* **2009**, *4*, 838–848.

(116) Kim, K.; Xu, X.; Guo, J.; Fan, D. L. Ultrahigh-Speed Rotating Nanoelectromechanical System Devices Assembled from Nanoscale Building Blocks. *Nat. Commun.* **2014**, *5*, 3632.

(117) Kim, M. R.; Lee, D. K.; Jang, D.-J. Template-Based Electrochemically Controlled Growth of Segmented Multimetal Nanorods. *J. Nanomater.* **2010**, *2010*, 203756.

(118) Martin, B. R.; Dermody, D. J.; Reiss, B. D.; Fang, M.; Lyon, L. A.; Natan, M. J.; Mallouk, T. E. Orthogonal Self-Assembly on Colloidal Gold-Platinum Nanorods. *Adv. Mater.* **1999**, *11*, 1021–1025.

(119) Chang, S.-S.; Shih, C.-W.; Chen, C.-D.; Lai, W.-C.; Wang, C. R. C. The Shape Transition of Gold Nanorods. *Langmuir* **1999**, *15*, 701–709.

(120) Yu, Y. -Y.; Chang, S.-S.; Lee, C.-L.; Wang, C. R. C. Gold Nanorods: Electrochemical Synthesis and Optical Properties. *J. Phys. Chem. B* **1997**, *101*, 6661–6664.

(121) Jana, N. R.; Gearheart, L.; Murphy, C. J. Seed-Mediated Growth Approach for Shape-Controlled Synthesis of Spheroidal and Rod-Like Gold Nanoparticles Using a Surfactant Template. *Adv. Mater.* **2001**, *13*, 1389–1393.

(122) Murphy, C. J.; Gole, A. M.; Hunyadi, S. E.; Orendorff, C. J. One-Dimensional Colloidal Gold and Silver Nanostructures. *Inorg. Chem.* **2006**, *45*, 7544–7554.

(123) Orendorff, C. J.; Murphy, C. J. Quantitation of Metal Content in the Silver-Assisted Growth of Gold Nanorods. *J. Phys. Chem. B* **2006**, *110*, 3990–3994.

(124) Park, K.; Drummy, L. F.; Wadams, R. C.; Koerner, H.; Nepal, D.; Fabris, L.; Vaia, R. A. Growth Mechanism of Gold Nanorods. *Chem. Mater.* **2013**, *25*, 555–563.

(125) Pérez-Juste, J.; Liz-Marzán, L. M.; Carnie, S.; Chan, D. Y. C.; Mulvaney, P. Electric-Field-Directed Growth of Gold Nanorods in Aqueous Surfactant Solutions. *Adv. Funct. Mater.* **2004**, *14*, 571–579.

(126) Jana, N. R.; Gearheart, L.; Murphy, C. J. Wet Chemical Synthesis of High Aspect Ratio Cylindrical Gold Nanorods. *J. Phys. Chem. B* **2001**, *105*, 4065–4067.

(127) Nikoobakht, B.; El-Sayed, M. A. Preparation and Growth Mechanism of Gold Nanorods (NRs) Using Seed-Mediated Growth Method. *Chem. Mater.* **2003**, *15*, 1957–1962.

(128) Zweifel, D. A.; Wei, A. Sulfide-Arrested Growth of Gold Nanorods. *Chem. Mater.* **2005**, *17*, 4256–4261.

(129) Ye, X.; Jin, L.; Caglayan, H.; Chen, J.; Xing, G.; Zheng, C.; Doan-Nguyen, V.; Kang, Y.; Engheta, N.; Kagan, C. R.; Murray, C. B. Improved Size-Tunable Synthesis of Monodisperse Gold Nanorods through the Use of Aromatic Additives. *ACS Nano* **2012**, *6*, 2804–2817.

(130) Smith, D. K.; Korgel, B. A. The Importance of the CTAB Surfactant on the Colloidal Seed-Mediated Synthesis of Gold Nanorods. *Langmuir* **2008**, *24*, 644–649.

(131) Esumi, K.; Matsuhisa, K.; Torigoe, K. Preparation of Rodlike Gold Particles by UV Irradiation Using Cationic Micelles as a Template. *Langmuir* **1995**, *11*, 3285–3287.

(132) Kim, F.; Song, J. H.; Yang, P. Photochemical Synthesis of Gold Nanorods. *J. Am. Chem. Soc.* **2002**, *124*, 14316–14317.

(133) Miranda, O. R.; Ahmadi, T. S. Effects of Intensity and Energy of CW UV Light on the Growth of Gold Nanorods. *J. Phys. Chem. B* **2005**, *109*, 15724–15734.

(134) Canizal, G.; Ascencio, J. A.; Gardea-Torresday, J.; Yacamán, M. J. Multiple Twinned Gold Nanorods Grown by Bio-Reduction Techniques. *J. Nanopart. Res.* **2001**, *3*, 475–481.

(135) Zhu, Y.-J.; Hu, X.-L. Microwave-Polyol Preparation of Single-Crystalline Gold Nanorods and Nanowires. *Chem. Lett.* **2003**, *32*, 1140–1141.

(136) Tsuji, M.; Hashimoto, M.; Nishizawa, Y.; Kubokawa, M.; Tsuji, T. Microwave-Assisted Synthesis of Metallic Nanostructures in Solution. *Chem. - Eur. J.* **2005**, *11*, 440–452.

(137) Cao, J.; Ma, X.; Zheng, M.; Liu, J.; Ji, H. Solvothermal Preparation of Single-Crystalline Gold Nanorods in Novel Non-aqueous Microemulsions. *Chem. Lett.* **2005**, *34*, 730–731.

(138) Millstone, J. E.; Hurst, S. J.; Métraux, G. S.; Cutler, J. I.; Mirkin, C. A. Colloidal Gold and Silver Triangular Nanoprisms. *Small* **2009**, *5*, 646–664.

(139) Antonietti, M. *Topics in Current Chemistry*; Springer: Berlin, 2003; Vol. 226.

(140) Pastoriza-Santos, I.; Alvarez-Puebla, R. A.; Liz-Marzán, L. M. Synthetic Routes and Plasmonic Properties of Noble Metal Nanoplates. *Eur. J. Inorg. Chem.* **2010**, *2010*, 4288–4297.

(141) Malikova, N.; Pastoriza-Santos, I.; Schierhorn, M.; Kotov, N. A.; Liz-Marzán, L. M. Layer-by-Layer Assembled Mixed Spherical and Planar Gold Nanoparticles: Control of Interparticle Interactions. *Langmuir* **2002**, *18*, 3694–3697.

(142) Shao, Y.; Jin, Y.; Dong, S. Synthesis of Gold Nanoplates by Aspartate Reduction of Gold Chloride. *Chem. Commun.* **2004**, 1104–1105.

(143) Tsuji, M.; Hashimoto, M.; Nishizawa, Y.; Tsuji, T. Preparation of Gold Nanoplates by a Microwave-Polyol Method. *Chem. Lett.* **2003**, *32*, 1114–1115.

(144) Sarma, T. K.; Chattopadhyay, A. Starch-Mediated Shape-Selective of Au Nanoparticles with Tunable Longitudinal Plasmon Resonance. *Langmuir* **2004**, *20*, 3520–3524.

(145) Millstone, J. E.; Park, S.; Shuford, K. L.; Qin, L.; Schatz, G. C.; Mirkin, C. A. Observation of a Quadrupole Plasmon Mode for a Colloidal Solution of Gold Nanoprisms. *J. Am. Chem. Soc.* **2005**, *127*, 5312–5313.

(146) Millstone, J. E.; Métraux, G. S.; Mirkin, C. A. Controlling the Edge Length of Gold Nanoprisms via a Seed-Mediated Approach. *Adv. Funct. Mater.* **2006**, *16*, 1209–1214.

(147) Millstone, J. E.; Wei, W.; Jones, M. R.; Yoo, H.; Mirkin, C. A. Iodide Ions Control Seed-Mediated Growth of Anisotropic Gold Nanoparticles. *Nano Lett.* **2008**, *8*, 2526–2529.

(148) Zhang, L.; Huang, C. Z.; Li, Y. F.; Li, Q. Morphology Control and Structural Characterization of Au Crystals: From Twinned Tabular Crystals and Single-Crystalline Nanoplates to Multitwinned Decahedra. *Cryst. Growth Des.* **2009**, *9*, 3211–3217.

(149) Ha, T. H.; Koo, H.-J.; Chung, B. H. Shape-Controlled Syntheses of Gold Nanoprisms and Nanorods Influenced by Specific Adsorption of Halide Ions. *J. Phys. Chem. C* **2007**, *111*, 1123–1130.

(150) Chu, H.-C.; Kuo, C.-H.; Huang, M. H. Thermal Aqueous Solution Approach for the Synthesis of Triangular and Hexagonal Gold Nanoplates with Three Different Size Ranges. *Inorg. Chem.* **2006**, *45*, 808–813.

(151) Black, K. C. L.; Wang, Y.; Luehmann, H. P.; Cai, X.; Xing, W.; Pang, B.; Zhao, Y.; Cutler, C. S.; Wang, L. V.; Liu, Y.; Xia, Y. Radioactive ¹⁹⁸Au-Doped Nanostructures with Different Shapes for *in Vivo* Analyses of their Biodistribution, Tumor Uptake, and Intratumoral Distribution. *ACS Nano* **2014**, *8*, 4385–4394.

(152) Chen, L.; Ji, F.; Xu, Y.; He, L.; Mi, Y.; Bao, F.; Sun, B.; Zhang, X.; Zhang, Q. High-Yield Seedless Synthesis of Triangular Gold Nanoplates through Oxidative Etching. *Nano Lett.* **2014**, *14*, 7201–7206.

(153) Shankar, S. S.; Bhargava, S.; Sastry, M. Synthesis of Gold Nanospheres and Nanotriangles by the Turkevich Approach. *J. Nanosci. Nanotechnol.* **2005**, *5*, 1721–1727.

- (154) Shankar, S. S.; Rai, A.; Ankamwar, B.; Singh, A.; Ahmad, A.; Sastry, M. Biological Synthesis of Triangular Gold Nanoprisms. *Nat. Mater.* **2004**, *3*, 482–488.
- (155) Shankar, S. S.; Rai, A.; Ahmad, A.; Sastry, M. Controlling the Optical Properties of Lemongrass Extract Synthesized Gold Nanotriangles and Potential Application in Infrared-Absorbing Optical Coating. *Chem. Mater.* **2005**, *17*, 566–572.
- (156) Xie, J.; Lee, J. Y.; Wang, D. I. C. Synthesis of Single-Crystalline Gold Nanoplates in Aqueous Solutions through Biomineralization by Serum Albumin Protein. *J. Phys. Chem. C* **2007**, *111*, 10226–10232.
- (157) Tan, Y. N.; Lee, J. Y.; Wang, D. I. C. Aspartic Acid Synthesis of Crystalline Gold Nanoplates, Nanoribbons, and Nanowires in Aqueous Solutions. *J. Phys. Chem. C* **2008**, *112*, 5463–5470.
- (158) Baigorri, R.; García-Mina, J. M.; Aroca, R. F.; Alvarez-Puebla, R. A. Optical Enhancing Properties of Anisotropic Gold Nanoplates Prepared with Different Fractions of a Natural Humic Substance. *Chem. Mater.* **2008**, *20*, 1516–1521.
- (159) Au, L.; Lim, B.; Colletti, P.; Jun, Y.-S.; Xia, Y. Synthesis of Gold Microplates Using Bovine Serum Albumin as a Reductant and a Stabilizer. *Chem. - Asian J.* **2010**, *5*, 123–129.
- (160) Xiong, Y.; Washio, I.; Chen, J.; Cai, H.; Li, Z.-Y.; Xia, Y. Poly(vinyl pyrrolidone): A Dual Functional Reductant and Stabilizer for the Facile Synthesis of Noble Metal Nanoplates in Aqueous Solutions. *Langmuir* **2006**, *22*, 8563–8570.
- (161) Lim, B.; Camargo, P. H. C.; Xia, Y. Mechanistic Study of the Synthesis of Au Nanotadpoles, Nanokites, and Microplates by Reducing Aqueous HAuCl₄ with Poly(vinyl pyrrolidone). *Langmuir* **2008**, *24*, 10437–10442.
- (162) Kan, C.; Zhu, X.; Wang, G. Single-Crystalline Gold Microplates: Synthesis, Characterization, and Thermal Stability. *J. Phys. Chem. B* **2006**, *110*, 4651–4656.
- (163) Zhu, J.; Jin, X.-L. Electrochemical Synthesis of Gold Triangular Nanoplates and Self-Organized into Rhombic Nanostructures. *Superlattices Microstruct.* **2007**, *41*, 271–276.
- (164) Li, C.; Cai, W.; Li, Y.; Hu, J.; Liu, P. Ultrasonically Induced Au Nanoprisms and their Size Manipulation based on Aging. *J. Phys. Chem. B* **2006**, *110*, 1546–1552.
- (165) Takezaki, M.; Kida, R.; Kato, Y.; Tominaga, T. Preparations of Triangular Gold Nanoplates by Chemical and Photoreduction Methods. *Chem. Lett.* **2009**, *38*, 1022–1023.
- (166) Oldenburg, S. J.; Averitt, R. D.; Westcott, S. L.; Halas, N. J. Nanoengineering of Optical Resonances. *Chem. Phys. Lett.* **1998**, *288*, 243–247.
- (167) Liu, H.; Chen, D.; Li, L.; Liu, T.; Tan, L.; Wu, X.; Tang, F. Multifunctional Gold Nanoshells on Silica Nanorattles: A Platform for the Combination of Photothermal Therapy and Chemotherapy with Low Systemic Toxicity. *Angew. Chem., Int. Ed.* **2011**, *50*, 891–895.
- (168) Wang, H.; Brandl, D. W.; Nordlander, P.; Halas, N. J. Plasmonic Nanostructures: Artificial Molecules. *Acc. Chem. Res.* **2007**, *40*, 53–62.
- (169) Shi, W.; Sahoo, Y.; Swihart, M. T.; Prasad, P. N. Gold Nanoshells on Polystyrene Cores for Control of Surface Plasmon Resonance. *Langmuir* **2005**, *21*, 1610–1617.
- (170) Jin, Y.; Gao, X. Plasmonic Fluorescent Quantum Dots. *Nat. Nanotechnol.* **2009**, *4*, 571–576.
- (171) Jin, Y.; Gao, X. Spectrally Tunable Leakage-Free Gold Nanocapsules. *J. Am. Chem. Soc.* **2009**, *131*, 17774–17776.
- (172) Ji, X.; Shao, R.; Elliott, A. M.; Stafford, R. J.; Esparza-Coss, E.; Bankson, J. A.; Liang, G.; Luo, Z.-P.; Park, K.; Markert, J. T.; Li, C. Biofunctional Gold Nanoshells with a Superparamagnetic Iron Oxide-Silica Core Suitable for Both MR Imaging and Photothermal Therapy. *J. Phys. Chem. C* **2007**, *111*, 6245–6251.
- (173) Jin, Y.; Jia, C.; Huang, S.-W.; O'Donnell, M.; Gao, X. Multifunctional Nanoparticles as Coupled Contrast Agents. *Nat. Commun.* **2010**, *1*, 41.
- (174) Charnay, C.; Lee, A.; Man, S.-Q.; Moran, C. E.; Radloff, C.; Bradley, R. K.; Halas, N. J. Reduced Symmetry Metallo-dielectric Nanoparticles: Chemical Synthesis and Plasmonic Properties. *J. Phys. Chem. B* **2003**, *107*, 7327–7333.
- (175) Zhou, H. S.; Honma, I.; Komiyama, H.; Haus, J. W. Controlled Synthesis and Quantum-Size Effect in Gold-Coated Nanoparticles. *Phys. Rev. B: Condens. Matter Mater. Phys.* **1994**, *50*, 12052–12056.
- (176) Hirsch, L. R.; Gobin, A. M.; Lowery, A. R.; Tam, F.; Drezek, R. A.; Halas, N. J.; West, J. L. Metal Nanoshells. *Ann. Biomed. Eng.* **2006**, *34*, 15–22.
- (177) Stöber, W.; Fink, A.; Bohn, E. Controlled Growth of Monodisperse Silica Spheres in the Micron Size Range. *J. Colloid Interface Sci.* **1968**, *26*, 62–69.
- (178) Park, H.; Yang, J.; Seo, S.; Kim, K.; Suh, J.; Kim, D.; Haam, S.; Yoo, K.-H. Multifunctional Nanoparticles for Photothermally Controlled Drug Delivery and Magnetic Resonance Imaging Enhancement. *Small* **2008**, *4*, 192–196.
- (179) Park, H.; Yang, J.; Lee, J.; Haam, S.; Choi, I.-H.; Yoo, K.-H. Multifunctional Nanoparticles for Combined Doxorubicin and Photothermal Treatments. *ACS Nano* **2009**, *3*, 2919–2926.
- (180) Ke, H.; Wang, J.; Dai, Z.; Jin, Y.; Qu, E.; Xing, Z.; Guo, C.; Yue, X.; Liu, J. Gold-Nanoshelled Microcapsules: A Theranostic Agent for Ultrasound Contrast Imaging and Photothermal Therapy. *Angew. Chem., Int. Ed.* **2011**, *50*, 3017–3021.
- (181) Bai, M.-Y.; Cheng, Y.-J.; Wickline, S. A.; Xia, Y. Colloidal Hollow Spheres of Conducting Polymers with Smooth Surface and Uniform, Controllable Sizes. *Small* **2009**, *5*, 1747–1752.
- (182) Radt, B.; Smith, T. A.; Caruso, F. Optically Addressable Nanostructured Capsules. *Adv. Mater.* **2004**, *16*, 2184–2189.
- (183) Angelatos, A. S.; Radt, B.; Caruso, F. Light-Responsive Polyelectrolyte/Gold Nanoparticle Microcapsules. *J. Phys. Chem. B* **2005**, *109*, 3071–3076.
- (184) Yang, Y.; Liu, J.; Fu, Z.-W.; Qin, D. Galvanic Replacement-Free Deposition of Au on Ag for Core-Shell Nanocubes with Enhanced Chemical Stability and SERS Activity. *J. Am. Chem. Soc.* **2014**, *136*, 8153–8156.
- (185) Skrabalak, S. E.; Chen, J.; Sun, Y.; Lu, X.; Au, L.; Cobley, L. M.; Xia, Y. Gold Nanocages: Synthesis, Properties, and Applications. *Acc. Chem. Res.* **2008**, *41*, 1587–1595.
- (186) Sun, Y.; Xia, Y. Shape-Controlled Synthesis of Gold and Silver Nanoparticles. *Science* **2002**, *298*, 2176–2179.
- (187) Wan, D.; Xia, X.; Wang, Y.; Xia, Y. Robust Synthesis of Gold Cubic Nanoframes through a Combination of Galvanic Replacement, Gold Deposition, and Silver Dealloying. *Small* **2013**, *9*, 3111–3117.
- (188) Au, L.; Chen, Y.; Zhou, F.; Camargo, P. H. C.; Lim, B.; Li, Z.-Y.; Ginger, D. S.; Xia, Y. Synthesis and Optical Properties of Cubic Gold Nanoframes. *Nano Res.* **2008**, *1*, 441–449.
- (189) Graf, C.; van Blaaderen, A. Metallo-dielectric Colloidal Core-Shell Particles for Photonic Applications. *Langmuir* **2002**, *18*, 524–534.
- (190) Urries, I.; Muñoz, C.; Gomez, L.; Marquina, C.; Sebastian, V.; Arruebo, M.; Santamaria, J. Magneto-Plasmonic Nanoparticles as Theranostic Platforms for Magnetic Resonance Imaging, Drug Delivery and NIR Hyperthermia Applications. *Nanoscale* **2014**, *6*, 9230–9240.
- (191) Landon, P. B.; Mo, A. H.; Zhang, C.; Emerson, C. D.; Printz, A. D.; Gomez, A. F.; DeLaTorre, C. J.; Colburn, D. A. M.; Anzenberg, P.; Eliceiri, M.; O'Connell, C.; Lal, R. Designing Hollow Nano Gold Golf Balls. *ACS Appl. Mater. Interfaces* **2014**, *6*, 9937–9941.
- (192) Wang, Y.; Wan, D.; Xie, S.; Xia, X.; Huang, C. Z.; Xia, Y. Synthesis of Silver Octahedra with Controlled Sizes and Optical Properties via Seed-Mediated Growth. *ACS Nano* **2013**, *7*, 4586–4594.
- (193) Lu, X.; Au, L.; McLellan, J.; Li, Z.-Y.; Marquez, M.; Xia, Y. Fabrication of Cubic Nanocages and Nanoframes by Dealloying Au/Ag Alloy Nanoboxes with an Aqueous Etchant Based on Fe(NO₃)₃ or NH₄OH. *Nano Lett.* **2007**, *7*, 1764–1769.
- (194) Sun, Y.; Mayers, B. T.; Xia, Y. Template-Engaged Replacement Reaction: A One-Step Approach to the Large-Scale Synthesis of Metal Nanostructures with Hollow Interiors. *Nano Lett.* **2002**, *2*, 481–485.
- (195) Sun, Y.; Xia, Y. Mechanistic Study on the Replacement Reaction between Silver Nanostructures and Chloroauric Acid in Aqueous Medium. *J. Am. Chem. Soc.* **2004**, *126*, 3892–3901.

- (196) Wang, Y.; Zheng, Y.; Huang, C. Z.; Xia, Y. Synthesis of Ag Nanocubes 18–32 nm in Edge Length: The Effects of Polyol on Reduction Kinetics, Size Control, and Reproducibility. *J. Am. Chem. Soc.* **2013**, *135*, 1941–1951.
- (197) Cobley, C. M.; Xia, Y. Engineering the Properties of Metal Nanostructures via Galvanic Replacement Reactions. *Mater. Sci. Eng., R* **2010**, *70*, 44–62.
- (198) Zhang, Q.; Li, W.; Moran, C.; Zeng, J.; Chen, J.; Wen, L.-P.; Xia, Y. Seed-Mediated Synthesis of Ag Nanocubes with Controllable Edge Lengths in the Range of 30–200 nm and Comparison of their Optical Properties. *J. Am. Chem. Soc.* **2010**, *132*, 11372–11378.
- (199) Zhang, Q.; Li, W.; Wen, L.-P.; Chen, J.; Xia, Y. Facile Synthesis of Ag Nanocubes of 30 to 70 nm in Edge Length with CF_3COOAg as a Precursor. *Chem. - Eur. J.* **2010**, *16*, 10234–10239.
- (200) Chen, J.; Yang, M.; Zhang, Q.; Cho, E. C.; Cobley, C. M.; Kim, C.; Glaus, C.; Wang, L. V.; Welch, M. J.; Xia, Y. Gold Nanocages: A Novel Class of Multifunctional Nanomaterials for Theranostic Applications. *Adv. Funct. Mater.* **2010**, *20*, 3684–3694.
- (201) Rycenga, M.; Cobley, C. M.; Zeng, J.; Li, W.; Moran, C. H.; Zhang, Q.; Qin, D.; Xia, Y. Controlling the Synthesis and Assembly of Silver Nanostructures for Plasmonic Applications. *Chem. Rev.* **2011**, *111*, 3669–3712.
- (202) Xia, Y.; Xiong, Y.; Lim, B.; Skrabalak, S. E. Shape-Controlled Synthesis of Metal Nanocrystals: Simple Chemistry Meets Complex Physics? *Angew. Chem., Int. Ed.* **2009**, *48*, 60–103.
- (203) Wiley, B.; Sun, Y.; Xia, Y. Synthesis of Silver Nanostructures with Controlled Shapes and Properties. *Acc. Chem. Res.* **2007**, *40*, 1067–1076.
- (204) Cobley, C. M.; Xia, Y. Engineering the Properties of Metal Nanostructures via Galvanic Replacement Reactions. *Mater. Sci. Eng., R* **2010**, *70*, 44–62.
- (205) Sun, Y.; Xia, Y. Alloying and Dealloying Processes Involved in the Preparation of Metal Nanoshells through a Galvanic Replacement Reaction. *Nano Lett.* **2003**, *3*, 1569–1572.
- (206) Zhang, Q.; Cobley, C. M.; Zeng, J.; Wen, L.-P.; Chen, J.; Xia, Y. Dissolving Ag from Au–Ag Alloy Nanoboxes with H_2O_2 : A Method for Both Tailoring the Optical Properties and Measuring the H_2O_2 Concentration. *J. Phys. Chem. C* **2010**, *114*, 6396–6400.
- (207) McEachran, M.; Keogh, D.; Pietrobon, B.; Cathcart, N.; Gourevich, I.; Coombs, N.; Kitaev, V. Ultrathin Gold Nanoframes through Surfactant-Free Templating of Faceted Pentagonal Silver Nanoparticles. *J. Am. Chem. Soc.* **2011**, *133*, 8066–8069.
- (208) Liang, H.-P.; Wan, L.-J.; Bai, C.-L.; Jiang, L. Gold Hollow Nanospheres: Tunable Surface Resonance Controlled by Interior-Cavity Sizes. *J. Phys. Chem. B* **2005**, *109*, 7795–7800.
- (209) Schwartzberg, A. M.; Olson, T. Y.; Talley, C. E.; Zhang, J. Z. Synthesis, Characterization, and Tunable Optical Properties of Hollow Gold Nanospheres. *J. Phys. Chem. B* **2006**, *110*, 19935–19944.
- (210) Melancon, M. P.; Lu, W.; Yang, Z.; Zhang, R.; Cheng, Z.; Elliot, A. M.; Stafford, J.; Olson, T.; Zhang, J. Z.; Li, C. *In Vitro* and *in Vivo* Targeting of Hollow Gold Nanoshells Directed at Epidermal Growth Factor Receptor for Photothermal Ablation Therapy. *Mol. Cancer Ther.* **2008**, *7*, 1730–1739.
- (211) You, J.; Zhang, G.; Li, C. Exceptionally High Payload of Doxorubicin in Hollow Gold Nanospheres for Near-Infrared Light-Triggered Drug Release. *ACS Nano* **2010**, *4*, 1033–1041.
- (212) Xie, S.; Jin, M.; Tao, J.; Wang, Y.; Xie, Z.; Zhu, Y.; Xia, Y. Synthesis and Characterization of $\text{Pd@M}_n\text{Cu}_{1-x}$ ($M = \text{Au}, \text{Pd}$, and Pt) Nanocages with Porous Walls and a Yolk-Shell Structure through Galvanic Replacement Reactions. *Chem. - Eur. J.* **2012**, *18*, 14974–14980.
- (213) Sun, Y.; Wiley, B.; Li, Z.-Y.; Xia, Y. Synthesis and Optical Properties of Nanorattles and Multiple-Walled Nanoshells/Nanotubes Made of Metal Alloys. *J. Am. Chem. Soc.* **2004**, *126*, 9399–9406.
- (214) Sun, Y.; Xia, Y. Multiple-Walled Nanotubes Made of Metals. *Adv. Mater.* **2004**, *16*, 264–268.
- (215) Yin, Y.; Rioux, R. M.; Erdonmez, C. K.; Hughes, S.; Somorjai, G. A.; Alivisatos, A. P. Formation of Hollow Nanocrystals through the Nanoscale Kirkendall Effect. *Science* **2004**, *304*, 711–714.
- (216) González, E.; Arbiol, J.; Puntès, V. F. Carving at the Nanoscale: Sequential Galvanic Exchange and Kirkendall Growth at Room Temperature. *Science* **2011**, *334*, 1377–1380.
- (217) Graf, C.; van Blaaderen, A. Metallo-dielectric Colloidal Core-Shell Particles for Photonic Applications. *Langmuir* **2002**, *18*, 524–534.
- (218) Ortac, I.; Simberg, D.; Yeh, Y.-S.; Yang, J.; Messmer, B.; Trogler, W. C.; Tsien, R. Y.; Esener, S. Dual-Porosity Hollow Nanoparticles for the Immunoprotection and Delivery of Nonhuman Enzymes. *Nano Lett.* **2014**, *14*, 3023–3032.
- (219) Chen, W. W.; Sun, X. H.; Wang, S. D.; Lee, S. T.; Teo, B. K. Etching Behavior of Silicon Nanowires with HF and NH_4F and Surface Characterization by Attenuated Total Reflection Fourier Transform Infrared Spectroscopy: Similarities and Differences between One-Dimensional and Two-Dimensional Silicon Surfaces. *J. Phys. Chem. B* **2005**, *109*, 10871–10879.
- (220) Loiola, A. R.; da Silva, L. R. D.; Cubillas, P.; Anderson, M. W. Synthesis and Characterization of Hierarchical Porous Materials Incorporating a Cubic Mesoporous Phase. *J. Mater. Chem.* **2008**, *18*, 4985–4993.
- (221) Velez, O. D.; Tessier, P. M.; Lenhoff, A. M.; Kaler, E. W. Materials: A Class of Porous Metallic Nanostructures. *Nature* **1999**, *401*, 548.
- (222) Shchukin, D. G.; Caruso, R. A. Template Synthesis of Porous Gold Microspheres. *Chem. Commun.* **2003**, 1478–1479.
- (223) Zhang, H.; Hussain, I.; Brust, M.; Cooper, A. I. Emulsion-Templated Gold Beads Using Gold Nanoparticles as Building Blocks. *Adv. Mater.* **2004**, *16*, 27–30.
- (224) Nyce, G. W.; Hayes, J. R.; Hamza, A. V.; Satcher, J. H. Synthesis and Characterization of Hierarchical Porous Gold Materials. *Chem. Mater.* **2007**, *19*, 344–346.
- (225) Zhao, B.; Collinson, M. M. Well-Defined Hierarchical Templates for Multimodal Porous Material Fabrication. *Chem. Mater.* **2010**, *22*, 4312–4319.
- (226) Saha, K.; Agasti, S. S.; Kim, C.; Li, X.; Rotello, V. M. Gold Nanoparticles in Chemical and Biological Sensing. *Chem. Rev.* **2012**, *112*, 2739–2779.
- (227) Khoury, C. G.; Vo-Dinh, T. Gold Nanostars for Surface-Enhanced Raman Scattering: Synthesis, Characterization and Optimization. *J. Phys. Chem. C* **2008**, *112*, 18849–18859.
- (228) Guerrero-Martínez, A.; Barbosa, S.; Pastoriza-Santos, I.; Liz-Marzán, L. M. Nanostars Shine Bright for You: Colloidal Synthesis, Properties and Applications of Branched Metallic Nanoparticles. *Curr. Opin. Colloid Interface Sci.* **2011**, *16*, 118–127.
- (229) Nalbant Esenturk, E.; Hight Walker, A. R. Surface-Enhanced Raman Scattering Spectroscopy via Gold Nanostars. *J. Raman Spectrosc.* **2009**, *40*, 86–91.
- (230) Rodríguez-Oliveros, R.; Sánchez-Gil, J. A. Gold Nanostars as Thermoplasmonic Nanoparticles for Optical Heating. *Opt. Express* **2012**, *20*, 621–626.
- (231) Cheng, L.; Wang, C.; Feng, L.; Yang, K.; Liu, Z. Functional Nanomaterials for Phototherapies of Cancer. *Chem. Rev.* **2014**, *114*, 10869–10939.
- (232) Grzelczak, M.; Pérez-Juste, J.; Mulvaney, P.; Liz-Marzán, L. M. Shape Control in Gold Nanoparticle Synthesis. *Chem. Soc. Rev.* **2008**, *37*, 1783–1791.
- (233) Zheng, Y.; Liu, W.; Lv, T.; Luo, M.; Hu, H.; Lu, P.; Choi, S.-I.; Zhang, C.; Tao, J.; Zhu, Y.; Li, Z.-Y.; Xia, Y. Seed-Mediated Synthesis of Gold Tetrahedra in High Purity and with Tunable, Well-Controlled Sizes. *Chem. - Asian J.* **2014**, *9*, 2635–2640.
- (234) Kim, F.; Connor, S.; Song, H.; Kuykendall, T.; Yang, P. Platonic Gold Nanocrystals. *Angew. Chem., Int. Ed.* **2004**, *43*, 3673–3677.
- (235) Personick, M. L.; Langille, M. R.; Zhang, J.; Harris, N.; Schatz, G. C.; Mirkin, C. A. Synthesis and Isolation of {110}-Faceted Gold Bipyramids and Rhombic Dodecahedra. *J. Am. Chem. Soc.* **2011**, *133*, 6170–6173.

- (236) Ming, T.; Feng, W.; Tang, Q.; Wang, F.; Sun, L.; Wang, J.; Yan, C. Growth of Tetrahedral Gold Nanocrystals with High-Index Facets. *J. Am. Chem. Soc.* **2009**, *131*, 16350–16351.
- (237) Seo, D.; Park, J. C.; Song, H. Polyhedra Gold Nanocrystals with O_h Symmetry: From Octahedra to Cubes. *J. Am. Chem. Soc.* **2006**, *128*, 14863–14870.
- (238) Seo, D.; Yoo, C. I.; Park, J. C.; Park, S. M.; Ryu, S.; Song, H. Directed Surface Overgrowth and Morphology Control of Polyhedral Gold Nanocrystals. *Angew. Chem., Int. Ed.* **2008**, *47*, 763–767.
- (239) Sau, T. K.; Murphy, C. J. Room Temperature, High-Yield Synthesis of Multiple Shapes of Gold Nanoparticles in Aqueous Solution. *J. Am. Chem. Soc.* **2004**, *126*, 8648–8649.
- (240) Carbó-Arribay, E.; Rodríguez-González, B.; Pacifico, J.; Pastoriza-Santos, I.; Pérez-Juste, J.; Liz-Marzán, L. M. Chemical Sharpening of Gold Nanorods: The Rod-to Octahedron Transition. *Angew. Chem., Int. Ed.* **2007**, *46*, 8983–8987.
- (241) Zhang, J.; Langille, M. R.; Personick, M. L.; Zhang, K.; Li, S.; Mirkin, C. A. Concave Cubic Gold Nanocrystals with High-Index Facets. *J. Am. Chem. Soc.* **2010**, *132*, 14012–14014.
- (242) Hao, F.; Nehl, C. L.; Hafner, J. H.; Nordlander, P. Plasmon Resonance of a Gold Nanostar. *Nano Lett.* **2007**, *7*, 729–732.
- (243) Cheng, K.; Kothapalli, S.-R.; Liu, H.; Koh, A. L.; Jokerst, J. V.; Jiang, H.; Yang, M.; Li, J.; Levi, J.; Wu, J. C.; Gambhir, S. S.; Cheng, Z. Construction and Validation of Nano Gold Tripods for Molecular Imaging of Living Subjects. *J. Am. Chem. Soc.* **2014**, *136*, 3560–3571.
- (244) Dam, D. H. M.; Culver, K. S. B.; Odom, T. W. Grafting Aptamers onto Gold Nanostars Increases *in Vitro* Efficacy in a Wide Range of Cancer Cell Types. *Mol. Pharmaceutics* **2014**, *11*, 580–587.
- (245) Dam, D. H. M.; Lee, R. C.; Odom, T. W. G. Improved *in Vitro* Efficacy of Gold Nanoconstructs by Increased Loading of G-Quadruplex Aptamer. *Nano Lett.* **2014**, *14*, 2843–2848.
- (246) Chen, S.; Wang, Z. L.; Ballato, J.; Foulger, S. H.; Carroll, D. L. Monopod, Bipod, Tripod, and Tetrapod Gold Nanocrystals. *J. Am. Chem. Soc.* **2003**, *125*, 16186–16187.
- (247) Xie, J.; Zhang, Q.; Lee, J. Y.; Wang, D. I. C. The Synthesis of SERS-Active Gold Nanoflower Tags for *in Vivo* Applications. *ACS Nano* **2008**, *2*, 2473–2480.
- (248) Barbosa, S.; Agrawal, A.; Rodríguez-Lorenzo, L.; Pastoriza-Santos, I.; Alvarez-Puebla, R. A.; Kornowski, A.; Weller, H.; Liz-Marzán, L. M. Tuning Size and Sensing Properties in Colloidal Gold Nanostars. *Langmuir* **2010**, *26*, 14943–14950.
- (249) Nehl, C. L.; Liao, H.; Hafner, J. H. Optical Properties of Star-Shaped Gold Nanoparticles. *Nano Lett.* **2006**, *6*, 683–688.
- (250) Wu, H.-L.; Chen, C.-H.; Huang, M. H. Seed-Mediated Synthesis of Branched Gold Nanocrystals Derived from the Side Growth of Pentagonal Bipyramids and the Formation of Gold Nanostars. *Chem. Mater.* **2009**, *21*, 110–114.
- (251) Kawamura, G.; Nogami, M. Application of a Conproportionation Reaction to a Synthesis of Shape-Controlled Gold Nanoparticles. *J. Cryst. Growth* **2009**, *311*, 4462–4466.
- (252) Li, N.; Zhao, P.; Astruc, D. Anisotropic Gold Nanoparticles: Synthesis, Properties, Applications, and Toxicity. *Angew. Chem., Int. Ed.* **2014**, *53*, 1756–1789.
- (253) Lohse, S. E.; Murphy, C. J. The Quest for Shape Control: A History of Gold Nanorod Synthesis. *Chem. Mater.* **2013**, *25*, 1250–1261.
- (254) Kuo, C.-H.; Huang, M. H. Synthesis of Branched Gold Nanocrystals by a Seeding Growth Approach. *Langmuir* **2005**, *21*, 2012–2016.
- (255) Xia, X.; Xie, S.; Liu, M.; Peng, H.-C.; Lu, N.; Wang, J.; Kim, M. J.; Xia, Y. On the Role of Surface Diffusion in Determining the Shape or Morphology of Noble-Metal Nanocrystals. *Proc. Natl. Acad. Sci. U. S. A.* **2013**, *110*, 6669–6673.
- (256) Yuan, H.; Ma, W.; Chen, C.; Zhao, J.; Liu, J.; Zhu, H.; Gao, X. Shape and SPR Evolution of Thorny Gold Nanoparticles Promoted by Silver Ions. *Chem. Mater.* **2007**, *19*, 1592–1600.
- (257) Zou, X.; Ying, E.; Dong, S. Seed-Mediated Synthesis of Branched Gold Nanoparticles with the Assistance of Citrate and their Surface-Enhanced Raman Scattering Properties. *Nanotechnology* **2006**, *17*, 4758–4764.
- (258) Pastoriza-Santos, I.; Liz-Marzán, L. M. N,N-Dimethylformamide as a Reaction Medium for Metal Nanoparticle Synthesis. *Adv. Funct. Mater.* **2009**, *19*, 679–688.
- (259) Kumar, P. S.; Pastoriza-Santos, I.; Rodríguez-González, B.; García de Abajo, F. J.; Liz-Marzán, L. M. High-Yield Synthesis and Optical Response of Gold Nanostars. *Nanotechnology* **2008**, *19*, 015606.
- (260) Pazos-Pérez, N.; Barbosa, S.; Rodríguez-Lorenzo, L.; Aldeanueva-Potel, P.; Pérez-Juste, J.; Pastoriza-Santos, I.; Alvarez-Puebla, R. A.; Liz-Marzán, L. M. Growth of Sharp Tips on Gold Leads to Increased Surface-Enhanced Raman Scattering Activity. *J. Phys. Chem. Lett.* **2010**, *1*, 24–27.
- (261) Kim, D. Y.; Yu, T.; Cho, E. C.; Ma, Y.; Park, O. O.; Xia, Y. Synthesis of Gold Nano-Hexapods with Controllable Arm Lengths and their Tunable Optical Properties. *Angew. Chem., Int. Ed.* **2011**, *50*, 6328–6331.
- (262) Burt, J. L.; Elechiguerra, J. L.; Reyes-Gasca, J.; Martin Montejano-Carrizales, J.; Jose-Yacamán, M. Beyond Archimedean Solid: Star Polyhedral Gold Nanocrystals. *J. Cryst. Growth* **2005**, *285*, 681–691.
- (263) Hao, E.; Bailey, R. C.; Schatz, G. C.; Hupp, J. T.; Li, S. Synthesis and Optical Properties of “Branched” Gold Nanocrystals. *Nano Lett.* **2004**, *4*, 327–330.
- (264) Lu, L.; Ai, K.; Ozaki, Y. Environmentally Friendly Synthesis of Highly Monodisperse Biocompatible Gold Nanoparticles with Urchin-Like Shape. *Langmuir* **2008**, *24*, 1058–1063.
- (265) Jena, B. K.; Raj, C. R. Seedless, Surfactantless Room Temperature Synthesis of Single Crystalline Fluorescent Gold Nanoflowers with Pronounced SERS and Electrocatalytic Activity. *Chem. Mater.* **2008**, *20*, 3546–3548.
- (266) Bakr, O. M.; Wunsch, B. H.; Stellacci, F. High-Yield Synthesis of Multi-Branched Urchin-Like Gold Nanoparticles. *Chem. Mater.* **2006**, *18*, 3297–3301.
- (267) Guo, S.; Dong, S.; Wang, E. Monodisperse Raspberry-Like Gold Submicrometer Spheres: Large-Scale Synthesis and Interface Assembling for Colloid Sphere Array. *Cryst. Growth Des.* **2008**, *8*, 3581–3585.
- (268) Su, Y. H.; Lai, W. H.; Chen, W.-Y.; Hon, M. H.; Chang, S.-H. Surface Plasmon Resonance of Gold Nano-Sea-Urchin. *Appl. Phys. Lett.* **2007**, *90*, 181905.
- (269) Xie, J.; Lee, J. Y.; Wang, D. I. C. Seedless, Surfactantless, High-Yield Synthesis of Branched Gold Nanocrystals in HEPES Buffer Solution. *Chem. Mater.* **2007**, *19*, 2823–2830.
- (270) Jena, B. K.; Raj, C. R. Synthesis of Flower-Like Gold Nanoparticles and their Electrocatalytic Activity towards the Oxidation of Methanol and the Reduction of Oxygen. *Langmuir* **2007**, *23*, 4064–4070.
- (271) Simard, J.; Briggs, C.; Boal, A. K.; Rotello, V. M. Formation and pH-Controlled Assembly of Amphiphilic Gold Nanoparticles. *Chem. Commun.* **2000**, 1943–1944.
- (272) Gao, J.; Huang, X.; Liu, H.; Zan, F.; Ren, J. Colloidal Stability of Gold Nanoparticles Modified with Thiol Compounds: Bioconjugation and Application in Cancer Cell Imaging. *Langmuir* **2012**, *28*, 4464–4471.
- (273) Karakoti, A. S.; Das, S.; Thevuthasan, S.; Seal, S. PEGylated Inorganic Nanoparticles. *Angew. Chem., Int. Ed.* **2011**, *50*, 1980–1994.
- (274) Knop, K.; Hoogenboom, R.; Fischer, D.; Schubert, U. S. Poly(ethylene glycol) in Drug Delivery: Pros and Cons as Well as Potential Alternatives. *Angew. Chem., Int. Ed.* **2010**, *49*, 6288–6308.
- (275) Yang, Y.; Chen, S. Surface Manipulation of the Electronic Energy of Subnanometer-Sized Gold Clusters: An Electrochemical and Spectroscopic Investigation. *Nano Lett.* **2003**, *3*, 75–79.
- (276) Doering, W. E.; Nie, S. Spectroscopic Tags Using Dy-Embedded Nanoparticles and Surface-Enhanced Raman Scattering. *Anal. Chem.* **2003**, *75*, 6171–6176.
- (277) Qian, X.; Peng, X.-H.; Ansari, D. O.; Yin-Goen, Q.; Chen, G. Z.; Shin, D. M.; Yang, L.; Young, A. N.; Wang, M. D.; Nie, S. In Vivo

Tumor Targeting and Spectroscopic Detection with Surface-Enhanced Raman Nanoparticle Tags. *Nat. Biotechnol.* **2008**, *26*, 83–90.

(278) He, J.; Huang, X.; Li, Y.-C.; Liu, Y.; Babu, T.; Aronova, M. A.; Wang, S.; Lu, Z.; Chen, X.; Nie, Z. Self-Assembly of Amphiphilic Plasmonic Micelle-Like Nanoparticle in Selective Solvents. *J. Am. Chem. Soc.* **2013**, *135*, 7974–7984.

(279) Hostetler, M. J.; Templeton, A. C.; Murray, R. W. Dynamics of Place-Exchange Reactions on Monolayer-Protected Gold Cluster Molecules. *Langmuir* **1999**, *15*, 3782–3789.

(280) Shichibu, Y.; Negishi, Y.; Tsukuda, T.; Teranishi, T. Large-Scale Synthesis of Thiolated Au₂₅ Clusters via Ligand Exchange Reactions of Phosphine-Stabilized Au₁₁ Clusters. *J. Am. Chem. Soc.* **2005**, *127*, 13464–13465.

(281) Taton, T. A.; Mucic, R. C.; Mirkin, C. A.; Letsinger, R. L. The DNA-Mediated Formation of Supramolecular Mono- and Multi-layered Nanoparticle Structures. *J. Am. Chem. Soc.* **2000**, *122*, 6305–6306.

(282) Perrault, S. D.; Walkey, C.; Jennings, T.; Fischer, H. C.; Chan, W. C. W. Mediating Tumor Targeting Efficiency of Nanoparticles through Design. *Nano Lett.* **2009**, *9*, 1909–1915.

(283) Elghanian, R.; Storhoff, J. J.; Mucic, R. C.; Letsinger, R. L.; Mirkin, C. A. Selective Colorimetric Detection of Polynucleotides Based on the Distance-Dependent Optical Properties of Gold Nanoparticles. *Science* **1997**, *277*, 1078–1081.

(284) Kinnear, C.; Dietsch, H.; Clift, M. J. D.; Endes, C.; Rothen-Rutishauser, B.; Petri-Fink, A. *Angew. Chem., Int. Ed.* **2013**, *52*, 1934–1938.

(285) Wu, H.; Zhu, H.; Zhuang, J.; Yang, S.; Liu, C.; Cao, Y. C. Water-Soluble Nanocrystals through Dual-Interaction Ligands. *Angew. Chem., Int. Ed.* **2008**, *47*, 3730–3734.

(286) Wang, Y.; Xu, J.; Xia, X.; Yang, M.; Vangveravong, S.; Chen, J.; Mach, R. H.; Xia, Y. SV119-Gold Nanocage Conjugates: A New Platform for Targeting Cancer Cells via Sigma-2 Receptors. *Nanoscale* **2012**, *4*, 421–424.

(287) Li, N.; Zhao, P.; Salmon, L.; Ruiz, J.; Zabawa, M.; Hosmane, N. S.; Astruc, D. “Click” Star-Shaped and Dendritic PEGylated Gold Nanoparticle-Carborane Assemblies. *Inorg. Chem.* **2013**, *52*, 11146–11155.

(288) Ghosh, P.; Yang, X.; Arvizo, R.; Zhu, Z.-J.; Agasti, S. S.; Mo, Z.; Rotello, V. M. Intracellular Delivery of a Membrane-Impermeable Enzyme in Active Form Using Functionalized Gold Nanoparticles. *J. Am. Chem. Soc.* **2010**, *132*, 2642–2645.

(289) Samanta, B.; Yang, X.-C.; Ofir, Y.; Park, M.-H.; Patra, D.; Agasti, S. S.; Miranda, O. R.; Mo, Z.-H.; Rotello, V. M. Catalytic Microcapsules Assembled from Enzyme-Nanoparticle Conjugates at Oil-Water Interfaces. *Angew. Chem., Int. Ed.* **2009**, *48*, 5341–5344.

(290) Lin, C.-A. J.; Sperling, R. A.; Li, J. K.; Yang, T.-Y.; Li, P.-Y.; Zanella, M.; Chang, W. H.; Parak, W. J. Design of an Amphiphilic Polymer for Nanoparticle Coating and Functionalization. *Small* **2008**, *4*, 334–341.

(291) Liz-Marzán, L. M.; Giersig, M.; Mulvaney, P. Synthesis of Nanosized Gold-Silica Core-Shell Particles. *Langmuir* **1996**, *12*, 4329–4335.

(292) Lu, Y.; Yin, Y.; Li, Z.-Y.; Xia, Y. Synthesis and Self-Assembly of Au@SiO₂ Core-Shell Colloids. *Nano Lett.* **2002**, *2*, 785–788.

(293) Xu, B.; Ju, Y.; Cui, Y.; Song, G.; Iwase, Y.; Hosoi, A.; Morita, Y. tLyP-1-Conjugated Au-Nanorod@SiO₂ Core-Shell Nanoparticles for Tumor-Targeted Drug Delivery and Photothermal Therapy. *Langmuir* **2014**, *30*, 7789–7797.

(294) Zhang, Z.; Wang, L.; Wang, J.; Jiang, X.; Li, X.; Hu, Z.; Ji, Y.; Wu, X.; Chen, C. Mesoporous Silica-Coated Gold Nanorods as a Light-Mediated Multifunctional Theranostic Platform for Cancer Treatment. *Adv. Mater.* **2012**, *24*, 1418–1423.

(295) Wang, X.; Chen, H.; Zheng, Y.; Ma, M.; Chen, Y.; Zhang, K.; Zeng, D.; Shi, J. Au-Nanoparticle Coated Mesoporous Silica Nanocapsule-Based Multifunctional Platform for Ultrasound Mediated Imaging, Cytoclastosis and Tumor Ablation. *Biomaterials* **2013**, *34*, 2057–2068.

(296) Mout, R.; Moyano, D. F.; Rana, S.; Rotello, V. M. Surface Functionalization of Nanoparticles for Nanomedicine. *Chem. Soc. Rev.* **2012**, *41*, 2539–2544.

(297) Kobayashi, K.; Wei, J.; Iida, R.; Ijio, K.; Niikura, K. Surface Engineering of Nanoparticles for Therapeutic Applications. *Polym. J.* **2014**, *46*, 460–468.

(298) Ling, D.; Hackett, M. J.; Hyeon, T. Surface Ligands in Synthesis, Modification, Assembly and Biomedical Applications of Nanoparticles. *Nano Today* **2014**, *9*, 457–477.

(299) Wilcoxon, J. P.; Martin, J. E.; Parsapour, F.; Wiedenman, B.; Kelley, D. F. Photoluminescence from Nanosize Gold Clusters. *J. Chem. Phys.* **1998**, *108*, 9137–9143.

(300) Zheng, J.; Nicovich, P. R.; Dickson, R. M. Highly Fluorescent Noble-Metal Quantum Dots. *Annu. Rev. Phys. Chem.* **2007**, *58*, 409–431.

(301) Häkkinen, H. Atomic and Electronic Structure of Gold Clusters: Understanding Flakes, Cages and Superatoms from Simple Concepts. *Chem. Soc. Rev.* **2008**, *37*, 1847–1859.

(302) Zheng, J.; Zhou, C.; Yu, M.; Liu, J. Different Sized Luminescent Gold Nanoparticles. *Nanoscale* **2012**, *4*, 4073–4083.

(303) Link, S.; Beeby, A.; FitzGerald, S.; El-Sayed, M. A.; Schaaff, T. G.; Whetten, R. L. Visible to Infrared Luminescence from a 28-Atom Gold Cluster. *J. Phys. Chem. B* **2002**, *106*, 3410–3415.

(304) Zheng, J.; Petty, J. T.; Dickson, R. M. High Quantum Yield Blue Emission from Water-Soluble Au₈ Nanodots. *J. Am. Chem. Soc.* **2003**, *125*, 7780–7781.

(305) Muhammed, M. A. H.; Verma, P. K.; Pal, S. K.; Retnakumari, A.; Koyakutty, M.; Nair, S.; Pradeep, T. Luminescent Quantum Clusters of Gold in Bulk by Albumin-Induced Core Etching of Nanoparticles: Metal Ion Sensing, Metal-Enhanced Luminescence, and Biolabeling. *Chem. - Eur. J.* **2010**, *16*, 10103–10112.

(306) Santiago González, B.; Rodríguez, M. J.; Blanco, C.; Rivas, J.; López-Quintela, M. A.; Martinho, J. M. G. One Step Synthesis of the Smallest Photoluminescent and Paramagnetic PVP-Protected Gold Atomic Clusters. *Nano Lett.* **2010**, *10*, 4217–4221.

(307) Kawasaki, H.; Hamaguchi, K.; Osaka, I.; Arakawa, R. pH-Dependent Synthesis of Pepsin-Mediated Gold Nanoclusters with Blue Green and Red Fluorescent Emission. *Adv. Funct. Mater.* **2011**, *21*, 3508–3515.

(308) Luo, Z.; Yuan, X.; Yu, Y.; Zhang, Q.; Leong, D. T.; Lee, J. Y.; Xie, J. From Aggregation-Induced Emission of Au(I)–Thiolate Complexes to Ultrabright Au(0)–Thiolate Core-Shell Nanoclusters. *J. Am. Chem. Soc.* **2012**, *134*, 16662–16670.

(309) Wu, Z.; Jin, R. On the Ligand's Role in the Fluorescence of Gold Nanoclusters. *Nano Lett.* **2010**, *10*, 2568–2573.

(310) Zhou, C.; Yu, J.; Qin, Y.; Zheng, J. Grain Size Effects in Polycrystalline Gold Nanoparticles. *Nanoscale* **2012**, *4*, 4228–4233.

(311) Wang, H.; Huff, T. B.; Zweifel, D. A.; He, W.; Low, P. S.; Wei, A.; Cheng, J.-X. *In Vitro* and *In Vivo* Two-Photon Luminescence Imaging of Single Gold Nanorods. *Proc. Natl. Acad. Sci. U. S. A.* **2005**, *102*, 15752–15756.

(312) Imura, K.; Nagahara, T.; Okamoto, H. Photoluminescence from Gold Nanoplates Induced by Near-Field Two-Photon Absorption. *Appl. Phys. Lett.* **2006**, *88*, 023104.

(313) Gao, L.; Vadakkan, T. J.; Nammalvar, V. Nanoshells for *In Vivo* Imaging Using Two-Photon Excitation Microscopy. *Nanotechnology* **2011**, *22*, 365102.

(314) Tong, L.; Cobley, C. M.; Chen, J.; Xia, Y.; Cheng, J.-X. Bright Three-Photon Luminescence from Gold/Silver Alloyed Nanostructures for Bioimaging with Negligible Photothermal Toxicity. *Angew. Chem., Int. Ed.* **2010**, *49*, 3485–3488.

(315) Yuan, H.; Khoury, C. G.; Hwang, H.; Wilson, C. M.; Grant, G. A.; Vo-Dinh, T. Gold Nanostars: Surfactant-Free Synthesis, 3D Modelling, and Two-Photon Photoluminescence Imaging. *Nanotechnology* **2012**, *23*, 075102.

(316) Chu, D. S.; Dai, C. M. Quantum Size Effects in CdS Thin Films. *Phys. Rev. B: Condens. Matter Mater. Phys.* **1992**, *45*, 11805–11810.

- (317) Pande, C. S.; Masumura, R. A. Grain Boundary and Grain Size Effects in High and Low Transition Temperature Superconductors. *Mater. Sci. Eng., B* **1995**, *32*, 247–253.
- (318) Zhao, X.; Schoenfeld, O.; Nomura, S.; Komuro, S.; Aoyagi, Y.; Sugano, T. Nanocrystalline Si: A Material Constructed by Si Quantum Dots. *Mater. Sci. Eng., B* **1995**, *35*, 467–471.
- (319) Braun, F.; von Delft, J. Superconductivity in Ultrasmall Metallic Grains. *Phys. Rev. B: Condens. Matter Mater. Phys.* **1999**, *59*, 9527–9544.
- (320) Mohamed, M. B.; Volkov, V.; Link, S.; El-Sayed, M. A. The 'Lightening' Gold Nanorods: Fluorescence Enhancement of over a Million Compared to the Gold Metal. *Chem. Phys. Lett.* **2000**, *317*, 517–523.
- (321) Brolo, A. G.; Kwok, S. C.; Moffitt, M. G.; Gordon, R.; Riordon, J.; Kavanagh, K. L. Enhanced Fluorescence from Arrays of Nanoholes in a Gold Film. *J. Am. Chem. Soc.* **2005**, *127*, 14936–14941.
- (322) Ueno, K.; Juodkazis, S.; Mizeikis, V.; Sasaki, K.; Misawa, H. Clusters of Closely Spaced Gold Nanoparticles as a Source of Two-Photon Photoluminescence at Visible Wavelengths. *Adv. Mater.* **2008**, *20*, 26–30.
- (323) Eustis, S.; El-Sayed, M. Aspect Ratio Dependent of the Enhanced Fluorescence Intensity of Gold Nanorods: Experimental and Simulation Study. *J. Phys. Chem. B* **2005**, *109*, 16350–16356.
- (324) Au, L.; Zhang, Q.; Cobley, C. M.; Gidding, M.; Schwartz, A. G.; Chen, J.; Xia, Y. Quantifying the Cellular Uptake of Antibody-Conjugated Au Nanocages by Two-Photon Microscopy and Inductively Coupled Plasma Mass Spectrometry. *ACS Nano* **2010**, *4*, 35–42.
- (325) Pelton, M.; Bryant, G. W. *Introduction to Metal-Nanoparticle Plasmonics*; John Wiley & Sons Inc.: Somerset, NJ, USA, 2013.
- (326) Neil, W.; Ashcroft, N. D. M. *Solid State Physics*; 1st ed.; Cengage Learning: Philadelphia, PA, USA, 1976.
- (327) Craig, F.; Bohren, D. R. H. *Absorption and Scattering of Light by Small Particles*; Wiley Professional Paperback ed.; John Wiley & Sons, Inc.: New York, 1998.
- (328) Kreibig, U.; Vollmer, M. *Optical Properties of Metal Clusters*; Springer: Berlin, 1995.
- (329) Jain, P. K.; Lee, K. S.; El-Sayed, I. H.; El-Sayed, M. A. Calculated Absorption and Scattering Properties of Gold Nanoparticles of Different Size, Shape, and Composition: Applications in Biological Imaging and Biomedicine. *J. Phys. Chem. B* **2006**, *110*, 7238–7248.
- (330) Sokolov, K.; Follen, M.; Aaron, J.; Pavlova, I.; Malpica, A.; Lotan, R.; Richards-Kortum, R. Real-Time Vital Optical Imaging of Precancer Using Anti-Epidermal Growth Factor Receptor Antibodies Conjugated to Gold Nanoparticles. *Cancer Res.* **2003**, *63*, 1999–2004.
- (331) El-Sayed, I. H.; Huang, X.; El-Sayed, M. A. Surface Plasmon Resonance Scattering and Absorption of Anti-EGFR Antibody Conjugated Gold Nanoparticles in Cancer Diagnostics: Applications in Oral Cancer. *Nano Lett.* **2005**, *5*, 829–834.
- (332) Ghosh, S. K.; Pal, T. Interparticle Coupling Effect on the Surface Plasmon Resonance of Gold Nanoparticles: From Theory to Applications. *Chem. Rev.* **2007**, *107*, 4797–4862.
- (333) Louis, C.; Pluchery, O. *Gold Nanoparticles for Physics, Chemistry and Biology*; Imperial College Press: London, 2012.
- (334) Draine, B. T.; Flatau, P. J. Discrete-Dipole Approximation for Scattering Calculations. *J. Opt. Soc. Am. A* **1994**, *11*, 1491–1499.
- (335) Kelly, K. L.; Coronado, E.; Zhao, L. L.; Schatz, G. C. The Optical Properties of Metal Nanoparticles: The Influence of Size, Shape, and Dielectric Environment. *J. Phys. Chem. B* **2003**, *107*, 668–677.
- (336) Oubre, C.; Nordlander, P. Optical Properties of Metallodielectric Nanostructures Calculated Using the Finite Difference Time Domain Method. *J. Phys. Chem. B* **2004**, *108*, 17740–17747.
- (337) Taflov, A. *IEEE Trans. Electromagn. Compat.* **1980**, EMC-22, 191–202.
- (338) García de Abajo, F. J.; Howie, A. Retarded Field Calculation of Electron Energy Loss in Inhomogeneous Dielectrics. *Phys. Rev. B: Condens. Matter Mater. Phys.* **2002**, *65*, 115418.
- (339) Tsai, M.-F.; Chang, S.-H. G.; Cheng, F.-Y.; Shanmugam, V.; Cheng, Y.-S.; Su, C.-H.; Yeh, C.-S. Au Nanorod Design as Light-Absorber in the First and Second Biological Near-Infrared Windows for *in Vivo* Photothermal Therapy. *ACS Nano* **2013**, *7*, 5330–5342.
- (340) Weissleder, R. A Clearer Vision for *in Vivo* Imaging. *Nat. Biotechnol.* **2001**, *19*, 316–317.
- (341) Creighton, J. A.; Eadon, D. G. Ultraviolet-Visible Absorption Spectra of the Colloidal Metallic Elements. *J. Chem. Soc., Faraday Trans.* **1991**, *87*, 3881–3891.
- (342) Karlsson, H. L.; Cronholm, P.; Gustafsson, J.; Möller, L. Copper Oxide Nanoparticles Are Highly Toxic: A Comparison between Metal Oxide Nanoparticles and Carbon Nanotubes. *Chem. Res. Toxicol.* **2008**, *21*, 1726–1732.
- (343) Li, F.; Lei, C.; Shen, Q.; Li, L.; Wang, M.; Guo, M.; Huang, Y.; Nie, Z.; Yao, S. Analysis of Copper Nanoparticles Toxicity Based on a Stress-Responsive Bacterial Biosensor Array. *Nanoscale* **2013**, *5*, 653–662.
- (344) van Aerle, R.; Lange, A.; Moorhouse, A.; Paszkiewicz, K.; Ball, K.; Johnston, B. D.; de-Bastos, E.; Booth, T.; Tyler, C. R.; Santos, E. M. Molecular Mechanisms of Toxicity of Silver Nanoparticles in Zebrafish Embryos. *Environ. Sci. Technol.* **2013**, *47*, 8005–8014.
- (345) Cho, E. C.; Kim, C.; Zhou, F.; Cobley, C. M.; Song, K. H.; Chen, J.; Li, Z.-Y.; Wang, L. V.; Xia, Y. Measuring the Optical Absorption Cross Sections of Au-Ag Nanocages and Au Nanorods by Photoacoustic Imaging. *J. Phys. Chem. C* **2009**, *113*, 9023–9028.
- (346) Willets, K. A.; Van Duyne, R. P. Localized Surface Plasmon Resonance Spectroscopy and Sensing. *Annu. Rev. Phys. Chem.* **2007**, *58*, 267–297.
- (347) Huang, X.; El-Sayed, M. A. Gold Nanoparticles: Optical Properties and Implementations in Cancer Diagnosis and Photothermal Therapy. *J. Adv. Res.* **2010**, *1*, 13–28.
- (348) Gans, R. Über die Form Ultramikroskopischer Goldteilchen. *Ann. Phys.* **1912**, *342*, 881–900.
- (349) Gans, R. Über die Form Ultramikroskopischer Silberteilehen. *Ann. Phys.* **1915**, *352*, 270–284.
- (350) Link, S.; El-Sayed, M. A. Optical Properties and Ultrafast Dynamics of Metallic Nanocrystals. *Annu. Rev. Phys. Chem.* **2003**, *54*, 331–366.
- (351) Link, S.; Mohamed, M. B.; El-Sayed, M. A. Simulation of the Optical Absorption Spectra of Gold Nanorods as a Function of their Aspect Ratio and the Effect of the Medium Dielectric Constant. *J. Phys. Chem. B* **1999**, *103*, 3073–3077.
- (352) Cho, E. C.; Liu, Y.; Xia, Y. A Simple Spectroscopic Method for Differentiating Cellular Uptakes of Gold Nanospheres and Nanorods from their Mixtures. *Angew. Chem., Int. Ed.* **2010**, *49*, 1976–1980.
- (353) Huang, X.; El-Sayed, I. H.; Qian, W.; El-Sayed, M. A. Cancer Cell Imaging and Photothermal Therapy in the Near-Infrared Region by Using Gold Nanorods. *J. Am. Chem. Soc.* **2006**, *128*, 2115–2120.
- (354) Neeves, A. E.; Birnboim, M. H. Composite Structures for the Enhancement of Nonlinear-Optical Susceptibility. *J. Opt. Soc. Am. B* **1989**, *6*, 787–796.
- (355) Averitt, R. D.; Sarkar, D.; Halas, N. J. Plasmon Resonance Shifts of Au-Coated Au₂S Nanoshells: Insight into Multicomponent Nanoparticle Growth. *Phys. Rev. Lett.* **1997**, *78*, 4217–4220.
- (356) Averitt, R. D.; Westcott, S. L.; Halas, N. J. Linear Optical Properties of Gold Nanoshells. *J. Opt. Soc. Am. B* **1999**, *16*, 1824–1832.
- (357) West, J. L.; Halas, N. J. Engineered Nanomaterials for Biophotonics Applications: Improving Sensing, Imaging, and Therapeutics. *Annu. Rev. Biomed. Eng.* **2003**, *5*, 285–292.
- (358) Prodan, E.; Radloff, C.; Halas, N. J.; Nordlander, P. A Hybridization Model for the Plasmon Response of Complex Nanostructures. *Science* **2003**, *302*, 419–422.
- (359) Le Ru, E. C.; Etchegoin, P. G. *Principles of Surface-Enhanced Raman Spectroscopy: And Related Plasmonic Effects*; 1st ed.; Elsevier: Amsterdam, 2009.
- (360) Cang, H.; Sun, T.; Li, Z.-Y.; Chen, J.; Wiley, B. J.; Xia, Y.; Li, X. Gold Nanocages as Contrast Agents for Spectroscopic Optical Coherence Tomography. *Opt. Lett.* **2005**, *30*, 3048–3050.

- (361) Chen, J.; Saeki, F.; Wiley, B.; Cang, H.; Cobb, M. J.; Li, Z.-Y.; Au, L.; Zhang, H.; Kimmey, M. B.; Li, X.; Xia, Y. Gold Nanocages: Bioconjugation and their Potential Use as Optical Imaging Contrast Agents. *Nano Lett.* **2005**, *5*, 473–477.
- (362) Chen, J.; Wiley, B.; Li, Z.-Y.; Campbell, D.; Saeki, F.; Cang, H.; Au, L.; Lee, J.; Li, X.; Xia, Y. Gold Nanocages: Engineering their Structure for Biomedical Applications. *Adv. Mater.* **2005**, *17*, 2255–2261.
- (363) Guo, Z.; Fan, X.; Liu, L.; Bian, Z.; Gu, C.; Zhang, Y.; Gu, N.; Yang, D.; Zhang, J. Achieving High-Purity Colloidal Gold Nanoprisms and their Application as Biosensing Platforms. *J. Colloid Interface Sci.* **2010**, *348*, 29–36.
- (364) O'Brien, M. N.; Jones, M. R.; Kohlstedt, K. L.; Schatz, G. C.; Mirkin, C. A. Uniform Circular Disks with Synthetically Tailorable Diameters: Two-Dimensional Nanoparticles for Plasmonics. *Nano Lett.* **2015**, *15*, 1012–1017.
- (365) Hong, S.; Shuford, K. L.; Park, S. Shape Transformation of Gold Nanoplates and their Surface Plasmon Characterizations: Triangular to Hexagonal Nanoplates. *Chem. Mater.* **2011**, *23*, 2011–2013.
- (366) Liu, X.; Atwater, M.; Wang, J.; Huo, Q. Extinction Coefficient of Gold Nanoparticles with Different Sizes and Different Capping Ligands. *Colloids Surf., B* **2007**, *58*, 3–7.
- (367) Pickering, J. W.; Prahl, S. A.; van Wieringen, N.; Beek, J. F.; Sterenborg, H. J. C. M.; van Gemert, M. J. C. Double-Integrating-Sphere System for Measuring the Optical Properties of Tissue. *Appl. Opt.* **1993**, *32*, 399–410.
- (368) Oldenburg, A.; Zweifel, D. A.; Xu, C.; Wei, A.; Boppart, S. A. Characterization of Plasmon-Resonant Gold Nanorods as Near-Infrared Optical Contrast Agents Investigated Using a Double-Integrating Sphere System. *Proc. SPIE* **2005**, *5703*, 50–60.
- (369) Aprile, E.; Bolotnikov, A. E.; Bolozdynya, A. I.; Doke, T. *Noble Gas Detectors*; Wiley-VCH: Weinheim, Germany, 2006.
- (370) Zeng, J.; Goldfeld, D.; Xia, Y. A Plasmon-Assisted Optofluidic (PAOF) System for Measuring the Photothermal Conversion Efficiencies of Gold Nanostructures and Controlling an Electrical Switch. *Angew. Chem., Int. Ed.* **2013**, *52*, 4169–4173.
- (371) Raman, C. V. A New Radiation. *Indian J. Phys.* **1928**, 387–398.
- (372) Kneipp, K.; Kneipp, H.; Itzkan, I.; Dasari, R. R.; Feld, M. S. Ultrasensitive Chemical Analysis by Raman Spectroscopy. *Chem. Rev.* **1999**, *99*, 2957–2976.
- (373) Tian, Z.-Q.; Ren, B.; Wu, D.-Y. Surface-Enhanced Raman Scattering: From Noble to Transition Metals and from Rough Surfaces to Ordered Nanostructures. *J. Phys. Chem. B* **2002**, *106*, 9463–9483.
- (374) Kneipp, K.; Kneipp, H.; Itzkan, I.; Dasari, R. R.; Feld, M. S. Surface-Enhanced Raman Scattering: A New Tool for Biomedical Spectroscopy. *Curr. Sci.* **1999**, *77*, 915–924.
- (375) Tong, L. M.; Zhu, T.; Liu, Z. F. Approaching the Electromagnetic Mechanism of Surface-Enhanced Raman Scattering: from Self-Assembled Arrays to Individual Gold Nanoparticles. *Chem. Soc. Rev.* **2011**, *40*, 1296–1304.
- (376) Schlucker, S. Surface-Enhanced Raman Spectroscopy: Concepts and Chemical Applications. *Angew. Chem., Int. Ed.* **2014**, *53*, 4756–4795.
- (377) Fleischmann, M.; Hendra, P. J.; McQuillan, A. J. Raman Spectra of Pyridine Adsorbed at a Silver Electrode. *Chem. Phys. Lett.* **1974**, *26*, 163–166.
- (378) Jeanmaire, D. L.; Van Duyne, R. P. Surface Raman Spectroelectrochemistry Part I. Heterocyclic, Aromatic, and Aliphatic Amines Adsorbed on the Anodized Silver Electrode. *J. Electroanal. Chem. Interfacial Electrochem.* **1977**, *84*, 1–20.
- (379) Albrecht, M. G.; Creighton, J. A. Anomalous Intense Raman Spectra of Pyridine at a Silver Electrode. *J. Am. Chem. Soc.* **1977**, *99*, 5215–5217.
- (380) Bantz, K. C.; Meyer, A. F.; Wittenberg, N. J.; Im, H.; Kurtulus, O.; Lee, S. H.; Lindquist, N. C.; Oh, S. H.; Haynes, C. L. Recent Progress in SERS Biosensing. *Phys. Chem. Chem. Phys.* **2011**, *13*, 11551–11567.
- (381) Abalde-Cela, S.; Aldeanueva-Potel, P.; Mateo-Mateo, C.; Rodriguez-Lorenzo, L.; Alvarez-Puebla, R. A.; Liz-Marzan, L. M. Surface-Enhanced Raman Scattering Biomedical Applications of Plasmonic Colloidal Particles. *J. R. Soc., Interface* **2010**, *7*, S435–S450.
- (382) Doering, W. E.; Piotti, M. E.; Natan, M. J.; Freeman, R. G. SERS as a Foundation for Nanoscale, Optically Detected Biological Labels. *Adv. Mater.* **2007**, *19*, 3100–3108.
- (383) Kambhampati, P.; Foster, M. C.; Campion, A. Two-Dimensional Localization of Adsorbate/Substrate Charge-Transfer Excited States of Molecules Adsorbed on Metal Surfaces. *J. Chem. Phys.* **1999**, *110*, 551–558.
- (384) Schatz, G. C.; Young, M. A.; Van Duyne, R. P. Electromagnetic Mechanism of SERS. *Top. Appl. Phys.* **2006**, *103*, 19–46.
- (385) Jensen, L.; Aikens, C. M.; Schatz, G. C. Electronic Structure Methods for Studying Surface-Enhanced Raman Scattering. *Chem. Soc. Rev.* **2008**, *37*, 1061–1073.
- (386) Persson, B. N. J.; Zhao, K.; Zhang, Z. Chemical Contribution to Surface-Enhanced Raman Scattering. *Phys. Rev. Lett.* **2006**, *96*, 207401.
- (387) Zhao, L. L.; Jensen, L.; Schatz, G. C. Surface-Enhanced Raman Scattering of Pyrazine at the Junction between Two Ag₂₀ Nanoclusters. *Nano Lett.* **2006**, *6*, 1229–1234.
- (388) Haes, A. J.; Haynes, C. L.; McFarland, A. D.; Schatz, G. C.; Van Duyne, R. R.; Zou, S. Plasmonic Materials for Surface-Enhanced Sensing and Spectroscopy. *MRS Bull.* **2005**, *30*, 368–375.
- (389) McCreery, R. L. *Raman Spectroscopy for Chemical Analysis*; John Wiley & Sons, Inc.: New York, 2000.
- (390) Yang, M.; Chen, T.; Lau, W. S.; Wang, Y.; Tang, Q.; Yang, Y.; Chen, H. Development of Polymer-Encapsulated Metal Nanoparticles as Surface-Enhanced Raman Scattering Probes. *Small* **2009**, *5*, 198–202.
- (391) Joseph, V.; Matschulat, A.; Polte, J.; Rolf, S.; Emmerling, F.; Kneipp, J. SERS Enhancement of Gold Nanospheres of Defined Size. *J. Raman Spectrosc.* **2011**, *42*, 1736–1742.
- (392) Jana, N. R.; Pal, T. Anisotropic Metal Nanoparticles for Use as Surface-Enhanced Raman Substrates. *Adv. Mater.* **2007**, *19*, 1761–1765.
- (393) Nikoobakht, B.; Wang, J. P.; El-Sayed, M. A. Surface-Enhanced Raman Scattering of Molecules Adsorbed on Gold Nanorods: Off-Surface Plasmon Resonance Condition. *Chem. Phys. Lett.* **2002**, *366*, 17–23.
- (394) Rycenga, M.; Wang, Z.; Gordon, E.; Cobley, C. M.; Schwartz, A. G.; Lo, C. S.; Xia, Y. Probing the Photothermal Effect of Gold-Based Nanocages with Surface-Enhanced Raman Scattering (SERS). *Angew. Chem., Int. Ed.* **2009**, *48*, 9924–9927.
- (395) Rycenga, M.; Hou, K. K.; Cobley, C. M.; Schwartz, A. G.; Camargo, P. H. C.; Xia, Y. Probing the Surface-Enhanced Raman Scattering Properties of Au–Ag Nanocages at Two Different Excitation Wavelengths. *Phys. Chem. Chem. Phys.* **2009**, *11*, 5903–5908.
- (396) Indrasekara, A. S. D. S.; Meyers, S.; Shubeita, S.; Feldman, L. C.; Gustafsson, T.; Fabris, L. Gold Nanostar Substrates for SERS-Based Chemical Sensing in the Femtomolar Regime. *Nanoscale* **2014**, *6*, 8891–8899.
- (397) Rodriguez-Lorenzo, L.; Alvarez-Puebla, R. A.; de Abajo, F. J. G.; Liz-Marzan, L. M. Surface Enhanced Raman Scattering Using Star-Shaped Gold Colloidal Nanoparticles. *J. Phys. Chem. C* **2010**, *114*, 7336–7340.
- (398) Brus, L. Noble Metal Nanocrystals: Plasmon Electron Transfer Photochemistry and Single-Molecule Raman Spectroscopy. *Acc. Chem. Res.* **2008**, *41*, 1742–1749.
- (399) Le Ru, E. C.; Etchegoin, P. G.; Meyer, M. Enhancement Factor Distribution Around a Single Surface-Enhanced Raman Scattering Hot Spot and Its Relation to Single Molecule Detection. *J. Chem. Phys.* **2006**, *125*, 204701.
- (400) Wustholz, K. L.; Henry, A.-I.; McMahon, J. M.; Freeman, R. G.; Valley, N.; Piotti, M. E.; Natan, M. J.; Schatz, G. C.; Van Duyne, R. P. Structure–Activity Relationships in Gold Nanoparticle Dimers and

Trimers for Surface-Enhanced Raman Spectroscopy. *J. Am. Chem. Soc.* **2010**, *132*, 10903–10910.

(401) Zhang, Q.; Ge, J.; Goebel, J.; Hu, Y.; Sun, Y.; Yin, Y. Tailored Synthesis of Superparamagnetic Gold Nanoshells with Tunable Optical Properties. *Adv. Mater.* **2010**, *22*, 1905–1909.

(402) Wang, H.; Halas, N. J. Mesoscopic Au “Meatball” Particles. *Adv. Mater.* **2008**, *20*, 820–825.

(403) Dieringer, J. A.; Lettan, R. B.; Scheidt, K. A.; Van Duyne, R. P. A Frequency Domain Existence Proof of Single-Molecule Surface-Enhanced Raman Spectroscopy. *J. Am. Chem. Soc.* **2007**, *129*, 16249–16256.

(404) Kleinman, S. L.; Ringe, E.; Valley, N.; Wustholz, K. L.; Phillips, E.; Scheidt, K. A.; Schatz, G. C.; Van Duyne, R. P. Single-Molecule Surface-Enhanced Raman Spectroscopy of Crystal Violet Isotopologues: Theory and Experiment. *J. Am. Chem. Soc.* **2011**, *133*, 4115–4122.

(405) Marz, A.; Henkel, T.; Cialla, D.; Schmitt, M.; Popp, J. Droplet Formation *via* Flow-Through Microdevices in Raman and Surface Enhanced Raman Spectroscopy—Concepts and Applications. *Lab Chip* **2011**, *11*, 3584–3592.

(406) Yin, Y.; Qiu, T.; Zhang, W. J.; Chu, P. K. Recent Developments in Optofluidic-Surface-Enhanced Raman Scattering Systems: Design, Assembly, and Advantages. *J. Mater. Res.* **2011**, *26*, 170–185.

(407) Wang, Y.; Wang, Y.; Zhou, F.; Kim, P.; Xia, Y. Protein-Protected Au Clusters as a New Class of Nanoscale Biosensor for Label-Free Fluorescence Detection of Proteases. *Small* **2012**, *8*, 3769–3773.

(408) Huang, C.-C.; Chiang, C.-K.; Lin, Z.-H.; Lee, K.-H.; Chang, H.-T. Bioconjugated Gold Nanodots and Nanoparticles for Protein Assays Based on Photoluminescence Quenching. *Anal. Chem.* **2008**, *80*, 1497–1504.

(409) Chen, C.-T.; Chen, W.-J.; Liu, C.-Z.; Chang, L.-Y.; Chen, Y.-C. Glutathione-Bound Gold Nanoclusters for Selective-Binding and Detection of Glutathione S-Transferase-Fusion Proteins from Cell Lysates. *Chem. Commun.* **2009**, 7515–7517.

(410) Triulzi, R. C.; Micic, M.; Giordani, S.; Serry, M.; Chiou, W.-A.; Leblanc, R. M. Immunoassay Based on the Antibody-Conjugated PAMAM-Dendrimer–Gold Quantum Dot Complex. *Chem. Commun.* **2006**, 5068–5070.

(411) Shiang, Y.-C.; Lin, C.-A.; Huang, C.-C.; Chang, H.-T. Protein A-Conjugated Luminescent Gold Nanodots as a Label-Free Assay for Immunoglobulin G in Plasma. *Analyst* **2011**, *136*, 1177–1182.

(412) Durgadas, C. V.; Sharma, C. P.; Sreenivasan, K. Fluorescent Gold Clusters as Nanosensors for Copper Ions in Live Cells. *Analyst* **2011**, *136*, 933–940.

(413) Chen, Y.; Wang, Y.; Wang, C.; Li, W.; Zhou, H.; Jiao, H.; Lin, Q.; Yu, C. Papain-Directed Synthesis of Luminescent Gold Nanoclusters and the Sensitive Detection of Cu^{2+} . *J. Colloid Interface Sci.* **2013**, *396*, 63–68.

(414) Huang, C.-C.; Yang, Z.; Lee, K.-H.; Chang, H.-T. Synthesis of Highly Fluorescent Gold Nanoparticles for Sensing Mercury(II). *Angew. Chem., Int. Ed.* **2007**, *46*, 6824–6828.

(415) Jin, L.; Shang, L.; Guo, S. J.; Fang, Y.; Wen, D.; Wang, L.; Yin, J.; Dong, S. Biomolecule-Stabilized Au Nanoclusters as a Fluorescence Probe for Sensitive Detection of Glucose. *Biosens. Bioelectron.* **2011**, *26*, 1965–1969.

(416) Shiang, Y.-C.; Huang, C.-C.; Chang, H.-T. Gold Nanodot-Based Luminescent Sensor for the Detection of Hydrogen Peroxide and Glucose. *Chem. Commun.* **2009**, 3437–3439.

(417) Wen, F.; Dong, Y.; Feng, L.; Wang, S.; Zhang, S.; Zhang, X. Horseradish Peroxidase Functionalized Fluorescent Gold Nanoclusters for Hydrogen Peroxide Sensing. *Anal. Chem.* **2011**, *83*, 1193–1196.

(418) Vennesland, B.; Comm, E. E.; Knowles, C. J.; Westly, J.; Wissing, F. *Cyanide in Biology*; Academic Press: London, 1981; p 93.

(419) Gettler, A. O.; Baine, J. O. The Toxicology of Cyanide. *Am. J. Med. Sci.* **1938**, *195*, 182–198.

(420) Jungreis, E. Microdetermination of Cyanides by Atomic Absorption Spectroscopy. *Isr. J. Chem.* **1969**, *7*, 583–588.

(421) Wang, X.-B.; Wang, Y.-L.; Yang, J.; Xing, X.-P.; Li, J.; Wang, L.-S. Evidence of Significant Covalent Bonding in $\text{Au}(\text{CN})_2^-$. *J. Am. Chem. Soc.* **2009**, *131*, 16368–16370.

(422) Liu, Y.; Ai, K.; Cheng, X.; Huo, L.; Lu, L. Gold-Nanocluster-Based Fluorescent Sensors for Highly Sensitive and Selective Detection of Cyanide in Water. *Adv. Funct. Mater.* **2010**, *20*, 951–956.

(423) Zhang, X.; Wu, F.-G.; Liu, P.; Gu, N.; Chen, Z. Enhanced Fluorescence of Gold Nanoclusters Composed of HAuCl_4 and Histidine by Glutathione: Glutathione Detection and Selective Cancer Cell Imaging. *Small* **2014**, *10*, 5170–5177.

(424) Zhu, R.; Zhou, Y.; Wang, X.-L.; Liang, L.-P.; Long, Y.-J.; Wang, Q.-L.; Zhang, H.-J.; Huang, X.-X.; Zheng, H.-Z. Detection of Hg^{2+} Based on the Selective Inhibition of Peroxidase Mimetic Activity of BSA-Au Clusters. *Talanta* **2013**, *117*, 127–132.

(425) Xie, J. P.; Zheng, Y. G.; Ying, J. Y. Highly Selective and Ultrasensitive Detection of Hg^{2+} Based on Fluorescence Quenching of Au Nanoclusters by Hg^{2+} – Au^+ Interactions. *Chem. Commun.* **2010**, 46, 961–963.

(426) Lin, Y.-H.; Tseng, W.-L. Ultrasensitive Sensing of Hg^{2+} and CH_3Hg^+ Based on the Fluorescence Quenching of Lysozyme Type VI-Stabilized Gold Nanoclusters. *Anal. Chem.* **2010**, *82*, 9194–9200.

(427) Paramanik, B.; Bhattacharyya, S.; Patra, A. Detection of Hg^{2+} and F^- Ions by Using Fluorescence Switching of Quantum Dots in an Au-Cluster–CdTe QD Nanocomposite. *Chem. - Eur. J.* **2013**, *19*, 5980–5987.

(428) Park, K. S.; Kim, M. I.; Woo, M.-A.; Park, H. G. A Label-Free Method for Detecting Biological Thiols Based on Blocking of Hg^{2+} -Quenching of Fluorescent Gold Nanoclusters. *Biosens. Bioelectron.* **2013**, *45*, 65–69.

(429) Yang, W.-H.; Schatz, G. C.; Van Duyne, R. P. Discrete Dipole Approximation for Calculating Extinction and Raman Intensities for Small Particles with Arbitrary Shapes. *J. Chem. Phys.* **1995**, *103*, 869–875.

(430) Reynolds, R. A.; Mirkin, C. A.; Letsinger, R. L. Homogeneous, Nanoparticle-Based Quantitative Colorimetric Detection of Oligonucleotides. *J. Am. Chem. Soc.* **2000**, *122*, 3795–3796.

(431) Storhoff, J. J.; Elghanian, R.; Mucic, R. C.; Mirkin, C. A.; Letsinger, R. L. One-Pot Colorimetric Differentiation of Polynucleotides with Single Base Imperfections Using Gold Nanoparticle Probes. *J. Am. Chem. Soc.* **1998**, *120*, 1959–1964.

(432) Xu, X.; Daniel, W. L.; Wei, W.; Mirkin, C. A. Colorimetric Cu^{2+} Detection Using DNA-Modified Gold-Nanoparticle Aggregates as Probes and Click Chemistry. *Small* **2010**, *6*, 623–626.

(433) Lee, J.-S.; Han, M. S.; Mirkin, C. A. Colorimetric Detection of Mercuric Ion (Hg^{2+}) in Aqueous Media Using DNA-Functionalized Gold Nanoparticles. *Angew. Chem., Int. Ed.* **2007**, *46*, 4093–4096.

(434) Liu, J.; Lu, Y. Colorimetric Cu^{2+} Detection with a Ligation DNzyme and Nanoparticles. *Chem. Commun.* **2007**, 4872–4874.

(435) Wang, Z.; Lee, J. H.; Lu, Y. Label-Free Colorimetric Detection of Lead Ions with a Nanomolar Detection Limit and Tunable Dynamic Range by Using Gold Nanoparticles and DNzyme. *Adv. Mater.* **2008**, *20*, 3263–3267.

(436) Liu, J.; Lu, Y. Stimuli-Responsive Disassembly of Nanoparticle Aggregates for Light-Up Colorimetric Sensing. *J. Am. Chem. Soc.* **2005**, *127*, 12677–12683.

(437) Liu, J.; Lu, Y. Accelerated Color Change of Gold Nanoparticles Assembled by DNzymes for Simple and Fast Colorimetric Pb^{2+} Detection. *J. Am. Chem. Soc.* **2004**, *126*, 12298–12305.

(438) Liu, J.; Lu, Y. Optimization of a Pb^{2+} -Directed Gold Nanoparticle/DNzyme Assembly and Its Application as a Colorimetric Biosensor for Pb^{2+} . *Chem. Mater.* **2004**, *16*, 3231–3238.

(439) Liu, J.; Lu, Y. A Colorimetric Lead Biosensor Using DNzyme-Directed Assembly of Gold Nanoparticles. *J. Am. Chem. Soc.* **2003**, *125*, 6642–6643.

(440) Lee, J. H.; Wang, Z.; Liu, J.; Lu, Y. Highly Sensitive and Selective Colorimetric Sensors for Uranyl (UO_2^{2+}): Development and Comparison of Labeled and Label-Free DNzyme-Gold Nanoparticle Systems. *J. Am. Chem. Soc.* **2008**, *130*, 14217–14226.

- (441) Yang, B.; Zhang, X.-B.; Liu, W.-N.; Hu, R.; Tan, W.; Shen, G.-L.; Yu, R.-Q. Fluorosurfactant-Capped Gold Nanoparticles-Based Label-Free Colorimetric Assay for Au³⁺ with Tunable Dynamic Range via a Redox Strategy. *Biosens. Bioelectron.* **2013**, *48*, 1–5.
- (442) Hurst, S. J.; Han, M. S.; Lytton-Jean, A. K. R.; Mirkin, C. A. Screening the Sequence Selectivity of DNA-Binding Molecules Using a Gold Nanoparticle-Based Colorimetric Approach. *Anal. Chem.* **2007**, *79*, 7201–7205.
- (443) Liu, J.; Lu, Y. Fast Colorimetric Sensing of Adenosine and Cocaine Based on a General Sensor Design Involving Aptamers and Nanoparticles. *Angew. Chem., Int. Ed.* **2006**, *45*, 90–94.
- (444) Liu, J.; Lu, Y. Adenosine-Dependent Assembly of Aptazyme-Functionalized Gold Nanoparticles and Its Application as a Colorimetric Biosensor. *Anal. Chem.* **2004**, *76*, 1627–1632.
- (445) Liu, J.; Lu, Y. Preparation of Aptamer-Linked Gold Nanoparticle Purple Aggregates for Colorimetric Sensing of Analytes. *Nat. Protoc.* **2006**, *1*, 246–252.
- (446) Zhu, Z.; Wu, C.; Liu, H.; Zou, Y.; Zhang, X.; Kang, H.; Yang, C. J.; Tan, W. An Aptamer Cross-Linked Hydrogel as a Colorimetric Platform for Visual Detection. *Angew. Chem., Int. Ed.* **2010**, *49*, 1052–1056.
- (447) Zhang, J.; Wang, L.; Pan, D.; Song, S.; Boey, F. Y. C.; Zhang, H.; Fan, C. Visual Cocaine Detection with Gold Nanoparticles and Rationally Engineered Aptamer Structures. *Small* **2008**, *4*, 1196–120.
- (448) Han, M. S.; Lytton-Jean, A. K. R.; Oh, B.-K.; Heo, J.; Mirkin, C. A. Colorimetric Screening of DNA-Binding Molecules with Gold Nanoparticle Probes. *Angew. Chem., Int. Ed.* **2006**, *45*, 1807–1810.
- (449) Xia, F.; Zuo, X.; Yang, R.; Xiao, Y.; Kang, D.; Vallee-Belisle, A.; Gong, X.; Yuen, J. D.; Hsu, B. B. Y.; Heeger, A. J.; Plaxco, K. W. Colorimetric Detection of DNA, Small Molecules, Proteins, and Ions Using Unmodified Gold Nanoparticles and Conjugated Polyelectrolytes. *Proc. Natl. Acad. Sci. U. S. A.* **2010**, *107*, 10837–10841.
- (450) Xu, X.; Han, M. S.; Mirkin, C. A. A Gold-Nanoparticle-Based Real-Time Colorimetric Screening Method for Endonuclease Activity and Inhibition. *Angew. Chem., Int. Ed.* **2007**, *46*, 3468–3470.
- (451) Li, H. X.; Rothberg, L. J. Colorimetric Detection of DNA Sequences Based on Electrostatic Interactions with Unmodified Gold Nanoparticles. *Proc. Natl. Acad. Sci. U. S. A.* **2004**, *101*, 14036–14039.
- (452) Li, H. X.; Rothberg, L. J. Label-Free Colorimetric Detection of Specific Sequences in Genomic DNA Amplified by the Polymerase Chain Reaction. *J. Am. Chem. Soc.* **2004**, *126*, 10958–10961.
- (453) Wei, H.; Li, B.; Li, J.; Wang, E.; Dong, S. Simple and Sensitive Aptamer-Based Colorimetric Sensing of Protein Using Unmodified Gold Nanoparticle Probes. *Chem. Commun.* **2007**, 3735–3737.
- (454) Li, B.; Dong, S.; Wang, E. Homogeneous Analysis: Label-Free and Substrate-Free Aptasensors. *Chem. - Asian J.* **2010**, *5*, 1262–1272.
- (455) Wang, L.; Liu, X.; Hu, X.; Song, S.; Fan, C. Unmodified Gold Nanoparticles as a Colorimetric Probe for Potassium DNA Aptamers. *Chem. Commun.* **2006**, 3780–3782.
- (456) Lee, J.-S.; Ulmann, P. A.; Han, M. S.; Mirkin, C. A. A DNA–Gold Nanoparticle-Based Colorimetric Competition Assay for the Detection of Cysteine. *Nano Lett.* **2008**, *8*, 529–533.
- (457) Li, B.; Du, Y.; Dong, S. DNA Based Gold Nanoparticles Colorimetric Sensors for Sensitive and Selective Detection of Ag(I) Ions. *Anal. Chim. Acta* **2009**, *644*, 78–82.
- (458) Laromaine, A.; Koh, L.; Murugesan, M.; Ulijn, R. V.; Stevens, M. M. Protease-Triggered Dispersion of Nanoparticle Assemblies. *J. Am. Chem. Soc.* **2007**, *129*, 4156–4157.
- (459) Breaker, R. R.; Joyce, G. F. A DNA Enzyme that Cleaves RNA. *Chem. Biol.* **1994**, *1*, 223–229.
- (460) Imura, K.; Okamoto, H.; Hossain, M. K.; Kitajima, M. Visualization of Localized Intense Optical Fields in Single Gold–Nanoparticle Assemblies and Ultrasensitive Raman Active Sites. *Nano Lett.* **2006**, *6*, 2173–2176.
- (461) Huang, X.; El-Sayed, I. H.; Qian, W.; El-Sayed, M. A. Cancer Cells Assemble and Align Gold Nanorods Conjugated to Antibodies to Produce Highly Enhanced, Sharp, and Polarized Surface Raman Spectra: A Potential Cancer Diagnostic Marker. *Nano Lett.* **2007**, *7*, 1591–1597.
- (462) Kamra, T.; Zhou, T.; Montelius, L.; Schnadt, J.; Ye, L. Implementation of Molecularly Imprinted Polymer Beads for Surface Enhanced Raman Detection. *Anal. Chem.* **2015**, *87*, S056–S061.
- (463) Tyler, T. P.; Henry, A.-I.; Van Duyne, R. P.; Hersam, M. C. Improved Monodispersity of Plasmonic Nanoantennas via Centrifugal Processing. *J. Phys. Chem. Lett.* **2011**, *2*, 218–222.
- (464) Rodríguez-Lorenzo, L.; Álvarez-Puebla, R. A.; Pastoriza-Santos, I.; Mazzucco, S.; Stéphan, O.; Kociak, M.; Liz-Marzán, L. M.; García de Abajo, F. J. Zeptomol Detection Through Controlled Ultrasensitive Surface-Enhanced Raman Scattering. *J. Am. Chem. Soc.* **2009**, *131*, 4616–4618.
- (465) Kneipp, K.; Wang, Y.; Kneipp, H.; Perelman, L. T.; Itzkan, I.; Dasari, R.; Feld, M. S. Single Molecule Detection Using Surface-Enhanced Raman Scattering (SERS). *Phys. Rev. Lett.* **1997**, *78*, 1667.
- (466) Li, Z.-Y.; Xia, Y. Metal Nanoparticles with Gain toward Single-Molecule Detection by Surface-Enhanced Raman Scattering. *Nano Lett.* **2010**, *10*, 243–249.
- (467) Li, J. F.; Huang, Y. F.; Ding, Y.; Yang, Z. L.; Li, S. B.; Zhou, X. S.; Fan, F. R.; Zhang, W.; Zhou, Z. Y.; Wu, D. Y.; Ren, B.; Wang, Z. L.; Tian, Z. Q. Shell-Isolated Nanoparticle-Enhanced Raman Spectroscopy. *Nature* **2010**, *464*, 392–395.
- (468) Wang, Y.; Yan, B.; Chen, L. SERS Tags: Novel Optical Nanoprobes for Bioanalysis. *Chem. Rev.* **2013**, *113*, 1391–1428.
- (469) Zamarion, V. M.; Timm, R. A.; Araki, K.; Toma, H. E. Ultrasensitive SERS Nanoprobes for Hazardous Metal Ions Based on Trimercaptotriazine-Modified Gold Nanoparticles. *Inorg. Chem.* **2008**, *47*, 2934–2936.
- (470) Tsoutsis, D.; Montenegro, J. M.; Dommershausen, F.; Koert, U.; Liz-Marzán, L. M.; Parak, W. J.; Alvarez-Puebla, R. A. Quantitative Surface-Enhanced Raman Scattering Ultradetection of Atomic Inorganic Ions: The Case of Chloride. *ACS Nano* **2011**, *5*, 7539–7546.
- (471) Wang, C.; Chen, Y.; Wang, T.; Ma, Z.; Su, Z. Monodispersed Gold Nanorod-Embedded Silica Particles as Novel Raman Labels for Biosensing. *Adv. Funct. Mater.* **2008**, *18*, 355–361.
- (472) Mulvaney, S. P.; Musick, M. D.; Keating, C. D.; Natan, M. J. Glass-Coated, Analyte-Tagged Nanoparticles: A New Tagging System Based on Detection with Surface-Enhanced Raman Scattering. *Langmuir* **2003**, *19*, 4784–4790.
- (473) Samanta, A.; Maiti, K. K.; Soh, K.-S.; Liao, X.; Vendrell, M.; Dinis, U. S.; Yun, S.-W.; Bhuvaneswari, R.; Kim, H.; Rautela, S.; Chung, J.; Olivo, M.; Chang, Y.-T. Ultrasensitive Near-Infrared Raman Reporters for SERS-Based In Vivo Cancer Detection. *Angew. Chem., Int. Ed.* **2011**, *50*, 6089–6092.
- (474) Huang, T.; Murray, R. W. Quenching of [Ru(bpy)₃]²⁺ Fluorescence by Binding to Au Nanoparticles. *Langmuir* **2002**, *18*, 7077–7081.
- (475) Xia, X.; Yang, M.; Oetjen, L. K.; Zhang, Y.; Li, Q.; Chen, J.; Xia, Y. An Enzyme-Sensitive Probe for Photoacoustic Imaging and Fluorescence Detection of Protease Activity. *Nanoscale* **2011**, *3*, 950–953.
- (476) Dubertret, B.; Calame, M.; Libchaber, A. J. Single-Mismatch Detection Using Gold-Quenched Fluorescent Oligonucleotides. *Nat. Biotechnol.* **2001**, *19*, 365–370.
- (477) Dulkeith, E.; Morteaux, A. C.; Niedereichholz, T.; Klar, T. A.; Feldmann, J.; Levi, S. A.; van Veggel, F.; Reinhoudt, D. N.; Möller, M.; Gittins, D. I. Fluorescence Quenching of Dye Molecules near Gold Nanoparticles: Radiative and Nonradiative Effects. *Phys. Rev. Lett.* **2002**, *89*, 203002.
- (478) Dulkeith, E.; Ringler, M.; Klar, T. A.; Feldmann, J.; Muñoz Javier, A.; Parak, W. J. Gold Nanoparticles Quench Fluorescence by Phase Induced Radiative Rate Suppression. *Nano Lett.* **2005**, *5*, 585–589.
- (479) Oh, E.; Hong, M.-Y.; Lee, D.; Nam, S.-H.; Yoon, H. C.; Kim, H.-S. Inhibition Assay of Biomolecules based on Fluorescence Resonance Energy Transfer (FRET) between Quantum Dots and Gold Nanoparticles. *J. Am. Chem. Soc.* **2005**, *127*, 3270–3271.
- (480) Ray, P. C.; Fortner, A.; Darbha, G. K. Gold Nanoparticle Based FRET Assay for the Detection of DNA Cleavage. *J. Phys. Chem. B* **2006**, *110*, 20745–20748.

- (481) He, X.; Liu, H. B.; Li, Y.; Wang, S.; Li, Y.; Wang, N.; Xiao, J.; Xu, X. H.; Zhu, D. Gold Nanoparticle-Based Fluorometric and Colorimetric Sensing of Copper(II) Ions. *Adv. Mater.* **2005**, *17*, 2811–2815.
- (482) Huang, C.-C.; Chang, H.-T. Selective Gold-Nanoparticle-Based “Turn-On” Fluorescent Sensors for Detection of Mercury(II) in Aqueous Solution. *Anal. Chem.* **2006**, *78*, 8332–8338.
- (483) Wang, H.; Wang, Y.; Jin, J.; Yang, R. Gold Nanoparticle-Based Colorimetric and “Turn-On” Fluorescent Probe for Mercury(II) Ions in Aqueous Solution. *Anal. Chem.* **2008**, *80*, 9021–9028.
- (484) Chen, Y.-M.; Cheng, T.-L.; Tseng, W.-L. Fluorescence Turn-On Detection of Iodide, Iodate and Total Iodine Using Fluorescein-5-Isothiocyanate-Modified Gold Nanoparticles. *Analyst* **2009**, *134*, 2106–2112.
- (485) Chen, S.-J.; Chang, H.-T. Nile Red-Adsorbed Gold Nanoparticles for Selective Determination of Thiols Based on Energy Transfer and Aggregation. *Anal. Chem.* **2004**, *76*, 3727–3734.
- (486) Yang, X.; Gan, L. F.; Han, L.; Li, D.; Wang, J.; Wang, E. K. Facile Preparation of Chiral Penicillamine Protected Gold Nanoclusters and Their Applications in Cell Imaging. *Chem. Commun.* **2013**, *49*, 2302–2304.
- (487) Chen, T.; Hu, Y.; Cen, Y.; Chu, X.; Lu, Y. A Dual-Emission Fluorescent Nanocomplex of Gold-Cluster-Decorated Silica Particles for Live Cell Imaging of Highly Reactive Oxygen Species. *J. Am. Chem. Soc.* **2013**, *135*, 11595–11602.
- (488) Lin, S.-Y.; Chen, N.-T.; Sum, S.-P.; Lo, L.-W.; Yang, C.-S. Ligand Exchanged Photoluminescent Gold Quantum Dots Functionalized with Leading Peptides for Nuclear Targeting and Intracellular Imaging. *Chem. Commun.* **2008**, 4762–4764.
- (489) Wang, Y.; Chen, J.-T.; Yan, X.-P. Fabrication of Transferrin Functionalized Gold Nanoclusters/Graphene Oxide Nanocomposite for Turn-On Near-Infrared Fluorescent Bioimaging of Cancer Cells and Small Animals. *Anal. Chem.* **2013**, *85*, 2529–2535.
- (490) Lin, C.-A. J.; Yang, T.-Y.; Lee, C.-H.; Huang, S. H.; Sperling, R. A.; Zanella, M.; Li, J. K.; Shen, J.-L.; Wang, H.-H.; Yeh, H.-I.; Parak, W. J.; Chang, W. H. Synthesis, Characterization, and Bioconjugation of Fluorescent Gold Nanoclusters toward Biological Labeling Applications. *ACS Nano* **2009**, *3*, 395–401.
- (491) Retnakumari, A.; Setua, S.; Menon, D.; Ravindran, P.; Muhammed, H.; Pradeep, T.; Nair, S.; Koyakutty, M. Molecular-Receptor-Specific, Non-Toxic, Near-Infrared-Emitting Au Cluster-Protein Nanoconjugates for Targeted Cancer Imaging. *Nanotechnology* **2010**, *21*, 055103.
- (492) Liu, C.-L.; Wu, H.-T.; Hsiao, Y.-H.; Lai, C.-W.; Shih, C.-W.; Peng, Y.-K.; Tang, K.-C.; Chang, H.-W.; Chien, Y.-C.; Hsiao, J.-K.; Cheng, J.-T.; Chou, P.-T. Insulin-Directed Synthesis of Fluorescent Gold Nanoclusters: Preservation of Insulin Bioactivity and Versatility in Cell Imaging. *Angew. Chem., Int. Ed.* **2011**, *50*, 7056–7060.
- (493) Shang, L.; Dorlich, R. M.; Brandholt, S.; Schneider, R.; Trouillet, V.; Bruns, M.; Gerthsen, D.; Nienhaus, G. U. Facile Preparation of Water-Soluble Fluorescent Gold Nanoclusters for Cellular Imaging Applications. *Nanoscale* **2011**, *3*, 2009–2014.
- (494) Wu, X.; He, X.; Wang, K.; Xie, C.; Zhou, B.; Qing, Z. Ultrasmall Near-Infrared Gold Nanoclusters for Tumor Fluorescence Imaging. *Nanoscale* **2010**, *2*, 2244–2249.
- (495) Liu, J.; Yu, M.; Zhou, C.; Yang, S.; Ning, X.; Zheng, J. Passive Tumor Targeting of Renal-Clearable Luminescent Gold Nanoparticles: Long Tumor Retention and Fast Normal Tissue Clearance. *J. Am. Chem. Soc.* **2013**, *135*, 4978–4981.
- (496) Wu, X.; Ming, T.; Wang, X.; Wang, P.; Wang, J.; Chen, J. High-Photoluminescence-Yield Gold Nanocubes: For Cell Imaging and Photothermal Therapy. *ACS Nano* **2010**, *4*, 113–120.
- (497) Zhang, Y. S.; Wang, Y.; Wang, L.; Wang, Y.; Cai, X.; Zhang, C.; Wang, L. V.; Xia, Y. Labeling Human Mesenchymal Stem Cells with Gold Nanocages for *in Vitro* and *in Vivo* Tracking by Two-Photon Microscopy and Photoacoustic Microscopy. *Theranostics* **2013**, *3*, 532–543.
- (498) Yguerabide, J.; Yguerabide, E. E. Light-Scattering Submicroscopic Particles as Highly Fluorescent Analogs and Their Use as Tracer Labels in Clinical and Biological Applications: I. Theory. *Anal. Biochem.* **1998**, *262*, 137–156.
- (499) Yguerabide, J.; Yguerabide, E. E. Light-Scattering Submicroscopic Particles as Highly Fluorescent Analogs and Their Use as Tracer Labels in Clinical and Biological Applications: II. Experimental Characterization. *Anal. Biochem.* **1998**, *262*, 157–176.
- (500) Hu, M.; Novo, C.; Funston, A.; Wang, H.; Staleva, H.; Zou, S.; Mulvaney, P.; Xia, Y.; Hartland, G. V. Dark-Field Microscopy Studies of Single Metal Nanoparticles: Understanding the Factors that Influence the Linewidth of the Localized Surface Plasmon Resonance. *J. Mater. Chem.* **2008**, *18*, 1949–1960.
- (501) Yu, C.; Nakshatri, H.; Irudayaraj, J. Identity Profiling of Cell Surface Markers by Multiplex Gold Nanorod Probes. *Nano Lett.* **2007**, *7*, 2300–2306.
- (502) Dickerson, E. B.; Dreaden, E. C.; Huang, X.; El-Sayed, I. H.; Chu, H.; Pushpanketh, S.; McDonald, J. F.; El-Sayed, M. A. Gold Nanorod Assisted Near-Infrared Plasmonic Photothermal Therapy (PPTT) of Squamous Cell Carcinoma in Mice. *Cancer Lett.* **2008**, *269*, 57–66.
- (503) Zysk, A. M.; Nguyen, F. T.; Oldenburg, A. L.; Marks, D. L.; Boppart, S. A. Optical Coherence Tomography: a Review of Clinical Development from Bench to Bedside. *J. Biomed. Opt.* **2007**, *12*, 051403.
- (504) Tong, L.; Wei, Q.; Wei, A.; Cheng, J.-X. Gold Nanorods as Contrast Agents for Biological Imaging: Optical Properties, Surface Conjugation and Photothermal Effects. *Photochem. Photobiol.* **2009**, *85*, 21–32.
- (505) Gobin, A. M.; Lee, M. H.; Halas, N. J.; James, W. D.; Drezek, R. A.; West, J. L. Near-Infrared Resonant Nanoshells for Combined Optical Imaging and Photothermal Cancer Therapy. *Nano Lett.* **2007**, *7*, 1929–1934.
- (506) Oldenburg, A. L.; Hansen, M. N.; Zweifel, D. A.; Wei, A.; Boppart, S. A. Plasmon-Resonant Gold Nanorods as Low Back-scattering Albedo Contrast Agents. *Opt. Express* **2006**, *14*, 6724–6738.
- (507) Troutman, T. S.; Barton, J. K.; Romanowski, M. Optical Coherence Tomography with Plasmon Resonant Nanorods of Gold. *Opt. Lett.* **2007**, *32*, 1438–1440.
- (508) Puppels, G. J.; de Mul, F. F. M.; Otto, C.; Greve, J.; Robert-Nicoud, M.; Arndt-Jovin, D. J.; Jovin, T. M. Studying Single Living Cells and Chromosomes by Confocal Raman Microspectroscopy. *Nature* **1990**, *347*, 301–303.
- (509) Caspers, P. J.; Lucassen, G. W.; Puppels, G. J. Combined *In Vivo* Confocal Raman Spectroscopy and Confocal Microscopy of Human Skin. *Biophys. J.* **2003**, *85*, 572–580.
- (510) Palonpon, A. F.; Ando, J.; Yamakoshi, H.; Dodo, K.; Sodeoka, M.; Kawata, S.; Fujita, K. Raman and SERS Microscopy for Molecular Imaging of Live Cells. *Nat. Protoc.* **2013**, *8*, 677–692.
- (511) Kneipp, K.; Haka, A. S.; Kneipp, H.; Badizadegan, K.; Yoshizawa, N.; Boone, C.; Shafer-Peltier, K. E.; Motz, J. T.; Dasari, R. R.; Feld, M. S. Surface-Enhanced Raman Spectroscopy in Single Living Cells Using Gold Nanoparticles. *Appl. Spectrosc.* **2002**, *56*, 150–154.
- (512) Eliasson, C.; Lorén, A.; Engblom, J.; Josefson, M.; Abrahamsson, J.; Abrahamsson, K. Surface-Enhanced Raman Scattering Imaging of Single Living Lymphocytes with Multivariate Evaluation. *Spectrochim. Acta, Part A* **2005**, *61*, 755–760.
- (513) Tang, H.-W.; Yang, X. B.; Kirkham, J.; Smith, D. A. Probing Intrinsic and Extrinsic Components in Single Osteosarcoma Cells by Near-Infrared Surface-Enhanced Raman Scattering. *Anal. Chem.* **2007**, *79*, 3646–3653.
- (514) Hamada, K.; Fujita, K.; Smith, N. I.; Kobayashi, M.; Inouye, Y.; Kawata, S. Raman Microscopy for Dynamic Molecular Imaging of Living Cells. *J. Biomed. Opt.* **2008**, *13*, 044027.
- (515) Veirs, D. K.; Ager, J. W., III; Loucks, E. T.; Rosenblatt, G. M. Mapping Materials Properties with Raman Spectroscopy Utilizing a 2-D Detector. *Appl. Opt.* **1990**, *29*, 4969–4980.
- (516) Okuno, M.; Hamaguchi, H.-O. Multifocus Confocal Raman Microspectroscopy for Fast Multimode Vibrational Imaging of Living Cells. *Opt. Lett.* **2010**, *35*, 4096–4098.

- (517) Kong, L.; Zhang, P.; Yu, J.; Setlow, P.; Li, Y.-Q. Rapid Confocal Raman Imaging Using a Synchro Multifoci-Scan Scheme for Dynamic Monitoring of Single Living Cells. *Appl. Phys. Lett.* **2011**, *98*, 213703.
- (518) Ling, J.; Weitman, S. D.; Miller, M. A.; Moore, R. V.; Bovik, A. C. Direct Raman Imaging Techniques for Study of the Subcellular Distribution of a Drug. *Appl. Opt.* **2002**, *41*, 6006–6017.
- (519) Fujita, K.; Ishitobi, S.; Hamada, K.; Smith, N. I.; Taguchi, A.; Inouye, Y.; Kawata, S. Time-Resolved Observation of Surface-Enhanced Raman Scattering from Gold Nanoparticles during Transport through a Living Cell. *J. Biomed. Opt.* **2009**, *14*, 024038.
- (520) Kneipp, J.; Kneipp, H.; Wittig, B.; Kneipp, K. One- and Two-Photon Excited Optical pH Probing for Cells Using Surface-Enhanced Raman and Hyper-Raman Nanosensors. *Nano Lett.* **2007**, *7*, 2819–2823.
- (521) Zavaleta, C. L.; Smith, B. R.; Walton, I.; Doering, W.; Davis, G.; Shojaei, B.; Natan, M. J.; Gambhir, S. S. Multiplexed Imaging of Surface Enhanced Raman Scattering Nanotags in Living Mice Using Noninvasive Raman Spectroscopy. *Proc. Natl. Acad. Sci. U. S. A.* **2009**, *106*, 13511–13516.
- (522) Keren, S.; Zavaleta, C.; Cheng, Z.; de la Zerda, A.; Gheysens, O.; Gambhir, S. S. Noninvasive Molecular Imaging of Small Living Subjects Using Raman Spectroscopy. *Proc. Natl. Acad. Sci. U. S. A.* **2008**, *105*, 5844–5849.
- (523) Park, H.; Lee, S.; Chen, L.; Lee, E. K.; Shin, S. Y.; Lee, Y. H.; Son, S. W.; Oh, C. H.; Song, J. M.; Kang, S. H.; Choo, J. SERS Imaging of HER2-Overexpressed MCF7 Cells Using Antibody-Conjugated Gold Nanorods. *Phys. Chem. Chem. Phys.* **2009**, *11*, 7444–7449.
- (524) Lee, S.; Chon, H.; Lee, J.; Ko, J.; Chung, B. H.; Lim, D. W.; Choo, J. Rapid and Sensitive Phenotypic Marker Detection on Breast Cancer Cells Using Surface-Enhanced Raman Scattering (SERS) Imaging. *Biosens. Bioelectron.* **2014**, *51*, 238–243.
- (525) Kircher, M. F.; de la Zerda, A.; Jokerst, J. V.; Zavaleta, C. L.; Kempen, P. J.; Mittra, E.; Pitter, K.; Huang, R.; Campos, C.; Habte, F.; Sinclair, R.; Brennan, C. W.; Mellinghoff, I. K.; Holland, E. C.; Gambhir, S. S. A Brain Tumor Molecular Imaging Strategy Using a New Triple-Modality MRI-Photoacoustic-Raman Nanoparticle. *Nat. Med.* **2012**, *18*, 829–834.
- (526) Huang, X.; Jain, P.; El-Sayed, I.; El-Sayed, M. Plasmonic Photothermal Therapy (PPTT) Using Gold Nanoparticles. *Lasers Med. Sci.* **2008**, *23*, 217–228.
- (527) Sigrist, M. W. Laser Generation of Acoustic Waves in Liquids and Gases. *J. Appl. Phys.* **1986**, *60*, R83–R121.
- (528) Xu, M.; Wang, L. V. Photoacoustic Imaging in Biomedicine. *Rev. Sci. Instrum.* **2006**, *77*, 041101.
- (529) Wang, L. V.; Hu, S. Photoacoustic Tomography: *In Vivo* Imaging from Organelles to Organs. *Science* **2012**, *335*, 1458–1462.
- (530) Beard, P. Biomedical Photoacoustic Imaging. *Interface Focus* **2011**, *1*, 602–631.
- (531) Yang, X.; Stein, E. W.; Ashkenazi, S.; Wang, L. V. Nanoparticles for Photoacoustic Imaging. *Wiley Interdiscip. Rev. Nanomed. Nanobiotechnol.* **2009**, *1*, 360–368.
- (532) Copland, J. A.; Eghtedari, M.; Popov, V. L.; Kotov, N.; Mamedova, N.; Motamedi, M.; Oraevsky, A. A. Bioconjugated Gold Nanoparticles as a Molecular Based Contrast Agent: Implications for Imaging of Deep Tumors Using Photoacoustic Tomography. *Mol. Imaging Biol.* **2004**, *6*, 341–349.
- (533) Wang, Y.; Xie, X.; Wang, X.; Ku, G.; Gill, K. L.; O'Neal, D. P.; Stoica, G.; Wang, L. V. Photoacoustic Tomography of a Nanoshell Contrast Agent in the *In Vivo* Rat Brain. *Nano Lett.* **2004**, *4*, 1689–1692.
- (534) Yang, X.; Skrabalak, S. E.; Li, Z.-Y.; Xia, Y.; Wang, L. V. Photoacoustic Tomography of a Rat Cerebral Cortex *in vivo* with Au Nanocages as an Optical Contrast Agent. *Nano Lett.* **2007**, *7*, 3798–3802.
- (535) Kim, C.; Cho, E. C.; Chen, J.; Song, K. H.; Au, L.; Favazza, C.; Zhang, Q.; Cobley, C. M.; Gao, F.; Xia, Y.; Wang, L. V. *In Vivo* Molecular Photoacoustic Tomography of Melanomas Targeted by Bioconjugated Gold Nanocages. *ACS Nano* **2010**, *4*, 4559–4564.
- (536) Song, K. H.; Kim, C.; Cobley, C. M.; Xia, Y.; Wang, L. V. Near-Infrared Gold Nanocages as a New Class of Tracers for Photoacoustic Sentinel Lymph Node Mapping on a Rat Model. *Nano Lett.* **2009**, *9*, 183–188.
- (537) Cai, X.; Li, W.; Kim, C.-H.; Yuan, Y.; Wang, L. V.; Xia, Y. *In Vivo* Quantitative Evaluation of the Transport Kinetics of Gold Nanocages in a Lymphatic System by Noninvasive Photoacoustic Tomography. *ACS Nano* **2011**, *5*, 9658–9667.
- (538) Song, K. H.; Kim, C.; Maslov, K.; Wang, L. V. Noninvasive *In Vivo* Spectroscopic Nanorod-Contrast Photoacoustic Mapping of Sentinel Lymph Nodes. *Eur. J. Radiol.* **2009**, *70*, 227–231.
- (539) Pan, D.; Pramanik, M.; Senpan, A.; Ghosh, S.; Wickline, S. A.; Wang, L. V.; Lanza, G. M. Near Infrared Photoacoustic Detection of Sentinel Lymph Nodes with Gold Nanobeacons. *Biomaterials* **2010**, *31*, 4088–4093.
- (540) Dorsey, J. F.; Sun, L.; Joh, D. Y.; Witztum, A.; Zaki, A. A.; Kao, G. D.; Alonso-Basanta, M.; Avery, S.; Tsourkas, A.; Hahn, S. M. Gold Nanoparticles in Radiation Research: Potential Applications for Imaging and Radiosensitization. *Transl. Cancer Res.* **2013**, *2*, 280–291.
- (541) Kim, D.; Park, S.; Lee, J. H.; Jeong, Y. Y.; Jon, S. Antibiofouling Polymer-Coated Gold Nanoparticles as a Contrast Agent for *In Vivo* X-ray Computed Tomography Imaging. *J. Am. Chem. Soc.* **2007**, *129*, 7661–7665.
- (542) Xie, H.; Wang, Z. J.; Bao, A.; Goins, B.; Phillips, W. T. *In Vivo* PET Imaging and Biodistribution of Radiolabeled Gold Nanoshells in Rats with Tumor Xenografts. *Int. J. Pharm.* **2010**, *395*, 324–330.
- (543) Xie, H.; Diagaradjane, P.; Deorukhar, A. A.; Goins, B.; Bao, A.; Phillips, W. T.; Wang, Z.; Schwartz, J.; Krishnan, S. Integrin $\alpha\beta 3$ -Targeted Gold Nanoshells Augment Tumor Vasculature-Specific Imaging and Therapy. *Int. J. Nanomed.* **2011**, *6*, 259–269.
- (544) Lu, W.; Melancon, M. P.; Xiong, C.; Huang, Q.; Elliott, A.; Song, S.; Zhang, R.; Flores, L. G.; Gelovani, J. G.; Wang, L. V.; Ku, G.; Stafford, R. J.; Li, C. Effects of Photoacoustic Imaging and Photothermal Ablation Therapy Mediated by Targeted Hollow Gold Nanospheres in an Orthotopic Mouse Xenograft Model of Glioma. *Cancer Res.* **2011**, *71*, 6116–6121.
- (545) Wang, Y.; Liu, Y.; Luehmann, H.; Xia, X.; Brown, P.; Jarreau, C.; Welch, M.; Xia, Y. Evaluating the Pharmacokinetics and *In Vivo* Cancer Targeting Capability of Au Nanocages by Positron Emission Tomography Imaging. *ACS Nano* **2012**, *6*, 5880–5888.
- (546) Wang, Y.; Liu, Y.; Luehmann, H.; Xia, X.; Wan, D.; Cutler, C.; Xia, Y. Radioluminescent Gold Nanocages with Controlled Radioactivity for Real-Time *In Vivo* Imaging. *Nano Lett.* **2013**, *13*, 581–585.
- (547) Phelps, M. E. PET: The Merging of Biology and Imaging into Molecular Imaging. *J. Nucl. Med.* **2000**, *41*, 661–681.
- (548) Xu, Y.; Liu, H.; Cheng, Z. Harnessing the Power of Radionuclides for Optical Imaging: Cerenkov Luminescence Imaging. *J. Nucl. Med.* **2011**, *52*, 2009–2018.
- (549) Rahmim, A.; Zaidi, H. PET Versus SPECT: Strengths, Limitations and Challenges. *Nucl. Med. Commun.* **2008**, *29*, 193–207.
- (550) Debbage, P.; Jaschke, W. Molecular Imaging with Nanoparticles: Giant Roles for Dwarf Actors. *Histochem. Cell Biol.* **2008**, *130*, 845–875.
- (551) Hahn, M.; Singh, A.; Sharma, P.; Brown, S.; Moudgil, B. Nanoparticles as Contrast Agents for *In Vivo* Bioimaging: Current Status and Future Perspectives. *Anal. Bioanal. Chem.* **2011**, *399*, 3–27.
- (552) Moses, W. W. Fundamental Limits of Spatial Resolution in PET. *Nucl. Instrum. Methods Phys. Res., Sect. A* **2011**, *648* (Suppl. 1), S236–S240.
- (553) Lusic, H.; Grinstaff, M. W. X-ray-Computed Tomography Contrast Agents. *Chem. Rev.* **2013**, *113*, 1641–1666.
- (554) Jackson, P. A.; Rahman, W. N. W. A.; Wong, C. J.; Ackerly, T.; Geso, M. Potential Dependent Superiority of Gold Nanoparticles in Comparison to Iodinated Contrast Agents. *Eur. J. Radiol.* **2010**, *75*, 104–109.
- (555) Hainfeld, J. F.; Slatkin, D. N.; Smilowitz, H. M. The Use of Gold Nanoparticles to Enhance Radiotherapy in Mice. *Phys. Med. Biol.* **2004**, *49*, N309–N315.

- (556) Hainfeld, J. F.; Slatkin, D. N.; Focella, T. M.; Smilowitz, H. M. Gold Nanoparticles: A New X-ray Contrast Agent. *Br. J. Radiol.* **2006**, *79*, 248–253.
- (557) Kattumuri, V.; Katti, K.; Bhaskaran, S.; Boote, E. J.; Casteel, S. W.; Fent, G. M.; Robertson, D. J.; Chandrasekhar, M.; Kannan, R.; Katti, K. V. Gum Arabic as a Phytochemical Construct for the Stabilization of Gold Nanoparticles: *In Vivo* Pharmacokinetics and X-ray-Contrast-Imaging Studies. *Small* **2007**, *3*, 333–341.
- (558) Kojima, C.; Umeda, Y.; Ogawa, M.; Harada, Y.; Magata, Y.; Kono, K. X-ray Computed Tomography Contrast Agents Prepared by Seeded Growth of Gold Nanoparticles in PEGylated Dendrimer. *Nanotechnology* **2010**, *21*, 245104.
- (559) Xu, C.; Tung, G. A.; Sun, S. Size and Concentration Effect of Gold Nanoparticles on X-ray Attenuation As Measured on Computed Tomography. *Chem. Mater.* **2008**, *20*, 4167–4169.
- (560) Aydogan, B.; Li, J.; Rajh, T.; Chaudhary, A.; Chmura, S.; Pelizzari, C.; Wietholt, C.; Kurtoglu, M.; Redmond, P. AuNP-DG: Deoxyglucose-Labeled Gold Nanoparticles as X-ray Computed Tomography Contrast Agents for Cancer Imaging. *Mol. Imaging Biol.* **2010**, *12*, 463–467.
- (561) Lijowski, M.; Caruthers, S.; Hu, G.; Zhang, H.; Scott, M. J.; Williams, T.; Erpelding, T.; Schmieder, A. H.; Kiefer, G.; Gulyas, G.; Athey, P. S.; Gaffney, P. J.; Wickline, S. A.; Lanza, G. M. High Sensitivity: High-Resolution SPECT-CT/MR Molecular Imaging of Angiogenesis in the Vx2 Model. *Invest. Radiol.* **2009**, *44*, 15–22.
- (562) Cai, Q.-Y.; Kim, S. H.; Choi, K. S.; Kim, S. Y.; Byun, S. J.; Kim, K. W.; Park, S. H.; Juhng, S. K.; Yoon, K.-H. Colloidal Gold Nanoparticles as a Blood-Pool Contrast Agent for X-ray Computed Tomography in Mice. *Invest. Radiol.* **2007**, *42*, 797–806.
- (563) Xiao, M.; Nyagilo, J.; Arora, V.; Kulkarni, P.; Xu, D.; Sun, X.; Davé, D. P. Gold Nanotags for Combined Multi-Colored Raman Spectroscopy and X-ray Computed Tomography. *Nanotechnology* **2010**, *21*, 035101.
- (564) Kim, D.; Jeong, Y. Y.; Jon, S. A Drug-Loaded Aptamer-Gold Nanoparticle Bioconjugate for Combined CT Imaging and Therapy of Prostate Cancer. *ACS Nano* **2010**, *4*, 3689–3696.
- (565) Gambhir, S. S. Molecular Imaging of Cancer with Positron Emission Tomography. *Nat. Rev. Cancer* **2002**, *2*, 683–693.
- (566) Schöder, H.; Gönen, M. Screening for Cancer with PET and PET/CT: Potential and Limitations. *J. Nucl. Med.* **2007**, *48*, 4S–18S.
- (567) Zhang, G.; Yang, Z.; Lu, W.; Zhang, R.; Huang, Q.; Tian, M.; Li, L.; Liang, D.; Li, C. Influence of Anchoring Ligands and Particle Size on the Colloidal Stability and *in Vivo* Biodistribution of Polyethylene Glycol-Coated Gold Nanoparticles in Tumor-Xenografted Mice. *Biomaterials* **2009**, *30*, 1928–1936.
- (568) Morales-Avila, E.; Ferro-Flores, G.; Ocampo-García, B. E.; De León-Rodríguez, L. M.; Santos-Cuevas, C. L.; García-Becerra, R. O.; Medina, L. A.; Gómez-Oliván, L. Multimeric System of ^{99m}Tc -Labeled Gold Nanoparticles Conjugated to c[RGDFK(C)] for Molecular Imaging of Tumor $\alpha(v)\beta(3)$ Expression. *Bioconjugate Chem.* **2011**, *22*, 913–922.
- (569) Ocampo-García, B. E.; Ramírez, F. d. M.; Ferro-Flores, G.; De León-Rodríguez, L. M.; Santos-Cuevas, C. L.; Morales-Avila, E.; de Murphy, C. A.; Pedraza-López, M.; Medina, L. A.; Camacho-López, M. A. ^{99m}Tc -Labelled Gold Nanoparticles Capped With HYNIC-Peptide/Mannose for Sentinel Lymph Node Detection. *Nucl. Med. Biol.* **2011**, *38*, 1–11.
- (570) You, J.; Zhang, R.; Xiong, C.; Zhong, M.; Melancon, M.; Gupta, S.; Nick, A. M.; Sood, A. K.; Li, C. Effective Photothermal Chemotherapy Using Doxorubicin-Loaded Gold Nanospheres That Target EphB4 Receptors in Tumors. *Cancer Res.* **2012**, *72*, 4777–4786.
- (571) Agarwal, A.; Shao, X.; Rajian, J. R.; Zhang, H.; Chamberland, D. L.; Kotov, N. A.; Wang, X. Dual-Mode Imaging with Radiolabeled Gold Nanorods. *J. Biomed. Opt.* **2011**, *16*, 051307.
- (572) Xiao, Y.; Hong, H.; Matson, V. Z.; Javadi, A.; Xu, W.; Yang, Y.; Zhang, Y.; Engle, J. W.; Nickles, R. J.; Cai, W.; Steeber, D. A.; Gong, S. Gold Nanorods Conjugated with Doxorubicin and cRGD for Combined Anticancer Drug Delivery and PET Imaging. *Theranostics* **2012**, *2*, 757–768.
- (573) Sun, X.; Huang, X.; Yan, X.; Wang, Y.; Guo, J.; Jacobson, O.; Liu, D.; Szajek, L. P.; Zhu, W.; Niu, G.; Kiesewetter, D. O.; Sun, S.; Chen, X. Chelator-Free ^{64}Cu -Integrated Gold Nanomaterials for Positron Emission Tomography Imaging Guided Photothermal Cancer Therapy. *ACS Nano* **2014**, *8*, 8438–8446.
- (574) Zhao, Y.; Sultan, D.; Detering, L.; Cho, S.; Sun, G.; Pierce, R.; Wooley, K. L.; Liu, Y. Copper-64-Alloyed Gold Nanoparticles for Cancer Imaging: Improved Radiolabel Stability and Diagnostic Accuracy. *Angew. Chem., Int. Ed.* **2014**, *53*, 156–159.
- (575) Zhao, Y.; Sultan, D.; Detering, L.; Luehmann, H.; Liu, Y. Facile Synthesis, Pharmacokinetic and Systemic Clearance Evaluation, and Positron Emission Tomography Cancer Imaging of ^{64}Cu -Au Alloy Nanoclusters. *Nanoscale* **2014**, *6*, 13501–13509.
- (576) Hu, H.; Huang, P.; Weiss, O. J.; Yan, X.; Yue, X.; Zhang, M. G.; Tang, Y.; Nie, L.; Ma, Y.; Niu, G.; Wu, K.; Chen, X. PET and NIR Optical Imaging Using Self-Illuminating (^{64}Cu) -Doped Chelator-Free Gold Nanoclusters. *Biomaterials* **2014**, *35*, 9868–9876.
- (577) Robertson, R.; Germanos, M. S.; Li, C.; Mitchell, G. S.; Cherry, S. R.; Silva, M. D. Optical Imaging of Cerenkov Light Generation from Positron-Emitting Radiotracers. *Phys. Med. Biol.* **2009**, *54*, N355–N365.
- (578) Kannan, R.; Rahing, V.; Cutler, C.; Pandrapragada, R.; Katti, K. K.; Kattumuri, V.; Robertson, J. D.; Casteel, S. J.; Jurisson, S.; Smith, C.; Boote, E.; Katti, K. V. Nanocompatible Chemistry toward Fabrication of Target-Specific Gold Nanoparticles. *J. Am. Chem. Soc.* **2006**, *128*, 11342–11343.
- (579) Zhou, C.; Hao, G.; Thomas, P.; Liu, J.; Yu, M.; Sun, S.; Öz, O. K.; Sun, X.; Zheng, J. Near-Infrared Emitting Radioactive Gold Nanoparticles with Molecular Pharmacokinetics. *Angew. Chem., Int. Ed.* **2012**, *51*, 10118–10122.
- (580) Cheng, Y.; C. Samia, A.; Meyers, J. D.; Panagopoulos, I.; Fei, B.; Burda, C. Highly Efficient Drug Delivery with Gold Nanoparticle Vectors for *in Vivo* Photodynamic Therapy of Cancer. *J. Am. Chem. Soc.* **2008**, *130*, 10643–10647.
- (581) Brown, S. D.; Nativo, P.; Smith, J.-A.; Stirling, D.; Edwards, P. R.; Venugopal, B.; Flint, D. J.; Plumb, J. A.; Graham, D.; Wheate, N. J. Gold Nanoparticles for the Improved Anticancer Drug Delivery of the Active Component of Oxaliplatin. *J. Am. Chem. Soc.* **2010**, *132*, 4678–4684.
- (582) Han, L.; Zhao, J.; Zhang, X.; Cao, W.; Hu, X.; Zou, G.; Duan, X.; Liang, X.-J. Enhanced siRNA Delivery and Silencing Gold-Chitosan Nanosystem with Surface Charge-Reversal Polymer Assembly and Good Biocompatibility. *ACS Nano* **2012**, *6*, 7340–7351.
- (583) Funkhouser, G. P.; Arevalo, M. P.; Glatzhofer, D. T.; O'Rear, E. A. Solubilization and Adsorption of Pyrrole by Sodium Dodecyl Sulfate: Polypyrrole Formation on Alumina Surfaces. *Langmuir* **1995**, *11*, 1443–1447.
- (584) Giljohann, D. A.; Seferos, D. S.; Prigodich, A. E.; Patel, P. C.; Mirkin, C. A. Gene Regulation with Polyvalent siRNA-Nanoparticle Conjugates. *J. Am. Chem. Soc.* **2009**, *131*, 2072–2073.
- (585) Cheng, Y.; Meyers, J. D.; Broome, A.-M.; Kenney, M. E.; Basilion, J. P.; Burda, C. Deep Penetration of a PDT Drug into Tumors by Noncovalent Drug-Gold Nanoparticle Conjugates. *J. Am. Chem. Soc.* **2011**, *133*, 2583–2591.
- (586) Cheng, Y.; Samia, A. C.; Li, J.; Kenney, M. E.; Resnick, A.; Burda, C. Delivery and Efficacy of a Cancer Drug as a Function of the Bond to the Gold Nanoparticle Surface. *Langmuir* **2010**, *26*, 2248–2255.
- (587) Gibson, J. D.; Khanal, B. P.; Zubarev, E. R. Paclitaxel-Functionalized Gold Nanoparticles. *J. Am. Chem. Soc.* **2007**, *129*, 11653–11661.
- (588) Dhar, S.; Daniel, W. L.; Giljohann, D. A.; Mirkin, C. A.; Lippard, S. J. Polyvalent Oligonucleotide Gold Nanoparticle Conjugates as Delivery Vehicles for Platinum(IV) Warheads. *J. Am. Chem. Soc.* **2009**, *131*, 14652–14653.
- (589) Bonoio, A. C.; Mahajan, S. D.; Ding, H.; Roy, I.; Yong, K.-T.; Kumar, R.; Hu, R.; Bergey, E. J.; Schwartz, S. A.; Prasad, P. N.

Nanotechnology Approach for Drug Addiction Therapy: Gene Silencing Using Delivery of Gold Nanorod-siRNA Nanoplex in Dopaminergic Neurons. *Proc. Natl. Acad. Sci. U. S. A.* **2009**, *106*, 5546–5550.

(590) Chakravarthy, K. V.; Bonoiu, A. C.; Davis, W. G.; Ranjan, P.; Ding, H.; Hu, R.; Bowzard, J. B.; Bergey, E. J.; Katz, J. M.; Knight, P. R.; Sambhara, S.; Prasad, P. N. Gold Nanorod Delivery of an ssRNA Immune Activator Inhibits Pandemic H1N1 Influenza Viral Replication. *Proc. Natl. Acad. Sci. U. S. A.* **2010**, *107*, 10172–10177.

(591) Yamauchi, F.; Koyamatsu, Y.; Kato, K.; Iwata, H. Layer-by-Layer Assembly of Cationic Lipid and Plasmid DNA onto Gold Surface for Stent-Assisted Gene Transfer. *Biomaterials* **2006**, *27*, 3497–3504.

(592) Lee, S. K.; Han, M. S.; Asokan, S.; Tung, C.-H. Effective Gene Silencing by Multilayered siRNA-Coated Gold Nanoparticles. *Small* **2011**, *7*, 364–370.

(593) Elbakry, A.; Zaky, A.; Liebl, R.; Rachel, R.; Goepferich, A.; Breunig, M. Layer-by-Layer Assembled Gold Nanoparticles for siRNA Delivery. *Nano Lett.* **2009**, *9*, 2059–2064.

(594) Gole, A.; Murphy, C. J. Polyelectrolyte-Coated Gold Nanorods: Synthesis, Characterization and Immobilization. *Chem. Mater.* **2005**, *17*, 1325–1330.

(595) Alkilany, A. M.; Frey, R. L.; Ferry, J. L.; Murphy, C. J. Gold Nanorods as Nanoadmicelles: 1-Naphthol Partitioning into a Nanorod-Bound Surfactant Bilayer. *Langmuir* **2008**, *24*, 10235–10239.

(596) Rosi, N. L.; Giljohann, D. A.; Thaxton, C. S.; Lytton-Jean, A. K. R.; Han, M. S.; Mirkin, C. A. Oligonucleotide-Modified Gold Nanoparticles for Intracellular Gene Regulation. *Science* **2006**, *312*, 1027–1030.

(597) Yavuz, M. S.; Cheng, Y.; Chen, J.; Cogley, C. M.; Zhang, Q.; Rycenga, M.; Xie, J.; Kim, C.; Song, K. H.; Schwartz, A. G.; Wang, L. V.; Xia, Y. Gold Nanocages Covered by Smart Polymers for Controlled Release with Near-Infrared Light. *Nat. Mater.* **2009**, *8*, 935–939.

(598) Moon, G. D.; Choi, S.-W.; Cai, X.; Li, W.; Cho, E. C.; Jeong, U.; Wang, L. V.; Xia, Y. A New Theranostic System Based on Gold Nanocages and Phase-Change Materials with Unique Features for Photoacoustic Imaging and Controlled Release. *J. Am. Chem. Soc.* **2011**, *133*, 4762–4765.

(599) Li, W.; Cai, X.; Kim, C.; Sun, G.; Zhang, Y.; Deng, R.; Yang, M.; Chen, J.; Achilefu, S.; Wang, L. V.; Xia, Y. Gold Nanocages Covered with Thermally-Responsive Polymers for Controlled Release by High-Intensity Focused Ultrasound. *Nanoscale* **2011**, *3*, 1724–1730.

(600) Sun, T.; Wang, Y.; Wang, Y.; Xu, J.; Zhao, X.; Vangveravong, S.; Mach, R. H.; Xia, Y. Using SV119-Gold Nanocage Conjugates to Eradicate Cancer Stem Cells Through a Combination of Photothermal and Chemo Therapies. *Adv. Healthcare Mater.* **2014**, *3*, 1283–1291.

(601) Hyun, D. C.; Levinson, N. S.; Jeong, U.; Xia, Y. Emerging Applications of Phase-Change Materials (PCMs): Teaching an Old Dog New Tricks. *Angew. Chem., Int. Ed.* **2014**, *53*, 3780–3795.

(602) Rothrock, A. R.; Donkers, R. L.; Schoenfish, M. H. Synthesis of Nitric Oxide-Releasing Gold Nanoparticles. *J. Am. Chem. Soc.* **2005**, *127*, 9362–9363.

(603) Polizzi, M. A.; Stasko, N. A.; Schoenfish, M. H. Water-Soluble Nitric Oxide-Releasing Gold Nanoparticles. *Langmuir* **2007**, *23*, 4938–4943.

(604) Kim, C. K.; Ghosh, P.; Pagliuca, C.; Zhu, Z.-J.; Menichetti, S.; Rotello, V. M. Entrapment of Hydrophobic Drugs in Nanoparticle Monolayers with Efficient Release into Cancer Cells. *J. Am. Chem. Soc.* **2009**, *131*, 1360–1361.

(605) Agasti, S. S.; Chompoosor, A.; You, C.-C.; Ghosh, P.; Kim, C. K.; Rotello, V. M. Photoregulated Release of Caged Anticancer Drugs from Gold Nanoparticles. *J. Am. Chem. Soc.* **2009**, *131*, 5728–5729.

(606) Takahashi, H.; Niidome, Y.; Yamada, S. Controlled Release of Plasmid DNA from Gold Nanorods Induced by Pulsed Near-Infrared Light. *Chem. Commun.* **2005**, 2247–2249.

(607) Jain, P. K.; Qian, W.; El-Sayed, M. A. Ultrafast Cooling of Photoexcited Electrons in Gold Nanoparticle-Thiolated DNA

Conjugates Involves the Dissociation of the Gold–Thiol Bond. *J. Am. Chem. Soc.* **2006**, *128*, 2426–2433.

(608) Lu, W.; Zhang, G. D.; Zhang, R.; Flores, L. G., II; Huang, Q.; Gelovani, J. G.; Li, C. Tumor Site-Specific Silencing of NF- κ B p65 by Targeted Hollow Gold Nanosphere-Mediated Photothermal Transfection. *Cancer Res.* **2010**, *70*, 3177–3188.

(609) Conde, J.; Tian, F.; Hernández, Y.; Bao, C.; Cui, D.; Janssen, K.-P.; Ibarra, M. R.; Baptista, P. V.; Stoeger, T.; de la Fuente, J. M. *In Vivo* Tumor Targeting via Nanoparticle-Mediated Therapeutic siRNA Coupled to Inflammatory Response in Lung Cancer Mouse Models. *Biomaterials* **2013**, *34*, 7744–7753.

(610) Poon, L.; Zandberg, W.; Hsiao, D.; Erno, Z.; Sen, D.; Gates, B. D.; Branda, N. R. Photothermal Release of Single-Stranded DNA from the Surface of Gold Nanoparticles Through Controlled Denaturing and Au–S Bond Breaking. *ACS Nano* **2010**, *4*, 6395–6403.

(611) Troutman, T. S.; Barton, J. K.; Romanowski, M. Biodegradable Plasmon Resonant Nanoshells. *Adv. Mater.* **2008**, *20*, 2604–2608.

(612) Yang, X.-C.; Samanta, B.; Agasti, S. S.; Jeong, Y.; Zhu, Z.-J.; Rana, S.; Miranda, O. R.; Rotello, V. M. Drug Delivery Using Nanoparticle-Stabilized Nanocapsules. *Angew. Chem., Int. Ed.* **2011**, *50*, 477–481.

(613) Sun, T.; Zhang, Y. S.; Pang, B.; Hyun, D. C.; Yang, M.; Xia, Y. Engineered Nanoparticles for Drug Delivery in Cancer Therapy. *Angew. Chem., Int. Ed.* **2014**, *53*, 12320–12364.

(614) He, Q.; Shi, J. MSN Anti-Cancer Nanomedicines: Chemotherapy Enhancement, Overcoming of Drug Resistance, and Metastasis Inhibition. *Adv. Mater.* **2014**, *26*, 391–411.

(615) Simon, S. M.; Schindler, M. Cell Biological Mechanisms of Multidrug Resistance in Tumors. *Proc. Natl. Acad. Sci. U. S. A.* **1994**, *91*, 3497–3504.

(616) Wang, F.; Wang, Y.-C.; Dou, S.; Xiong, M.-H.; Sun, T.-M.; Wang, J. Doxorubicin-Tethered Responsive Gold Nanoparticles Facilitate Intracellular Drug Delivery for Overcoming Multidrug Resistance in Cancer Cells. *ACS Nano* **2011**, *5*, 3679–3692.

(617) Wood, K. C.; Chuang, H. F.; Batten, R. D.; Lynn, D. M.; Hammond, P. T. Controlling Interlayer Diffusion to Achieve Sustained, Multiagent Delivery from Layer-by-Layer Thin Films. *Proc. Natl. Acad. Sci. U. S. A.* **2006**, *103*, 10207–10212.

(618) Kim, B.-S.; Smith, R. C.; Poon, Z.; Hammond, P. T. MAD (Multiagent Delivery) Nanolayer: Delivering Multiple Therapeutics from Hierarchically Assembled Surface Coating. *Langmuir* **2009**, *25*, 14086–14092.

(619) Poon, Z.; Lee, J. B.; Morton, S. W.; Hammond, P. T. Controlling *In Vivo* Stability and Biodistribution in Electrostatically Assembled Nanoparticles for Systemic Delivery. *Nano Lett.* **2011**, *11*, 2096–2103.

(620) He, Q.; Gao, Y.; Zhang, L.; Zhang, Z.; Gao, F.; Ji, X.; Li, Y.; Shi, J. A pH-Responsive Mesoporous Silica Nanoparticles-Based Multi-Drug Delivery System for Overcoming Multi-Drug Resistance. *Biomaterials* **2011**, *32*, 7711–7720.

(621) Qiu, L.; Chen, T.; Öçsoy, I.; Yasun, E.; Wu, C.; Zhu, G.; You, M.; Han, D.; Jiang, J.; Yu, R.; Tan, W. A Cell-Targeted, Size-Photocontrollable, Nuclear-Uptake Nanodrug Delivery System for Drug-Resistant Cancer Therapy. *Nano Lett.* **2015**, *15*, 457.

(622) Svaasand, L.; Gomer, C.; Morinelli, E. On the Physical Rationale of Laser Induced Hyperthermia. *Lasers Med. Sci.* **1990**, *5*, 121–128.

(623) Philipp, C. M.; Rohde, E.; Berlien, H.-P. Nd:YAG Laser Procedures in Tumor Treatment. *Semin. Surg. Oncol.* **1995**, *11*, 290–298.

(624) Prudhomme, M.; Tang, J.; Rouy, S.; Delacretaz, G.; Salathe, R. P.; Godlewski, G. Interstitial Diode Laser Hyperthermia in the Treatment of Subcutaneous Tumor. *Lasers Surg. Med.* **1996**, *19*, 445–450.

(625) Seki, T.; Wakabayashi, M.; Nakagawa, T.; Imamura, M.; Tamai, T.; Nishimura, A.; Yamashiki, N.; Okamura, A.; Inoue, K. Percutaneous Microwave Coagulation Therapy for Patients with Small Hepatocellular Carcinoma. *Cancer* **1999**, *85*, 1694–1702.

- (626) Mirza, A. N.; Fornage, B. D.; Sneige, N.; Kuerer, H. M.; Newman, L. A.; Ames, F. C.; Singletary, S. E. Radiofrequency Ablation of Solid Tumors. *Cancer J.* **2001**, *7*, 95–102.
- (627) Jolesz, F. A.; Hynynen, K. Magnetic Resonance Image-Guided Focused Ultrasound Surgery. *Cancer J.* **2002**, *8*, S100–S112.
- (628) Rengan, A. K.; Bukhari, A. B.; Pradhan, A.; Mallhotra, R.; Banerjee, R.; Srivastava, R.; De, A. *In Vivo* Analysis of Biodegradable Liposome Gold Nanoparticles as Efficient Agents for Photothermal Therapy of Cancer. *Nano Lett.* **2015**, *15*, 842–848.
- (629) Matsumoto, K.; Yamamoto, T.; Kamata, R.; Maeda, H. Pathogenesis of Serratia Infection: Activation of the Hageman Factor-Prekallikrein Cascade by Serratia Protease. *J. Biochem.* **1984**, *96*, 739–749.
- (630) Chen, W. R.; Adams, R. L.; Bartels, K. E.; Nordquist, R. E. Chromophore-Enhanced *In Vivo* Tumor Cell Destruction Using an 808-nm Diode Laser. *Cancer Lett.* **1995**, *94*, 125–131.
- (631) Chen, W. R.; Adams, R. L.; Higgins, A. K.; Bartels, K. E.; Nordquist, R. E. Photothermal Effects on Murine Mammary Tumors Using Indocyanine Green and an 808-nm Diode Laser: An *In Vivo* Efficacy Study. *Cancer Lett.* **1996**, *98*, 169–173.
- (632) Link, S.; El-Sayed, M. A. Spectral Properties and Relaxation Dynamics of Surface Plasmon Electronic Oscillations in Gold and Silver Nanodots and Nanorods. *J. Phys. Chem. B* **1999**, *103*, 8410–8426.
- (633) Hirsch, L. R.; Stafford, R. J.; Bankson, J. A.; Sershen, S. R.; Rivera, B.; Price, R. E.; Hazle, J. D.; Halas, N. J.; West, J. L. Nanoshell-Mediated Near-Infrared Thermal Therapy of Tumors under Magnetic Resonance Guidance. *Proc. Natl. Acad. Sci. U. S. A.* **2003**, *100*, 13549–13554.
- (634) Dutz, S.; Hergt, R. *Nanotechnology* **2014**, *25*, 452001.
- (635) O'Neal, D. P.; Hirsch, L. R.; Halas, N. J.; Payne, J. D.; West, J. L. Photo-Thermal Tumor Ablation in Mice Using Near Infrared-Absorbing Nanoparticles. *Cancer Lett.* **2004**, *209*, 171–176.
- (636) von Maltzahn, G.; Park, J.-H.; Agrawal, A.; Bandaru, N. K.; Das, S. K.; Sailor, M. J.; Bhatia, S. N. Computationally Guided Photothermal Tumor Therapy Using Long-Circulating Gold Nanorods Antennas. *Cancer Res.* **2009**, *69*, 3892–3900.
- (637) Chen, J.; Glaus, C.; Laforest, R.; Zhang, Q.; Yang, M.; Gidding, M.; Welch, M. J.; Xia, Y. Gold Nanocages as Photothermal Transducers for Cancer Treatment. *Small* **2010**, *6*, 811–817.
- (638) Loo, C.; Lowery, A.; Halas, N. J.; West, J. L.; Drezek, R. Immunotargeted Nanoshells for Integrated Cancer Imaging and Therapy. *Nano Lett.* **2005**, *5*, 709–711.
- (639) El-Sayed, I. H.; Huang, X. H.; El-Sayed, M. A. Selective Laser Photo-Thermal Therapy of Epithelial Carcinoma Using Anti-EGFR Antibody Conjugated Gold Nanoparticles. *Cancer Lett.* **2006**, *239*, 129.
- (640) Lu, W.; Xiong, C.; Zhang, G.; Huang, Q.; Zhang, R.; Zhang, J. Z.; Li, C. Targeted Photothermal Ablation of Murine Melanomas with Melanocyte-Stimulating Hormone Analog-Conjugated Hollow Gold Nanospheres. *Clin. Cancer Res.* **2009**, *15*, 876–886.
- (641) Melancon, M. P.; Zhou, M.; Zhang, R.; Xiong, C. Y.; Allen, P.; Wen, X. X.; Huang, Q.; Wallace, M.; Myers, J. N.; Stafford, R. J.; Liang, D.; Ellington, A. D.; Li, C. Selective Uptake and Imaging of Aptamer- and Antibody-Conjugated Hollow Nanospheres Targeted to Epidermal Growth Factor Receptors Overexpressed in Head and Neck Cancer. *ACS Nano* **2014**, *8*, 4530–4538.
- (642) Huff, T. B.; Tong, L.; Zhao, Y.; Hansen, M. N.; Cheng, J.-X.; Wei, A. Hyperthermic Effects of Gold Nanorods on Tumor Cells. *Nanomedicine* **2007**, *2*, 125–132.
- (643) Chen, J.; Wang, D.; Xi, J.; Au, L.; Siekkinen, A.; Warsen, A.; Li, Z.-Y.; Zhang, H.; Xia, Y.; Li, X. Immuno Gold Nanocages with Tailored Optical Properties of Targeted Photothermal Destruction of Cancer Cells. *Nano Lett.* **2007**, *7*, 1318–1322.
- (644) He, J.; Huang, X.; Li, Y.-C.; Liu, Y.; Babu, T.; Aronova, M. A.; Wang, S.; Lu, Z.; Chen, X.; Nie, Z. Self-Assembly of Amphiphilic Plasmonic Micelle-Like Nanoparticles in Selective Solvents. *J. Am. Chem. Soc.* **2013**, *135*, 7974–7984.
- (645) Qin, Z. P.; Bischof, J. C. Thermophysical and Biological Responses of Gold Nanoparticle Laser Heating. *Chem. Soc. Rev.* **2012**, *41*, 1191–1217.
- (646) Boulais, É.; Lachaine, R.; Meunier, M. Plasma-Mediated Nanocavitation and Photothermal Effects in Ultrafast Laser Irradiation of Gold Nanorods in Water. *J. Phys. Chem. C* **2013**, *117*, 9386–9396.
- (647) Tong, L.; Zhao, Y.; Huff, T. B.; Hansen, M. N.; Wei, A.; Cheng, J.-X. Gold Nanorods Mediate Tumor Cell Death by Compromising Membrane Integrity. *Adv. Mater.* **2007**, *19*, 3136–3141.
- (648) American National Standard for Safe Use of Lasers. ANSI Z136.1-2007.
- (649) Kennedy, L. C.; Bickford, L. R.; Lewinski, N. A.; Coughlin, A. J.; Hu, Y.; Day, E. S.; West, J. L.; Drezek, R. A. A New Era for Cancer Treatment: Gold-Nanoparticle-Mediated Thermal Therapies. *Small* **2011**, *7*, 169–183.
- (650) Lu, F.; Doane, T. L.; Zhu, J. J.; Burda, C. Gold Nanoparticles for Diagnostic Sensing and Therapy. *Inorg. Chim. Acta* **2012**, *393*, 142–153.
- (651) Hone, D. C.; Walker, P. I.; Evans-Gowing, R.; FitzGerald, S.; Beeby, A.; Chambrier, I.; Cook, M. J.; Russell, D. A. Generation of Cytotoxic Singlet Oxygen via Phthalocyanine-Stabilized Gold Nanoparticles: A Potential Delivery Vehicle for Photodynamic Therapy. *Langmuir* **2002**, *18*, 2985–2987.
- (652) Wieder, M. E.; Hone, D. C.; Cook, M. J.; Handsley, M. M.; Gavrilovic, J.; Russell, D. A. Intracellular Photodynamic Therapy with Photosensitizer-Nanoparticle Conjugates: Cancer Therapy Using a “Trojan Horse”. *Photochem. Photobiol. Sci.* **2006**, *5*, 727–734.
- (653) Camerin, M.; Magaraggia, M.; Soncin, M.; Jori, G.; Moreno, M.; Chambrier, I.; Cook, M. J.; Russell, D. A. The *In Vivo* Efficacy of Phthalocyanine-Nanoparticle Conjugates for the Photodynamic Therapy of Amelanotic Melanoma. *Eur. J. Cancer* **2010**, *46*, 1910–1918.
- (654) Pasparakis, G. Light-Induced Generation of Singlet Oxygen by Naked Gold Nanoparticles and its Implications to Cancer Cell Phototherapy. *Small* **2013**, *9*, 4130–4134.
- (655) Vankayala, R.; Sagadevan, A.; Vijayaraghavan, P.; Kuo, C.-L.; Hwang, K. C. Metal Nanoparticles Sensitize the Formation of Singlet Oxygen. *Angew. Chem., Int. Ed.* **2011**, *50*, 10640.
- (656) Zhao, T. T.; Shen, X. Q.; Li, L.; Guan, Z. P.; Gao, N. Y.; Yuan, P. Y.; Yao, S. Q.; Xu, Q. H.; Xu, G. Q. Gold Nanorods as Dual Photo-Sensitizing and Imaging Agents for Two-Photon Photodynamic Therapy. *Nanoscale* **2012**, *4*, 7712–7719.
- (657) Vankayala, R.; Huang, Y. K.; Kalluru, P.; Chiang, C. S.; Hwang, K. C. First Demonstration of Gold Nanorods-Mediated Photodynamic Therapeutic Destruction of Tumors via Near Infra-Red Light Activation. *Small* **2014**, *10*, 1612–1622.
- (658) Vankayala, R.; Lin, C. C.; Kalluru, P.; Chiang, C. S.; Hwang, K. C. Gold Nanoshells-Mediated Bimodal Photodynamic and Photothermal Cancer Treatment Using Ultra-Low Doses of Near Infra-Red Light. *Biomaterials* **2014**, *35*, 5527–5538.
- (659) Gao, L.; Liu, R.; Gao, F. P.; Wang, Y. L.; Jiang, X. L.; Gao, X. Y. Plasmon-Mediated Generation of Reactive Oxygen Species from Near-Infrared Light Excited Gold Nanocages for Photodynamic Therapy *in Vitro*. *ACS Nano* **2014**, *8*, 7260–7271.
- (660) Vijayaraghavan, P.; Liu, C. H.; Vankayala, R.; Chiang, C. S.; Hwang, K. C. Designing Multi-Branched Gold Nanoechinus for NIR Light Activated Dual Modal Photodynamic and Photothermal Therapy in the Second Biological Window. *Adv. Mater.* **2014**, *26*, 6689–6695.
- (661) Tubiana, M.; Dutreix, J.; Wambersie, A. *Introduction to Radiobiology*; Taylor & Francis: London, 1990.
- (662) Boudaïffa, B.; Cloutier, P.; Hunting, D.; Huels, M. A.; Sanche, L. Resonant Formation of DNA Strand Breaks by Low-Energy (3 to 20 eV) Electrons. *Science* **2000**, *287*, 1658–1660.
- (663) Beyzadeoglu, M.; Ozyigit, G.; Ebruli, C. *Basic Radiation Oncology*; Springer-Verlag: Berlin, 2010.
- (664) Kobayashi, K.; Usami, N.; Porcel, E.; Lacombe, S.; Le Sech, C. Enhancement of Radiation Effect by Heavy Elements. *Mutat. Res., Rev. Mutat. Res.* **2010**, *704*, 123–131.

- (665) Herold, D. M.; Das, I. J.; Stobbe, C. C.; Iyer, R. V.; Chapman, J. D. Gold Microspheres: A Selective Technique for Producing Biologically Effective Dose Enhancement. *D. Int. J. Radiat. Biol.* **2000**, *76*, 1357–1364.
- (666) Chien, C. C.; Wang, C. H.; Hua, T. E.; Tseng, P. Y.; Yang, T. Y.; Hwu, Y.; Chen, Y. J.; Chung, K. H.; Je, J. H.; Margaritondo, G. Synchrotron X-ray Synthesized Gold Nanoparticles for Tumor Therapy. *AIP Conf. Proc.* **2007**, *879*, 1908–1911.
- (667) Yasui, H.; Takeuchi, R.; Nagane, M.; Meike, S.; Nakamura, Y.; Yamamori, T.; Ikenaka, Y.; Kon, Y.; Murotani, H.; Oishi, M.; et al. Radiosensitization of Tumor Cells through Endoplasmic Reticulum Stress Induced by PEGylated Nanogel Containing Gold Nanoparticles. *Cancer Lett.* **2014**, *347*, 151–158.
- (668) Chang, M.-Y.; Shiau, A.-L.; Chen, Y.-H.; Chang, C.-J.; Chen, H.-W.; Wu, C.-L. Increased Apoptotic Potential and Dose-Enhancing Effect of Gold Nanoparticles in Combination with Single-Dose Clinical Electron Beams on Tumor-Bearing Mice. *Cancer Sci.* **2008**, *99*, 1479–1484.
- (669) Kong, T.; Zeng, J.; Wang, X.; Yang, X.; Yang, J.; McQuarrie, S.; McEwan, A.; Roa, W.; Chen, J.; Xing, J. Z. Enhancement of Radiation Cytotoxicity in Breast-Cancer Cells by Localized Attachment of Gold Nanoparticles. *Small* **2008**, *4*, 1537–1543.
- (670) Potters, L.; Cao, Y.; Calugaru, E.; Torre, T.; Fearn, P.; Wang, X.-H. A Comprehensive Review of CT-Based Dosimetry Parameters and Biochemical Control in Patients Treated with Permanent Prostate Brachytherapy. *Int. J. Radiat. Oncol., Biol., Phys.* **2001**, *50*, 605–614.
- (671) Yang, J.; Lee, J.; Kang, J.; Oh, S. J.; Ko, H. J.; Son, J. H.; Lee, K.; Suh, J. S.; Huh, Y. M.; Haam, S. Smart Drug-Loaded Polymer Gold Nanoshells for Systemic and Localized Therapy of Human Epithelial Cancer. *Adv. Mater.* **2009**, *21*, 4339–4342.
- (672) You, J.; Zhang, R.; Zhang, G.; Zhong, M.; Liu, Y.; Van Pelt, C. S.; Liang, D.; Wei, W.; Sood, A. K.; Li, C. Photothermal-Chemotherapy with Doxorubicin-Loaded Hollow Gold Nanospheres: A Platform for Near-Infrared Light-Trigged Drug Release. *J. Controlled Release* **2012**, *158*, 319–328.
- (673) Lee, S. M.; Park, H.; Yoo, K. H. Synergistic Cancer Therapeutic Effects of Locally Delivered Drug and Heat Using Multifunctional Nanoparticles. *Adv. Mater.* **2010**, *22*, 4049–4053.
- (674) Lee, S. M.; Park, H.; Choi, J. W.; Park, Y. N.; Yun, C. O.; Yoo, K. H. Multifunctional Nanoparticles for Targeted Chemophotothermal Treatment of Cancer Cells. *Angew. Chem., Int. Ed.* **2011**, *50*, 7581–7586.
- (675) Chen, H.; Zhang, X.; Dai, S.; Ma, Y.; Cui, S.; Achilefu, S.; Gu, Y. Multifunctional Gold Nanostar Conjugates for Tumor Imaging and Combined Photothermal and Chemo-Therapy. *Theranostics* **2013**, *3*, 633–649.
- (676) Liu, H.; Liu, T.; Wu, X.; Li, L.; Tan, L.; Chen, D.; Tang, F. Targeting Gold Nanoshells on Silica Nanorattles: A Drug Cocktail to Fight Breast Tumors via a Single Irradiation with Near-Infrared Laser Light. *Adv. Mater.* **2012**, *24*, 755–761.
- (677) Ma, M.; Chen, H.; Chen, Y.; Wang, X.; Chen, F.; Cui, X.; Shi, J. Au Capped Magnetic Core/Mesoporous Silica Shell Nanoparticles for Combined Photothermal-/Chemo-Therapy and Multimodal Imaging. *Biomaterials* **2012**, *33*, 989–998.
- (678) Zhang, Z.; Wang, J.; Chen, C. Near-Infrared Light-Mediated Nanoplatforams for Cancer Thermo-Chemotherapy and Optical Imaging. *Adv. Mater.* **2013**, *25*, 3869–3880.
- (679) Shen, S.; Tang, H.; Zhang, X.; Ren, J.; Pang, Z.; Wang, D.; Gao, H.; Qian, Y.; Jiang, X.; Yang, W. Targeting Mesoporous Silica-Encapsulated Gold Nanorods for Chemo-Photothermal Therapy with Near-Infrared Radiation. *Biomaterials* **2013**, *34*, 3150–3158.
- (680) Yang, X.; Liu, Z.; Li, Z.; Pu, F.; Ren, J.; Qu, X. Near-Infrared-Controlled, Targeted Hydrophobic Drug-Delivery System for Synergistic Cancer Therapy. *Chem. - Eur. J.* **2013**, *19*, 10388–10394.
- (681) Zhong, Y.; Wang, C.; Cheng, L.; Meng, F.; Zhong, Z.; Liu, Z. Gold Nanorod-Cored Biodegradable Micelles as a Robust and Remotely Controllable Doxorubicin Release System for Potent Inhibition of Drug Sensitive and – Resistant Cancer Cells. *Biomacromolecules* **2013**, *14*, 2411–2419.
- (682) Sun, T.; Wang, Y.; Wang, Y.; Xu, J.; Zhao, X.; Vangveravong, S.; Mach, R. H.; Xia, Y. Using SV119-Gold Nanocage Conjugates to Eradicate Cancer Cells Through a Combination of Photothermal and Chemo Therapies. *Adv. Healthcare Mater.* **2014**, *3*, 1283–1291.
- (683) Hong, G.; Wu, J. Z.; Robinson, J. T.; Wang, H.; Zhang, B.; Dai, H. Three-Dimensional Imaging of Single Nanotube Molecule Endocytosis on Plasmonic Substrates. *Nat. Commun.* **2012**, *3*, 700.
- (684) Feng, L.; Yang, X.; Shi, X.; Tan, X.; Peng, R.; Wang, J.; Liu, Z. Polyethylene Glycol and Polyethylenimine Dual-Functionalized Nano-Graphene Oxide for Photothermally Enhanced Gene Delivery. *Small* **2013**, *9*, 1989–1997.
- (685) Shi, S.; Zhu, X.; Zhao, Z.; Fang, W.; Chen, M.; Huang, Y.; Chen, X. Photothermally Enhanced Photodynamic Therapy Based on Mesoporous Pd@Ag@mSiO₂ Nanocarriers. *J. Mater. Chem. B* **2013**, *1*, 1133–1141.
- (686) Jang, B.; Park, J. Y.; Tung, C. H.; Kim, I. H.; Choi, Y. Gold Nanorod-Photosensitizer Complex for Near-Infrared Fluorescence Imaging and Photodynamic/Photothermal Therapy in Vivo. *ACS Nano* **2011**, *5*, 1086–1094.
- (687) Huang, P.; Bao, L.; Zhang, C.; Lin, J.; Luo, T.; Yang, D.; He, M.; Li, Z.; Gao, G.; Gao, B.; Fu, S.; Cui, D. Folic Acid-Conjugated Silica-Modified Gold Nanorods for X-ray/CT Imaging-Guided Dual-Mode Radiation and Photothermal Therapy. *Biomaterials* **2011**, *32*, 9796–9809.
- (688) Lin, J.; Wang, S.; Huang, P.; Wang, Z.; Chen, S.; Niu, G.; Li, W.; He, J.; Cui, D.; Lu, G.; Chen, X.; Nie, Z. Photosensitizer-Loaded Gold Vesicles with Strong Plasmonic Coupling Effect for Imaging-Guided Photothermal/Photodynamic Therapy. *ACS Nano* **2013**, *7*, 5320–5329.
- (689) Topete, A.; Alatorre-Meda, M.; Iglesias, P.; Villar-Alvarez, E. M.; Barbosa, S.; Costoya, J. A.; Taboada, P.; Mosquera, V. Fluorescent Drug-Loaded, Polymeric-Based, Branched Gold Nanoshells for Localized Multimodal Therapy and Imaging of Tumoral Cells. *ACS Nano* **2014**, *8*, 2725–2738.
- (690) Hirn, S.; Semmler-Behnke, M.; Schleh, C.; Wenk, A.; Lipka, J.; Schäffler, M.; Takenaka, S.; Möller, W.; Schmid, G.; Simon, U.; Kreyling, W. G. Particle Size-Dependent and Surface Charge-Dependent Biodistribution of Gold Nanoparticles after Intravenous Administration. *Eur. J. Pharm. Biopharm.* **2011**, *77*, 407–416.
- (691) Albanese, A.; Tang, P. S.; Chan, W. C. W. The Effect of Nanoparticle Size, Shape, and Surface Chemistry on Biological Systems. *Annu. Rev. Biomed. Eng.* **2012**, *14*, 1–16.
- (692) Yoo, J.-W.; Chambers, E.; Mitragotri, S. Factors that Control the Circulation Time of Nanoparticles in Blood: Challengers, Solutions and Future Prospects. *Curr. Pharm. Des.* **2010**, *16*, 2298–2307.
- (693) Xia, X.; Yang, M.; Wang, Y.; Zheng, Y.; Li, Q.; Chen, J.; Xia, Y. Quantifying the Coverage Density of Poly(ethylene glycol) Chains on the Surface of Gold Nanostructures. *ACS Nano* **2012**, *6*, 512–522.
- (694) Sykes, E. A.; Chen, J.; Zheng, G.; Chan, W. C. W. Investigating the Impact of Nanoparticle Size on Active and Passive Tumor Targeting Efficiency. *ACS Nano* **2014**, *8*, 5696–5706.
- (695) Chou, L. Y. T.; Chan, W. C. W. Fluorescence-Tagged Gold Nanoparticles for Rapid Characterization the Size-Dependent Biodistribution in Tumor Models. *Adv. Healthcare Mater.* **2012**, *1*, 714–721.
- (696) Longmire, M.; Choyke, P. L.; Kobayashi, H. Clearance Properties of Nano-Sized Particles and Molecules as Imaging Agents: Considerations and Caveats. *Nanomedicine* **2008**, *3*, 703–717.
- (697) Cedervall, T.; Lynch, I.; Lindman, S.; Berggard, T.; Thulin, E.; Nilsson, H.; Dawson, K. A.; Linse, S. Understanding the Nanoparticle-Protein Corona Using Methods to Quantify Exchange Rates and Affinities of Proteins for Nanoparticles. *Proc. Natl. Acad. Sci. U. S. A.* **2007**, *104*, 2050–2055.
- (698) Gessner, A.; Lieske, A.; Paulke, B. R.; Müller, R. H. Influence of Surface Charge Density on Protein Adsorption on Polymeric Nanoparticles: Analysis by Two-Dimensional Electrophoresis. *Eur. J. Pharm. Biopharm.* **2002**, *54*, 165–170.

- (699) Vonarbourg, A.; Passirani, C.; Saulnier, P.; Benoit, J.-P. Parameters Influencing the Stealthiness of Colloidal Drug Delivery Systems. *Biomaterials* **2006**, *27*, 4356–4373.
- (700) Moghimi, S. M.; Szebeni, J. Stealth Liposomes and Long Circulating Nanoparticles: Critical Issues in Pharmacokinetics, Opsonization and Protein-Binding Properties. *Prog. Lipid Res.* **2003**, *42*, 463–478.
- (701) Moghimi, S. M.; Hunter, A. C.; Murray, J. C. Long-Circulating and Target-Specific Nanoparticles: Theory to Practice. *Pharmacol. Rev.* **2001**, *53*, 283–318.
- (702) Anderson, J. M.; Van Itallie, C. M. Physiology and Function of the Tight Junction. *Cold Spring Harbor Perspect. Biol.* **2009**, *1*, a002584.
- (703) Maeda, H.; Nakamura, H.; Fang, J. The EPR Effect for Macromolecular Drug Delivery to Solid Tumors: Improvement of Tumor Uptake, Lowering of Systemic Toxicity, and Distinct Tumor Imaging *in Vivo*. *Adv. Drug Delivery Rev.* **2013**, *65*, 71–79.
- (704) Perrault, S. D.; Chan, W. C. W. In Vivo Assembly of Nanoparticle Components to Improve Targeted Cancer Imaging. *Proc. Natl. Acad. Sci. U. S. A.* **2010**, *107*, 11194–11199.
- (705) Matsumura, Y.; Maeda, H. A New Concept for Macromolecular Therapeutics in Cancer Chemotherapy: Mechanism of Tumorotropic Accumulation of Proteins and the Antitumor Agent Smancs. *Cancer Res.* **1986**, *46*, 6387–6392.
- (706) Yuan, F.; Dellian, M.; Fukumura, D.; Leunig, M.; Berk, D. A.; Torchilin, V. P.; Jain, R. K. Vascular Permeability in a Human Tumor Xenograft: Molecular Size Dependence and Cutoff Size. *Cancer Res.* **1995**, *55*, 3752–3756.
- (707) Jain, R. K.; Stylianopoulos, T. Delivering Nanomedicine to Solid Tumors. *Nat. Rev. Clin. Oncol.* **2010**, *7*, 653–664.
- (708) Semmler-Behnke, M.; Kreyling, W. G.; Lipka, J.; Fertsch, S.; Wenk, A.; Takenaka, S.; Schmid, G.; Brandau, W. Biodistribution of 1.4- and 18- nm Gold Particles in Rats. *Small* **2008**, *4*, 2108–2111.
- (709) Niidome, T.; Yamagata, M.; Okamoto, Y.; Akiyama, Y.; Takahashi, H.; Kawano, T.; Katayama, Y.; Niidome, Y. PEG-Modified Gold Nanorods with a Stealth Character for *in Vivo* Applications. *J. Controlled Release* **2006**, *114*, 343–347.
- (710) Akiyama, Y.; Mori, T.; Katayama, Y.; Niidome, T. The Effects of PEG Grafting Level and Injection Dose on Gold Nanorod Biodistribution in the Tumor-Bearing Mice. *J. Controlled Release* **2009**, *139*, 81–84.
- (711) Zhang, X.-D.; Wu, D.; Shen, X.; Liu, P.-X.; Fan, F.-Y.; Fan, S.-J. *In Vivo* Renal Clearance, Biodistribution, Toxicity of Gold Nanoclusters. *Biomaterials* **2012**, *33*, 4628–4638.
- (712) Garay, R. P.; El-Gewely, R.; Armstrong, J. K.; Garratty, G.; Richette, P. Antibodies Against Polyethylene Glycol in Healthy Subjects and in Patients Treated with PEG-Conjugated Agents. *Expert Opin. Drug Delivery* **2012**, *9*, 1319–1323.
- (713) Shimizu, T.; Ichihara, M.; Yoshioka, Y.; Ishida, T.; Nakagawa, S.; Kiwada, H. Intravenous Administration of Polyethylene Glycol-Coated (PEGylated) Proteins and PEGylated Adenovirus Elicits an Anti-PEG Immunoglobulin M Response. *Biol. Pharm. Bull.* **2012**, *35*, 1336–1342.
- (714) Niidome, Y.; Nishioka, K.; Kawasaki, H.; Yamada, S. Rapid Synthesis of Gold Nanorods by the Combination of Chemical Reduction and Photoirradiation Process; Morphological Changes Depending on the Growing Processes. *Chem. Commun.* **2003**, 2376–2377.
- (715) Chen, H.; Dorrigan, A.; Saad, S.; Hare, D. J.; Cortie, M. B.; Valenzuela, S. M. *In Vivo* Study of Spherical Gold Nanoparticles: Inflammatory Effects and Distribution in Mice. *PLoS One* **2013**, *8*, e58208.
- (716) Wang, H.; Zheng, L.; Peng, C.; Shen, M.; Shi, X.; Zhang, G. Folic Acid-Modified Dendrimer-Entrapped Gold Nanoparticles as Nanoprobes for Targeted CT Imaging of Human Lung Adenocarcinoma. *Biomaterials* **2013**, *34*, 470–480.
- (717) Marega, R.; Karmani, L.; Flamant, L.; Nageswaran, P. G.; Valembos, V.; Masereel, B.; Feron, O.; Borghet, T. V.; Lucas, S.; Michiels, C.; Gallez, B.; Bonifazi, D. Antibody-Functionalized Polymer-Coated Gold Nanoparticles Targeting Cancer Cells: An *in Vitro* and *in Vivo* Study. *J. Mater. Chem.* **2012**, *22*, 21305–21312.
- (718) Dam, D. H. M.; Culver, K. S. B.; Kandela, I.; Lee, R. C.; Chandra, K.; Lee, H.; Mantis, C.; Ugolkov, A.; Mazar, A. P.; Odom, T. W. Biodistribution and *in Vivo* Toxicity of Aptamer-Loaded Gold Nanostars. *Nanomedicine* **2015**, *11*, 671–679.
- (719) Farokhzad, O. C.; Langer, R. Impact of Nanotechnology on Drug Delivery. *ACS Nano* **2009**, *3*, 16–20.
- (720) Pirolo, K. F.; Chang, E. H. Does a Targeting Ligand Influence Nanoparticle Tumor Localization or Uptake? *Trends Biotechnol.* **2008**, *26*, 552–558.
- (721) Kirpotin, D. B.; Drummond, D. C.; Shao, Y.; Shalaby, M. R.; Hong, K.; Nielsen, U. B.; Marks, J. D.; Benz, C. C.; Park, J. W. Antibody Targeting of Long-Circulating Lipidic Nanoparticles Does not Increase Tumor Localization but Does Increase Internalization in Animal Models. *Cancer Res.* **2006**, *66*, 6732–6740.
- (722) Dass, C. R.; Choong, P. F. M. Selective Gene Delivery for Cancer Therapy using Cationic Liposomes: *In Vivo* Proof of Applicability. *J. Controlled Release* **2006**, *113*, 155–163.
- (723) Hilgenbrink, A. R.; Low, P. S. Folate Receptor-Mediated Drug Targeting: From Therapeutics to Diagnostics. *J. Pharm. Sci.* **2005**, *94*, 2135–2146.
- (724) Daniels, T. R.; Delgado, T.; Rodriguez, J. A.; Helguera, G.; Penichet, M. L. The Transferrin Receptor Part I: Biology and Targeting with Cytotoxic Antibodies for the Treatment of Cancer. *Clin. Immunol.* **2006**, *121*, 144–158.
- (725) Neri, D.; Bicknell, R. Tumor Vascular Targeting. *Nat. Rev. Cancer* **2005**, *5*, 436–446.
- (726) von Maltzahn, G.; Park, J.-H.; Lin, K. Y.; Singh, N.; Schwoeppe, C.; Mesters, R.; Berdel, W. E.; Ruoslahti, E.; Sailor, M. J.; Bhatia, S. N. Nanoparticles that Communicate *in Vivo* to Amplify Tumor Targeting. *Nat. Mater.* **2011**, *10*, 545–552.
- (727) Wang, Y.; Brown, P.; Xia, Y. Nanomedicine: Swarming towards the Target. *Nat. Mater.* **2011**, *10*, 482–483.
- (728) Lukianova-Hleb, E. Y.; Ren, X.; Zasadzinski, J. A.; Wu, X.; Lapotko, D. O. Plasmonic Nanobubbles Enhance Efficacy and Selectivity of Chemotherapy Against Drug-Resistant Cancer Cells. *Adv. Mater.* **2012**, *24*, 3831–3837.
- (729) Delcea, M.; Sternberg, N.; Yashchenok, A. M.; Georgieva, R.; Bäuml, H.; Möhwald, H.; Skirtach, A. G. Nanoplasmonics for Dual-Molecule Release through Nanopores in the Membrane of Red Blood Cells. *ACS Nano* **2012**, *6*, 4169–4180.
- (730) Alkilany, A. M.; Murphy, C. J. Toxicity and Cellular Uptake of Gold Nanoparticles: What We Have Learnt so Far? *J. Nanopart. Res.* **2010**, *12*, 2313–2333.
- (731) Chen, Y.-S.; Hung, Y.-C.; Liao, I.; Huang, G. S. Assessment of the *in Vivo* Toxicity of Gold Nanoparticles. *Nanoscale Res. Lett.* **2009**, *4*, 858–864.
- (732) Khlebtsov, N.; Dykman, L. Biodistribution and Toxicity of Engineered Gold Nanoparticles: A Review of *in Vitro* and *in Vivo* Studies. *Chem. Soc. Rev.* **2011**, *40*, 1647–1671.
- (733) Soenen, S. J.; Rivera-Gil, P.; Montenegro, J.-M.; Parak, W. J.; De Smedt, S. C.; Braeckmans, K. Cellular Toxicity of Inorganic Nanoparticles: Common Aspects and Guidelines for Improved Nanotoxicity Evaluation. *Nano Today* **2011**, *6*, 446–465.
- (734) Hauck, T. S.; Ghazani, A. A.; Chan, W. C. W. Assessing the Effect of Surface Chemistry on Gold Nanorod Uptake, Toxicity, and Gene Expression in Mammalian Cells. *Small* **2008**, *4*, 153–159.
- (735) Cho, W.-S.; Cho, M.; Jeong, J.; Choi, M.; Han, B. S.; Shin, H.-S.; Hong, J.; Chung, B. H.; Jeong, J.; Cho, M.-H. Size-Dependent Tissue Kinetics of PEG-Coated Gold Nanoparticles. *Toxicol. Appl. Pharmacol.* **2010**, *245*, 116–123.
- (736) Huang, X.-L.; Zhang, B.; Ren, L.; Ye, S.-F.; Sun, L.-P.; Zhang, Q.-Q.; Tan, M.-C.; Chow, G.-M. *In Vivo* Toxic Studies and Biodistribution of Near Infrared Sensitive Au-Au₂S Nanoparticles as Potential Drug Delivery Carriers. *J. Mater. Sci.: Mater. Med.* **2008**, *19*, 2581–2588.

- (737) Sadauskas, E.; Danscher, G.; Stoltenberg, M.; Vogel, U.; Larsen, A.; Wallin, H. Protracted Elimination of Gold Nanoparticles from Mouse Liver. *Nanomedicine* **2009**, *5*, 162–169.
- (738) Libutti, S. K.; Paciotti, G. F.; Byrnes, A. A.; Alexander, H. R., Jr.; Gannon, W. E.; Walker, M.; Seidel, G. D.; Yuldasheva, N.; Tamarkin, L. Phase I and Pharmacokinetic Studies of CYT-6091, a Novel PEGylated Colloidal Gold-rhTNF Nanomedicine. *Clin. Cancer Res.* **2010**, *16*, 6139–6149.
- (739) Simpson, C. A.; Salleng, K. J.; Cliffl, D. E.; Feldheim, D. L. *In Vivo* Toxicity, Biodistribution, and Clearance of Glutathione-Coated Gold Nanoparticles. *Nanomedicine* **2013**, *9*, 257–263.
- (740) Dreaden, E. C.; Mackey, M. A.; Huang, X.; Kang, B.; El-Sayed, M. A. Beating Cancer in Multiple Ways Using Nanogold. *Chem. Soc. Rev.* **2011**, *40*, 3391–3404.
- (741) Deen, W. M.; Lazzara, M. J.; Myers, B. D. Structural Determinants of Glomerular Permeability. *Am. J. Physiol.* **2001**, *281*, F579–F596.
- (742) Ohlson, M.; Sörensson, J.; Haraldsson, B. A Gel-Membrane Model of Glomerular Charge and Size Selectivity in Series. *Am. J. Physiol.* **2001**, *280*, F396–F405.
- (743) Choi, H. S.; Liu, W.; Misra, P.; Tanaka, E.; Zimmer, J. P.; Ipe, B. I.; Bawendi, M. G.; Frangioni, J. V. Renal Clearance of Quantum Dots. *Nat. Biotechnol.* **2007**, *25*, 1165–1170.
- (744) Zhou, C.; Long, M.; Qin, Y.; Sun, X.; Zheng, J. Luminescent Gold Nanoparticles with Efficient Renal Clearance. *Angew. Chem., Int. Ed.* **2011**, *50*, 3168–3172.
- (745) Alric, C.; Miladi, I.; Kryza, D.; Taleb, J.; Lux, F.; Bazzi, R.; Billotey, C.; Janier, M.; Perriat, P.; Roux, S.; Tillement, O. The Biodistribution of Gold Nanoparticles Designed for Renal Clearance. *Nanoscale* **2013**, *5*, 5930–5939.
- (746) Zhang, X.-D.; Wu, D.; Shen, X.; Liu, P.-X.; Fan, F.-Y.; Fan, S.-J. *In Vivo* Renal Clearance, Biodistribution, Toxicity of Gold Nanoclusters. *Biomaterials* **2012**, *33*, 4628–4638.
- (747) Liu, J.; Yu, M.; Ning, X.; Zhou, C.; Yang, S.; Zheng, J. PEGylation and Zwitterionization: Pros and Cons in the Renal Clearance and Tumor Targeting of Near-IR-Emitting Gold Nanoparticles. *Angew. Chem., Int. Ed.* **2013**, *52*, 12572–12576.
- (748) Tam, J. M.; Tam, J. O.; Murthy, A.; Ingram, D. R.; Ma, L. L.; Travis, K.; Johnston, K. P.; Sokolov, K. V. Controlled Assembly of Biodegradable Plasmonic Nanoclusters for Near-Infrared Imaging and Therapeutic Applications. *ACS Nano* **2010**, *4*, 2178–2184.
- (749) Chou, L. Y. T.; Zagorovsky, K.; Chan, W. C. W. DNA Assembly of Nanoparticle Superstructures for Controlled Biological Delivery and Elimination. *Nat. Nanotechnol.* **2014**, *9*, 148–155.
- (750) <http://www.nanospectra.com/index.html>.
- (751) Draine, B. T.; Hensley, B. Magnetic Nanoparticles in the Interstellar Medium: Emission Spectrum and Polarization. *Astrophys. J.* **2013**, *765*, 159.
- (752) Gupta, A. K.; Gupta, M. Synthesis and Surface Engineering of Iron Oxide Nanoparticles for Biomedical Applications. *Biomaterials* **2005**, *26*, 3995–4021.
- (753) Laurent, S.; Forge, D.; Port, M.; Roch, A.; Robic, C.; Vander Elst, L.; Muller, R. N. Magnetic Iron Oxide Nanoparticles: Synthesis, Stabilization, Vectorization, Physicochemical Characterizations, and Biological Applications. *Chem. Rev.* **2008**, *108*, 2064–2110.
- (754) Gao, J.; Gu, H.; Xu, B. Multifunctional Magnetic Nanoparticles: Design, Synthesis, and Biomedical Applications. *Acc. Chem. Res.* **2009**, *42*, 1097–1107.